

© 2021 by Jackson Ang'ong'a. All rights reserved.

TOWARDS SYNTHETIC RYDBERG LATTICES WITH OPTICAL TWEEZER
ARRAYS

BY

JACKSON ANG'ONG'A

DISSERTATION

Submitted in partial fulfillment of the requirements
for the degree of Doctor of Philosophy in Physics
in the Graduate College of the
University of Illinois Urbana-Champaign, 2021

Urbana, Illinois

Doctoral Committee:

Associate Professor Virginia Lorenz, Chair
Associate Professor Bryce Gadway, Director of Research
Professor Vidya Madhavan
Professor Paul Kwiat

Abstract

Trapped neutral atoms in optical tweezers have emerged as a viable platform for quantum simulation, metrology and quantum information processing due to their simple design yet versatile application. Recent developments in loading, cooling and re-arrangement techniques have been combined with Rydberg interactions and have led to insightful studies of quantum many-body phenomena based on analog simulation of Ising and XY models. So far, such systems have mostly been limited to interactions that involve one or two Rydberg states. Concurrently, synthetic lattices have also emerged as a viable platform for quantum simulation of many-body systems through site-by-site engineering of many-body Hamiltonians. Synthetic lattices feature both full spectroscopic control and tunability of every single-body term in the simulated Hamiltonian and thereby enable a bottom-up approach to studying emergent phenomena when combined with interactions. In our experiment, we bring the idea of synthetic lattices to a system of potassium atoms trapped in optical tweezer arrays, where tweezer-trapped atoms are excited to a Rydberg state followed by applying multi-tone microwave fields to drive transitions to neighboring Rydberg levels. While such a synthetic lattice can be used to study topology and disorder in 1D, our system allows us to bring Rydberg interaction into the picture and study the interplay between topology, disorder and interactions. One novel phenomenon that has been identified to appear in such a system is the spontaneous formation of quantum strings in the synthetic dimension.

This work also presents some technical studies on cooling and imaging of single atoms in optical tweezers in preparation for Rydberg excitation. Specifically, we demonstrate a simple approach to in-trap imaging which involves using a near-detuned (780 nm) optical tweezer, which leads to relatively minor differential (ground vs. excited state) Stark shifts. We

demonstrate that simple and robust loading, cooling, and imaging can be achieved through a combined addressing of the D1 (770 nm) and D2 (767 nm) transitions. While imaging on the D2 transition, we can simultaneously apply Λ -enhanced gray molasses (GM) on the D1 transition, preserving low backgrounds for single-atom imaging through spectral filtering. Using D1 cooling during and after trap loading, we demonstrate enhanced (75%) loading efficiencies as well as cooling to low temperatures ($\approx 15 \mu\text{K}$). These results suggest a simple and robust path for loading and cooling large arrays of potassium atoms in optical tweezers, through the use of resource-efficient near-detuned optical tweezers and GM cooling.

For Juma, Sellah, Charlie, Zippy and Joseph

Acknowledgments

First I would like to thank my advisor Bryce Gadway for guidance throughout my time at Illinois. Thank you for teaching me how to think as an experimentalist, how to select useful experimental questions to be addressed and for equipping me with the skills to investigate these. Thank you for always finding a way to keep the experiment going especially at difficult times. I would like to thank Jake Covey for inspiring carefulness and experimental rigor, that enabled us to make rapid progress at the later stages of the experiment. Your ability to ask the questions that do matter and useful suggestions have helped propel the project forward. Special thanks to Brian DeMarco for very important advice regarding different experimental challenges. Your vast knowledge on experimental tricks of the cold atom trade was invaluable for getting our experiment to run more smoothly and efficiently. Special thanks to Zeyun Liu, who was instrumental in the development of both potassium experiments in our lab. Your work ethic and resilience was definitely key in getting the experiment up and running at later stages. I would like to thank Huang Chen (Chenxi) for helping with numerical calculations at the later stages. Your eagerness to learn, ability to quickly understand new concepts and unmatched work ethic will definitely be invaluable for the project as we move forward to a more exciting phase. Thank you Sai for helping out at the beginning stages of the experiment and later for collaborating with me on different sub-projects. Your infectious laugh (already immortalized on youtube) will forever be remembered. Thank you Shraddha for your impeccable work ethic when our experiments were intertwined and for your interest in learning about just about any concept relevant to cold atom physics, and for all the fries I owe you for always being right. Garrett Williams, thanks for your eagerness to learn about how things work and for asking questions that probe me to really try to understand topics that I have otherwise overlooked. Thank you for very useful feedback on my presentation slides that has helped me improve my presentation and for producing remarkable artwork.

I would like to thank Michael Highman, not only for stimulating intellectual discussions but also for fun goofy times that have made all of us laugh. Thank you also for advise on how to deal with different experimental challenges and your role in inviting literal geniuses to join our lab. Special thanks to Eric Meier for very fruitful collaborations at different stages of my time. Your ability to understand and troubleshoot just about any equipment was definitely critical for the development of my apparatus. Thank you for the fun times while operating the iconic Rubidium MSL experiments. Thank you to Kristina Meier for directly helping out with fiber splicing and educating us on proper fiber handling practices. Special thanks to Alex An for impressive attention to detail, godlike alignment skills and for making us laugh during my time at Illinois. Also I appreciate your help with editing different pieces I have written throughout my time here. Thank you Samantha, Hannah I (Manetsch), Hannah II (Ullberg) and Rithi for helping out with optical and electronic set up during early stages of the experiment. I would like to thank Andreas Buchleitner, Vyacheslav Shatokhin and the QOS group at Freiburg for initial exposure to quantum optics and quantum information. This opportunity definitely sparked my interest in quantum science and encouraged my choice to join a cold atom lab. I would like to thank Ralf Möller at the RPLab for delivering high quality 3D printed parts for different purposes in the experiment. You have always handed us what we needed. I am particularly appreciative to Jim Brownfield for personally educating us on proper machining practices and for great conversations we have had. Thank you to Ernie Northen for helping us machine critical components that were necessary for setting up our vacuum chamber. Special recognition to my friends and family beyond UIUC: Claudia, Timo and Dennis for fun times during breaks. I am particularly grateful to Vince for support throughout the years. Daniel Kim for setting a good example as a scientist and for friendship over the years. Oli, thank you for amazing friendship throughout the years and for Martin's Bräu Bierdecker. Thank you to local friends in Champaign, Eva for helping out with edits by providing a perspective outside of physics; Asad, Thomas and Manthos for adventurous times and very intellectual discussions; and Sam Rubeck for working together on homeworks and on our theses. Finally, special thanks to my girlfriend Megan, your incredible support has enabled a smooth finish to my Ph.D.

Table of Contents

List of Figures	ix
Chapter 1: Introduction and background	1
1.1 Quantum simulation of many-body physics	1
1.2 Rydberg states of alkali atoms	3
1.3 Pair interactions and quantum simulation of spin models	4
1.4 A synthetic lattice of coupled Rydberg states	7
1.5 Proposed Experiment	10
1.5.1 Emergent bound states in Rydberg synthetic lattices of tweezer-trapped single atoms	10
1.5.2 Interplay between topology and interactions	12
1.6 Outline	16
Chapter 2: Methods I: Experimental apparatus for cold ^{39}K atoms	17
2.1 A four-chamber UHV design	18
2.1.1 Construction of the vacuum chamber	20
2.2 Details on laser preparation	22
2.3 Laser frequency stabilization	35
2.3.1 Polarization rotation spectroscopy	36
2.4 Construction and optimization of magneto-optical traps (MOTs) of ^{39}K atoms	42
2.5 Rapid transport of atoms between two sections	55
2.5.1 Transport of atoms in multi-section chambers	55
2.5.2 Transport using blue-detuned pulsed push beam	58
2.6 Capturing, cooling and optimization of a MOT from transferred atoms	62
2.6.1 Cooling	64
2.6.2 Optimization of experimental parameters using machine learning	77
Chapter 3: Single atom trapping in optical tweezers	87
3.1 Introduction	87
3.2 Optical set up	89
3.2.1 Science MOT setup	89
3.2.2 Optical tweezers	90
3.2.3 Optical tweezer set up	91
3.2.4 Tweezer alignment	94
3.3 Imaging and cooling set up for 780 nm trap	99
3.3.1 Setting up in-trap imaging and cooling	103

3.4	Loading a 780 nm trap: from zero to few atoms	104
3.4.1	Background sources	104
3.4.2	Loading multiple atoms in a mini-trap	107
3.5	Parity projection: killing two birds with one stone	109
3.5.1	Any beam can cause light-assisted collisions	111
3.5.2	Trap depth estimates	114
3.6	Enhanced loading: the biased coin-flip	118
3.6.1	Background: Blue-detuned inelastic light-assisted collisions	118
3.6.2	Enhanced loading in an optical tweezer	119
3.7	Cooling and non-destructive imaging	123
3.7.1	Release-recapture temperature measurement	123
3.7.2	Rampdown temperature measurement	126
3.7.3	Non-destructive interleaved imaging	130
3.8	Conclusion	133
Chapter 4: Outlook: Towards Rydberg synthetic lattices	135
4.1	Rydberg two-photon excitations	135
4.2	PDH locking	137
4.2.1	Background	137
4.2.2	PDH setup	139
4.2.3	Power amplification	147
4.3	Outlook	148
References	150
Appendix A: 3D MOT games	158
A.1	Test MOT	158
A.2	Fun with MOTs	159
A.3	Nominal Octagon MOT parameters	160
Appendix B: Retired erbium project	161
B.1	Erbium 2D MOT preparation	161
B.1.1	Creating quadrupole magnetic fields using permanent magnets	162
B.2	Injection locking of multi-mode diodes at 401nm	164
B.2.1	Optical set up	164
Appendix C: Thorlabs USB camera MATLAB control	167
Appendix D: Simulating Polarization Spectroscopy Signals	172
D.1	Theoretical modeling of polarization spectroscopy signal	172
D.2	Solving rate equations with Mathematica	176

List of Figures

1.1	Rydberg pair interactions	5
1.2	Rydberg blockade	6
1.3	Synthetic lattice of Rydberg levels	8
1.4	Microwave control of synthetic lattice of Rydberg states	9
1.5	Quantum strings in dipolar systems	10
1.6	1D SSH model of polyacetylene	12
1.7	1D SSH model band structure	13
1.8	Dipolar-interaction-modified chiral displacement in interacting SSH model .	14
2.1	Picture of the chamber <i>ca.</i> 2020	17
2.2	A four section vacuum chamber	19
2.3	Vacuum chamber assembly and bake-out	22
2.4	Tapered amplifier design	25
2.5	Laser system for trapping and cooling ^{39}K atoms	26
2.6	Potassium level diagram	27
2.7	Optimizing EOM sidebands	30
2.8	Polarization spectroscopy set up	37
2.9	Modeling polarization spectroscopy signal	39
2.10	Polarization spectroscopy signal optimization	40
2.11	Quantization field for $4S_{1/2} \rightarrow 5P_{3/2}$ PS signal	41
2.12	3D printed 3D MOT gradient coils	42
2.13	3D printed field cancellation coil holder	44
2.14	Magneto-optical traps	47
2.15	Transition strengths for $\sigma^+ 4S_{1/2} \rightarrow 4P_{3/2}$	48
2.16	2D MOT optical set up	49
2.17	^{39}K 2D MOT	50
2.18	Beam configuration for octagon chamber MOT	51
2.19	^{39}K 3D MOT loading and lifetime in the octagon chamber	52
2.20	Combining cycling and repump beams.	54
2.21	Top view of beam layout for transport of atoms from the octagon chamber to the science chamber	60
2.22	Transport of atoms from MOT1 to MOT2	61
2.23	Rapid transport of atoms between the octagon and science chamber using a blue-detuned beam	64
2.24	Polarization gradient in $\sigma^+ - \sigma^-$ configuration	66
2.25	Λ -enhanced gray molasses using ^{39}K D1 transition at 770nm	68

2.26	D1 laser preparation set up.	72
2.27	Initial optimization of gray molasses cooling parameters	74
2.28	Stray magnetic field cancellation	75
2.29	Time of flight fits after gray molasses cooling	75
2.30	Gray molasses cooling optimization	76
2.31	Cartoon showing online optimization using GP regression	79
2.32	Optimization of gray molasses cooling stage using MLOOP	81
2.33	Comparison between GP generated settings with manually optimized settings	83
2.34	Summary of the machine learning sequence	84
2.35	Final experimental sequence	85
3.1	Objectives mounted next to cell for single atom trapping <i>ca.</i> 2021	87
3.2	MOT beam layout at the science chamber	90
3.3	Optical set up for generating an array of optical tweezers	92
3.4	Mounting opto-mechanics for the Mitutoyo objective.	94
3.5	Alignment procedure for overlapping tweezer traps with MOT	95
3.6	Reconstructed beam profile	98
3.7	Tweezer light shifts on the D1 and D2 transitions	101
3.8	Compensating for Stark shift with a double pass AOM	103
3.9	Background reduction using narrow-line filters.	106
3.10	Blocking MOT beam stray light at focus points in the Fourier plane.	107
3.11	First signal of trapped potassium atoms in a dipole trap.	108
3.12	Multi-atom loading in a mini-trap	109
3.13	Attractive red-detuned inelastic light-assisted collisions	110
3.14	Single atom preparation using parity projection	111
3.15	Pairwise loss induced by imaging beam	112
3.16	Non-destructive imaging using Λ -enhanced gray molasses	114
3.17	Trap depth estimate based on D1 loading	115
3.18	Trap depth measurement	116
3.19	Blue-detuned inelastic light-assisted collisions	118
3.20	Single-atom loading using blue-detuned inelastic collisions	121
3.21	Gray molasses cooling sequence	124
3.22	Release-and-recapture technique	125
3.23	Temperature measurement using rampdown technique	127
3.24	Calculating x_{\max} for a potential without/with gravity.	129
3.25	Deviation due to gravity.	129
3.26	Non-destructive imaging.	131
3.27	Imaging fidelity with interleaved cooling.	132
3.28	Histogram showing high detection fidelity of potassium atoms in optical tweezers	133
4.1	Picture of the Pound-Drever-Hall set up <i>ca.</i> 2021	135
4.2	Rydberg excitation pathways	136
4.3	Cavity finesse estimation by ringdown spectroscopy	140
4.4	Potassium level diagram for the $4S \rightarrow 5P$ transition	141
4.5	Setup for locking 973 nm and 405 nm lasers to an ultra-high finesse cavity	142

4.6	Cost-saving Pound-Drever-Hall signal unit	143
4.7	Error signal generated using PDH-1000-5C	143
4.8	Comparison between PS signal and cavity reflection	144
4.9	Loss spectroscopy of the $4S \rightarrow 5P$ transition	144
4.10	Transmission peaks corresponding to incident beam driven using two RF tones (12.4 MHz and 400 MHz)	146
4.11	Frequency stabilization using MOGLabs Fast Servo Controller	147
4.12	Fiber based injection-seeding of a 980 nm ECDL.	147
4.13	Adding a quantization B field to separated unwanted transitions from a Rydberg synthetic lattice.	149
A.1	Test MOT in the source cell	159
A.2	Manipulating MOTs using near-resonant beams	159
B.1	Quadrupole high B field generation using permanent magnets for erbium 2DMOTs	162
B.2	Erbium 2D MOT Monte Carlo simulation	164
B.3	Injection locking set up	165
B.4	Multi-mode diode wavelength dependence on temperature	166
B.5	Erbium dispenser	166

Chapter 1

Introduction and background

1.1 Quantum simulation of many-body physics

Emergent phenomena that manifest in materials found in nature have generated a lot of interest and led to development of different experimental and theoretical techniques. In condensed matter physics a top-down approach is typically taken where crystals of interest are synthesized and characterized to directly reveal emergent many body phenomena. While this top-down approach has been incredibly successful, characterization at the microscopic level is still challenged by material defects, as well as the innate short length scales and fast time scales associated with electronic motion. Recent advances have been seen in systems that take a bottom-up approach where a simple system is constructed piece-by-piece and designed to realize a target Hamiltonian being studied. This idea was proposed in the context of quantum simulation [1] where a simple, well-controlled quantum system is used to simulate a more complex system. In such quantum simulators precise control over each parameter in the tailored Hamiltonian provides a means to explore different parameter regimes and enables quantum simulation of emergent phenomena in a controlled manner.

Quantum simulators have recently gained popularity because they have already made useful contributions to relevant research questions in a clean and **controlled** way. To this end, particle **interactions** have been included and combined with the ability to engineer arbitrary site **geometries** to implement many-body Hamiltonians that host a variety of interesting emergent phenomena. Compared to materials studies, quantum simulators have the advantage that one knows exactly the Hamiltonian being realized in experiment. Compared to numerical studies, one clear advantage of quantum simulators is that the numerical simulation of many-body systems becomes in general intractable very quickly with an increasing number of particles, due to the exponential scaling of the Hilbert space.

One promising new direction for quantum simulation is to utilize so-called “synthetic dimensions” [2], where field-driven transitions between the quantum states of a particle (e.g., internal spin states of an atom or molecule) are used to mimic the tunneling along a discrete extra dimension. This synthetic dimensions approach can enable the engineering of certain Hamiltonian terms, such as fine-tuned “disorder” or Abelian gauge fields for neutral atoms. Moreover, it also holds the potential to enable explorations of physics that would be hard to investigate in most natural settings, such as the physics associated with exotic interactions (multi-body, long-ranged), higher-dimensional ($> 3D$) models, curved space, and exotic topologies.

Again, in the synthetic dimension one emulates particle hopping through the field-driven transition of a particle between discrete quantum states. For a set of states with unique energy separations a lattice can be constructed where each site energy is directly controlled via detuning the corresponding driving field and each tunneling amplitude and phase bears a direct relationship to the amplitude and phase of the driving field. Since the properties of the driving field can be controlled precisely we can construct a synthetic lattice with full control over every term of the engineered Hamiltonian. Synthetic lattices have been realized using hyperfine states [3, 4], momentum states [5, 6], and electronic states [7, 8] among other platforms not mentioned.

Neutral atoms in optical tweezers arrays (OTAs) have recently emerged as a viable quantum simulation platform due to their simple design yet versatile applications. Here, individual atoms are trapped in deep conservative traps (depths of $U/k_B \approx$ few mK) created by tightly-focused beams which then enable the steering of the position of the atom [9, 10] and creation of arbitrary defect-free geometries [11]. Interactions have also been added through excitation of trapped atoms to high-lying Rydberg states that feature enhanced dipole moments. As a result neighboring Rydberg-excited atoms exhibit long-range dipole-dipole interactions ($V_{dd} \propto 1/r^3$ where r is the inter-atomic separation) that already enable the study of quantum magnetism using an Heisenberg XY model [12, 13] (as will be detailed in Section 1.3). Large Van der Waals interactions can also enable the exploration of quantum Ising models [9, 14–17], *i.e.*, via the same interactions that underly Rydberg blockade-based gates [18].

In this chapter we will introduce the idea of synthetic lattices to a system of potassium atoms trapped in OTAs. In particular, trapped atoms will first be excited to a Rydberg state followed by coupling to neighboring Rydberg states using microwave fields to create a synthetic lattice of Rydberg levels. Such a synthetic Rydberg lattice has recently been demonstrated in the Killian group at Rice University where bulk Rydberg-excited strontium atoms were used to realized a one-dimensional topological Su-Schrieffer-Heeger model [19]. In addition to studying topology and disorder in just one 1D (and 2D) synthetic lattices, our system will allow us to the study the interplay between topology, disorder and interactions in an effective two dimensional lattice. Here a real space array of trapped atoms form one or more real dimensions while the synthetic Rydberg lattice forms additional dimensions in the internal space.

In the next section we will first go through some background on Rydberg excitation and describe quantum simulation work already done using Rydberg excited atoms in OTAs. We will then describe our extension of this platform by coupling more than two Rydberg levels in an effort to create synthetic lattices of Rydberg levels.

1.2 Rydberg states of alkali atoms

Rydberg states are electronic states of neutral atoms where at least one valence electron is excited to a high-lying principle quantum number. Rydberg states of alkali atoms, which have one valence electron, are similar to the hydrogen atom because the inner electrons screen the nuclear charge less one proton charge. The energy of a generic Rydberg state is, therefore, described by the Rydberg formula. This is given by $E_{\text{ion}} - R_{\infty}/(n - \delta_{nlj})^2 = E_{\text{ion}} - R_{\infty}/(n^*)^2$ [20], where n , l and $j = l + s$ are the principle, orbital angular momentum and total angular momentum quantum numbers, respectively and s is the spin angular momentum quantum number. The Rydberg constant and the ionization energy are given by R_{∞} and E_{ion} , respectively. Imperfect screening by the inner shell electrons (pronounced for lower-lying Rydberg states) leads to a shift in the Rydberg levels. This shift is accounted for by the quantum defect, δ_{nlj} , which scales with n and is negligible for $l > 2$. The Rydberg formula for alkali atoms is, therefore, written in terms of an effective principle

quantum number, n^* . As expected, Rydberg atomic properties feature tremendous scaling with n^* [20, 21].

The highly-excited electron of a Rydberg atom is weakly bound and is characterized by a large separation from the atom’s center of mass position. One key consequence of this large separation between the nucleus and the outer electron is that Rydberg atoms are strongly polarizable. This makes Rydberg atoms very sensitive to applied electric fields, and thus potentially useful for electric field sensing. Of greater importance to us, this enhanced polarizability (scaling as $(n^*)^7$) corresponds to extreme transition dipole moments on the order of several thousand Debye. This results in extremely large dipole-dipole interactions between pairs of Rydberg atoms, which will be detailed shortly.

1.3 Pair interactions and quantum simulation of spin models

The huge dipole moments characteristic of Rydberg energy levels lead to strong interactions between Rydberg atoms. In the limit where the distance between the atomic cores of two Rydberg atoms is much larger than the size of the respective Rydberg atoms [22], the interaction between the two atoms is dominated by dipole-dipole interactions. These interactions are mediated by virtual photon exchange between the atoms. For example, if we consider two Rydberg atoms initialized in $|n, l\rangle$ states, $|70, s\rangle$ and $|69, p\rangle$ ¹. The first atom can decay to $|69, p\rangle$ and emit a photon via spontaneous emission. This process on its own occurs likely on timescales much longer than the Rydberg state lifetime. However, the (virtually) emitted photon could then be (virtually) absorbed by the second atom, leading to its excitation to the state $|70, s\rangle$ [23]. The dipole-dipole interaction strength between these Rydberg atoms (at positions j and j') is $V_{dd}^{j,j'} = -C_3^{j,j'}/R^3$, where $C_3^{j,j'} = \frac{1}{4\pi\epsilon_0}(\hat{d}_j \cdot \hat{d}_{j'} - 3(\hat{d}_j \cdot \hat{r}_{j,j'})(\hat{d}_{j'} \cdot \hat{r}_{j,j'}))(n_j^*)^2(n_{j'}^*)^2$ is the dipole-dipole coefficient, with \hat{d}_j being the dipole matrix element of atom j and $\hat{r}_{j,j'} = \vec{R}_{j,j'}/|\vec{R}_{j,j'}|$, where $\vec{R}_{j,j'}$ is a vector joining the two atoms and $|\vec{R}_{j,j'}| = R$, for brevity. The R^{-3} scaling reflects the strength of the virtually emitted photon field from one Rydberg atom at the position of the other.

¹As explained later in Section 1.4 we plan to excite individually trapped potassium atoms to $|70, s\rangle$ before turning on microwave drives to create synthetic lattices.

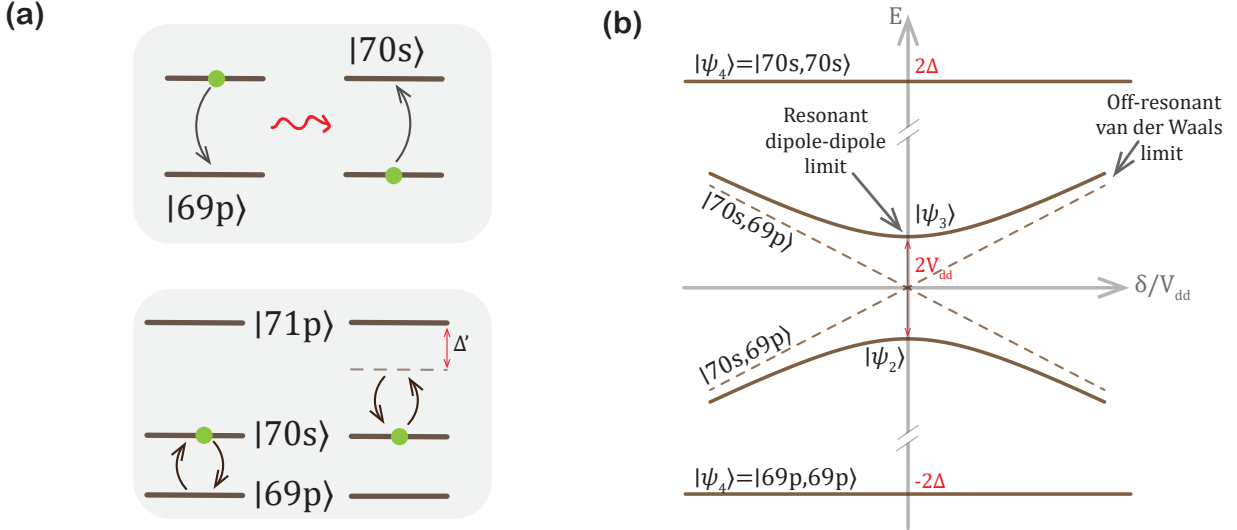


Figure 1.1: Pair interactions between two atoms excited to high-lying Rydberg levels. (a) Top, exchange interaction due to resonant dipole-dipole coupling in the short range limit. Bottom, off-resonant van der Waals interaction in the long range limit. (b) Avoided crossing picture. Interactions between two Rydberg atoms can be adiabatically tuned from dipole-dipole interactions to van der Waals interaction by varying δ/V_{dd} .

Two types of interactions arise from this description as detailed in Fig. 1.1. Here, we define $\delta = \Delta_2 - \Delta_1$ and $2\Delta = \Delta_1 + \Delta_2$, such that $\Delta \gg \delta$.

In the resonant case, $\delta \approx 0$, the two states are strongly coupled and the dynamics of the system are dominated by dipole-dipole exchange interactions which scale as $V_{dd} \propto (n^*)^4/R^3$. The two initial states hybridize to form $|\psi_3\rangle = \frac{1}{\sqrt{2}}(|70s, 69p\rangle + |70s, 69p\rangle)$ and $|\psi_2\rangle = \frac{1}{\sqrt{2}}(|70s, 69p\rangle - |70s, 69p\rangle)$. In this limit, transitions are governed by dipole selection rules, *i.e.* $\delta l = \pm 1$. If two different Rydberg states (satisfying dipole selection rules) are populated in a sample, then so long as there are no spatially varying “field” terms, Δ_j , dipole-dipole exchange interactions will be resonant.

By including a microwave field drive between the two states, *i.e.*, such the $\hbar\omega_{\mu\text{wave}} = E_{70s,j} - E_{69p,j}$ we can implement an Heisenberg XY spin model which is written as

$$H_{XY} = \frac{\hbar\Omega_{\mu\text{wave}}}{2} \sum_j \sigma_j^x - \hbar\delta_{\mu\text{wave}} \sum_j \sigma_j^z + \sum_{j,j'<j'} V_{dd}^{j,j'} (\sigma_j^+ \sigma_{j'}^- + \sigma_j^+ \sigma_{j'}^-) \quad (1.1)$$

where the first two terms correspond to transverse and longitudinal fields created by microwave fields characterized by detuning $\delta_{\mu\text{wave}}$ and Rabi frequency $\Omega_{\mu\text{wave}}$.

In the off-resonant case, $V_{dd} \ll \delta$, $|70s, 69p\rangle$ is only weakly hybridized with $|70s, 69p\rangle$. This leads to van der Waals interactions which occur at second-order, where Rydberg atoms initialized on the same state, $|70s, 70s\rangle$, can interact as illustrated in Fig. 1.1(a), bottom. The interaction strength is given by $\frac{1}{2\Delta'} V_{dd}^2 \propto (n^*)^{11}/R^6$.

An interesting feature of pair interaction of Rydberg atoms is the position dependent energy shift of the Rydberg states of an atom due to the presence of a highly excited Rydberg atom nearby. Consider beginning with the two atoms above, 1 and 2 in the ground state and Rydberg state, respectively. By applying an optical field that addresses the energy difference between the ground state and the Rydberg state, it is possible to excite atom 1 to its Rydberg state. However, as the distance between the two atoms is reduced, the Rydberg states corresponding to atom 2 are shifted by the interaction between the two atoms. At some distance R_B , the energy shift due to interaction between the two atoms is larger than the transition linewidth, Γ of the excited Rydberg state, which is effectively set by the Rabi rate of the microwave drive. This leads to an excitation blockade where atom 2 cannot be excited to its Rydberg state within a blockade radius R_B around atom 1.

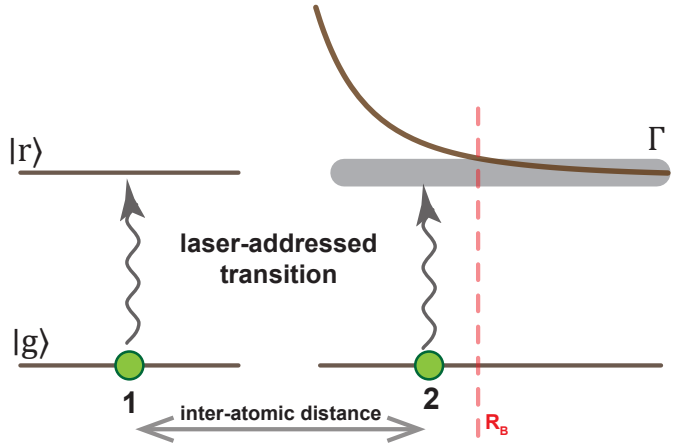


Figure 1.2: Rydberg blockade.

The Rydberg blockade can be used to implement the Ising model. Specifically, the distance between atoms is designed such that the blockade radius spans nearest neighboring sites. By mapping the ground and Rydberg states (which experience no dipole-dipole interaction and a practically negligible van der Waals interaction unless both atoms are in the

Rydberg level) to spin $|\downarrow\rangle$ and $|\uparrow\rangle$ a spin-1/2 system realized is described as

$$H_{\text{Ising}} = \frac{\hbar\Omega_L}{2} \sum_i \sigma_i^x - \hbar\delta_L \sum_i n_i + \sum_{i < j} \frac{C_6}{R_{i,j}^6} n_i n_j \quad (1.2)$$

where C_6 is the van der Waals interaction coefficient and $n_i = \frac{\sigma_i^z + 1}{2}$ is an operator describes whether the atom at site i is in the ground or Rydberg state (0 or 1). The first two terms correspond to transverse (B_\perp) and longitudinal (B_\parallel) fields that are implemented using a laser field detuned by δ_L and driving a transition at a Rabi rate Ω_L . Ising models realized in OTAs have been extensively studied over the past several years [9, 14–17].

1.4 A synthetic lattice of coupled Rydberg states

In this section, I describe our experimental scheme, where a synthetic lattice can be realized by first exciting an atom to a Rydberg state using optical fields, then resonantly driving transitions between Rydberg states using microwave fields. Since Rydberg levels are typically about a thousand THz above the ground state, direct excitation to these levels requires intense laser light deep in the ultraviolet.

Due to the lack of convenient lasers in this range, it is more common to access Rydberg levels through two-photon processes, which use lower-lying excited states as a virtual intermediary. Conveniently, the two light sources of such a two-photon approach can be in the optical or near-infrared range. In our case of potassium, we intend to couple the $4S_{1/2}$ valence electron to high-lying Rydberg levels by using the $5P_{3/2}$ as a virtual intermediary. This requires near-ultraviolet light at 405 nm (conveniently available due to blue-ray diode technology) for the $4S$ - $5P$ transition, as well as near-infrared light in the range of 970 – 980 nm to couple to S or D states in the range from roughly $n = 50$ to $n = 80$.

Once the atom is excited to Rydberg levels, such as $69S_{1/2}$, it can be coherently coupled to other Rydberg levels by microwave transitions in range of a few to tens of GHz. The microwave Rabi rates for such transitions can be strong (MHz rates and higher), much faster than the Rydberg level decay rates (as well as decoherence rates due to black-body radiation [24, 25]). Moreover, the spectrum of transitions between various Rydberg levels is

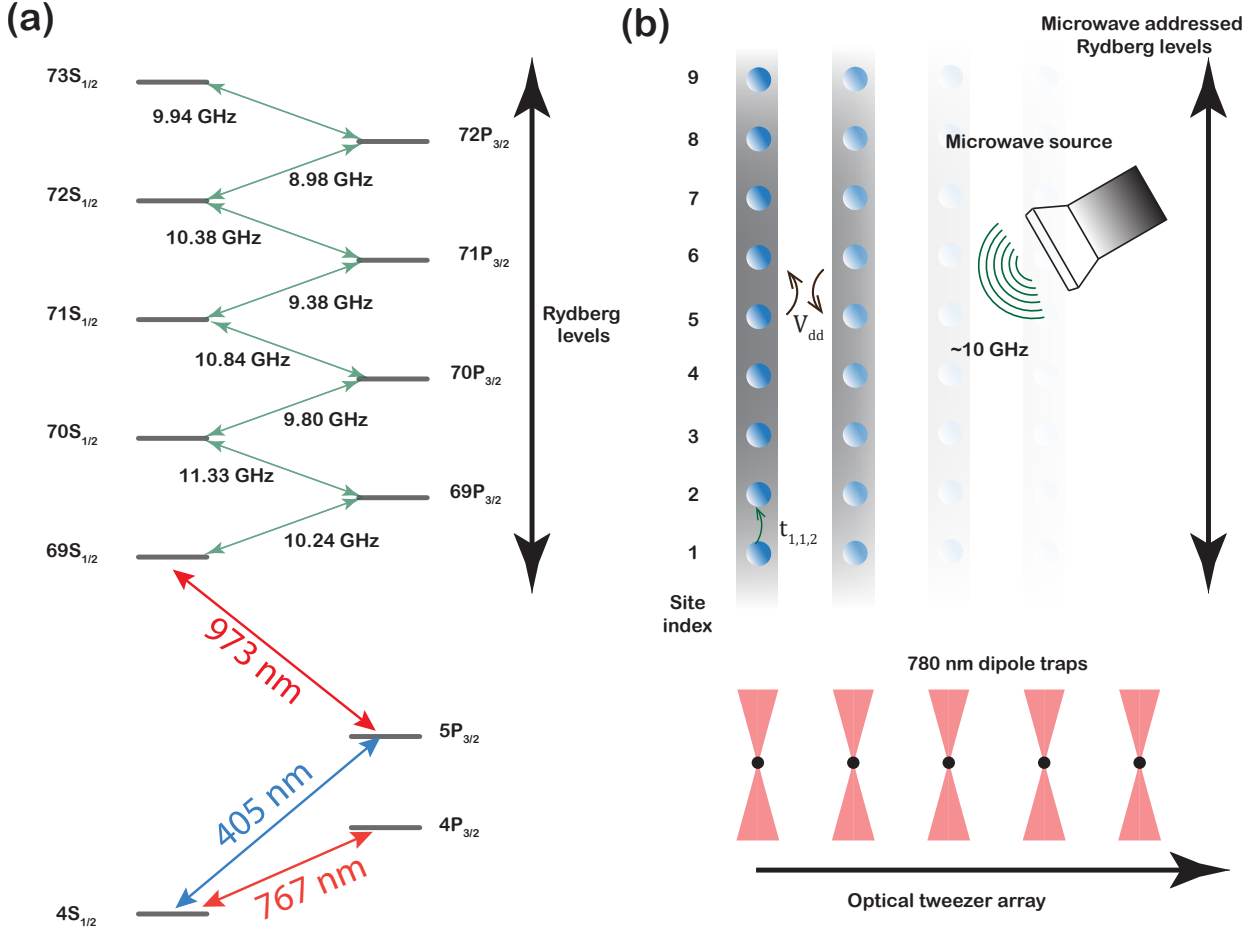


Figure 1.3: Synthetic lattice of Rydberg levels. (a) Level diagrams showing a set of Rydberg states coupled to form a synthetic lattice. (b) Two-dimensional lattice in which coupled Rydberg states forming the synthetic dimension and the OTA forming the real space lattice.

relatively sparse, such that a particular state-to-state transition can be driven at MHz rates with not too much concern of off-resonantly driving or affecting another transition.

This approach requires coherent control of microwaves at the multi-GHz range, ideally producing multiple frequencies simultaneously. To achieve our requirements on simultaneously driving multiple microwave transitions, we plan to combine agile frequency synthesis at lower frequencies (DC-1GHz) with frequency mixing to up-convert to higher frequencies. By tuning the amplitude and phase of the various frequency components, we can directly control the effective “tunneling” rates and phases between the various parametrically coupled Rydberg levels. As depicted in Fig. 1.3(c), further control over the effective landscape of single-particle site energies is enabled by the various detunings of the driving frequencies

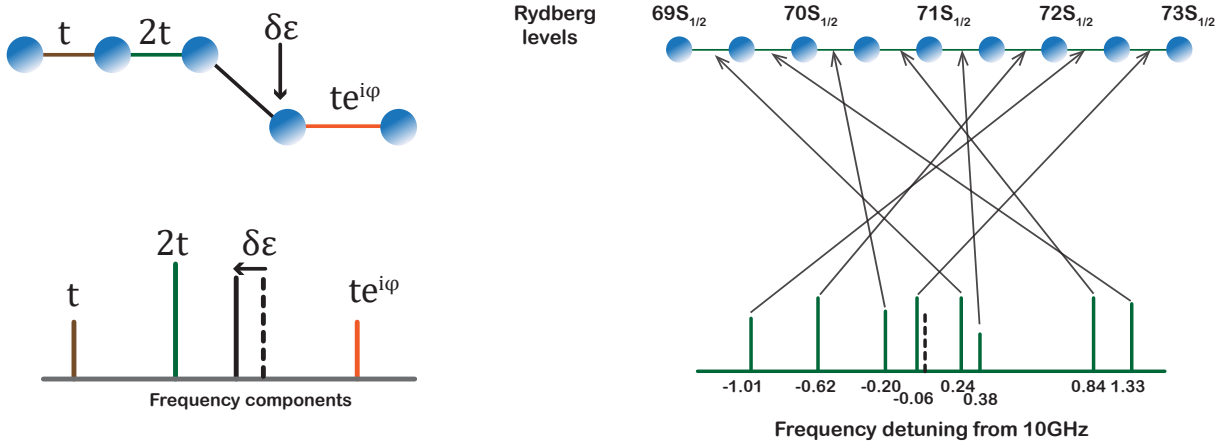


Figure 1.4: Microwave control of synthetic lattice of Rydberg states. Left, an effective tight-binding model can be fully controlled by tuning the properties of applied microwave field components. Right, tunneling between lattice sites are generated by tailored microwave fields. The ordering of the frequency do not directly match the tunnelings between adjacent Rydberg level. This is because the energy spacings between adjacent Rydberg levels that we link are not monotonic.

from their respective resonance conditions.

In addition to this described control of the effective single-particle Hamiltonian, the pairwise interactions between different Rydberg atoms, as described in Section 1.3, show up naturally as well. Considering only these resonant dipole-dipole interactions, our system is described by the Hamiltonian,

$$\hat{H} = \sum_{j,\sigma} t_{j,\sigma,\sigma+1} \hat{a}_{j,\sigma}^\dagger \hat{a}_{j,\sigma+1} + \varepsilon_{j,\sigma} \hat{a}_{j,\sigma}^\dagger \hat{a}_{j,\sigma} + \sum_{j,j',\sigma} V_{dd}^{j,j',\sigma}(R_{j,j'}) \hat{a}_{j,\sigma}^\dagger \hat{a}_{j,\sigma+1} \hat{a}_{j',\sigma+1}^\dagger \hat{a}_{j',\sigma} + \text{h.c.}, \quad (1.3)$$

where $\hat{a}_{j,\sigma}^\dagger (\hat{a}_{j,\sigma})$ represent creation (annihilation) of an atom at site j in the real space dimension and site σ in the synthetic dimension. Microwave tunable complex tunneling within the synthetic lattice, between sites σ and $\sigma + 1$, is given by $t_{j,\sigma,\sigma+1}$ while the site energy corresponding to site σ is given by $\varepsilon_{j,\sigma}$. The second term represents dipole exchange interaction between adjacent Rydberg atoms where $V_{dd}^{j,j',\sigma}(R_{j,j'})$ is the dipole-dipole coupling strength relating to synthetic sites σ and $\sigma + 1$ between two atoms at positions j and j' , and separated by a distance $R_{j,j'}$. The ability to accurately tune the parameters of this Hamiltonian will allow us to investigate how strong interactions can modify various transport phenomena associated with, *e.g.*, topology and disorder, and additionally how new types of

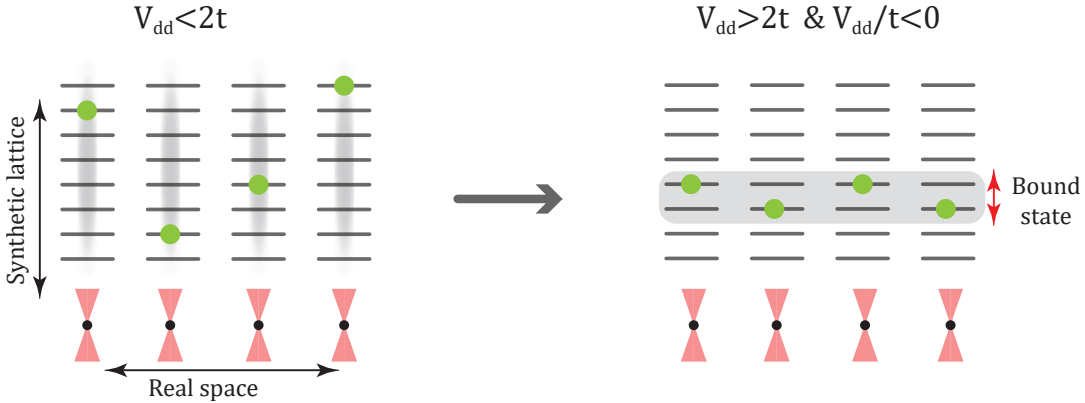


Figure 1.5: Emergence of quantum strings in the synthetic dimension. Tuning the relative strength between V_{dd} and t leads to confinement of atoms in only two of the states in the synthetic dimension.

collective phenomena might result from such interactions.

1.5 Proposed Experiment

1.5.1 Emergent bound states in Rydberg synthetic lattices of tweezer-trapped single atoms

In this section, I discuss an experimental study enabled by the proposed system of microwave-coupled atomic Rydberg levels. In particular, I discuss a proposal of a new type of quantum phase, so-called quantum strings or quantum membranes, expected to emerge naturally for the simplest type of coupling along the synthetic dimension [19, 26, 27]. Here, arrays of atoms trapped in real space undergo a phase transition from a state where each atom can tunnel throughout the synthetic dimension, to a state where the entire array of atoms is confined to roughly 2-3 adjacent synthetic lattice sites [26]. We consider a two-dimensional lattice with a real space dimension consisting of OTAs and a synthetic dimension composed of a set of microwave-coupled Rydberg levels. The system is initialized by loading each micro-trap with a single atom and then exciting the atoms to their Rydberg levels by globally shining on the 973 nm and 405 nm Rydberg lasers for a short time (less than 1 μ s). We note that this uniform excitation to the Rydberg state requires either inter-trap distances that are much longer than the so-called Rydberg blockade radius (roughly a few microns), or a modification

to the two-photon resonance condition. Uniform tunneling in the synthetic dimension is then turned on for all the atoms by applying a set of appropriately chosen microwave fields. Again, we emphasize that tunneling between the real-space trapping positions is suppressed.

After a varied amount of time, the microwave fields are turned off and the final state of the system is measured. In particular, state measurement can involve successively transferring population to $69S_{1/2}$ (by sequentially turning on the tunnelings to $69S_{1/2}$ for a π -time) followed by de-excitation to the ground state. The ground state atoms can then be imaged in a position-resolved manner by trapping in the OTA and collecting fluorescence light while cooling atoms via optical molasses. However, in the simplest scenario one can just measure the probability for the atoms to remain in the Rydberg state to which they were initially excited.

As predicted in the directly analogous case of dipole molecules [26, 27], dipolar interactions in the effective two-dimensional lattice, with uniform tunnelings in the synthetic dimension and suppressed tunneling in real space, can lead to interesting many-body phenomena.

In particular, varying the dipole-dipole interaction strength can lead to a phase transition from a case in which the atoms move freely and independently along the synthetic dimension (free gas of atoms), to a case where the atoms cannot move independently from one another, but rather become bound in a type of “quantum string”. That is, in the thermodynamic limit, the system is predicted to undergo a spontaneous dimensional reduction, in which the translational symmetry along the synthetic dimension is broken and only a particular two-to-three-site strip along that direction is occupied. This is illustrated in Fig. 1.5. The atoms then form a one-dimensional string in a two-dimensional lattice.

In the case of a two dimensional array of tweezer-trapped atoms, an analogous transition to a “quantum membrane” phase is expected. A number of questions about these emergent “quantum string” phases remain unanswered, such as the details of the phase diagram for larger system sizes (the mere existence of such a string phase is at the moment only supported by mean-field arguments and by DMRG calculations on moderately large two-dimensional strips) and questions regarding the stability of such strings to (thermal and quenched) disorder and other perturbations. We note that the physics of this system in the

strong interaction (weak hopping) limit can also be connected to the physics of fracton matter [Kaden Hazzard, private communication]. That is, when the microwave hopping terms are small, the only transport of charges is enabled by dipole-dipole exchange interactions, and the system naturally possesses sub-system symmetry.

1.5.2 Interplay between topology and interactions

In this section we present numerical simulations on the effect of dipolar interactions on topology as probed in a 1D Su-Schrieffer-Heeger (SSH) model in a synthetic Rydberg lattice. The 1D SSH model was developed to explain the unexpectedly high conductivity observed in

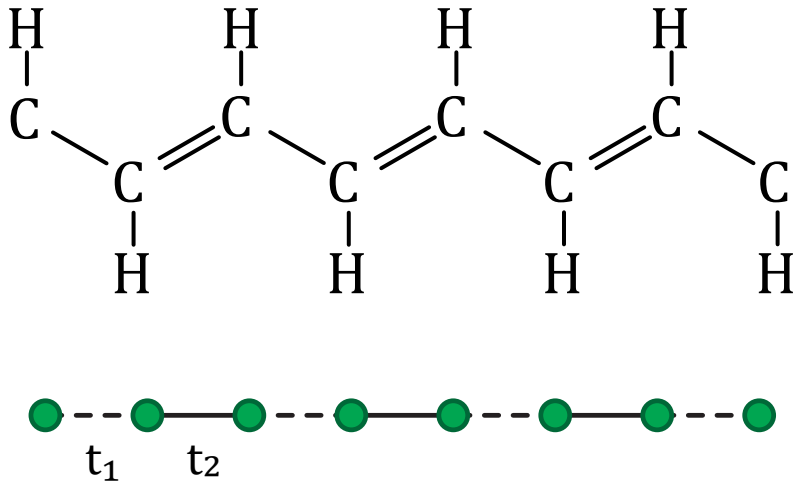


Figure 1.6: **1D SSH model of polyacetylene molecule.** Top, chemical structure of *trans*-polyacetylene. Single and double lines correspond to single and double bonds. Bottom, 1D SSH model that consists of alternating strong (solid) and weak (dashed) tunneling terms.

doped *trans*-polyacetylene molecules. The molecular structure of *trans*-polyacetylene consists of C-H monomers connected with alternating double and single bonds as shown in Figure 1.6 (top). The SSH model mimics this structure in form of a 1D lattice with uniform site energies and alternating weak and strong tunneling terms, *i.e.*,

$$H_{\text{SSH}} = -t_1 \sum_{n \in \text{even}} (c_{n+1}^\dagger c_n + \text{h.c.}) - t_2 \sum_{n \in \text{odd}} (c_{n+1}^\dagger c_n + \text{h.c.}) \quad (1.4)$$

where $c_n^\dagger(c_n)$ represent creation (annihilation) of an atom at site n , t_1 is a uniform tunneling term and m defines the relative strength between alternating (odd and even) tunneling links. Despite its simplicity the SSH model already shows many of the hallmark features of topological band structures. As depicted in the system band structures shown in Figure 1.7, the system begins in a trivial phase for $t_1 < t_2$. Here the band structure consists of two bands with a gap between them. If t_1 is increased a phase transition happens at $t_1 = t_2$ and the system goes from a trivial phase to a topological phase for $t_1 > t_2$. For the topological phase localized (zero energy) edge states appear at the defect/boundary and manifest in form of zero-energy states in the band gap at $|q| = \pi/a$.

It is worth mentioning at this point that the 1D SSH model was recently realized [19] in the Killian group at Rice University in a system of strontium Rydberg atoms. In our experiment we seek not only to realize this model using single potassium atoms in optical tweezer arrays, we propose a study to explore the effect of dipolar interaction between neighboring atoms on the dynamics of the 1D SSH model.

In our experiment we propose to implement the SSH model in a system of trapped potassium atoms in OTAs. Here each atom is excited to a Rydberg state where the SSH Hamiltonian is quenched on by turning on microwave driving fields. When the interaction between the atoms is weak, *i.e.*, when the distance between the atoms is relatively large, the system consist of independent SSH chains corresponding to each atom. Our system of single

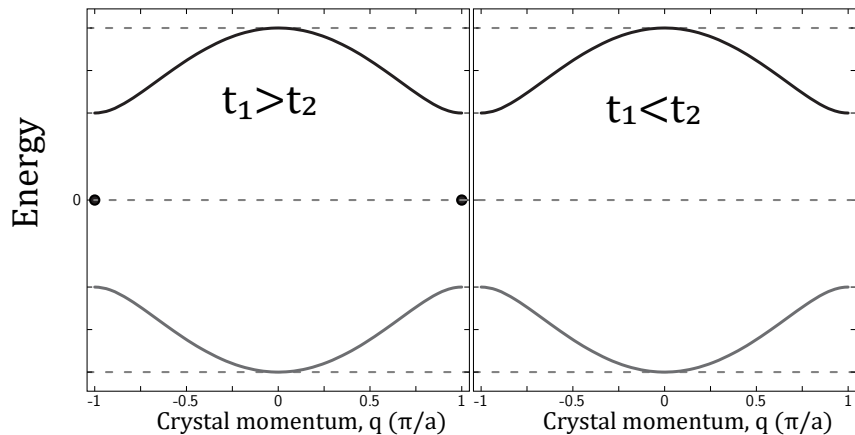


Figure 1.7: **1D SSH model band structure.** Left, topological phase of the SSH model where localized edge modes occur for $t_1 > t_2$. Right, trivial phase of the 1D SSH model. No modes appear within the band gap.

atoms in optical tweezers affords us the ability to tune the interaction between the atoms by varying the inter-atomic distance. When the system is prepared to allow dipole-dipole interaction between neighboring atoms, we can probe the effect of dipole-dipole interactions on the topological nature of the system. Figure 1.8 represents numerical results on the effect of interaction on the topological nature of a 1D SSH model. In this simulation a 2D lattice system is imagined. Here, one dimension is a 1D synthetic lattice where the atom is allowed to tunnel while the second dimension is a real space dimension where tunneling is suppressed. In a system of 15 internal states and two tweezer-trapped atoms, we numerically simulate the dynamics of the atoms in the presence of varying interaction strengths (compared to tunneling strength in the synthetic dimension).

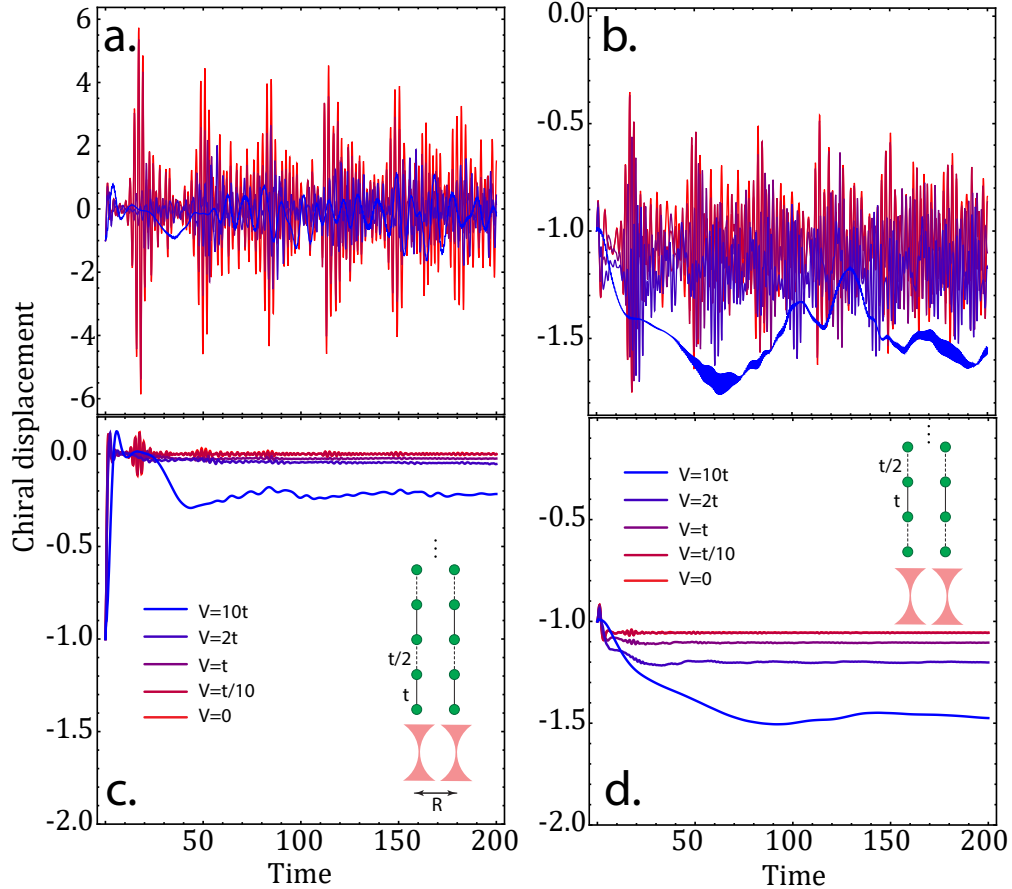


Figure 1.8: **Effect of dipolar interaction in a 1D SSH model as measured by chiral displacement** (a, b) Unaveraged \mathcal{C} for a trivial and topological system. (c,d) $\bar{\mathcal{C}}$ for trivial and topological phases. When averaged, the chiral displacement converges to the winding number. Red to blue indicates increasing interaction strength as shown in the legend.

To characterize the topology of our system we compute the *chiral displacement* of the atoms given by

$$\mathcal{C} = 2\langle \Gamma X \rangle \quad (1.5)$$

where Γ is the chiral operator and X is the unit cell operator [28]. Chiral displacement is displays an oscillatory behavior, *i.e.*, fluctuating about 0 for a trivial phase and about -1 for a topological phase. As simulated in Figure 1.8, the time-averaged or mean chiral displacement, $\bar{\mathcal{C}}$ (displayed in Figure 1.8(c,d)), paints a clearer picture on the effect of interaction on topology. Here, in the absence of interaction, $\bar{\mathcal{C}}$ converges to the winding number ν which is a measure of topology.

Here the interaction strength is varied from 0 (red) to 10 times the tunneling strength (blue) for both trivial and topological phases of the system. For both trivial and topological cases increasing the interaction strength leads to a deviation in $\bar{\mathcal{C}}$ away from 0 and -1, respectively. This numerical observation perhaps suggests that interactions can enrich the properties of atoms in engineered topological lattices. One outstanding question relates to how such interactions between hard-core bosons could enrich the system if topological flat bands were engineered in the synthetic space, in particular, if they could give rise to fractional quantum Hall-like excitations.

In this section we have shown that implementing a synthetic lattice of Rydberg levels in a system of tweezer-trapped atoms has intriguing prospects. In particular, designer Hamiltonians have been realized so far in synthetic lattices that have allowed the study of topology and disorder in a single particle regime. Our system presents the possibility to study the interplay between topology, disorder and interactions by adding Rydberg interactions to a topological and/or disordered system.

Although not discussed in this manuscript, I was involved in previous works (discussed in the thesis of Dr. Eric J. Meier and Dr. Alex An) where a synthetic lattice is created by driving Raman-Bragg transitions between momentum states of a rubidium-87 BEC [29–31].

1.6 Outline

The rest of this document is organized as follows:

- [Chapter 2: Experimental apparatus for cold \$^{39}\text{K}\$ atoms](#): Here we explain the design and construction of an experimental apparatus for trapping and cooling potassium atoms in magneto-optical traps (MOTs) in preparation for single atom trapping.
- [Chapter 3: Single atom trapping in optical tweezers](#): We talk about our work in trapping, cooling and imaging single potassium atoms in optical tweezers which was facilitated by Λ -enhanced gray molasses on the D1 line of ^{39}K .
- [Chapter 4: Towards Rydberg synthetic lattices](#): We talk about recent and current work done towards the realization of a synthetic lattice of Rydberg levels.

The appendices detail (1) some details on initial procedure followed during initial trapping of potassium atoms (2) work done toward trapping and cooling erbium atoms in an initial phase of the experiment (3) Matlab control software for Thorlabs CCD cameras, and (4) derivation and simulation of polarization spectroscopy signals which has been abundantly used for laser stabilization at different parts of the experiment.

Chapter 2

Methods I: Experimental apparatus for cold ^{39}K atoms

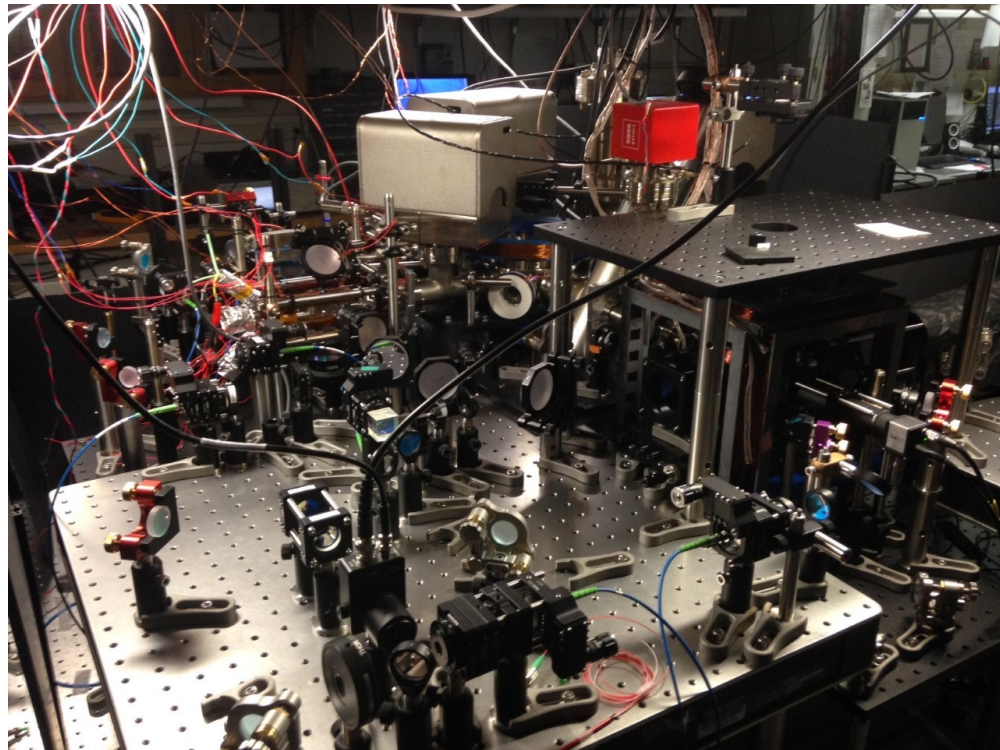


Figure 2.1: Picture of the chamber *ca.* 2020

This chapter describes the experimental apparatus in 6 sections:

1. A four-chamber ultra-high vacuum (UHV) design for trapping and cooling multiple atomic species.
2. Details on laser preparation.
3. Laser stabilization using polarization spectroscopy.
4. Creation and optimization of magneto-optical traps (MOTs) of potassium-39.
5. Rapid transport of atoms between two 3D-MOTs.

6. Capturing, cooling and optimization of science MOT.

2.1 A four-chamber UHV design

Our experimental apparatus is made up of the following components:

1. **Source chamber:** This consists of a glass cell (produced by Precision Glass Blowing Inc.) that contains alkali metal dispensers (AMDs)¹. Specifically, our glass cell contains two dispensers that can produce (non-enriched, isotopic abundance) vapors of potassium and rubidium, respectively. Each AMD consists of three cathode leads which are expected to operate over several years. The decision to include two species allows us to either combine these species in a gas mixtures experiment or to change species without disassembling the vacuum chamber. The opposite end of the apparatus consists of another source chamber that contains erbium dispensers designed by AlfaVacuo e.U as can be seen in Fig. 2.2. Due to technical issues (potential contamination during transport or installation) activation of erbium dispensers was unsuccessful (as described more on appendix B).
2. The two source chambers are attached to a middle **octagon chamber**.² The design was chosen to allow the trapping and cooling of combinations of the three species in the same area. The octagon chamber consists of two 6" diameter glass windows at the top and bottom and two pairs of orthogonal 2.75" diameter windows (NW-SE and SW-NE) through which MOT beams are passed so that they overlap at the center of the chamber for atom trapping. A 2.75" diameter view port (facing West) provides a good angle for low background imaging of atoms collected in the octagon chamber. We find this port very useful for aligning a push beam used for transport of atoms between the octagon chamber and the science chamber.
3. The **science chamber** consists of a 28 mm × 28 mm × 100 mm quartz cell (4 mm thickness). This cell is attached to the vacuum system by a flange with an additional

¹AMDs consist of an anode and a cathode where the cathode contains stable salts of the desired alkali atoms. Passing current induces a reduction reaction that releases controllable amounts of alkali vapor

²MCF600-SphOct-f2C8 acquired from Kimball Physics Inc

(~ 10 cm glass to metal adapter, allowing the cell to protrude further out from the stainless steel vacuum components to allow for increased optical access. The relatively small size of the cell increases proximity to the atoms which is essential in this experiment for bringing trapped atoms within working distance of high numerical aperture (NA) objectives for high-resolution imaging.

4. The different chambers are connected via **differential pumping tubes** ($\approx \phi 5$ mm) which allow us to maintain a pressure difference between them. While high vapor pressures are needed at the source chambers to create large fluxes of atoms, we need to maintain lower pressures in the octagon and science chamber. This is to avoid loss of atoms from optical traps in the science and octagon chambers due to collisions with background gas atoms.

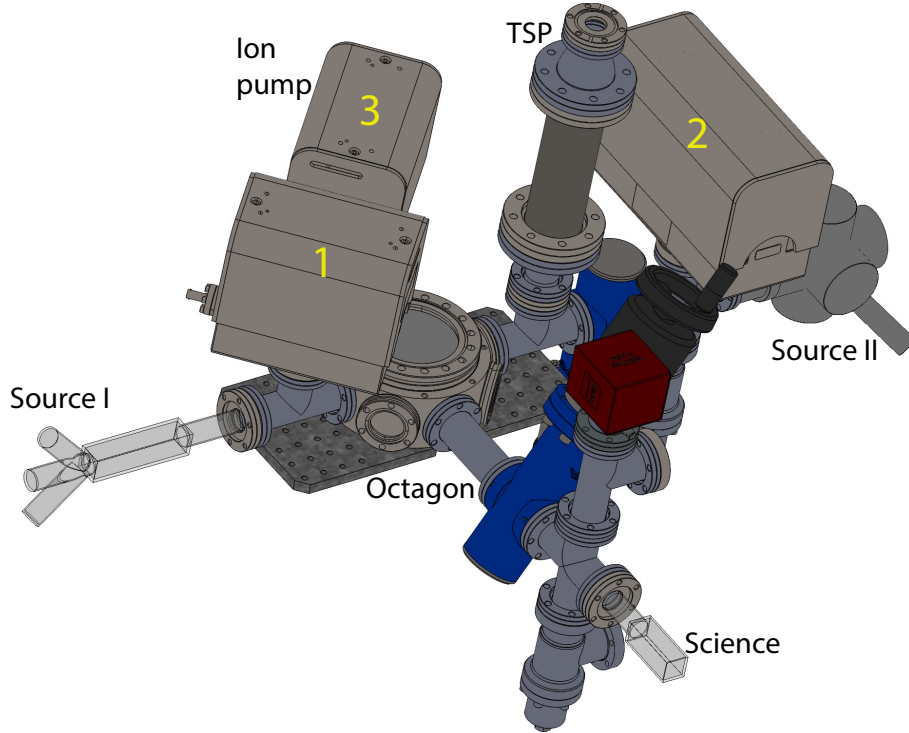


Figure 2.2: A four section vacuum chamber. Initial collection of atoms happens in the source chambers. The atoms are first transported to the octagon chamber and trapped in a 3D MOT and finally moved to the science chamber where experiments are performed.

5. Each chamber is also equipped with an **ion pump** that help to maintain low pressure ($\approx 10^{-11}$ Torr) thus providing an ideal environment for trapping and cooling atoms.

The pump works by ionizing background gas and accelerating the ions created into solid electrodes. At the electrodes the particles are trapped by chemosorption. Ion pumps 1 and 2 (45 L/s) from Gamma Vacuum maintain low pressure environments at the two source chambers while ion pump 3 (75 L/s) works to maintain high vacuum in the octagon chamber. We chose a higher speed ion pump for the octagon chamber not only to handle a larger volume but also because we intend to trap atoms in 3D MOTs in a lower pressure environment. For the science chamber we install a NexTorr D-100-5 pump (designed by Saes group). Due to its relatively smaller size (105 mm × 80 mm × 75 mm), the NexTorr pump is ideal for this chamber because it allows more optical access. The pressure on each pump can be monitored on ion pump controllers. Between source chamber II and the octagon chamber we installed a titanium sublimation pump (TSP). The TSP is fired right after the bake out procedure in order to coat the inner walls of the nearby nipple with titanium to provide another source of pumping.

6. We include two all-metal gate valves (VAT 481 series) separating the octagon chamber from source chamber II and from the science chamber. These were used, in combination with nearby angle valves, to separately pump out (with a turbo pumping station, for the initial pump down) different sections of the vacuum chamber. But, these can also be used to seal off a section of the vacuum chamber in case a source or science cell were to require replacement.

2.1.1 Construction of the vacuum chamber

Cleaning, bake-out and assembly

Before assembling the vacuum parts as described above, we first decontaminate them following the standard AIM procedure i.e. cleaning with acetone, followed by isopropanol and lastly using methanol. In particular the parts are cleaned first with acetone in an ultrasonic bath for 30 minutes then rinsed with distilled water. This process is repeated with isopropanol followed by methanol. Each part is then air dried and is then covered in aluminum foil to avoid deposition of dust particles after cleaning. We then assembled the vacuum

chamber as described above, sealing physical joints between different components that are screwed together using copper gaskets. We attach a turbo pump to the apparatus to pump out a majority of the air before the bake-out stage. In preparation for bake-out, we wrap the entire apparatus in vacuum safe metal foil. Above the layer of foil we wrap seven heater tapes across the chamber.³ These are evenly distributed around the chamber in order to maintain homogeneous temperatures during bake-out and to avoid any cold points where out-gased material could collect in the chamber. Around the atomic source and science cells, we constructed an oven, i.e., a cage of opto-mechanical posts around the cell without any physical contact with the cell (any contact could either scratch the surface or create drastic temperature gradients across the cell wall). We wrap aluminum foil around the cage followed by heater tapes on top of the foil cover. An extra layer of foil is wrapped around the heater tapes to distribute heat more evenly around the chamber. The heater tapes are each attached to a variable AC power supply (red in Fig. 2.3(a)) which we adjusted in tandem to homogeneously raise the temperature around the apparatus. We connect six thermocouples, evenly distributed around the chamber, to monitor temperature.

Before bake-out the turbo pump is used to initially pump the chamber to $\approx 10^{-6}$ Torr. On 9th March 2017 we started raising the temperature at 10 °C/h. We monitor the temperature at different parts of the chamber and feedback between the variable power supplies and the thermocouples to maintain similar temperatures at each reading. For each reading we also record the pressure corresponding to ion pumps 1, 2 and 3 (as shown in Fig. 2.3 (c)). The temperature reached at the end of the day is kept constant overnight e.g 150° C at the end of the second day. We raise the temperature up to ≈ 195 °C on day 5. Going to higher temperatures is discouraged since it could have an adverse effect on various vacuum components (magnets for the ion pumps, angle valves, and the vacuum current feedthrough connections for the AMDs).

On the 8th day, we saw that it was good, and we started lowering the temperature around the vacuum chamber at 10 °C/h (while maintaining homogeneous temperature). The pres-

³Omega DHT051040LD

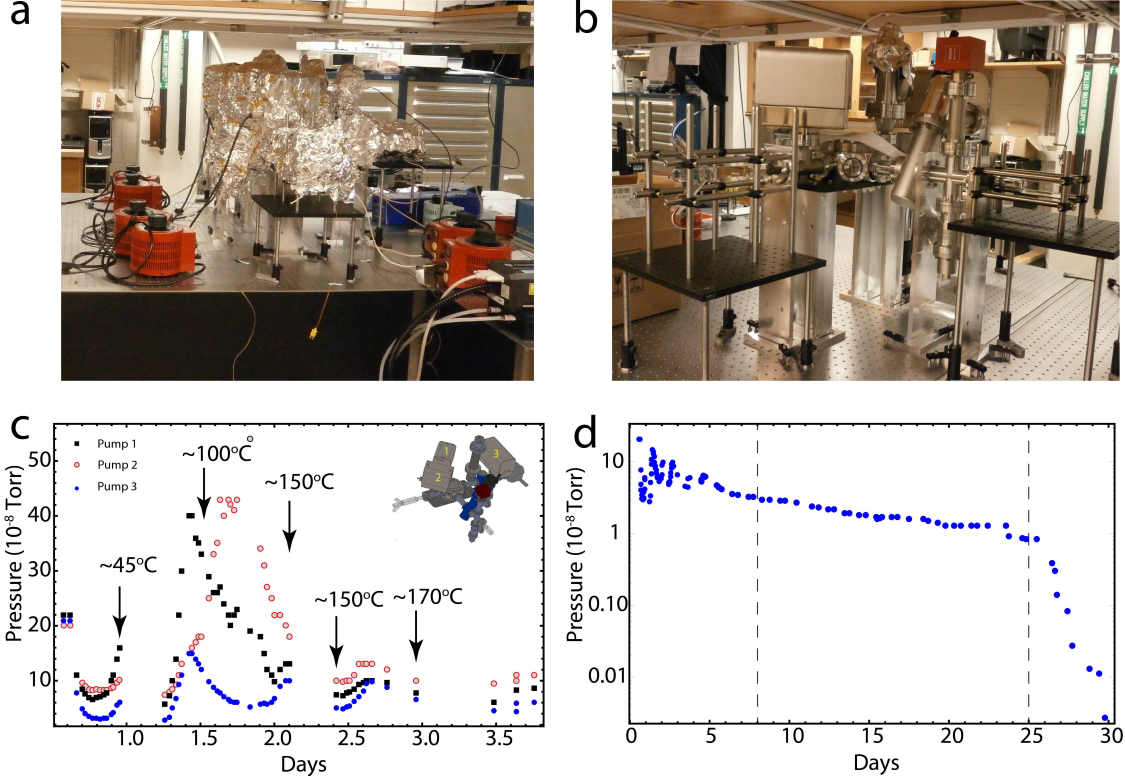


Figure 2.3: Vacuum chamber assembly and bake-out. (a) Vacuum chamber wrapped in **vacuum safe UHV foil** for bake-out. Variable power supplies are connected to heater tapes around the chamber for temperature control. Thermocouples are attached around the chamber to monitor temperature. (b) Assembled vacuum chamber ready for bake-out. (c) Pressure corresponding to ion pumps 1-3 over the first four days. (d) Pressure corresponding to ion pump 3 over 30 days.

sure, as read on the ion pump controllers also drops accordingly. The temperature dropped off to 10^{-9} Torr after cooling down to room temperature and unwrapping the vacuum chamber and continued to drop steadily afterward and finally bottomed out around 10^{-11} Torr over the following weeks.

2.2 Details on laser preparation

In this Section we detail the set up that we use to prepare laser beam paths for addressing the D2 (767 nm) and D1 (770 nm) transitions in ^{39}K .

Lasers

Our laser preparation set up consists of (1) a Toptica DL 100 ECDL (External Cavity Diode Laser) operated at 767 nm that supplies ≈ 60 mW. (2) A Toptica DL Pro laser operated at 770 nm provides power used for gray molasses cooling, loading and non-destructive imaging of single atoms in optical tweezers. (3) A Toptica DL100 ECDL is used to provide power at 780 nm for creating optical microtraps at a later stage of the experiment. (4) The 780 nm ECDL will be replaced with a Ti:Sapphire Tekhnoscan TIS-SF-07 laser which will be tuned around 785 nm⁴ with the goal of increasing the amount of trap power. This will be useful for scaling up the number of microtraps in our system. (5) For Rydberg excitation we address a two-photon transition using a 405 nm and a 973 nm laser. The MOGLabs Littrow ECDL (LDL) at 405 nm is used to address the $4S_{1/2} \rightarrow 5P_{3/2}$ transition. This laser consists a monoblock chassis with no springs or fixtures, a feature that reduces vibrations. The second transition at 973 nm ($5P_{3/2} \rightarrow nS_{1/2}$ where $n \approx 70$) is driven using a MOGLabs tunable cateye laser (CEL) where, in contrast to the other ECDLs mentioned, diffraction gratings are replaced with a combination of cateye reflector and an ultra-narrow filter [32].

Tapered amplifiers

The ECDLs used in our lab produce total beam power of ≈ 70 mW. For $\approx 600\text{-}1000$ nm lasers, tapered amplifiers (TAs) are customarily used to increase the amount of power delivered at the atoms. The TA is based on a semi-conductor amplifier chip (labeled 2c) with an input- and a tapered region. Current to the chip is provided through a cathode that sticks out (labeled 2a) and an anode housing labeled (2b) on Fig. 2.4. A current applied through the electrode induces population inversion in the TA chip which leads to fluorescence either spontaneously or can be stimulated by a seeding beam whose polarization and mode profile matches the input region at the TA chip. At maximum current, the output power of the TA is a factor of ≈ 40 more than the seeding light. The TA is, however, operated at lower

⁴As will be explained in Chapter 3, this choice of wavelength for a dipole trap corresponds to the minimum differential Stark shift for some fixed trap depth, i.e., $\frac{\alpha_{\text{excited}} - \alpha_{\text{ground}}}{\alpha_{\text{ground}}}$ is minimum at 785nm for the D2 transition in ³⁹K. Here α denotes polarizability.

currents to preserve the lifetime of the chip. The TA chip⁵ is mounted on a custom, home-made mount shown on Fig. 2.4 (design provided by Jacob Covey of the Saffman lab at UW Madison). The mount consists of a brass housing where the TA is mounted and an aluminum base (labeled 9) which acts a heat sink during operation. As shown in Fig. 2.4 (b), the TA fits into a groove at the center of the brass housing, so that the cathode sticks out at the side. Wires that supply current to the chip are directly soldered to the cathode. The brass housing also consists of SM1-threaded mounting holes for aspherical lens mounts⁶. This lens is used to shape the seeding beam at the input and the TA output beam. The brass housing sits on a Peltier element⁷ which is used to regulate the temperature of the housing and hence the TA chip. The Peltier element acts as a heat pump between the brass housing and the aluminum base depending on the current (supplied by a TEC temperature controller⁸) passing through it. Additionally, a temperature controller is also connected to a thermistor⁹ placed in direct thermal contact with the brass housing for temperature measurement. This allows for temperature stabilization through a PID feedback loop. The brass housing is firmly screwed onto the aluminum base (with the TEC element between them) using plastic screws¹⁰ to prevent electrical contact. The aluminum base consists of two holes (labeled 7) for direct mounting on the optical table and two holes (labeled 6) to pass wires through that are connected to the TEC element, the TA chip cathode, the thermistor and a ground. In our case, the wires are soldered onto a DB9 solder connector screwed directly into the rectangular hole on the side of the aluminum base. We can then plug in a standard DB15M/F data cable that is connected to the current controller¹¹ and temperature controller using CAB400 and CAB420-15 cables, respectively. The entire set up is covered in a plexiglass housing with anti-reflection-coated glass windows¹² to allow seeding beam input and the TA output to pass through. At the output of the TA set up a

⁵Eagleyard EYP-TPA-0765-01500-3006-CMT03-0000

⁶Thorlabs C560TME-B

⁷TEC3-6

⁸TED 200C

⁹Digikey 495-2143-ND

¹⁰Digikey RPC7350-ND

¹¹LDC240C

¹²WG10530-B

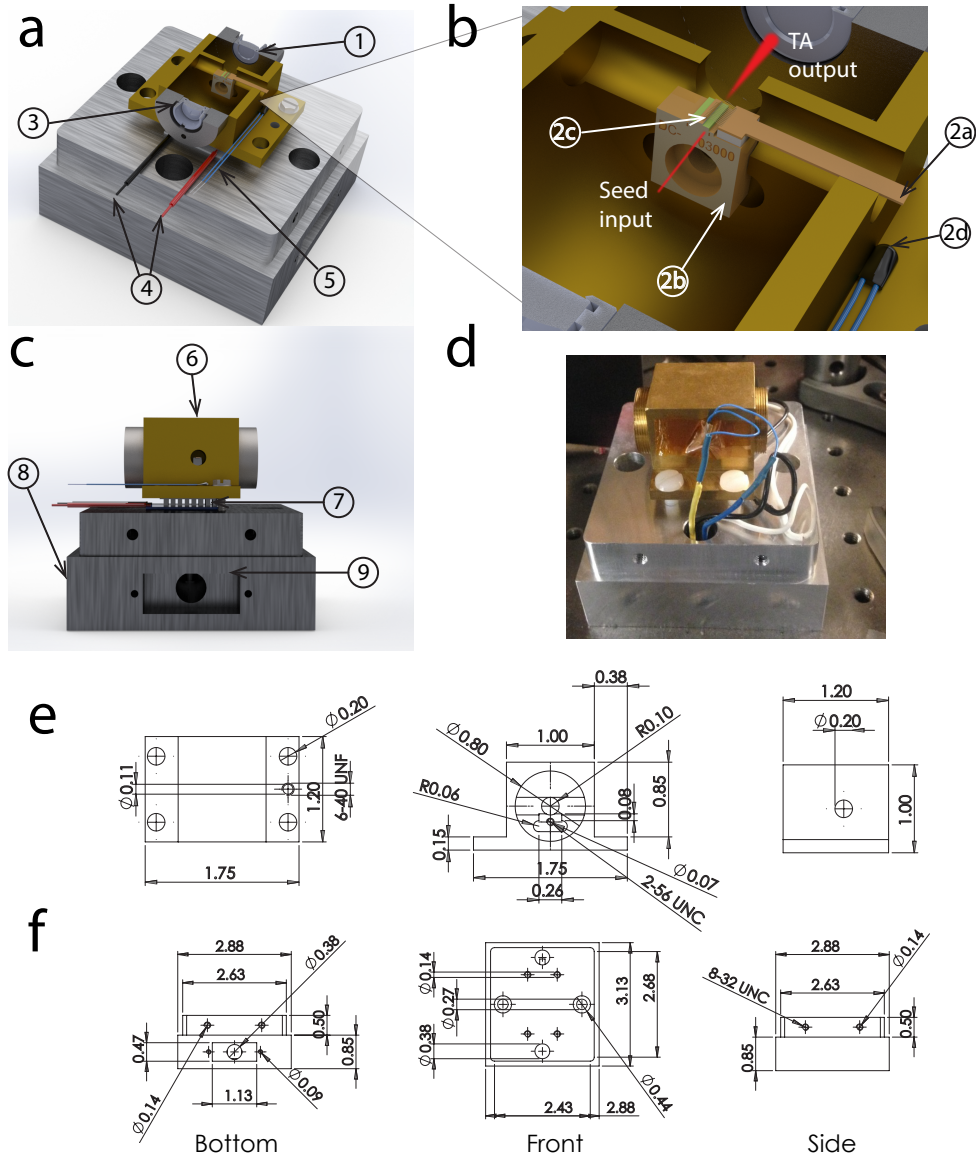


Figure 2.4: Home-built tapered amplifier design for laser beam power amplification courtesy of J. Covey, Saffman Lab

Faraday isolator¹³ is necessary to prevent back-reflection of light into the TA which could damage the chip. TA mode matching and shaping of the TA output are described in more detail in the thesis of Alex An [33].

¹³Thorlabs IO-5-780-VLP

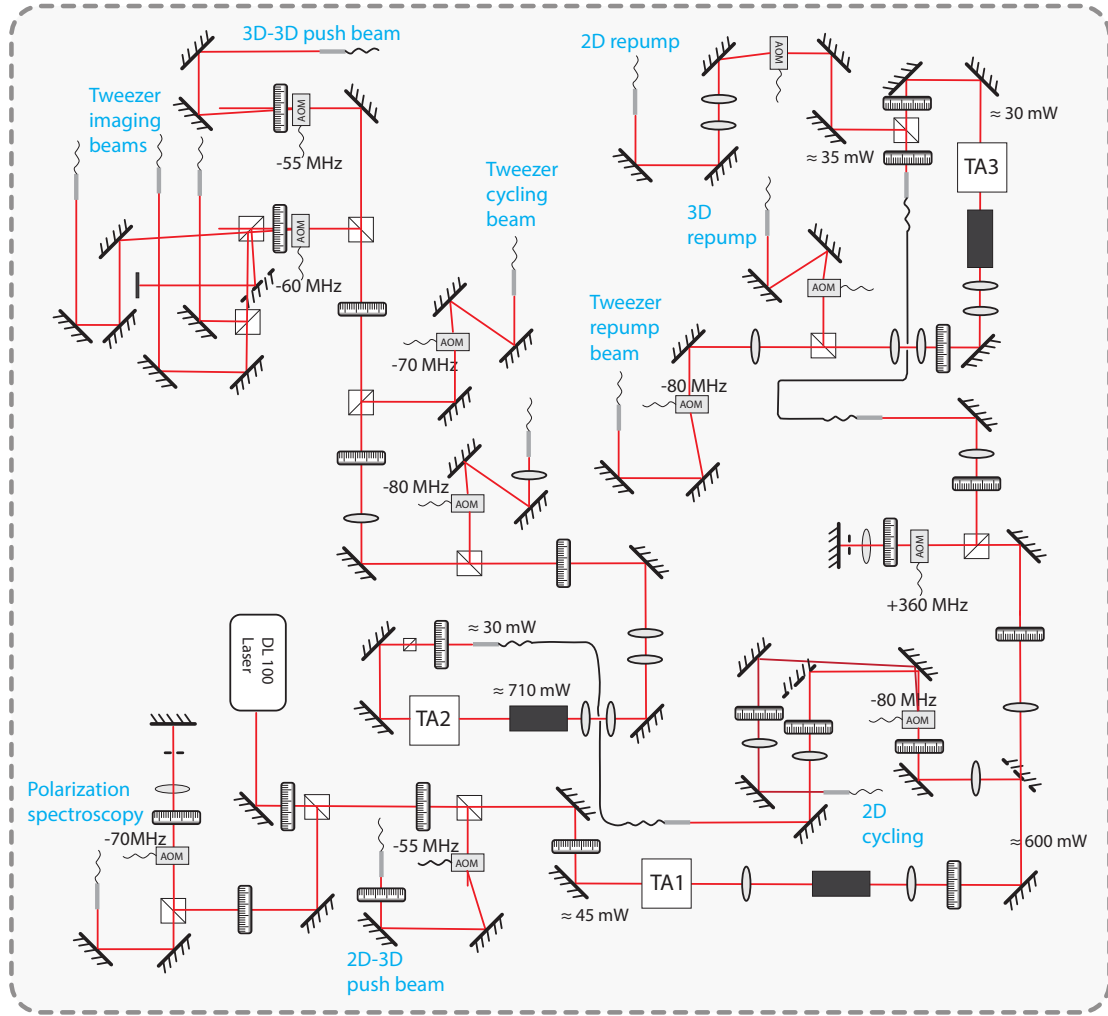


Figure 2.5: Laser system for trapping and cooling ^{39}K atoms. TA1 amplifies light from the Toptica DL 100 laser which is divided into seed light for TA2 (D2 cycling TA) and through a double pass AOM system to seed TA3 (D2 repump TA).

Controlling beam frequencies

Acousto-optic modulators

Beam frequencies in our experiment are controlled using acousto-optic modulators. These consist of a crystal (typically TeO_2) with a strain transducer attached to it. RF signals are used to drive the strain transducer causing acoustic waves to form in the crystal. The periodic change in mechanical strain associated with the acoustic plane waves leads to a periodic change in the refractive index of the crystal. In the frame of an incoming wave,

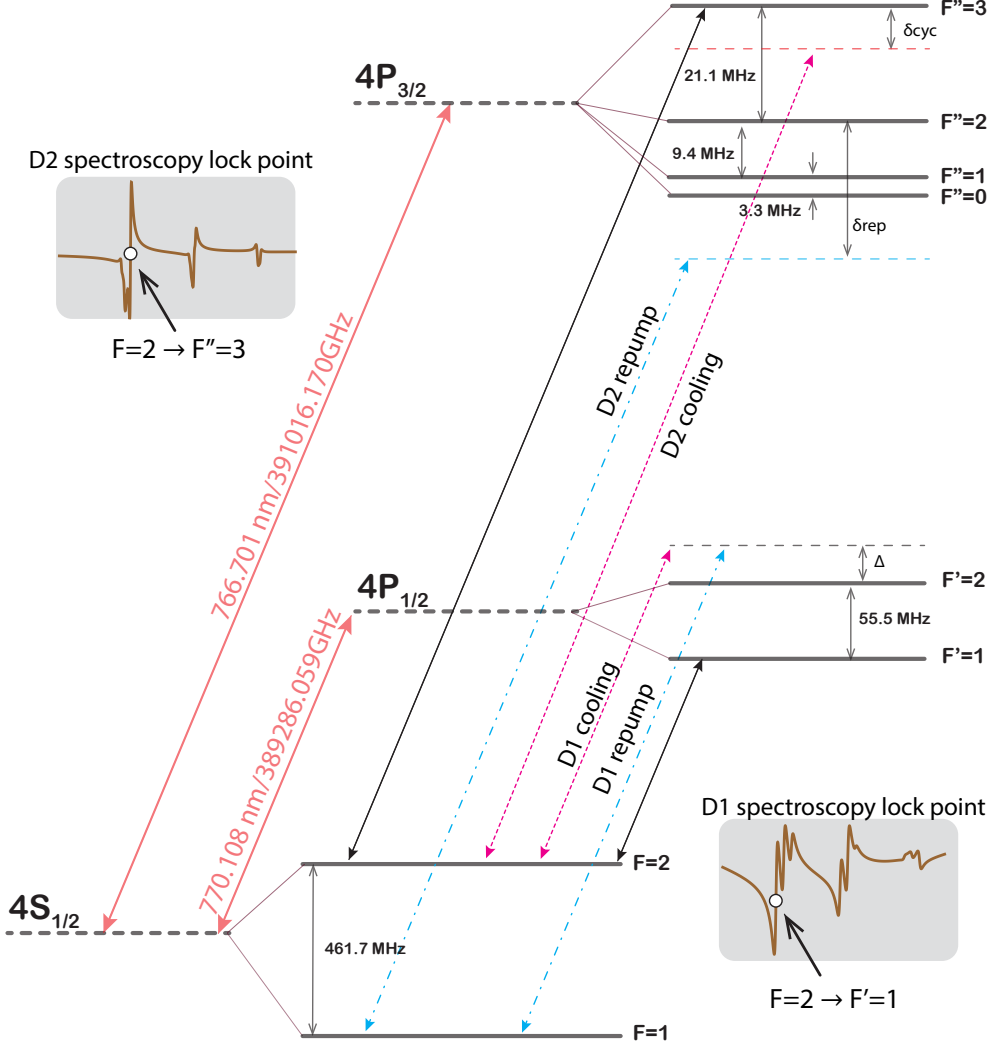


Figure 2.6: Potassium level diagram. The D2 transition is used for initial trapping and cooling while the D1 transition is used for cooling at later stages of the experiment.

the acoustic plane waves effectively form a diffraction grating. When operated in the Bragg regime, i.e., so that the incoming beam is incident on the acoustic plane wave 'grating' at an angle, the incoming beam undergoes diffraction. At a special Bragg angle the amount of light in the diffracted beam can be $\approx 90\%$ of the incoming beam power. Since the acoustic wave moves at some velocity related to the frequency of the RF drive, the diffracted beam is Doppler shifted with respect to the incoming beam. The frequency of the diffracted beam can therefore be controlled using the RF frequency of the RF drive at the strain transducer. As a result we can construct different beam paths at appropriate frequencies (detuned from

the transition to which the laser is *locked* as shown in Fig. 2.6) to address cycling and repump transitions. With AOMs we also have the ability to control the power in the chosen diffracted order by changing the amplitude of the RF drive. Since the Bragg angle of a diffracted beam depends on the frequency of the drive it is often impractical to control the frequency of the AOM with just one pass through the AOM, since the final power delivered to the atoms depends on the coupling efficiency into optical fibers. A double-pass AOM arrangement [34] is normally used to allow frequency tuning with minimal change in beam alignment (and thus minimal change in final intensity at the atoms). In this configuration, an informed choice of lens positioning after AOM in a retro-reflected beam path leads to an output path for the light that is nearly invariant to the frequency of the RF drive. The output of the double-pass is thus shifted by twice the frequency of the driving RF signal. Due to their fast rising times ($\mathcal{O}(\text{tens of ns})$), AOMs are used in our experiment for switching beams on and off during critical stages of the experiment. For example during the transfer stage where atoms are pushed from the octagon chamber to the science chamber, a $200 \mu\text{s}$ square pulse that pushes atoms requires fast rise times to be effective.

We typically use Gooch & Housego [35] AOMs operated around 80 MHz. We have, however, noticed that when preparing laser paths around 400 nm AOMs produced by IntraAction Corp [36] require less RF driving power to achieve the maximum amount of power in the diffracted order of the output.

Electro-optic phase modulators

To address the frequency difference between the cycling and repump transitions i.e. 461.7 MHz, we have used a double pass AOM system ($2 \times +180 \text{ MHz}$) in addition to a single pass AOM shift ($\approx +80 \text{ MHz}$). The spectroscopy AOM (which defines the locking point of the laser) was set to -70 MHz in this case as shown in Fig. 2.5. While we are able address the ground state splitting in a tunable fashion with this arrangement, we lose a lot of power due to imperfect AOM diffraction efficiency and general loss at different optical elements. However, this arrangement does allow for a completely separate repumping beam, which can be useful

for certain imaging and optical pumping needs. Electro-optic modulators (EOMs)¹⁴ can be used instead of AOMs to add frequency sidebands to beams without incurring the loss associated with diffracting the beam.

In Figure 2.7 we demonstrate how we read out the carrier-to-sideband ratio when setting up and testing out EOMs for our apparatus. For our experiment we test a resonant Qubig EO-K39M3-NIR and a double resonance Qubig PM-K39/41_K3 EOM which are conveniently tuned and AR coated for $^{39}\text{K}/^{41}\text{K}$ systems. For practical purposes these EOMs are not necessarily resonant at 461.7 MHz but can actually be manually tuned over a large range (385-484 MHz for Qubig EO-K39M3-NIR) with a resonance bandwidth of ≈ 2 MHz. In the test set up a laser beam (ω_L) passes through a polarizing beamsplitter (PBS) and is aligned through the EOM. A $\lambda/2$ plate is included to tune the polarization of the incoming beam. The EOM is driven at 461.7 MHz. The reflected beam is passed through an AOM driven at 80 MHz so that the frequency of the laser is now $\omega_L + 80$ MHz. The first diffraction order is coupled into one arm of a 2 by 2 fiber coupler/combiner¹⁵. The output of the EOM (now with frequency components, $\omega_L \pm 461.7$ MHz) is sent onto the second arm of the combiner thus creating a beat note at 461.7 ± 80 MHz. The output of the combiner is sent to a fiber-coupled photo-diode¹⁶. The resulting signal is then displayed on a frequency spectrum analyzer. Figure 2.7 (lower) shows the dependence of the first-order sideband and carrier on the driving RF power. Beginning with no drive, the beam passing through the EOM has all the power in the carrier component. As we increase the driving amplitude, and subsequently the modulation depth, the sideband-to-carrier ratio increases following the Bessel function form associated with sinusoidal modulation. We can easily identify a driving amplitude that corresponds to V_π .

RF sources

RF signals in our lab were originally generated using a home-built set up based on voltage-controlled oscillators (VCO). These allow for direct control of RF signals sent to AOMs / EOMs

¹⁴An EOM consists of a Pockels cell driven at some modulation frequency ω_{mod} such that beam (initially with frequency ω_L) passing through the EOM undergoes phase modulation and acquires sidebands at ω_{mod} .

¹⁵Thorlabs TW805R5A2

¹⁶Menlo Systems FPD-310-V

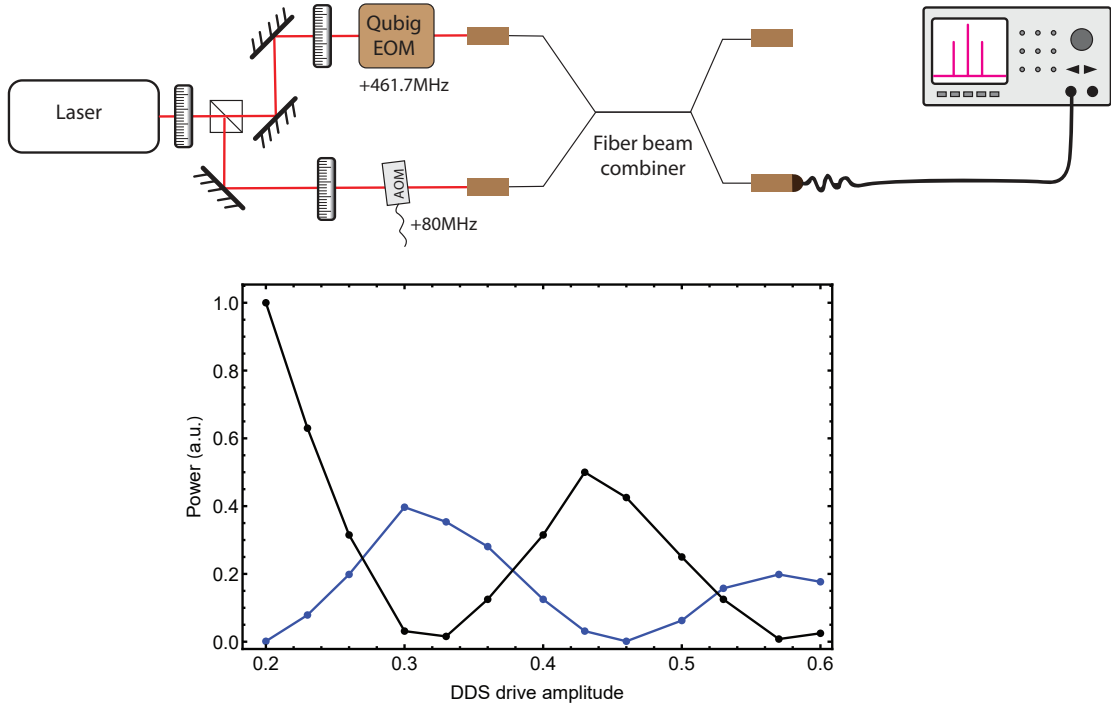


Figure 2.7: Set up for testing and optimizing EOM sideband to carrier ratio.

using an analog voltage input. The VCO output is passed on to a voltage variable attenuator (VVA)¹⁷ which controls the amplitude of the output RF signal based on an analog voltage input. In the experiment this corresponds to directly controlling the power on some diffracted beam at an AOM using an analog voltage input. Finally, to allow us to safely and rapidly switch the RF signal (and thus a corresponding laser beam path) on and off, we add an isolation switch¹⁸.

In order to monitor the output frequency of the VCO while still in operation, an RF coupler¹⁹ is added between the VVA and the VCO. This directs a small fraction of the VCO output power to a BNC output at which frequencies can be read out using a frequency counter (Optoelectronics M1 TCXO).

The RF power supplied at the main output of the home-built source is typically on the order of 1dBm. Since this is too low to cause any reasonable diffraction when sent to the AOMs,

¹⁷ZX73-2500M

¹⁸ZASWA2-50DR-FT+

¹⁹ZFDC-10-S+

we add a 2W (+29dB) RF amplifier²⁰. The output of the amplifier is sent to the AOMs through a BNC connection. In short, the components are connected as: VCO → Coupler → VVA → Isolation Switch → Amplifier.

A great feature of this home-built frequency source is the ease of assembly and operation. However, we found that the stability and noise profile of the output signal highly depends on the quality of the voltage supply units used to power different components. For instance, while supplying 461.7 MHz to a Qubig EOM for gray molasses cooling (described in Section 2.6.1) we initially had a difficult time cooling the atoms. This was because the efficiency of cooling was very sensitive to the two-photon detuning (which corresponds to deviation from 461.7 MHz). The RF signal from the VCO source was actually drifting and fluctuating due to unstable voltage from a relatively cheap voltage supply, thus compromising the stability of the RF signal sent to the EOM.

The range of the frequencies we could generate using VCOs was also limited. Since most of the AOMs in our lab were operated around 80 MHz (chosen based on availability of AOMs with good diffraction efficiency), most of our sources use Mini-circuits ZX95-100 VCOs (50-100 MHz). Upon adapting our home-built frequency sources to include Direct Digital Synthesizer (DDS) sources instead of VCOs, we have had no stability issues.

Commercial RF sources

In addition to and as replacement for home-built frequency sources, we have alternatively used arbitrary waveform generators (AWGs) to control RF frequencies in our set up. The AWGs²¹ provide an interface that allows us to directly set the amplitude, phase and frequency of the output RF signal. Specifically, the **mod** features allows modulation of either the frequency or amplitude of the RF output while a **burst** feature can be used for rapid switching of the output signal based on an external trigger input²². With the AWGs we are also able to generate and output arbitrary waveforms. We use this feature to generate multi-

²⁰ZHL-1-2W+

²¹BK Precision 4064

²²Caveat: the **mod** and **burst** features cannot be used simultaneously on the same channel. Besides while BK Precision 4064 has two channels independent control of the modulation and TTL is not possible since there is only one modulation input and one TTL input.

frequency outputs that drive an acousto-optic deflector (AODs) to create multiple frequency components of a first diffracted (and deflected) order. These are used to create arrays of optical micro-traps for single atom trapping (described in Chapter 3).

We have recently added commercial frequency sources designed and built by MOG Laboratories into our system. The quad RF synthesizer (QRF241) has four channels which can output frequencies (10-200 MHz). A front panel GUI allows for easy selection and setting of the amplitude and frequency of the RF signal outputs which go out at the back via SMA connection. Each channel has (1) a modulation input at the back for either frequency or amplitude control using an external analog input and (2) a TTL input for fast and secure switching of the RF outputs and of course (3) an RF SMA output. Perhaps the most impressive feature of this device is the fact that each channel has an integrated amplifier. In addition to saving a lot of space, this simple design reduces noise levels in the output signal in comparison with home-built RF sources (while also being cheaper and saving time, to boot).

Shutters

As will be explained in Chapter 3, imaging single atoms is challenging since it requires very low background in order to distinguish signal from background. Non-destructive imaging works well when the scattering rate of the atom is reduced (by imaging using lower intensities) thus reducing heating rates and imaging longer to acquire enough photons above the background. While AOMs are used to switch beam paths on and off, a very small amount of light can leak through the fiber even when the AOMs are off. This residual leak-through not only increases the background during imaging it can also heat up atoms thus reducing imaging fidelity. In addition to AOMs, we use Vincent Associates Uniblitz shutters (VS25S1ZM0 controlled by VMM-D4 shutter drivers) in our apparatus to physically block fiber input ports and guarantee that no light leaks through during imaging²³. In some cases we use shutters to block light while the AOM generating the beam path is **on**. Specifically, this is done for AOMs that only participate in the experimental sequence for a very short time but

²³Shutters turn on and off on $\approx 5\text{ms}$ timescale, while this is relatively slow compared to AOM switch off time (ns) the timescale for background accumulation and heating is usually longer.

are required to *stay warm* during the rest of the sequence (since the eventual fiber-coupling efficiency of light passed through an AOM can depend strongly on the temperature of the crystal).

Control hardware and software

Our experiments involve trapping, cooling and transporting atoms between the source, octagon and science chambers (as presented on Figure 2.35) before finally confining individual atoms in optical tweezers. The experimental sequence, therefore, requires precise timing at each experimental stage. For example, transporting atoms between the octagon and science chamber (described in Section 2.5), requires us to turn off magnetic fields and laser beams while turning on a very short pulse ($\approx 150 \mu\text{s}$) that imparts momentum on the atoms. Cooling atoms on the other hand (e.g. using gray molasses) requires ramping down cooling beam intensity on a ms timescale right after turning off a magnetic field gradient. Smooth and repeatable operation of the apparatus therefore requires a control system that can communicate with a wide range of hardware (shutters, AWGs, AOMs etc) while providing a time reference between them. For our experiment we use Cicero Word Generator, developed by Aviv Keshet (building on work from previous generations of Word Generator) in Wolfgang Ketterle's group at MIT [37]. Cicero communicates with an FPGA (Opal Kelly XEM3001) to provide a time-reference and is then connected to National Instruments (NI) hardware that can receive commands and send digital (TTL voltage) and analog (variable voltage) signals to the experiment. To prevent any back-propagating signals from interfering with or damaging the control hardware, we isolate the experiment by sending the signals through digital and analog isolation circuitry described in more detail in the thesis of Eric Meier [38].

D2 laser preparation

The main goal of the laser prep set up is to set up beam paths for creation of magneto-optical traps (MOTs) in the source, octagon and science chambers as explained in more detail in Section 2.4. Each of these beam paths consist of a cycling and repump component that drives $F = 2 \rightarrow F'' = 3$ and $F = 1 \rightarrow F'' = 2$, respectively (Fig. 2.15). Additionally

we need to set up push beam paths used to transport atoms between the chambers. These are set up to be blue detuned from the D2 transitions so that they exert a repulsive force that pushes atoms in the direction of propagation of the beam. While imaging of atoms in MOTs is automatically done using the MOT beams for fluorescence imaging, for single atoms trapped in optical micro-traps at the science chamber separate imaging paths are set up. This affords us the freedom to send in the imaging beams at the direction that scatters the least number of photons into the imaging system due to reflection on the glass cell surface. The ability to independently tune the frequency of the imaging beam also allows us to compensate for AC Stark shifts while imaging atoms in an optical tweezer.

Now we describe the D2 laser preparation set up used to manipulate atoms at different stages of the experiment (by addressing the D2 transition shown on Figure 2.6).

We begin with ≈ 60 mW of 767 nm light from a Toptica DL100 laser, first passed through a Faraday isolator to prevent back-reflected beams at later stages from getting into the laser. A small amount of light is reflected at a PBS to a double-pass AOM system centered around -35 MHz. The light out of the double-pass (shifted by ≈ -70 MHz in total) is coupled into a fiber that leads into a polarization spectroscopy set up to be used for frequency referencing (Section 2.3.1). The transmitted light is then reflected on a second PBS and passed through a single pass AOM. The first-order diffraction at -55 MHz from this AOM is used as a push beam between the source chamber and the octagon chamber. We seed TA1 with the remaining ≈ 45 mW and get an output power of ≈ 600 mW. Since the spatial profile of this output is not Gaussian but rather looks nearly like a TEM₀₁ mode, we use a D-shaped pick-off mirror to reflect one half of the beam. The reflected half is passed through a single pass AOM driven at -80 MHz. While the 1st order is used to supply light to address the cycling transition for the 2D MOT, we use the 0th order to seed TA2 (D2 cycling TA). The D2 cycling TA is intended to provide cycling light for the 3D MOTs in the octagon and the science chamber as well as imaging and cooling beams for single atoms trapped in optical tweezers. The second unreflected half of the mode from TA1 is intended to take care of all our repump needs. We first pass it through a double-pass AOM system that shifts its frequency by +360 MHz. (we set this to ≈ 80 MHz away from 440 MHz (i.e. the frequency difference between resonant cycling and repump beams) to allow us the freedom to shift

the repump frequency during different stages of the experiment). Light from the repump double-pass set up is coupled into a fiber and the output is divided on a PBS. The reflected beam is used to supply repump power for the 2D MOT set up while the transmitted beam is used to seed TA3 (D2 repump TA). This TA provides repump light for both 3D MOTs in the octagon and science chamber in addition to repump power for imaging and cooling in optical micro-traps.

2.3 Laser frequency stabilization

The main goal of the apparatus is to prepare laser beam paths that will be used to trap, transport and cool atoms during different stages of the experiment. In order to efficiently manipulate atoms in the chamber, the beams are prepared at frequencies that correspond to different atomic transitions (D1 and D2 transitions) availed to us by nature. For reproducibility and efficient manipulation of the atoms, it is necessary to stabilize the frequency of the laser sources used. Ideally, the linewidth of the laser should only be limited by the properties its resonator i.e. Shawlow-Townes linewidth [39]. However, in reality the frequency of a running laser is actually dependent on temperature fluctuations, mechanical vibrations of the resonator, power fluctuations of the pump beam to the gain medium etc. The frequency of an *unlocked* laser thus drifts over longer timescales and fluctuates on shorter timescales (causing a concomitant linewidth broadening). A general approach for laser stabilization involves comparing the laser frequency to some reference (whose frequency is stable and known) then using a feedback loop to correct for deviations in laser frequency i.e. *locking* the laser frequency to a more stable reference. Since atomic transitions happen at known and absolute frequencies, atomic vapor cells are a popular reference for laser frequency stabilization. While different techniques have been developed for laser frequency stabilization [40–48] , I will focus on polarization rotation spectroscopy [49–55] in this section. For laser stabilization of Rydberg excitation lasers we used Pound-Drever-Hall locking as described in more detail in Chapter 4.

2.3.1 Polarization rotation spectroscopy

Doppler-free polarization rotation spectroscopy (PS) [49] is a modulation-free technique that relies on light-induced birefringence of an atomic medium. Specifically, a circularly-polarized pump beam causes anisotropic population redistribution of the magnetic sublevels ($|F, m_F\rangle$) states in the atomic medium through optical pumping, which induces a rotational birefringence (unequal refractive indices ($\delta n = n_+ - n_-$) experienced by light with orthogonal circular polarizations) and circular dichroism (unequal absorption coefficients ($\delta\alpha = \alpha_+ - \alpha_-$) experienced by light with orthogonal circular polarizations). Additional birefringence is caused by pressure gradient across the vapor cell glass window ($\delta n_{w\pm}$). A linearly-polarized probe beam overlapping the pump beam experiences a rotation of its polarization ($\phi = \frac{2\pi\delta n}{\lambda}l$) due to the different interactions of the right- and left-circular components of the light with the anisotropic atomic medium. Here λ and l are the wavelength of the probe beam and the length of the region of interaction between the atomic medium and overlapped pump and probe beams.

For a laser scanning across one transition $\delta\alpha$ is a Lorentzian i.e. $\delta\alpha = \delta\alpha_{\max}/(1 + x^2)$. Here $x = \frac{2\omega - \omega_0}{\Gamma}$ is the detuning from resonance in units of saturated linewidth Γ . By the Kramers-Kronig relation [56–58], $\delta n = \frac{c}{\omega_0}\delta\alpha_{\max}\frac{x}{1+x^2}$. The difference signal due to the anisotropic atomic medium is given by [54]

$$S_{\text{diff}} = I_0 e^{-(\bar{\alpha}l + \text{Im}[n_w l])} (\delta\alpha_{\max} l \frac{x}{1+x^2} + \text{Re}[n_w l] \frac{\omega}{c}). \quad (2.1)$$

The difference error signal is measured at a polarimeter (consisting of a PBS and a balanced photo-diode²⁴) and is relayed to a feedback loop that adjusts the laser frequency toward resonance.

Spectroscopy set up

In the spectroscopy setup, the laser beam passes through a half-wave plate (HWP) and a polarizing beam-splitter (PBS). The setting of this first HWP allows us to control the relative powers of the pump (reflected at the PBS) and probe (transmitted through the

²⁴Thorlabs PDB210A

PBS) beams. The horizontally-polarized probe beam is aligned in a forward-going fashion through the central part of the vapor cell. The path of the pump beam features a quarter-wave plate (QWP) that allows for the initial vertical polarization of the reflected light to be either kept linear or transformed into either right- or left-circular polarization (elliptical polarizations for intermediate settings). This pump beam is then overlapped with the probe beam in the central region of the vapor cell. The use of a D-shaped pickoff mirror²⁵ combines these beams at a small incidence angle, i.e. in a nearly counter-propagating fashion, to enhance the size of the overlap region contributing to the nearly Doppler-free signal. After

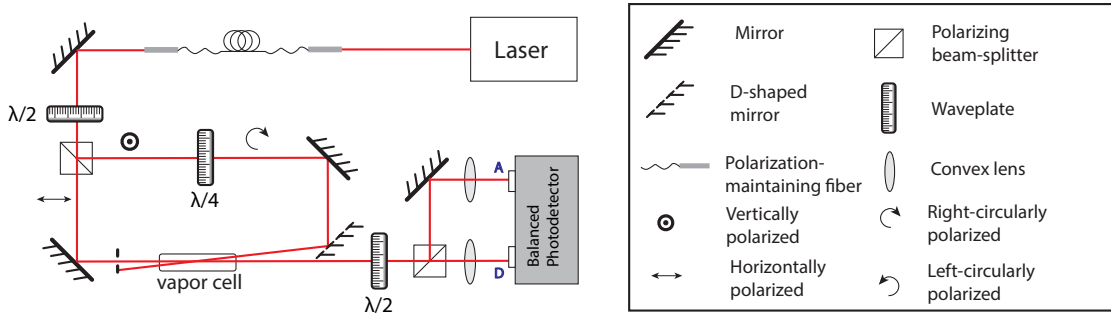


Figure 2.8: Polarization spectroscopy set up (adapted from [53]).

propagating through the vapor cell, the probe beam passes through a HWP and a PBS, and the laser powers in the transmitted and reflected paths are measured at two ports (*A* and *D*) of a balanced photodetector. The difference signal between the measurements at these two ports constitutes the polarization spectroscopy signal. The setting of the final HWP effectively allows the final PBS to project the probe light onto its diagonal (*D*) and anti-diagonal (*A*) linear polarization components. In the absence of rotation of the incident horizontally-polarized probe induced by potassium atoms in the vapor cell, the measured powers in the *A* and *D* paths will be equal, such that their measured difference signal at the photodetector will be zero. Non-zero difference signals relate to a combination of dichroism and birefringence induced in the potassium atomic medium, due to anisotropic population redistribution by the pump beam. The polarization spectroscopy traces are recorded by capturing the response of this setup as the source laser current (and thus laser frequency) is scanned in a symmetric (triangle wave) fashion.

²⁵Thorlabs BBD1-E03

Modeling the PS signal

In order to identify the different spectral features of a PS signal, we develop a theoretical model based on solving rate equations. In this section we showcase the results of this model (described in more detail in Appendix D). While the model can be applied to any transition, we apply it to the D1 transition ($4S_{1/2} \rightarrow 4P_{1/2}$) of ^{39}K . Our choice is not only motivated by the simplicity of this transition but also by the fact that, to the best of our knowledge, the PS signal for this transition had not been presented in literature. Since the 770 nm laser is the workhorse of the sub-Doppler cooling scheme based on gray molasses (Section 2.6.1), it was imperative that we correctly identify the transitions from acquired PS signal.

In Appendix D we derive an expression for expected PS signal by solving rate equations for population dynamics when the pump and probe beams address the $F \rightarrow F'$ transition where the hyperfine quantum number, F , ranges from $F = |I - J|$ to $F = |I + J|$, where $I = 3/2$ and $J = 1/2$. The projection of F onto the z -axis, m_F , is the hyperfine sub-level. The expression is given by

$$S_{\text{diff}}(\omega) \propto \sum_{\{F, F'\}} \frac{T(\omega)}{T_{\max}} \left(\mathcal{A}(F, F') l' \frac{x(\omega)}{1 + x(\omega)^2} \right). \quad (2.2)$$

where we have replaced I_0 in Eq. 2.1 with a normalized absorption (transmission) profile, $\frac{T(\omega)}{T_{\max}}$ which is read out from one of the ports of the balanced photo-diode and replacing $\delta\alpha$ with a time-averaged population anisotropy $\mathcal{A}(F, F')$ obtained from solving rate equations to reveal population dynamics. The birefringence due to the glass window is assumed to be small in this case and is therefore not considered. The total signal is obtained by summing up dispersive signals pertinent to different $F \rightarrow F'$ transitions evaluated at the correct detunings relative to the $F = 2 \rightarrow F' = 2$ transitions as shown in Fig. 2.9.

Additional cross-over peaks occur at a frequency half-way between two transitions. This happens where the velocity of some atoms in the vapor cell (at a frequency exactly half-way between two frequencies) leads to a Doppler shift of either the pump beam to a higher frequency or the probe beam to a lower frequency. We therefore end up with 9 transitions to consider for the D1 line. Finally, as shown in Fig. 2.9 (c,d), including the effects of power

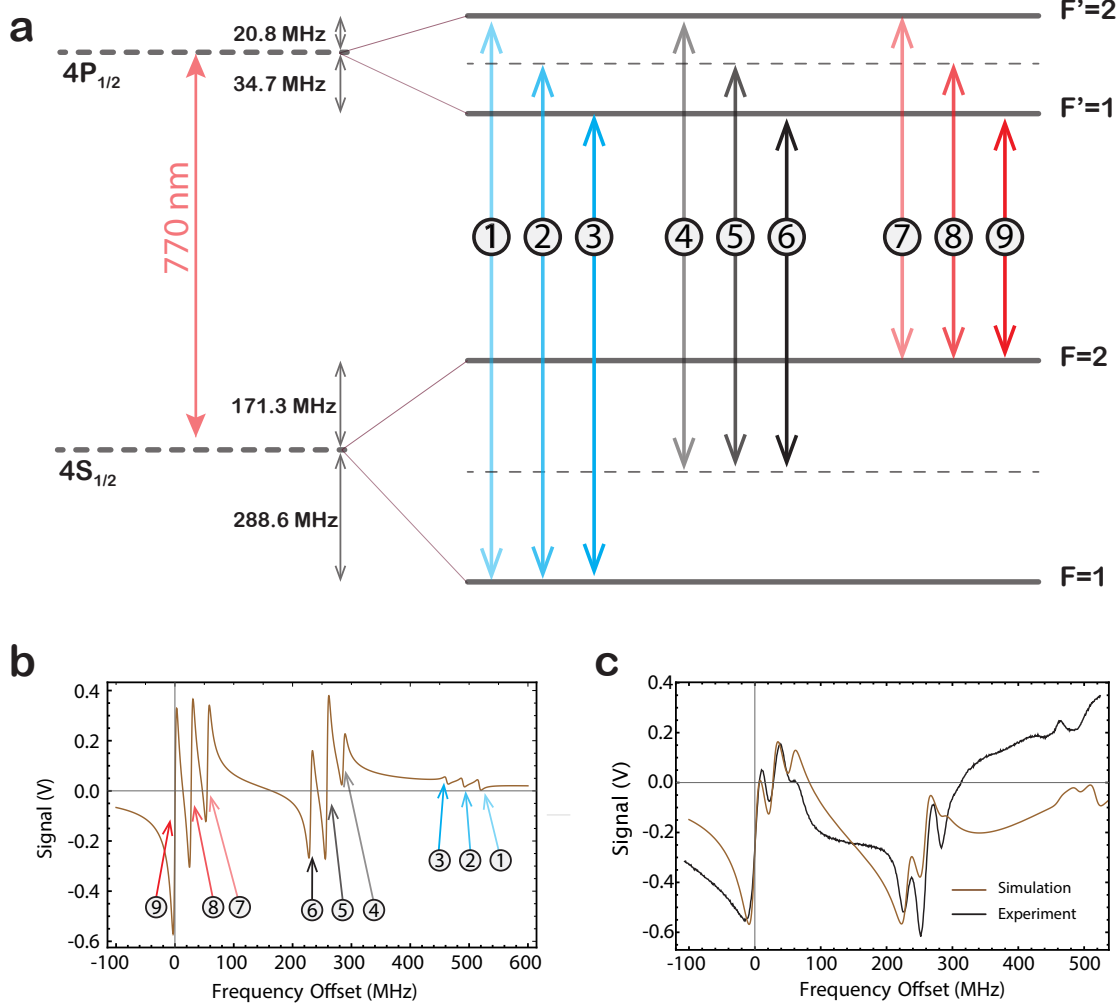


Figure 2.9: Polarization spectroscopy signal for the D1 transition of potassium 39 atoms. (a) D1 transitions that will contribute to a polarization spectroscopy signal. Transitions labeled 2,4,6 and 8 are crossover transitions. (b) Simulated PS signal with the transition linewidth of Γ . (c) Simulated PS signal including power broadening.

broadening ($I'_0 = \sqrt{1 + I_0/I_{\text{sat}}}$) leads to a more realistic model curve.

Vapor pressure for potassium

The size of the PS signal obtained highly depends on the density of atoms in the area of interrogation. Potassium has low vapor pressure at room temperature ($\approx 2 \times 10^{-8}$ Torr)²⁶. In order to get enough vapor pressure to build up a reasonable signal, we heat up the vapor cell so that the average temperature is ≈ 60 °C. For the dispenser source cell at the 2D MOT,

²⁶Compared to $\approx 2 \times 10^{-7}$ Torr for ⁸⁷Rb at room temperature. ⁸⁷Rb sources therefore do not need to be heated up to acquire a good signal.

we attach Mincos Polyimide thermofoil heaters (Mincos HK6909) along the edges and wrap both the top and bottom arms of the cell and the area around the differential pumping tube using Thorlabs HT10K heater tapes. The tapes around the outside edges, i.e. the dispenser arms and around the differential pumping tube, are set at ≈ 70 °C while those along the four edges of the cell are set at ≈ 50 °C. We measure the size of the PS signal as a function of temperature as shown in Figure 2.10 below.

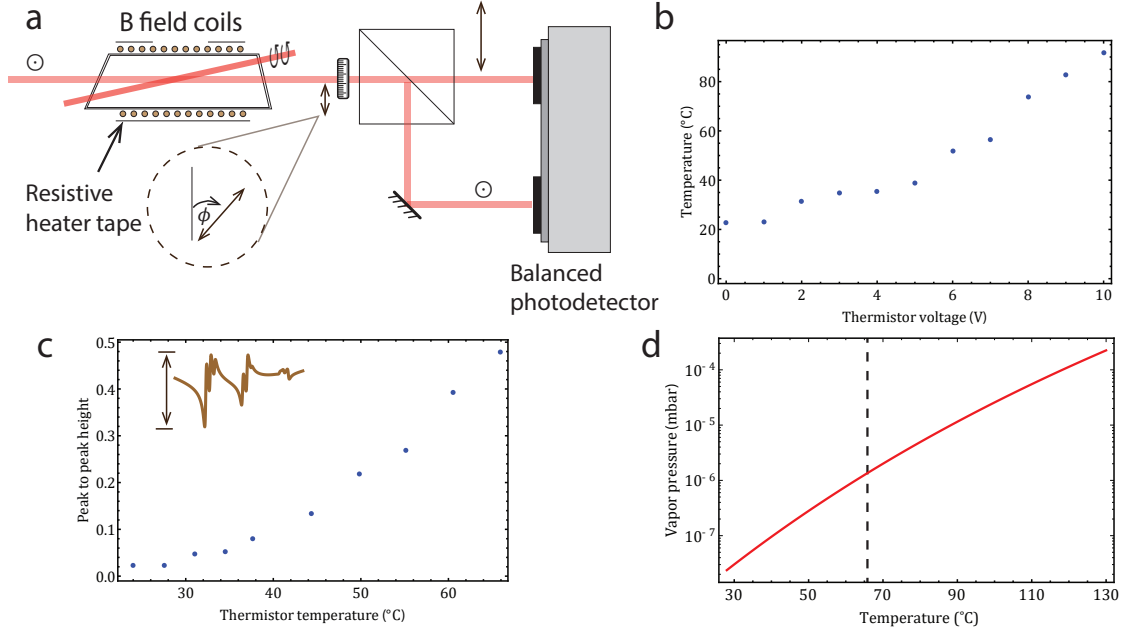


Figure 2.10: Polarization spectroscopy signal optimization. (a) Polarization spectroscopy set up with resistive heaters that increase the vapor pressure and a magnetic field solenoid that sets the quantization axis. (b) Temperature increase with voltage applied to resistive heater tapes. (c) and (d) Sufficient vapor pressure can be achieved by heating the cell close to the melting point.

In addition to heating the cell to get enough vapor pressure to acquire a good PS signal a small quantization B field is typically added along the direction of pump beam propagation. This improves optical pumping from the pump beam and leads to a more extreme anisotropy in the population distribution. In Figure 2.11 we demonstrate the importance of setting a quantization field. Since the 405nm $4S_{1/2} \rightarrow 5P_{3/2}$ transition is much weaker compared to the D1 and D2 transition (≈ 1.19 MHz/6 MHz²⁷), it is more difficult to get a reasonable (if any) PS signal. The black line corresponds to the PS signal without applying

²⁷Even though the bare linewidth of the $4S_{1/2} \rightarrow 5P_{3/2}$ transition is $2\pi \times 185$ kHz, the total linewidth considering all decay channels is $2\pi \times 1.19$ MHz.

any magnetic fields to set a quantization axis. The signal (barely above the background) was identified by tuning the laser to the correct frequency (741091 GHz as confirmed by a Bristol 671 series wavemeter) and then rotating a $\lambda/4$ plate to change the sign of its slope. We witness a dramatic improvement in signal-to-noise by applying a small B field (≈ 1 G). We identify the three features as the $F = 1 \rightarrow F' = 2$, a cross-over peak and the $F = 2 \rightarrow F' = 3$ transition (from left to right).

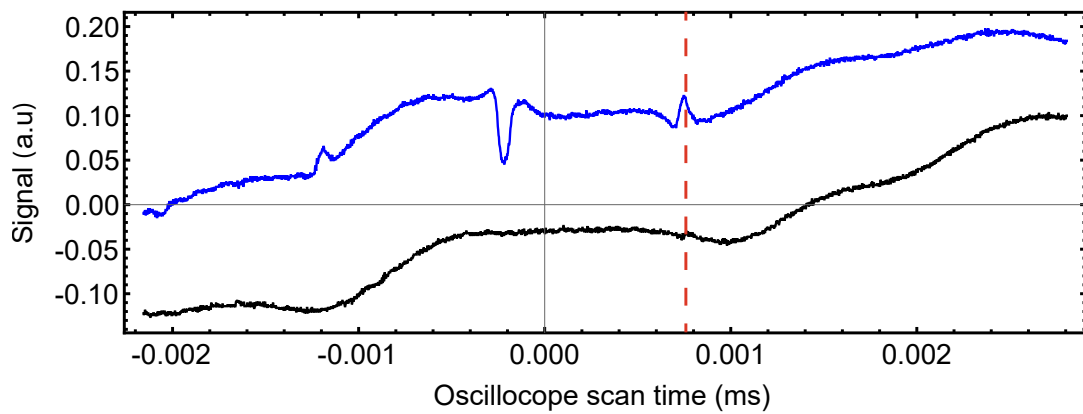


Figure 2.11: Polarization spectroscopy of the $4S_{1/2} \rightarrow 5P_{3/2}$ transition. Black shows the signal without applying a B field. Red dashed line shows the $F = 2 \rightarrow F' = 3$ transition which is barely above the noise. Blue is the signal after applying a small B field along the pump beam propagation axis. Adding a quantization field to polarization spectroscopy **massively** increases the size of the signal.

2.4 Construction and optimization of magneto-optical traps (MOTs) of ^{39}K atoms.

Coil design

To trap atoms in different chambers in the apparatus a combination optical fields and magnetic field gradients (that shift atomic Zeeman levels in a position dependent way) are arranged to confine atoms in space centered at a magnetic field zero point (as described in Section 2.4). While this infrastructure is required to trap atoms in each of the three chambers, we only detail the coil structure and design used at the final science chamber. We produce a magnetic field gradient at the center of a magneto-optical trap (MOT) using a pair of 250-turn circularly-coiled, 22-gauge magnetic wire (Digikey MW35-C HY). The wire features a Polyamide coating that allows us to wind many turns of the wire without risk of shorting. Selecting a 22-gauge wire enables us to wind many turns in a small volume thus increasing the magnitude of magnetic fields that can be produced. In other words, for N coils of radius R and current I flowing through, the total magnetic field at position y (along a

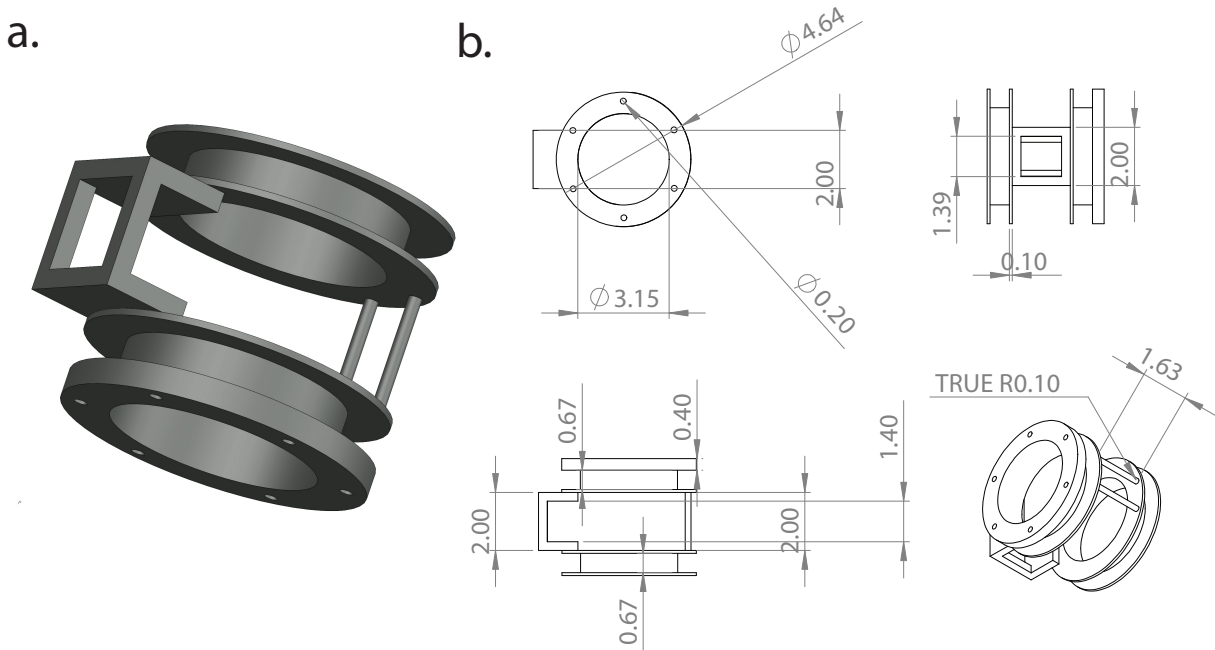


Figure 2.12: 3D MOT gradient coils. Mounting holes (for 1/4-20 set screws) are tapped at the bottom after 3D printing. At the front side of the coil holder two tiny pillars are used to increase optical access.

line perpendicular to the plane of the coil) produced is $N \times B_{\text{coil}}$ where $B_{\text{coil}} = \frac{\mu_0}{4\pi} \frac{2\pi R^2 I}{(y^2 + R^2)^{3/2}}$ ²⁸. These coils are set up in an anti-Helmholz configuration i.e. with current flowing in opposite directions to produce a quadrupole field at the center which can be used to spatially confine atoms when combined with three-pairs of retro-reflected beams in a MOT. Additionally, a pair of 100-turn coil sets are set up in Helmholtz configuration to apply a uniform field at the center of the science chamber useful for *Zeeman shifting* atomic levels for isolation of specific states for microwave driving in proposed synthetic Rydberg lattices (explained in Chapter 4).

For mechanical support we wind the coils around a 3D printed support-structure shown in Figure 2.12. These coil holders were printed by Ralf Möller at the Rapid Prototyping Lab at UIUC using a Fused Deposition Modeling (FDM) Fortus 360 MC printer²⁹. ABS (Acrylonitrile Butadiene Styrene) plastic is chosen as printing material, since it can be easily machined and glued. In particular, we design our gradient coils to include six equidistant through holes that can be tapped to enable mounting onto Thorlabs TR series optical posts using a 1/4"-20 set screws. While the coil holder provides mechanical support, we also use the structure as an alignment reference for MOT beams. Particularly, the structure is centered as best as possible with respect to the science cell followed by attaching extra parts that mate into the circular openings at the top and bottom and to the side pillars for alignment.

In an ideal scenario, the magnetic field zero of the gradient field should be at the center of the overlapping MOT beams. As you might have guessed, the magnetic field zero is usually shifted away from the center due to stray magnetic field from ion pumps and lab equipment or even due to the effect of the earth's magnetic field. Cold atom experiments, therefore, typically include magnetic field cancellation coils (which we refer to as shimming coils in our lab). These are usually designed to produce low fields and gradients (≈ 1 G and 1 G/cm,

²⁸Based on Biot-Savart law

²⁹FDM works by depositing a thermoplastic material where a printer head moves in two dimensions according to a programmed control based on a 3D CAD design. The work head onto which material is deposited shifts vertically when each layer is done in order for the printer head to start depositing the next layer.

respectively) in all three directions to allow for full cancellation of unwanted magnetic fields. We use three pairs of 180 turns of 22-gauge and Polyamide-sleeved magnetic wire placed at $\approx 4.15''$ from the center of the cell to produce uniform fields in all three directions. The coils are wound on a 3D printed cubic holder (shown in Figure 2.13) which consists of a single 8.4" cube structure with two pairs of 0.55" deep troughs in each direction. Four extensions at the bottom (each including tap holes) allow for mounting onto Thorlabs optical posts using 1/4"-20 set screws. Although the size of the holder is limited by chamber support structure, we find that it is large enough for MOT optics to be mounted within the structure.

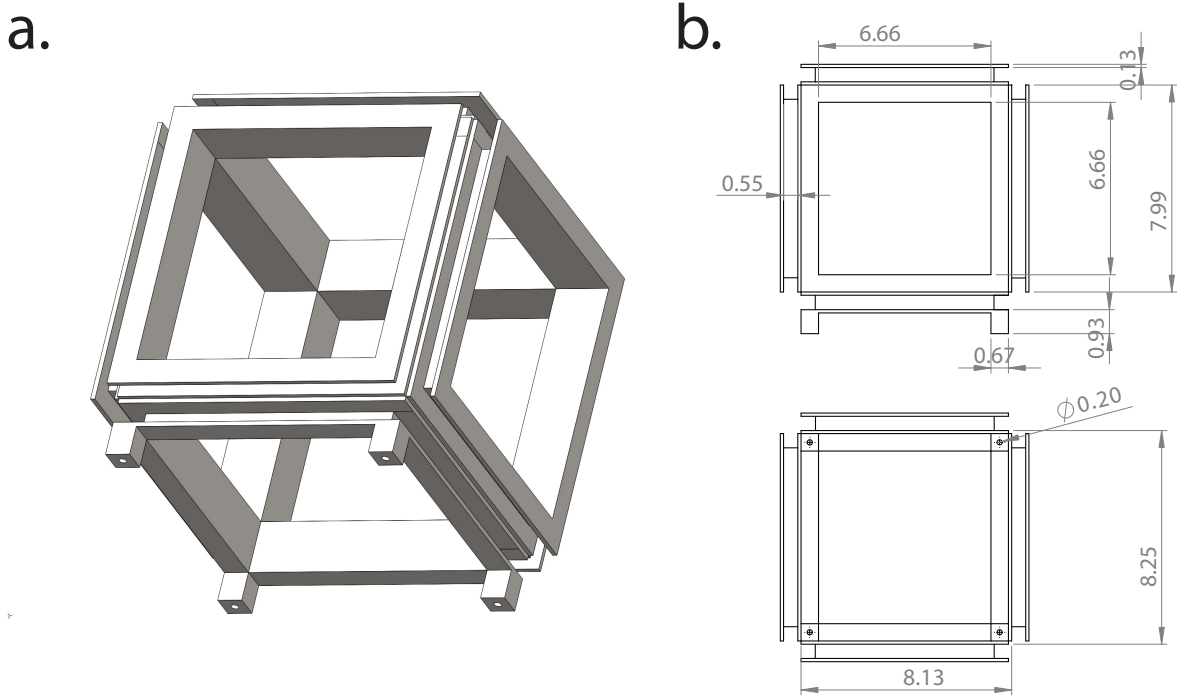


Figure 2.13: 3D printed coil holder for field cancellation coils at the science chamber.

The field cancellation structure is also useful for alignment. For instance, while setting up MOT optics to transfer atoms for the first time, we drill holes at the corners and pass beams to define near-perfect 90 degree intersection of horizontal MOT beams at the center. The structures are also later used in the final design where horizontal MOT beams are overlapped at 120 degree with respect to each other (Fig. 3.2) to avoid clipping MOT beams with high-NA objective lenses. Additional sets of coils 30 turns are included as extra gradient

shims. Later on, we find these extra set of coils really useful as a tool for moving the MOT around at different stages of the experiment. Specifically, the first set of shimming coils are optimized for a cooling stage as explained in Section 2.6.1. Since we find it rather difficult to efficiently overlap optical micro-traps to a pre-determined molasses position³⁰, we use an extra set of shimming coils to move the MOT around to improve overlap with fixed optical traps.

In Table 2.1 we present magnetic field and gradient measurements done for shimming coils and gradient coils, respectively. The first two rows refer to the gradient coils and field coils wound on the coil holder described on Figure 2.12 while the last six rows are the 2 sets of 3 pairs of shimming magnetic field cancellation coils. Using a Hall probe (Lakeshore Cryotronics HST), we perform magnetic field measurements for coils in Helmholtz configuration by placing the probe at the center then varying the current passed through the coils. The measurements are close to calculated target of 1.2 G/A . For magnetic gradients, we set up the hall probe on a μm -moving stage. For each position of the probe we record the magnetic fields measured as function of current passed through the coil pair. Magnetic field gradients derived from these measurements are also close to calculated target gradients of 1 G/cm/A. The measurements are read off on a Lakeshore Cryotronics model 460 gaussmeter.

Trapping and cooling in MOTs

Trapping and cooling in cold atom experiments relies on knowledge of electronic energy levels of atoms and the use of lasers to impart forces on them. Consider an atom in the ground state of a two level system. If the atom interacts with a photon whose frequency matches the energy difference between the ground and excited state, the atom can absorb the photon and move to the excited state. Due to finite lifetime of the excited state, the atom can spontaneously decay to the ground state and re-emit a photon in a random direction.

Now consider an atom interacting with two counter-propagating beams at some frequency.

³⁰Adjusting the focus and position of tightly focused optical microtraps is much more tedious than changing current values sent to shimming coils.

Coil set	Helmholtz(G/A)	Anti-Helmholtz (G/cm/A)
Science MOT Gradient	-	10.04 ± 0.002
Science MOT Field	14.75 ± 0.002	-
E-W field shim	1.07 ± 0.0002	-
T-B field shim	1.21 ± 0.005	-
N-S field shim	1.16 ± 0.001	-
E-W grad. shim	-	0.83 ± 0.015
T-B grad. shim	-	0.92 ± 0.003
N-S grad. shim	-	0.89 ± 0.007

Table 2.1: Magnetic gradient and field measurements. The first two rows correspond to primary gradient and field coil pairs used for creation of a 3DMOT. These two sets are wound on the magnetic gradient holder described in Figure 2.12. The last six rows corresponding to stray field and gradient cancellation coil pairs (Figure 2.13). These were especially useful for providing zero magnetic field and gradient where the MOT forms. The shorthand E/W, N/S corresponds to the cardinal directions in the lab while T/B refers to top and bottom directions. The character - indicates that the coil pair was not designed to be operated in the given configuration.

In the reference frame of the atom the frequency detuning of the right- and left-propagating beams are Doppler shifted away and towards resonance respectively as shown in Figure 2.14 (a). An atom with velocity $v > 0$ therefore absorbs a photon from the left propagating beam and re-emits in a random direction while an atom with $v < 0$ absorbs from the right propagating beam and re-emits in a random direction. This leads to a velocity dependent scattering force that slows down the atom. This phenomenon is referred to as optical molasses. While optical molasses reduces the velocity of the atom, it does not provide confinement. In a magneto-optical trap, confinement is achieved by introducing a quadrupole magnetic field gradient.

On Figure 2.14 (b,c) we illustrate how this works. Considering a simple $J = 0 \rightarrow J = 1$ transition. A magnetic field leads to linear Zeeman shifts in the magnetic sublevels, $m_J = 0, \pm 1$ of the excited state $J = 1$. For the case where the right and left-propagating beam have σ^+ and σ^- polarizations respectively, atomic selection rules only allow transitions such that $\Delta M_J = +1$ and $\Delta M_J = -1$. In the arrangement shown in Figure 2.14 (b,c), the *position-dependent* Zeeman shift for $m_J = -1$ and $m_J = +1$ brings them closer to resonance with the σ^+ and σ^- polarized beams. This creates a restoring force that pushes the atom toward the center of the trap (position $z = 0$). The combination of position-dependent and velocity-dependent force in the magneto-optical trap is expressed as [59, 60]

$$F_{\text{MOT}} = - \left(\frac{8\hbar k^2 s_0 \delta / \Gamma}{(1 + (2\delta/\Gamma)^2)^2} \right) v - \frac{1}{k} \left(\frac{8\hbar k^2 s_0 \delta / \Gamma}{[1 + (2\delta/\Gamma)^2]^2} \right) \left(\frac{\mu \partial B}{\hbar \partial z} \right) \vec{z} \quad (2.3)$$

where $s_0 = I/I_{\text{sat}}$ is the saturation parameter, δ is the detuning from resonance, $\Gamma = 2\pi \times 6 \text{ MHz}$ is the transition linewidth, $k = 2\pi/\lambda$ is the wavevector associated with the beam μ is the magnetic moment of the transition and $\frac{\partial B}{\partial z}$ is the magnetic field gradient.

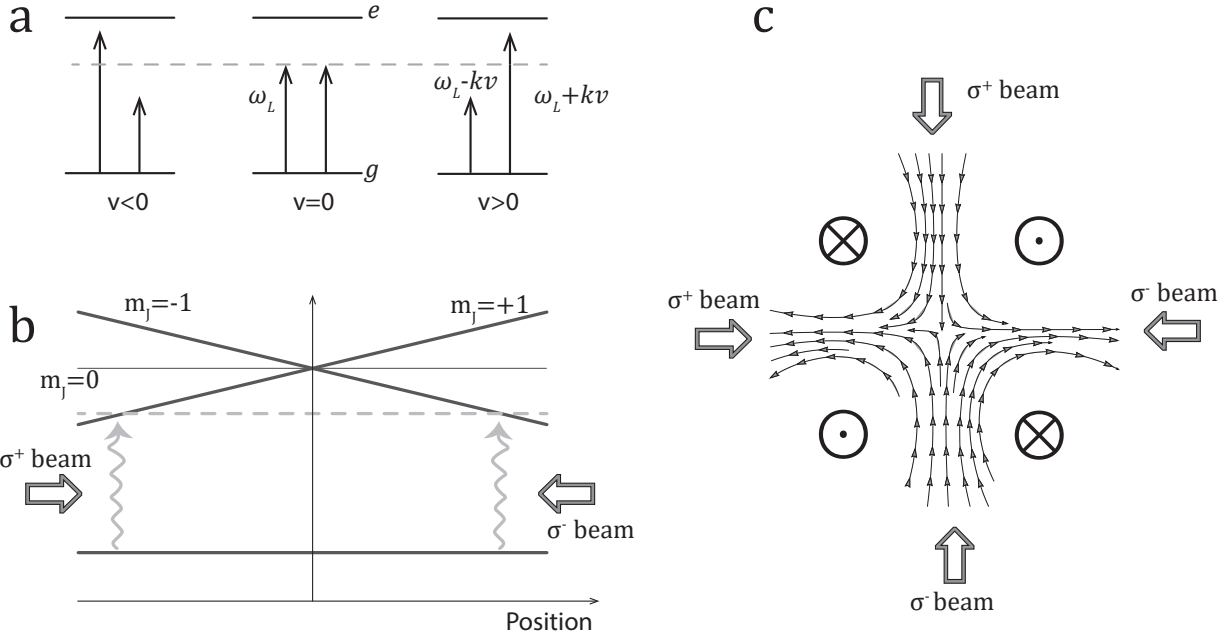


Figure 2.14: Magneto-optical traps. (a) Doppler shifts leading to velocity-dependent forces. (b) Spatially varying magnetic fields cause restoring forces toward the center of the trap. (c) Quadrupole field lines from rectangular coil set in an anti-Helmholtz configuration in a 2D MOT configuration.

Cycling transitions for ^{39}K

Alkali atoms are popular for laser cooling due to a relatively simple ground state and first excited state configurations. They feature a D1 transition $nS_{1/2} \rightarrow nP_{1/2}$ and a D2 transition $nS_{1/2} \rightarrow nP_{3/2}$ where n is the principle quantum number. Due to atomic selection rules $m_J = 0, \pm 1$, the D2 transition exhibit a closed transition when the atom interacts with a σ^+/σ^- polarized photon. Specifically, as illustrated for ^{39}K in Figure 2.15, an atom excited from $\{F, m_F\} = \{2, 2\}$ to $\{F', m_{F'}\} = \{3, 3\}$ by a σ^+ polarized photon can only decay back to $\{F, m_F\} = \{2, 2\}$. Occasionally the atom can decay out of the loop into the $F = 1$

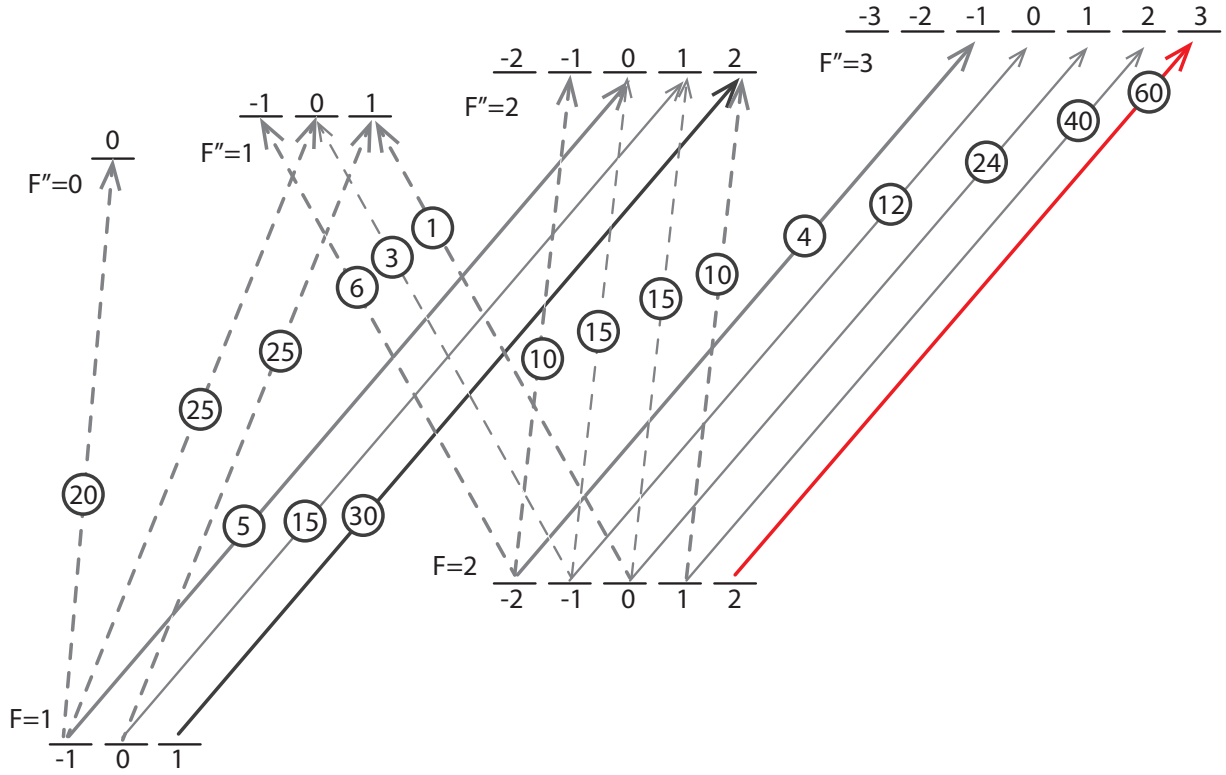


Figure 2.15: Transition strengths for σ^+ . The red arrow shows the cycling transition for ^{39}K . The transition strengths relative to the weakest transitions are shown in the circles for each transition.

manifold, following off-resonant excitation to an $F' = 2$ state.. A single repump beam between $F = 1$ and $F'' = 2$ on the D2 transition is sufficient to bring the atom back into the loop. Combining cycling and repump beams in MOTs allows us to trap and cool atoms at different stages of the experiment. Now we move ahead and describe trapping and cooling achieved in our experiment.

2D MOT set up

Our experiment begins with the creation of two-dimensional magneto-optical trap (2D MOT) in the source cell section of the vacuum chamber. The ^{39}K atoms are produced from a dispenser source (described in more detail in section 2.1). Due to a high vapor pressure required, we wrap the 2D MOT source cell with resistive heater tape to avoid condensation of atoms on the glass cell, only allowing access for beams required for creation of a 2D MOT. The heater tapes are heated to an average of 50 °C. The 2D MOT beams are derived from

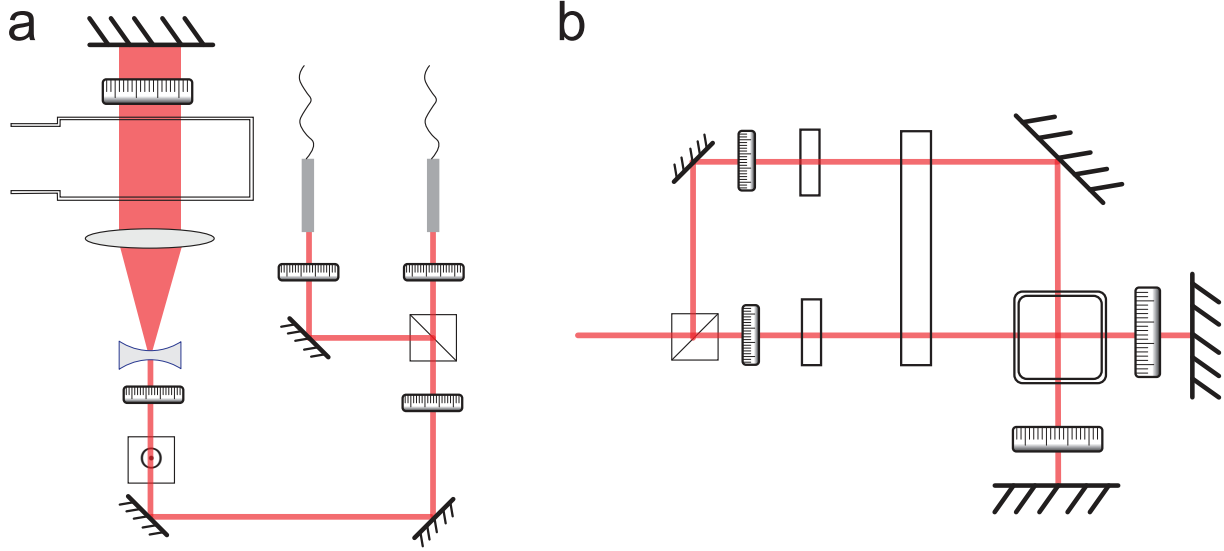


Figure 2.16: 2D MOT optical set up. (a) Top view showing only horizontal beam path. (b) Side view showing separation of combined cycling and repump beams using a PBS.

two single mode PM fibers (delivering cycling and repump beams)³¹. These two collimated beams (≈ 35 mW of cycling and 35 mW of repump³²) are then combined on a PBS, passed through a $\lambda/2$ waveplate set to 22.5° and then encounter another PBS that divides the combined cycling and repump beams into two paths to be used to trap atoms in the vertical and in the horizontal direction. The 22.5° waveplate setting mentioned above rotates the orthogonal polarizations of the combined cycling and repump beams so that they each have equal components in the horizontal and vertical 2D MOT trapping directions. The two separate beam paths are then passed through a cylindrical telescope which magnifies them by a factor of 5 in the horizontal direction so that the final beam are elongated along the 2D MOT cell. This allows for trapping atoms along a line. The beams are then passed into the 2D MOT cell in the horizontal and vertical directions as shown in Figure 2.16 and then retro-reflected to allow for cooling in both directions. We set up $\lambda/4$ waveplates before the cylindrical telescopes and also before the mirrors used for retro-reflection.

³¹Chronologically, we actually first set up a 3D MOT in the 2D MOT chamber in order to get the laser frequencies and polarizations right.

³²Even though we began with 1:1 cycling to repump power ratio for the 2D MOT at the beginning, we have since optimized this over time and found a good working ratio at or below 3:1 cycling to repump power ratio.

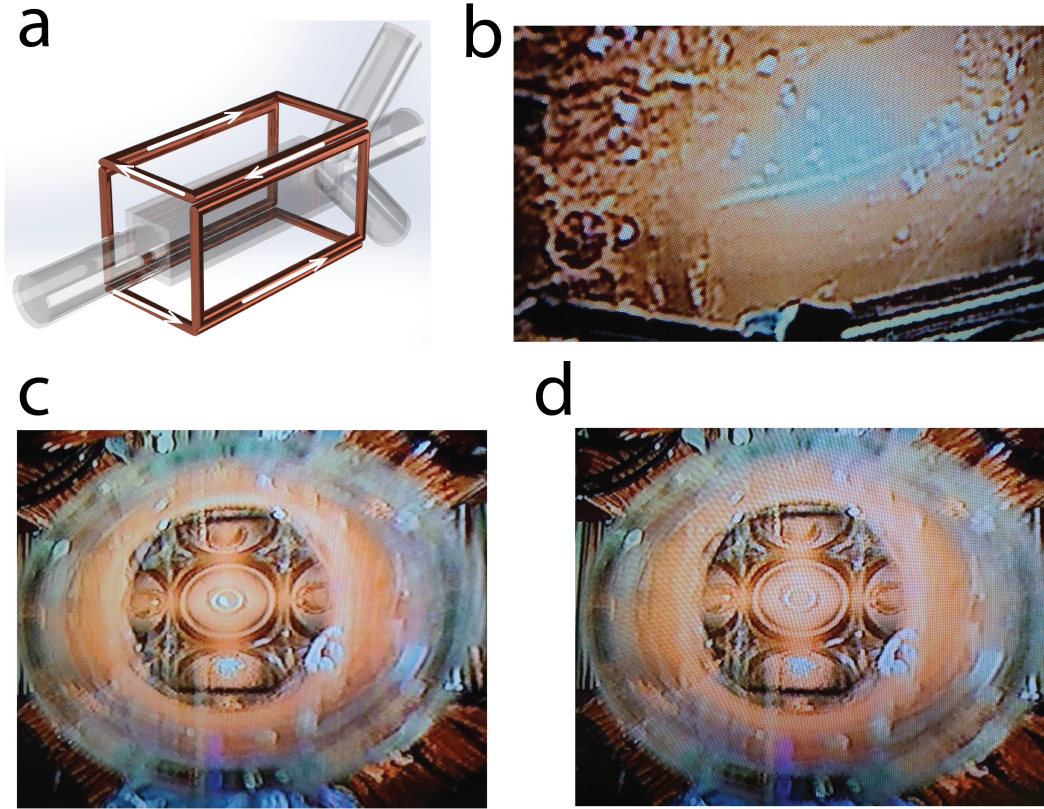


Figure 2.17: ^{39}K 2D MOT (a) Rectangular coil set for two dimensional quadrupole magnetic field gradients. The position of zero field can be moved around by tuning the relative currents between coil sets in opposite directions. The white arrow lines show the direction of current flow for an anti-Helmholtz configuration. (b) Unprocessed image of ^{39}K atoms in a 2D MOT forming a line (c) ^{39}K atoms in a 2D MOT with (left) and without (right) magnetic field gradient. The line of atoms can be centered to the differential pumping tube (circle at the center), by tuning the relative currents on opposing coils. Alignment of the MOT beams to the center of the cell can be easily done with respect to the differential pumping tube.

2D MOT magnetic field coils

A magnetic field gradient in both directions is necessary for the creation of a 2D MOT. In our set up we use two pairs of 48 turn gauge 16 copper coils operating around 2A to generate magnetic field gradients. The coils are wound in a rectangular shape to provide quadrupole magnetic field in the vertical and horizontal direction as shown in Figure 2.17(a). A push beam ($\approx 1 \text{ mW}$ of slightly blue-detuned at $+3\Gamma$) is shone along the 2D source cell to push atoms trapped in the 2D MOT through a differential pumping tube to the second section of the vacuum chamber where they can be trapped in a 3D MOT as described in 2.4.

3D MOT in octagon chamber

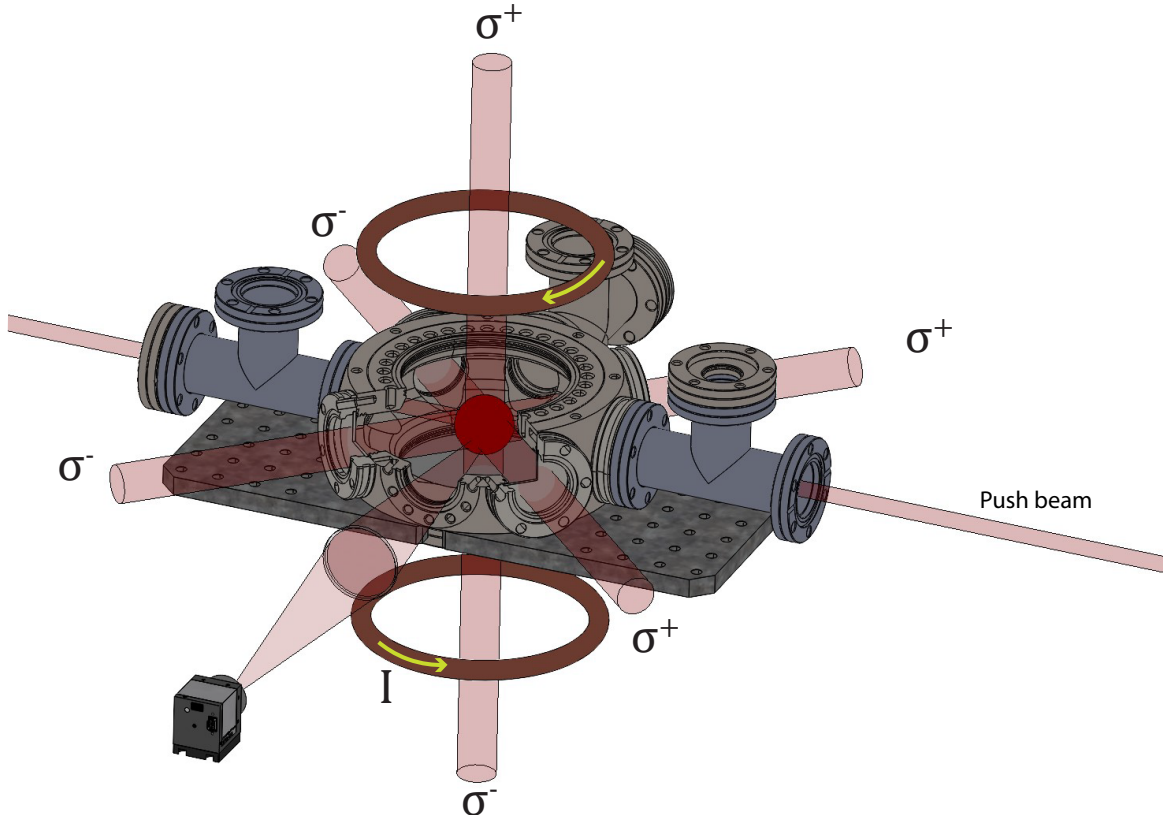


Figure 2.18: Beam configuration for the MOT1 set up. Three sets of counter-propagating circularly polarized beams intersect at the field zero of a quadrupole magnetic field gradient. The field gradient is generated using two sets of copper coils in an anti-Helmholtz configuration ie. current flows in opposite directions creating B fields that both point towards the center of the chamber. A push beam provides a steady source of atoms from a high vapor pressure 2D MOT source chamber described in Section 2.4. Imaging is done in a 2f-2f configuration with a 300mm lens on to a Thorlabs CCD Camera (DCC3260M). The imaging view port perpendicular to the push beam directions enables low background imaging.

Atoms pushed out of the source chamber through the differential pumping tube are captured in a 3D MOT in the octagon chamber. As mentioned earlier, we set up the 3D MOT in a section of the vacuum chamber with lower vapor pressure to minimize one-body loss due to collision with background gas. Low background pressure therefore enhances their lifetime in the trap. The 3D MOT is of course a three dimensional version of the 2D MOT we just discussed, where three retro-reflected laser beams (arranged at 90 degrees to each other) are combined with a quadrupole magnetic field gradient to trap atoms. The magnetic field gradient in this case is generated using two sets of circular coils as shown in Figure 2.18. We use polyamide-coated 22 gauge magnetic wires for this purpose operated at 1.4 A to provide

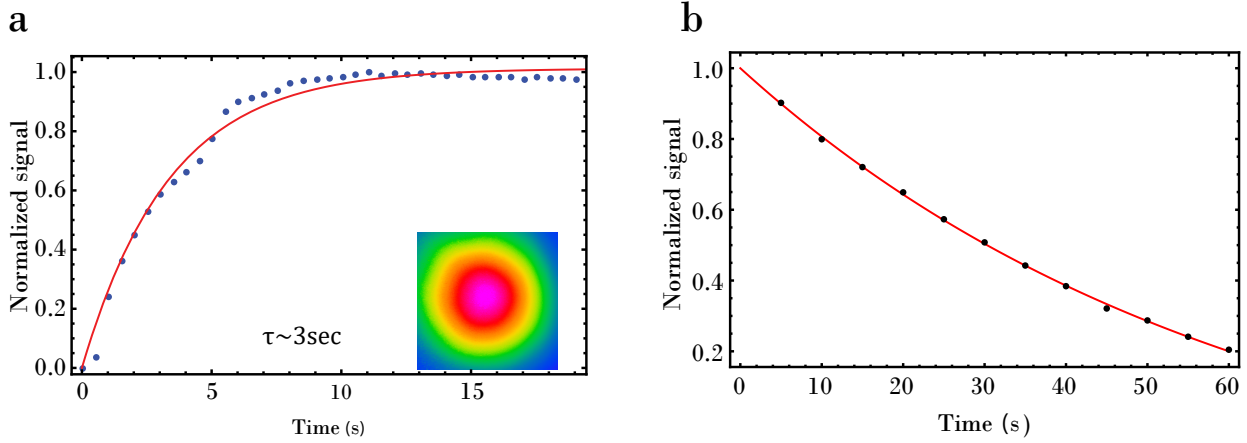


Figure 2.19: ^{39}K 3D MOT loading and lifetime in the octagon chamber. (a)Initial loading time achieved was ≈ 3 sec. Inset, False color image of ^{39}K 3D MOT containing 10^7 atoms. (b) MOT lifetime when source push beam is turned off. The MOT stays around for ≈ 1 min.

$a \approx 15 \text{ G/cm}$ gradient across the center.

Beams out of the final PM fibers are then magnified by $\times 4$ to a final size of $\approx \varnothing 25 \text{ mm}$. The three pairs of beams are overlapped at 90° to each other at the center of the octagon chamber and retro-reflected as shown in Figure 2.18. A clean-up PBS³³ is set up at each of the output to ensure linear polarization. Right before going into the vacuum chamber the forward propagating beams encounter a $\lambda/4$ plate that turns their polarization from linear to circular polarization. Slight polarization contamination that might occur at the glass window at the entrance of the chamber is too small to affect the performance of the MOT. The forward going beams pass through glass windows on the opposite side and are then retro-reflected. A $\lambda/4$ plate is placed right before the retro-reflection mirror to rotate the polarization of the beam from right-to left-circular polarization.

With knowledge acquired from initially setting up a test 3D MOT in the source chamber, we were able to find a reasonable range of cycling and repump frequencies where the 3D MOT works.

³³A PBS at the output to guarantees that the output beam polarization sent to experiment is purely linear.

Combining cycling and repump beams

Due to a small hyperfine splitting in the excited state in ^{39}K , the repump beam turns out to be very important for a well functioning MOT. Misalignments between repump and cycling beams while setting up a MOT are less forgiving for ^{39}K , compared to ^{87}Rb , for example. Proper spatial combination of repump and cycling beams is therefore a critical topic of discussion. Besides, the polarization of combined repump and cycling beam necessarily needs to match.

In order to combine cycling and repump beams while also matching their polarizations, we considered the following scenarios:

1. Using 2×2 Thorlabs fused fiber optic couplers (PN780R3A2 or TW805R5A2) the cycling and repump beams can be directly coupled into two input ports. Light from the output ports are then ready to be sent to experiment. While this method is simple, polarization matching between cycling and repump has to be done either before or after coupling. Additionally using these couplers was sensitive to polarization rotation of the input beams caused by temperature variation, stress points at any part of the fiber and slight mismatch of the polarization of the incoming beam with the slow axis of the fiber as set at the input port. The performance of the coupler could however be improved by physical contact with the optical table (which acts a thermal bath) and avoiding turning the fibers at sharp corners.
2. Combining the beams while they are still small ($\approx \varnothing 1\text{mm}$) on a D-shaped pick-off mirror (Fig. 2.20(c)) followed by magnifying both beams using a telescope so that they are mostly overlapped in the vacuum chamber. This technique allows one to individually match the polarizations of both beams just using separate $\lambda/2$ plates before combining.
3. Combining on a PBS (Fig. 2.20(a)) with highest extinction ratio followed by passing the orthogonal output polarizations (horizontal/vertical) through a $\lambda/2$ plate at 22.5° . This first wave plate rotates the polarizations so that they are anti-diagonal (A)/diagonal (D). The A/D polarized combined beams are passed through a final PBS

that transmits a horizontal and reflects a vertical component of combined cycling and repump beams thus creating two paths that can be sent to experiment. This method was used in our 2DMOT set up.

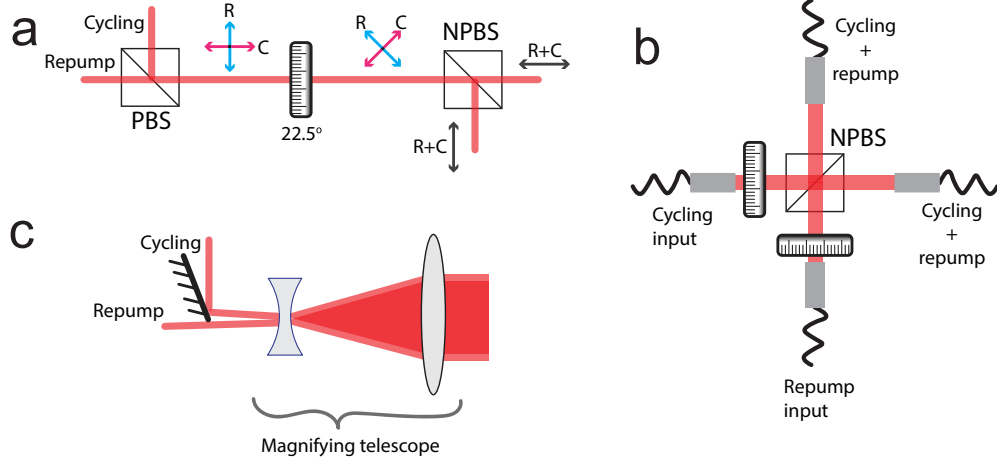


Figure 2.20: Combining cycling and repump beams.

4. Combining on non-polarizing 50:50 beam-splitter (NPBS) (Fig. 2.20(b)). For this method, we coupled the cycling and repump beams into separate PM fibers. The output of these fibers are aligned using mirrors into orthogonal input faces of an NPBS in order to combine them. The combined beams from the output faces are then coupled into two separate PM fibers. We ensure minimal distance between optics to reduce thermally-induced alignment changes. We chose this technique over 1-3, because we could get really good coupling efficiencies (because the beams could be well-collimated) and high polarization extinction ratios using independent $\lambda/2$ plate at each of the path before combining on a NPBS.
5. Spliceless PM coupler arrays: Since our vacuum chamber design requires setting up of two 3D MOTs setting up beam combination using NPBSs gets complicated. We invest in a 4×4 spliceless PM coupler arrays from Evanescent Optics Inc. The spliceless array relies on evanescent wave coupling between two polished fibers in *optical contact*. In particular cladding is removed from one side of the core (while keeping the core intact) and fiber halves placed in physical contact with the stress core matched (which corresponds to matching their polarizations). Our 4×4 coupler array consists of 4

fiber inputs and 4 fiber outputs with the combining section housed in a 4" × 3.5" × 0.5" aluminum enclosure. The aluminum housing acts as a heat sink to minimize temperature fluctuations.

For each of the input we get $\approx 25\%$ of the light on each output. We send in cycling and repump beams from our laser preparation set up into two of the inputs and send the first two outputs to the octagon chamber 3D MOT. One of the outputs is used to provide light for the top-down beam while the second output is divided into two paths on a 50-50 beam-splitter and further sent to two PM fibers that will provide light for two horizontal beam paths. The last two outputs (initially terminated) are used to provide light for the science chamber 3D MOT where one of the outputs is passed through an intermediate 50:50 NPBS that creates two separate paths for horizontal MOT beams.

We later use the last two input connections on the 4×4 coupler array to deliver 770nm light to the science chamber MOT. This is ideal because the alignment at the octagon and science chambers is only done once when setting up the 3D MOTs and subsequent beams added are already aligned by design.

2.5 Rapid transport of atoms between two sections

2.5.1 Transport of atoms in multi-section chambers

The requirement to prepare samples of ultracold atoms requires initial capture of a large number of atoms in a high vapor pressure environment. Since further cooling is more efficient in a lower vapor pressure environment (due to reduced one-body loss of atoms due to collisions with background gas), it is customary to construct a multi-section chamber separated by a differential pumping stage that maintains a pressure difference between the two regions. As already described in Section 2.4, this involves creating a 2D MOT in a high vapor pressure source cell and using a blue-detuned beam aligned to the 2D MOT to push atoms through the differential pumping tube to a lower vapor pressure section of the chamber where a 3D MOT is loaded.

Trapping single atoms in optical tweezers requires good optical access to get atoms within working distance of high-NA objectives used for creation of tightly-focused optical dipole traps and also to collect enough photons from trapped atoms. This kind of optical access is not available at the octagon chamber due to presence of ion pumps around the chamber and large distance to the center of the octagon chamber. Typical solutions include (1) using in-vacuum mounted high-NA lenses ([61–63]), (2) having a recessed part of the vacuum chamber where the objective can be set to get close to the atoms ([64], others) and (3) mounting objectives outside a protruding science cell whose dimensions allow the objectives to get close to the atoms ([10], others).

Our vacuum chamber conveniently includes a fourth section featuring a protruding science cell³⁴. The science cell is 28 mm × 28 mm × 100 mm quartz cell (4mm thickness) which allows us to bring atoms within the working distance of our high-NA (Mitutoyo G Plan Apo 50X) objective. To allow more space for optics on this side of the chamber we use a NextTorr D-100-5 ion pump for their small size compared to standard Gamma Vacuum ion pumps.

Having successfully loaded a 3D MOT in the octagon chamber, we are now faced with the challenge of transporting atoms to the science cell, where the final cooling and trapping can take place.

³⁴Historically the chamber was designed to allow trapping and cooling of an alkali (³⁹K) and a lanthanide (¹⁶⁶Er), either together or separately initially mixing at the octagon chamber and further transport of either or both to the science chamber.

Some methods already used in cold atom experiments include:

1. **A moving magnetic coil pair.** This involves using a pair of magnetic coils that translated using a mechanical stage [65–68].
2. **Array of static magnetic coil pairs.** Here the magnetic trap is moved by turning on the magnetic coils one after the other in a "hot potato game" fashion.[69].
3. **Moving red-detuned optical dipole traps**
 - (a) In one case one or more components of an optical telescope used to focus down the ODT is placed on to a moving stage, thus moving the focus of the dipole trap (and thus the atoms) between different positions.
 - (b) The focus position of a dipole trap can also be moved using focus-tunable lenses (from *Optotune*[70]). These lenses consist of a polymer membrane that contains a low absorption optical fluid. A current-controlled actuator can be used to vary pressure applied to the elastic membrane thus re-distributing the fluid to change the curvature of the lens (which in turn varies the focal length of the lens). By changing the focal length of one or more components of an optical telescope used to create the ODT, the position of the trap can be electronically controlled *without any moving parts in the experiment*[71, 72].
4. **Push beams** have been used to move atoms not only from a 2D MOT to a 3D MOT but also between two 3D MOTs [73–78]. The working principle involves either
 - (a) **Continuously** applying an optical force using a far-detuned push beam that creates a leaking MOT. Here a red-detuned push beam leading out of the first 3D MOT creates radiation pressure imbalance that causes atoms to flow out [73, 79–81]. This can be combined with a confining magnetic field gradient (hexapole fields) or gravity [74] to improve transfer efficiency. Another variation involves using a blue-detuned beam to guide atoms falling under gravity into a second 3D MOT.

- (b) Using a **pulsed-near-resonant** beam [73, 78]. This method involves turning on a high power beam for a short time to impart momentum on the atoms in the source 3D MOT. The atoms are accelerated by the optical force from the push beam and move towards the second 3D MOT region.

Our experiment requires short cycle times due to the probabilistic nature of single-atom loading in the final chamber. While methods 1-4(a), work best only when the transport of atoms remains adiabatic i.e. usually on the order of 5 sec for $\approx 50\text{cm}$ distance, using a pulsed push beam best suits our need.

2.5.2 Transport using blue-detuned pulsed push beam

Near-resonant beam interaction with atoms result in a scattering force where the atom absorbs photons from the beam and emit in a random direction. For blue-detuned beams the atoms experience a repulsive force that accelerates them in the direction of propagation of the push beam. In this Section we will describe the steps we took to align the blue-detuned push beam to transport atoms towards the science chamber.

Alignment and imaging

Having set up 3D MOT beams at the science chamber as described in Section 2.6, we first begin rough alignment of a collimated push beam to the center of the viewport (East) at the octagon chamber and the center of the westward facing science cell at the opposite end of the chamber. We begin with $\approx 10 \text{ mW}$ of collimated 3 mm ($1/e^2$) waist detuned to $\approx 2\Gamma$. Even though the MOT beams at the octagon chamber could be very well aligned based on the geometric placement of the input windows, we found that the MOT was still slightly misplaced (most likely due to power imbalance between forward- and back-propagating beams). Slight misalignment of the back-propagating beam centers the MOT.

A live view of the MOT on an IR security camera facing upward, below the chamber, allows us to do rough alignment of the MOT to a resonant beam. Specifically, we begin aligning by blasting away the MOT (as viewed from an IR security camera) using the resonant beam, then reducing the power until the MOT is barely misplaced. This allows us to

”eye ball” the alignment that corresponds to the push beam hitting the MOT squarely at the middle. We then check on the opposite side, initially on an illuminated IR beam viewer card (Thorlabs VRC5)(we later switched to using a CCD camera centered on the science cell face) and iterate the alignment until we have the beam centered both at the MOT and at the opposite end of the chamber.

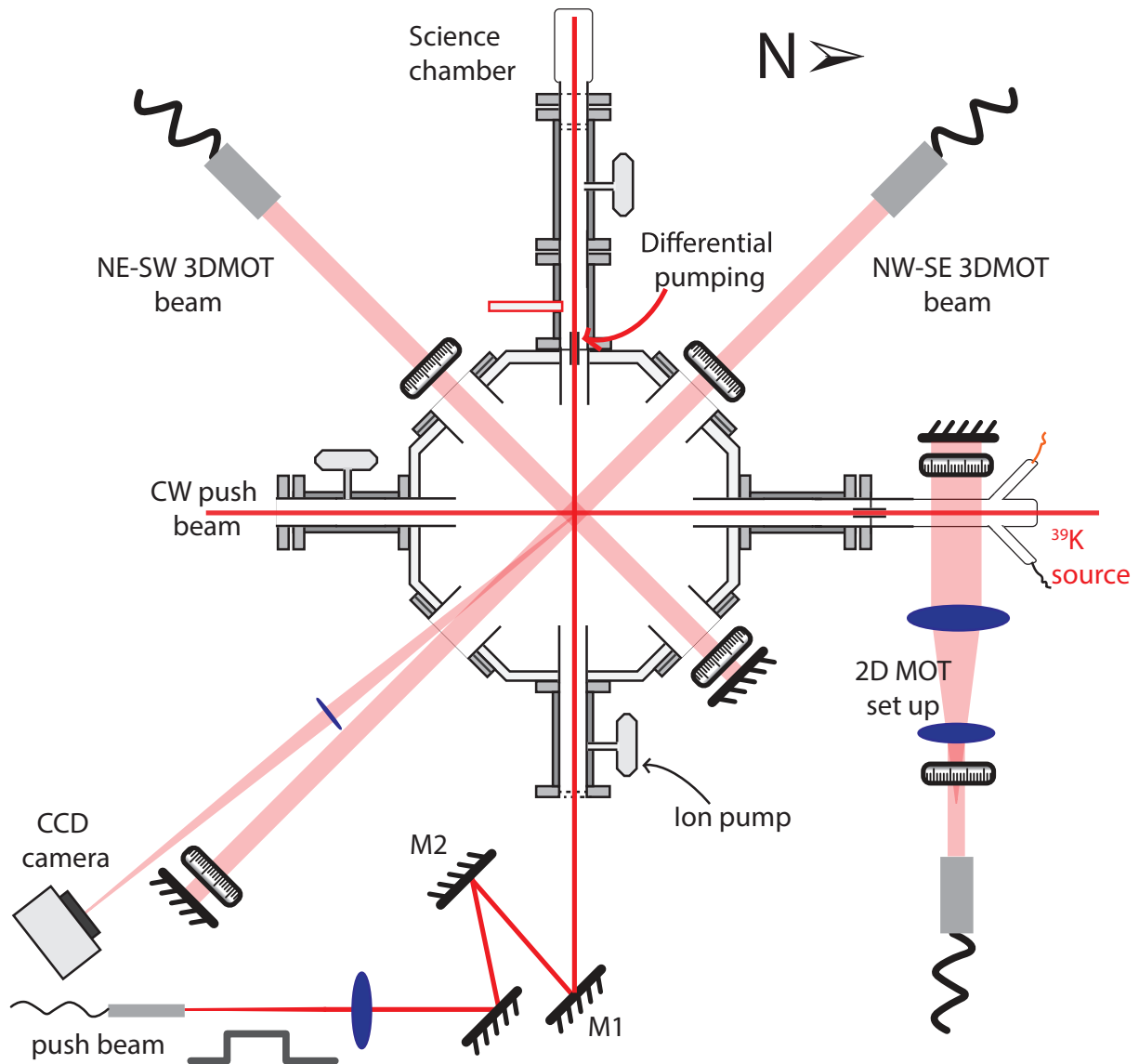


Figure 2.21: Top view of beam layout for transport of atoms from the octagon chamber to the science chamber (not to scale). A continuous wave push beam provides a steady source of atoms to the 3D MOT in the octagon chamber. A blue detuned push beam turned on for $\approx 250\mu\text{s}$ to impart momentum on atoms at the MOT right after 3D MOT beams and gradient fields are turned off (more detail on Fig 2.22) to release the atoms. Atoms are accelerated westwards towards the science chamber where yet another 3D MOT will be turned on to capture atoms (described in section 2.6). A CCD camera set up to view the MOT proved useful for initially diagnosing best conditions for transport out of the octagon chamber.

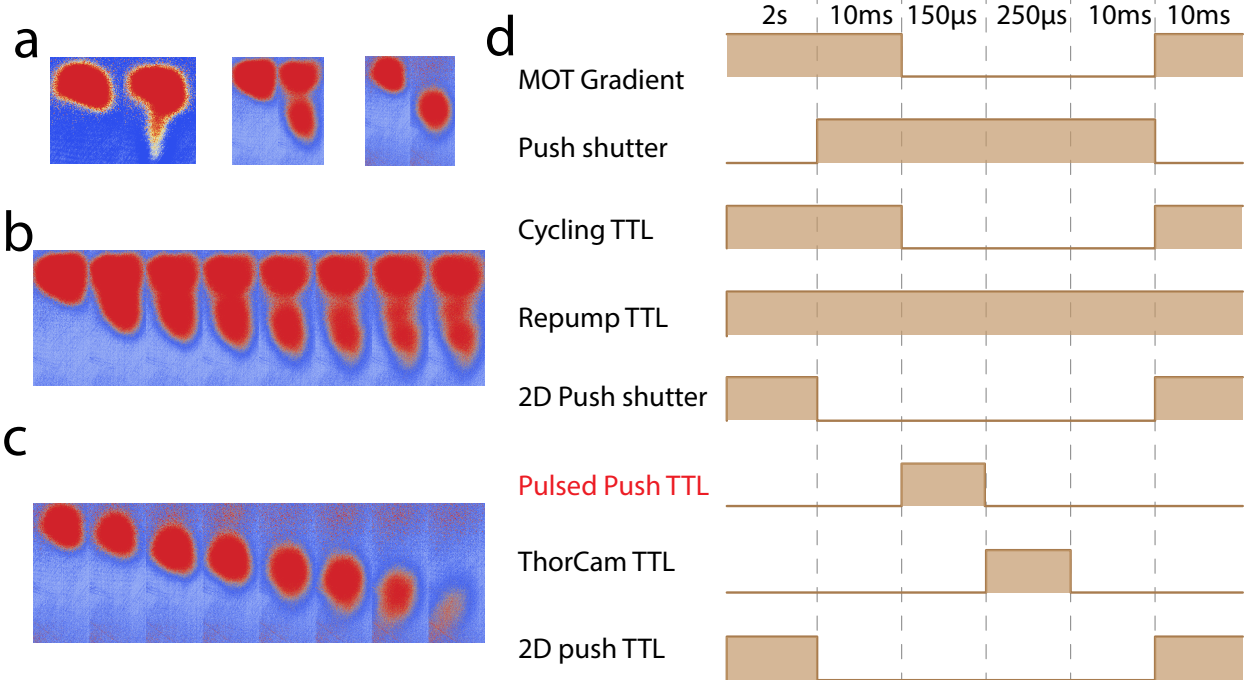


Figure 2.22: Transport of atoms from MOT1 to MOT2. (a) Left, for a 1mm waist collimated push beam atoms in only a small section of the 3D MOT are pushed out creating a leaking MOT. Middle/Right for a larger sized push beam a lot more atoms are pushed out of the 3D MOT. When the alignment is right the entire MOT can be displaced by the push beam initiating transport to the science chamber. Typical initial velocity of atoms is ≈ 25 m/s. (b) Unoptimized partial transfer of atoms as a function of time. (c) Here the entire MOT experiences a momentum kick when the push beam parameters are optimized and all the atoms begin moving towards the science chamber. (d) Pulse sequence for testing transport of atoms out of the octagon chamber. The 3D MOT is loaded for 2s followed by turning off shutters to block the 2D push beam while turning on shutters to allow the 3D blue-detuned push beam. The magnetic fields are also turned off to at this stage. The blue detuned push beam pulse if turned on for 150 μ s while everything else apart from the 3D MOT repump beams turned off. Images are taken for some varied time right after the push pulse is turned off.

In the next step we use a Thorcam CCD camera set up to view the MOT through the South-East MOT input window³⁵ in order to determine displacement in the East-West direction. This camera is especially useful because it allows us to take triggered snapshots that can be used for fine alignment and to determine the short-time behavior of the MOT when impinged upon by a near-resonant beam.

Now we use the CCD camera on live mode to repeat the previous step i.e. aligning the beam to hit the MOT squarely (point of maximum displacement) and then use another CCD

³⁵Setting a camera to view atoms through the viewport on the east end of the chamber was blind to displacement of the atoms in the East-West direction, we therefore decided to view at an angle as shown in the Figure.

camera with marked center view³⁶.

We then take snapshots as a function of time to watch whether the atoms are displaced in the correct direction³⁷. In order to impart momentum on the atoms it is important to turn off both the continuous wave push beam that feeds the 3D MOT and to also turn off the 3D MOT gradient fields and optical molasses beams, so that the atoms are no longer confined in the MOT and can therefore respond to the pulsed push beam without experiencing a restoring force as they attempt to leave the MOT region.

By monitoring short-time images taken by the CCD camera we quickly develop an understanding of pulse sequences that allow for successful transport of atoms out of the octagon MOT region. For example, we learn that **leaving the repump on after turning off the magnetic field gradient, the 2D MOT and 3D MOT beams was especially useful**. We also learn that either right-or-left circularly polarized beam is most efficient at pushing the atoms out of the octagon chamber MOT area. The alignment here is now done by slightly tweaking mirror M2 at the East input side of the chamber to maximize displacement at some fixed push time and centering the beam on the opposite side with mirror M1. Figure 2.22(a,c) shows successful alignment so that the entire MOT is displaced by the beam!

2.6 Capturing, cooling and optimization of a MOT from transferred atoms

Once we are sure that atoms are indeed set in motion towards the science chamber, we set up the MOT beams at the science chamber to catch the atoms. For successful loading of a MOT at the science chamber, the pulsed push beam needs to be set at an angle to counter the effect of gravity during time-of-flight (TOF). This arrangement is also typically chosen

³⁶Neutral density filters (Thorlabs NDK01) are added so as not to saturate the camera. We also set the camera to shortest exposure times and lowest gain settings.

³⁷Initially, it was difficult to get the atoms pushed because the MOT would fly off in some direction due to imbalance in radiation pressure from the MOT beams. We minimize this by applying small magnetic fields and tweaking the alignment so that the MOT mostly stays at the same position in the absence of a pulsed push beam. This ensures that the atoms only feel the force from the pulsed push beam so that they can move directly towards and through a differential pumping tube separating the octagon chamber and the science chamber.

to minimize destruction of the final MOT by the push beam.

We found that setting up imaging of the MOT at the science chamber was critical for initial capture and optimization of a MOT at the science chamber. In particular a 2f-2f imaging configuration with a 50 mm lens (very close to the cell to increase solid angle for photon collection) and with the CCD camera facing eastward (as shown in Figure 2.23(a)) was best. To reduce uncertainties about the alignment, we use the 3D printed field quantization coil holders (described in section 2.4) which are cubical. Holes drilled through the corners allow us to align two sets of beams at 90° to each other. Both the quantization coil holder and a gradient coil holder are also centered to the science cell using the platform mount (Thorlabs MB1218) regular one inch mounting hole spacings.

Our MOT beams are derived from the two remaining arms of the 4 by 4 combiner with cycling and repump already combined and initially set to some frequencies that already work for the octagon chamber MOT (Table A.2). Additionally we match the beam sizes at the final MOT to ensure the same beam intensities. This design, however, comes at the disadvantage that we cannot independently turn off the MOT beams between the two 3D MOTs. Our transfer sequence therefore involves turning on the MOT beams at the science chamber after some time of flight estimated based on images (such as one displayed on Figure 2.22). A typical wait time of ≈ 20 ms over the ≈ 54 cm distance between the two chambers is used. The beams roughly at 25 mm waist are then passed through $\lambda/4$ plates before finally intersecting in the science cell. Once passed through the science cell the MOT beams are retro-reflected. A $\lambda/4$ plate is also set on the right before the retro-reflecting mirrors to rotate the polarization so that the reflected beam is of opposite circular polarization. On Table 2.2 we display the initial wave plate settings.

Although a magnetic field gradient of ≈ 15 G/cm is initially used, we found improvement in capture efficiency for field gradient values around 18 G/cm.

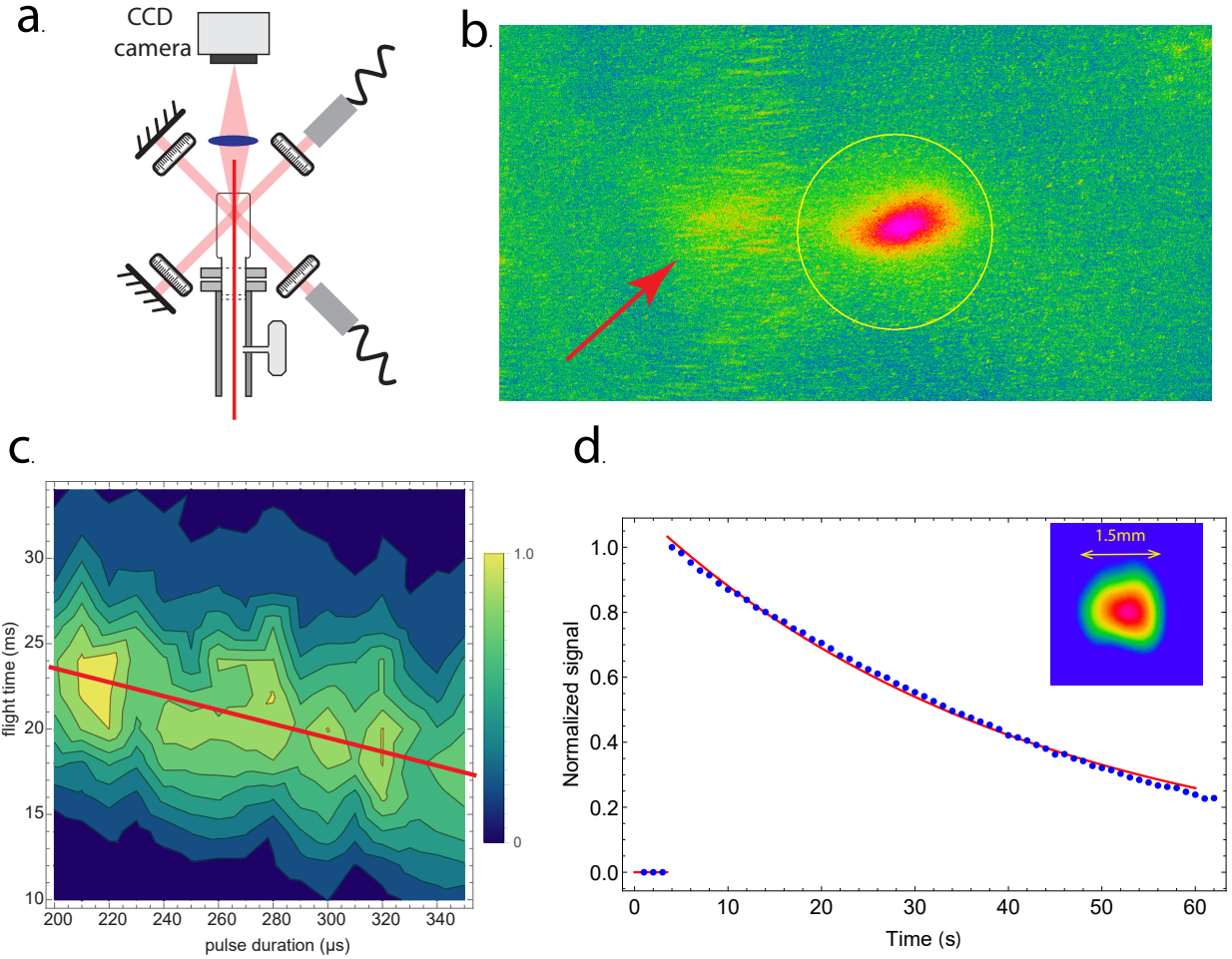


Figure 2.23: Rapid transport of atoms between the octagon and science chamber using a blue-detuned beam. (a) MOT beam layout for MOT2 while optimizing transfer. A CCD camera facing eastwards enabled us to very clearly optimize the position of MOT1 with respect to the push beam as well as detect a weak signal from MOT2. (b) False color image of second MOT taken using a CCD camera directly facing the push beam at the science chamber. The red arrow shows light from atoms in MOT1 that make it to the CCD. The yellow circle shows the position of the MOT2 in the science chamber. (c) 2D plot of average signal (proportional to atom number in MOT2) as a function of the duration of pushing at MOT1 (x-axis) which corresponds to the force imparted on atoms at departure. The y-axis is the wait time after pushing atoms before the MOT beams are turned on in the science chamber. (d) Lifetime of captured atoms in MOT2 ($\tau \approx 40$ s). The first couple of points are taken while MOT1 in the octagon chamber is loading. Inset: Image of a MOT loaded in the science chamber.

2.6.1 Cooling

Doppler cooling

Captured atoms at the science 3D MOT are initially Doppler-cooled through repeated cycles of absorption and spontaneous emission as described in Section 2.4. This cooling is however

Beam arm	Polarization out of fiber	$\lambda/4$ plate fast axis	Polarization after $\lambda/4$ plate
Top-Bottom	Horizontal	Anti-Diagonal	σ^-
NE-SW	Horizontal	Diagonal	σ^+
NW-SE	Vertical	Anti-Diagonal	σ^-

Table 2.2: Waveplate settings (for Thorlabs WPQ10M-780 $\lambda/4$ plates) for MOT loading in the science chamber. Three beams intersecting at the center of the science cell are set up in a $\sigma^+ \text{-} \sigma^-$ configuration. The waveplate setting of the fast axis for the $\lambda/4$ plate right before the retro-reflecting mirror is matched to the input setting. The linear polarizations before the waveplates are set using Thorlabs PBS122 clean-up PBS at the fiber output. The shorthand E/W/N/S correspond to the cardinal directions in the lab.

limited when the Doppler shift corresponding to the velocity of the atoms becomes comparable to the linewidth of the transition used. In other words, when the kinetic energy of the atom is given by

$$mv_{Doppler}^2 = k_B T_{Doppler} = \frac{\hbar\Gamma}{2}. \quad (2.4)$$

For Doppler cooling on the D2 transition of ^{39}K (where $\Gamma = 6$ MHz), the Doppler limit is given by $T_{Doppler} = 145\mu\text{K}$ and $v_{Doppler} = 18\text{cm/s}$.

In experiment, however, we initially measure MOT temperatures of around 1 mK without any optimization. We scan through beam parameters i.e. cycling and repump intensities and detunings, magnetic field gradient values, beam polarizations (slightly tweaking the fast axis of the $\lambda/4$ plates right before the cell), beam alignments (most importantly the retro-reflected beams), and **most importantly** magnetic field cancellation. After an initial round of optimization we get down to temperatures of roughly $250\ \mu\text{K}$. Subsequent rounds of optimization barely lowers the temperature below $\approx 200\ \mu\text{K}$.

Sub-Doppler polarization gradient cooling

Further cooling below the Doppler limit is typically achieved in alkali atoms using optical molasses [82] i.e. turning off the magnetic field gradients while leaving the MOT beams on. Here cooling happens due to presence of hyperfine levels which are not included in the Doppler cooling discussion. Typically, spatially varying polarization of the optical molasses beams (due to interference or counter-propagating beams) lead to spatially varying light-

shifts of the ground state sublevels. In the work by Dalibard et al. [83], polarization gradient cooling related to two kinds of 1D standing waves is described. The lin \perp lin configuration that involves interference of two orthogonal linearly polarized beams leading to alternating circular and linear polarizations is popularly used to explain sub-Doppler cooling in the context of a Sisyphus polarization gradient³⁸. However, in experiments the $\sigma^+ - \sigma^-$

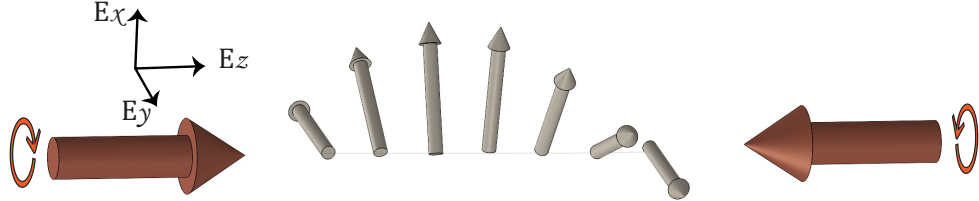


Figure 2.24: Polarization gradient in $\sigma^+ - \sigma^-$ configuration. Counter-propagating beams with opposite circular polarization lead to a rotating linear polarization which leads to a velocity-dependent force that slows down moving atoms but vanishes for static atoms.

configuration is normally used. Here, the interference between two circularly polarized beams leads to a spatial rotating linear polarization as shown in Figure 2.24. Consider atoms with a two-level system ($J_g \rightarrow J_e = J_g + 1$, with $J_g = 1$) [83]. When at rest the atoms see a local linear polarization (say $E_y \hat{y}$) which leads to equal population distribution between $m_g^y = \pm 1$ and highest occupation of $m_g^y = 0$. When the atoms move in the \hat{z} direction, in the rest frame of the atoms, the polarization appears to be rotating. Moving into the rotating frame such that the polarization appears to be static, the atoms experience a fictitious field in the \hat{z} direction which is dependent on the velocity of the atoms. This fictitious field leads to population imbalance in the magnetic sublevels (with respect to \hat{z}) i.e. population in $m_g^z = +1$ being larger than population in $m_g^z = -1$. In other words, for $v_z > 0 / v_z < 0$ atoms are pumped to the $m_g^z = +1 / -1$ (highest/lowest) states leading to a velocity-dependent anisotropy in population distribution within the magnetic sublevels. For $v_z > 0 / v_z < 0$

³⁸In the lin \perp lin configuration (described in more detail in Ref. [59, 60]), asymmetric light shifts of the two states ($m_J = \pm \frac{1}{2}$ for a $J_g \rightarrow J_e$ transition discussed by [83]) i.e. three times bigger light-shift for $m_J = \pm \frac{1}{2}$ due to σ^\pm light acts in tandem with optical pumping between the two states (also induced by the same σ^\pm light) to continually cool the atoms. Specifically, moving atoms in $m_J = 1/2$ go up a potential "hill" due to spatially varying light-shifts until they encounter σ^+ polarization which occurs where $m_J = -1/2$ is maximally shifted. At this position the atoms absorb photons from the beam and spontaneously decay down to $m_J = -1/2$, thus repeating the process. Due to the energy difference between the absorbed and emitted photon, energy is lost from the atoms with each cycle.

atoms scatter more from the σ^+/σ^- beam causing a radiation pressure imbalance that slows down the atoms.

Sub-Dopper cooling works well for atomic species where the excited state splitting, Δ is either much larger or much smaller compared to the linewidth of the transition, Γ . For ^{39}K , $\Delta \approx 3\Gamma$. This small separation makes it difficult to cool below the Doppler limit since any cooling (red-detuned) with respect to the $F' = 3$ transition eventually becomes limited by heating (blue-detuned) due to the $F' = 0, 1, 2$ states just 3Γ below. This problem has, however, been overcome in a few groups [64, 84, 85] by using near resonant optical molasses³⁹ where the presence of $F' = 0, 1, 2$ depumps atoms to $F = 1$ state which is dark to the cycling laser (preventing photon re-absorption [86]). Controlled repump can then get the atoms back into the cooling loop. While Ref.[64, 84, 85] report low temperatures by cooling using the D2 transition, our efforts to implement this cooling scheme hit a wall at $\approx 100\mu\text{K}$. We think this inability to re-produce the results reported in Ref.[64, 84, 85] might be due to phase incoherences between our cycling and repump beams that probably lead to less efficient depumping to dark states.

Gray-molasses cooling

Unable to break through the $\approx 100\mu\text{K}$ barrier , we move on to set up Λ -enhanced gray molasses⁴⁰. Initially implemented on the D2 transition [87], gray molasses involves optical pumping of atoms between (light-shifted) bright states and Zeeman dark states (isolated relative to polarized light due to dipole selection rules). While this works well for alkali atoms with well-separated hyperfine levels in the excited state [88–91], cooling is inefficient for smaller separation. Alternatively for atoms with small excited state hyperfine splitting, gray molasses cooling has more efficiently been realized using the D1 transition in a Λ -configuration [85, 92–98].

In this configuration a cycling beam addresses the $F = 2 \rightarrow F' = 2$ transition while a re-

³⁹As opposed to the usual case where the cycling laser is detuned below the entire excited state manifold.

⁴⁰Terminology: gray molasses is generally used to refer to cooling using a Sisyphus like cooling combined with velocity-selective-coherent population trapping (VSCPT). Here the dark states used could be (and were usually) Zeeman dark states (isolated states due to selection rules when a transition is driven). Λ -enhanced gray molasses refers to above but enhanced to do additional states that appear in a Λ three-level system.

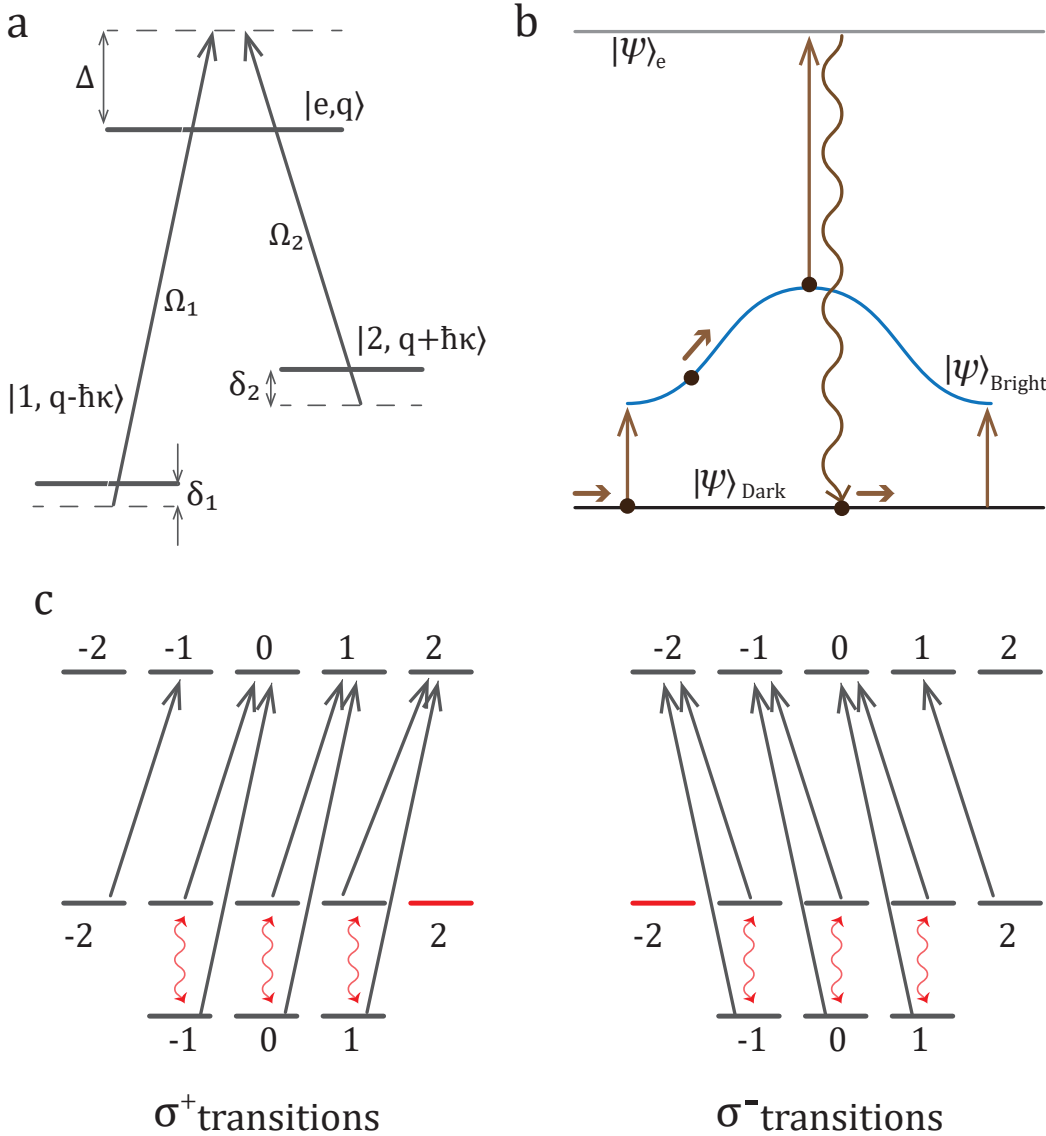


Figure 2.25: Λ -enhanced gray molasses using ^{39}K D1 transition at 770nm. (a) Λ configuration in ^{39}K . (b) Gray molasses cooling. Atoms in the dark state are motionally coupled to a bright state. The bright state is spatially modulated due to polarization gradients from interfering gray molasses beams. The atoms climb a potential hill and are then optically pumped to the dark state once they reach the top of the "hill". Energy is lost during each cycle corresponds to frequency difference between the photon absorbed and photon lost by stimulated emission. (c) Dark states. (c) Dark states that participate in gray molasses cooling. Squiggly red lines show superposition of states that constitute dark states. Left corresponds to dark states that emerge when σ^+ transitions are driven while the figure on the left shows dark states due to σ^- transitions.

pump beam drives the $F = 1 \rightarrow F' = 2$ as shown in Figure 2.25. For this discussion we label the three states using the basis $\{|1, q-\hbar k\rangle, |2, q+\hbar k\rangle, |e, q\rangle\}$, where q refers to the momentum of the atoms. The states $\{|1\rangle, |2\rangle, |e\rangle\}$ refer to internal states $\{|F = 1\rangle, |F = 2\rangle, |F' = 2\rangle\}$.

Here, so far, we are ignoring the magnetic sublevel for brevity.

These states are written as tensor product between internal and momentum states since stimulated absorption and emission using the cycling and repump beams involve momentum transfer to the atom. The Rabi rate associated with driving transitions using repump and cycling are represented as Ω_1 and Ω_2 , respectively. The detunings of the cycling/repump driving fields is denoted by δ_1/δ_2 and Δ refers to the overall one-photon detuning above the $F' = 2$ manifold.

In the dressed state picture (more carefully shown in Appendix three-level diagram), the eigenstates of the system include

$$\begin{aligned} |e, q\rangle \\ |\psi_{\text{dark}}\rangle &= \frac{1}{\sqrt{\Omega_1^2 + \Omega_2^2}} (\Omega_1|1, q - \hbar k\rangle - \Omega_2|2, q + \hbar k\rangle) \\ |\psi_{\text{bright}}\rangle &= \frac{1}{\sqrt{\Omega_1^2 + \Omega_2^2}} (\Omega_1|1, q - \hbar k\rangle + \Omega_2|2, q + \hbar k\rangle) \end{aligned} \quad (2.5)$$

The dark state, $|\psi_{\text{dark}}\rangle$, is completely decoupled from the cycling and repump beam and arises due to destructive quantum interference between the cycling and repump beams when the Raman condition is fulfilled, i.e. $\delta_1 = \delta_2$. However, when atoms in the dark state have non-zero velocity, the cycling and repump beams are Doppler shifted and the Raman condition is broken leading to coupling into $|\psi_{\text{bright}}\rangle$ given by $\approx \frac{\hbar k q}{M}$, where M is the mass of the atom. This dependence on momentum q (motional coupling or velocity-selective-coherent population trapping (VSCPT)) leads to non-adiabatic coupling where hotter atoms are more strongly coupled to the bright states. Since the bright states experience light shifts, a Sisyphus cooling like scheme is combined with VSCPT to optically pump atoms between the dark states and the bright states as shown in Figure 2.25(c). Here by creating a polarization gradient (in lin \perp lin configuration) the bright state, are modulated in space. For blue-detuned cycling and repump, i.e. $\Delta > 0$, the spatially modulated bright states lie above the dark states. Considering atoms that exist in the dark state manifold, motional

coupling happens at a position in space where the energy difference between the two states is smallest. Once in the bright states these atoms climb up a potential "hill" and are optically pumped back to the dark states once they get to the top. The atom thus loses energy equal to the energy difference between the absorbed and emitted photon during each optical pumping cycle. Eventually the atoms do not have enough energy to be promoted up to the bright states. While the dark and bright states in the discussion so far are simply written as a combination of two states, the real picture includes Zeeman sub-levels. Figure 2.25(c) shows all the states that participate when considering the D1 transition of potassium.

The state $|\tilde{\psi}_{\text{dark}}\rangle$ with respect to σ^+ transition (dropping the momentum label) is given by

$$\begin{aligned}
 |\tilde{\psi}_{\text{dark}}\rangle = & \frac{1}{\sqrt{\Omega_{1,-1 \rightarrow 2,0}^2 + \Omega_{2,-1 \rightarrow 2,0}^2}} (\Omega_{1,-1 \rightarrow 2,0}|1, -1\rangle - \Omega_{2,-1 \rightarrow 2,0}|2, -1\rangle) \\
 & + \frac{1}{\sqrt{\Omega_{1,0 \rightarrow 2,1}^2 + \Omega_{2,0 \rightarrow 2,1}^2}} (\Omega_{1,0 \rightarrow 2,1}|1, 0\rangle - \Omega_{2,0 \rightarrow 2,1}|2, 0\rangle) \\
 & + \frac{1}{\sqrt{\Omega_{1,1 \rightarrow 2,2}^2 + \Omega_{2,1 \rightarrow 2,2}^2}} (\Omega_{1,1 \rightarrow 2,2}|1, 1\rangle - \Omega_{2,1 \rightarrow 2,2}|2, 1\rangle) \\
 & + |2, 2\rangle.
 \end{aligned} \tag{2.6}$$

The Rabi rates $\Omega_{F,mF \rightarrow F'mF'}$ can be calculated from Clebsch-Gordan coefficients just like in Appendix D.

Laser preparation of 770 nm light

Our laser system consists of a commercial diode laser (Toptica DL PRO) which provides ≈ 70 mW of 770 nm ($f_{D1}=389286.058$ GHz) light. The beam then passes through a PBS that diverts a small amount of light ≈ 5 mW through an AOM driven at +55 MHz. A $\lambda/2$ waveplate is set before the PBS to control the ratio of the transmitted and reflected signal during initial optimization. The first order of this AOM is coupled into a polarization spectroscopy (PS) setup described in Section 2.3.1.

Here we lock to a crossover transition of a PS error signal (27.5 MHz below the $F = 2 \rightarrow F' = 2$ transition). The transmitted beam is passed through a free space EOM (Qubig

EO-K39M3-NIR), driven at 461.7 MHz to match the hyperfine splitting in the ground state. We found that setting up a 1:1 telescope (with $f=50$ mm) around the EOM to focus the beam at the crystal enables us to achieve higher modulation depths at a given driving RF power (compared to modulating a collimated beam through the EOM)⁴¹. The modulation (here diagnosed in terms of carrier-to-sideband amplitude ratios) are also sensitive to the input polarization. We suspect that the two mirrors and final lens before the EOM muck up the polarization. We therefore add a $\lambda/2$ plate before the EOM despite effectively having cleaned up the polarization at the initial PBS. The final lens after the EOM is used to re-collimate the beam to allow us to easily couple the light into a fiber that goes towards the experiment. Right after the re-collimating lens, we set up a mirror on a 90° flip mount (Thorlabs TRF90) which re-directs light during EOM optimization to two mirrors that couple light into a fiber (F2). In conjunction to this detour, another flip mount is set up right before the fiber to spectroscopy that redirects the first order of the spectroscopy AOM (at 55 MHz) to a set of two mirrors that are used to couple light into another fiber (F3). Light from fibers F2 and F3 are combined to create a beat-note using a 2 by 2 fiber combiner (Thorlabs TW805R5A2) on to a fiber coupled photodiode (Menlo Systems FPD-310-V). The output of this photodiode then read onto a frequency spectrum analyzer. In our case we can infer the amplitude carrier signal from the peak at 55 MHz as seen on the spectrum analyzer (from beating f_{D1} with $f_{D1}+55$ MHz) and the amplitude of the sidebands at 406.7 MHz and 516.7 MHz (from beating $f_{D1}+461.7$ MHz with $f_{D1}+55$ MHz). Upon optimization of the EOM carrier-sideband ratios, the flip mounts can be turned to allow light to go into spectroscopy (F1) and towards the experiment (F4)⁴². This part of the laser preparation is set up on an optical breadboard (Thorlabs PBG12118) mounted onto the main optical table by rubber feet for vibrational isolation (specifically so that the shutters on the main table do not disturb laser locking). A plexiglass enclosure (Thorlabs XE25C10) is built up around

⁴¹We also observed that our carrier-to-sideband ratios also became more stable after focusing the beam on to the EOM crystal.

⁴²The first design of this set up involved re-directing $\approx 10\%$ using a beam sampler (Thorlabs BSF10-B) instead of using flip mounts. We were however power limited while setting up a home-made TA using coupled light out of the EOM. Using flip mounts enables us to diagnose the sideband signal whenever we need and also have as much laser power as we need during normal operation.

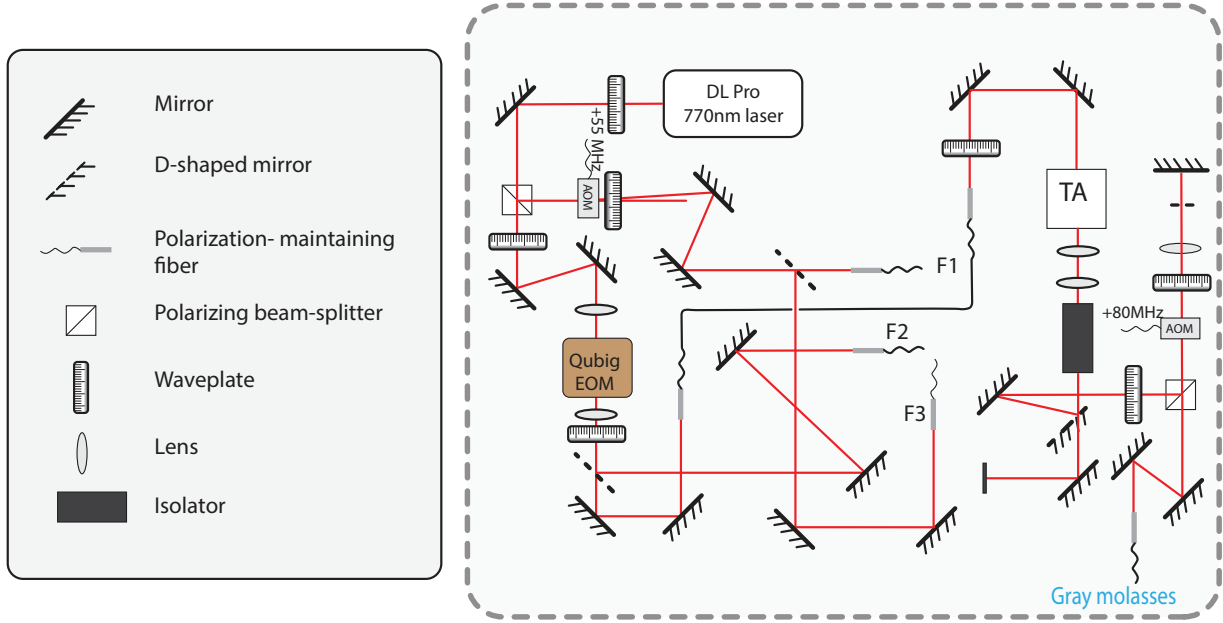


Figure 2.26: D1 laser preparation set up.

this set up to isolate the environment and minimize drifts in fiber coupling⁴³.

The output of fiber F4 (≈ 35 mW) is used to seed a home-made tapered amplifier (described in Section 2.2). A $\lambda/2$ plate and a clean-up PBS are set at the fiber output to ensure linear polarization of the seed light while two mirrors are used to align the seed through the TA. With the TA driven at ≈ 2.5 A we can get up to ≈ 550 mW of light. Right after the TA we set up two cylindrical telescopes to collimate the beam in both directions and an optical isolator (Thorlabs IO-5-780-VLP) to prevent back-reflection into the TA. Ideally, the optical isolator should be set up right after the TA. Due to typical fast expansion of the TA output (despite using a collimating convex aspherical lens at the output), we end up installing the isolator right after the first collimating lens. The lens is set up at a slight angle with respect to the TA to avoid reflection back into the TA. Similar to the case of the main experiment TA1, the most dominant output mode of this particular TA (when seeded) happens to be shaped nearly like a TEM_{01} . We set up a D-shaped pickoff mirror (Thorlabs BBD1-E03) to spatially reflect one part of the beam while letting the other one through. The

⁴³We later add Thorlabs BKF12 black foil along the inside wall of the enclosure to block stray light from the set up.

reflected beam is fiber coupled and sent to the second ^{39}K BEC experiment being constructed and operated by Sai Paladugu and Shraddha Agrawal⁴⁴. The unaffected part of the beam is aligned into an AOM double pass system (centered around $2 \times +80$ MHz) which detunes the beam (which contains $f_{D1} \pm 461.7$ MHz) above the $F = 2 \rightarrow F' = 2$ transition. We couple the output into the 4 by 4 combiner that delivers already-aligned light to the atoms for gray molasses cooling.

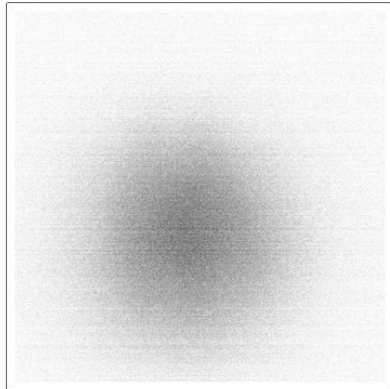
Optimizing D1 parameters

Our optimization process begins with a release-recapture diagnostics of the atomic cloud temperature. Based on work by Ref. [92] we set the one-photon detuning $\Delta \approx 5\Gamma$ above the $F = 2 \rightarrow F' = 2$. The cycling-torepump ratio is set to 1:3 (5 dB) and a total power of 50 mW is used at the beginning. The two-photon detuning $\delta = 0$ by design (since we write sidebands on the 770 nm light before shifting both the cycling and repump components using a double-pass set up as shown in Fig. 2.26)⁴⁵. At the end of the normal D2 molasses stage of a typical sequence we turn on D1 molasses beams (while turning off the D2 molasses beams) for a couple of milliseconds. This is followed by a TOF stage (≈ 20 ms) where the molasses beams are turned off to allow the atoms to expand. At the end both D2 molasses beams and the magnetic field gradient are turned on again and an image is taken. We choose the release-recapture method since it allows us to optimize both the number and the temperature of the atoms after D1 molasses. This specifically avoids the situation where only a small fraction of the atoms are cooled. When the parameters are not optimal the cloud expands quickly and most of the atoms get out of the capture range of the MOT leading to a small number of recaptured atoms. Increasing the number of re-captured atoms therefore corresponds to lowering the cloud temperature while also increasing the number atoms that remain. We manually optimize D1 parameters by scanning through all the parameters (beam intensity, cycling to repump ratio, one-photon detuning and the duration

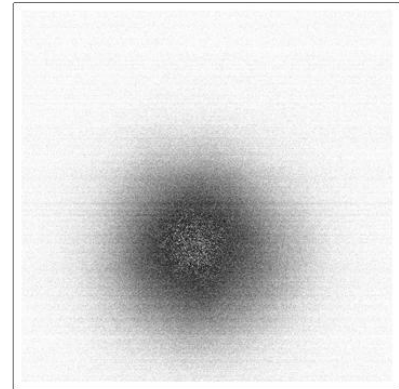
⁴⁴Eventually we experienced instabilities in our TA power and had to replace the TA. The second ^{39}K BEC experiment now derives 770 nm D1 light from a totally separate Toptica DL100 diode laser.

⁴⁵For this to work well we find that it is important for the frequency source at 461.7 MHz to be stable. Using voltage-controlled oscillators (VCOs) here was actually not a very good idea. We moved on to using DDS based sources which improved the stability of our cooling scheme.

MOT after 5 ms flight

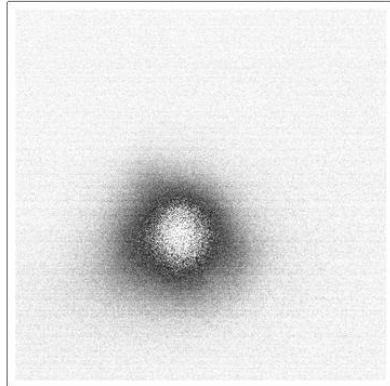


Without D1 light

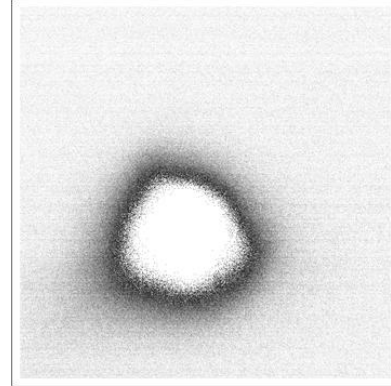


With D1 light

Recapture after 50 ms flight



Without D1 light



With 2.5 ms D1 light

Figure 2.27: Initial optimization of gray molasses cooling parameters. Top, waist of the atomic cloud waist after 5ms time of flight. Bottom, recaptured atoms after 50 ms. Both measurement indicate cooling due to the presence of D1 beams.

of cooling) followed by optimizing field cancellation fields. This is repeated a couple of times until all the parameters converge to some setting.

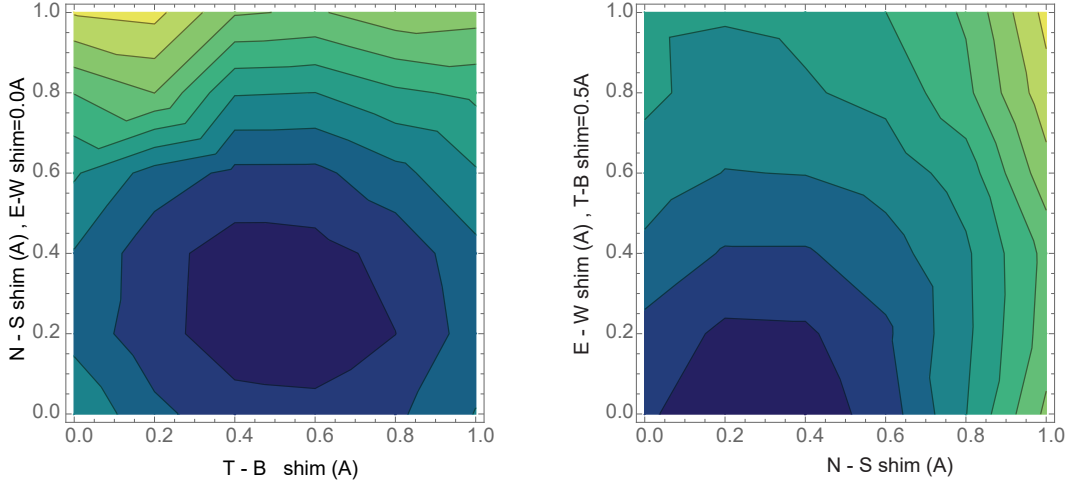


Figure 2.28: Stray magnetic field cancellation. Yellow/blue corresponds to large/small waist after 15ms TOF. The optimum field cancellation parameters are $\{N\text{-}S, E\text{-}W, T\text{-}B\} = \{0.25, 0, 0.5\}$ A corresponding to $\{0.29, 0, 0.61\}$ G. The shorthand T-B refers to top-bottom direction while E/W & N/S correspond to the cardinal directions in the lab.

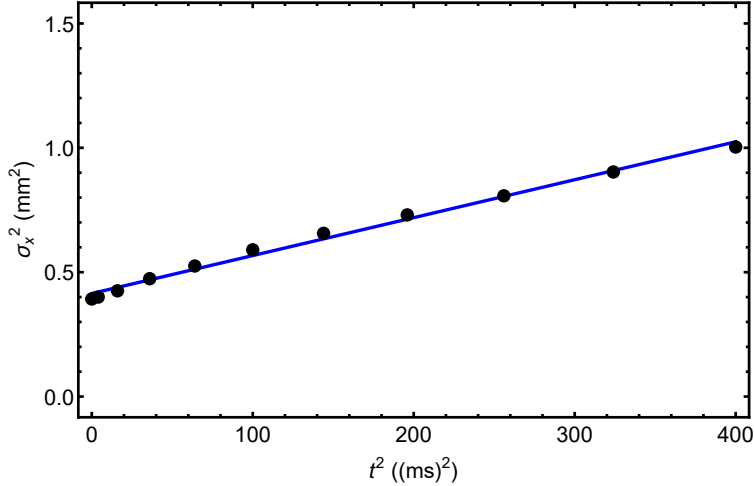


Figure 2.29: Time of flight fits in the North-South direction at $7.2(8)$ μ K after manual optimization of gray molasses cooling.

At the end of each optimization cycle we take TOF measurements to determine the temperature of the cloud. In Fig. 2.30 we show some of the measurements of the atomic cloud waist (as a proxy for temperature) after 15 ms time of flight i.e. dark blue corresponds to smaller waist signifying lower temperatures. We learn that the cooling efficiency can be improved by ramping parameters during the D1 molasses stage. For example, the final one-photon detuning (controlled by the frequency at the double-pass AOM) seems to be

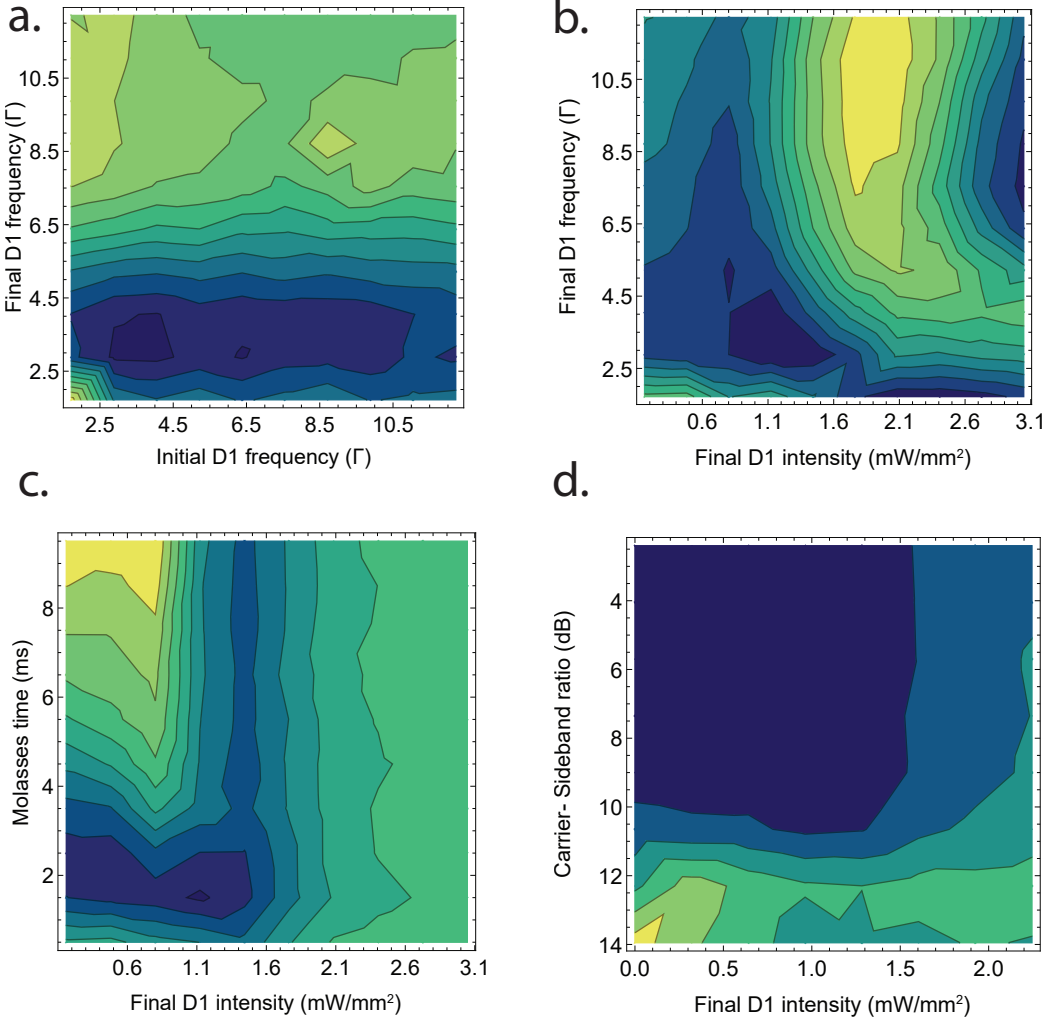


Figure 2.30: Gray molasses cooling optimization. (a). The final frequency ($\Delta \approx 3\Gamma$) works best. (b,d) A low final intensity of $\approx 0.08I_{\text{sat}}$ is optimal for cooling. (c) A duration of cooling of around 2 ms is ideal in our case. The measurement is taken by releasing and recapturing the cloud where a large recapture fraction corresponds to lower temperatures.

more important than the initial detuning. The final D1 intensity seems to be the most sensitive parameter. For example, plotted against duration of cooling in Fig.2.30 (c), the final intensity seems to work in a small region for a longer durations of cooling. In general low final intensities in a ramping scheme lead to lower temperatures (≈ 1.4 mW/mm², $0.08 I_{\text{sat}}$). Here this is probably because the temperature of the atoms is proportional to the number of photons present that can be re-absorbed by the atoms and heat up the sample. On the other hand, one-photon detuning (labeled D1 frequency) at the beginning of the ramp seems

to be the least sensitive parameter. Following a few iterations of manual optimization we achieve a final temperature of $T_{\text{Mean}} = 7.16(7) \mu\text{K}$ (averaged over the Top-Bottom and the North-South direction where the imaging CCD is facing East as in Figure 2.23 (a).)

2.6.2 Optimization of experimental parameters using machine learning

In an effort to further improve our transfer, capture and cooling schemes we implemented machine learning techniques. Manual optimization by experienced experimentalists rely on theoretical assumptions/predictions based on a large body of work followed by scanning through the N -dimensional parameter space. Here N refers to the number of free parameters i.e. laser beam intensities, detunings, magnetic field gradients and duration at different stages of the experimental sequence. Real experiments are usually imperfect due to noise caused by fluctuations and variations in the N parameters. For example, slow drifts in laser power due to polarization drifts of laser beams at the fibers, variations in laser frequency detunings due to imperfect laser locking and temperature induced shifts of polarization spectroscopy signals, imperfect trap geometries due to laser beam radiation pressure imbalance and imperfectly wound magnetic field gradient coils. The ideal sequence for a specific experimental apparatus, for the cooling stage for example, might vary from a proposed sequence based on past literature. A major advantage of using machine learning techniques is that a machine learner, compared to an experienced experimentalist, does not have preconceived notions about which parameter combinations should work. Counter-intuitive parameter combinations and ramping strategies, which might be ideal for apparatus, are therefore treated on equal footing with any other combinations.

Implementing machine learning in our system is made incredibly easy by already developed open-source software package (Machine Learning Online Optimization Package (MLOOP [99])) which has successfully been implemented for optimization in cold-atom experiments [99–104]. Our modus operandi involves first configuring the MLOOP routine with initial parameter values. These are chosen randomly to avoid trapping the machine learner in some local minimum that corresponds to already manually optimized set of parameters. The routine is also provided limits for each set of parameters which make sure that unphysical

values (which could damage equipments) are not sent to the apparatus. MLOOP also allows us to define a trust region which relates to a rough estimate in the error expected for each parameter based on the number of repetitions on the experiment and the voltage resolution of the experimental control software (Cicero). One optimization loop entails the following:

1. Initializing Cicero with N parameters provided by the MLOOP routine. We represent this in terms of a vector \vec{X}_0 with length N and where the subscript refers to the zeroeth iteration. These parameters correspond to analog voltages sent from hardware (controlled by Cicero) to VVAs and VCOs on our RF source circuits. These analog voltages, through the RF sources, control the RF powers and frequencies driving different AOMs and EOMs that in turn directly control the power and frequencies of the laser beams that interact with the atoms.
2. An experiment is performed by running Cicero and an image of the atoms is saved. During the experimental run Cicero co-ordinates the timing between different stages and then triggers the camera used to save a corresponding image.
3. The saved image is analyzed and a cost function $f(\vec{X}_0)$ is evaluated. The cost function quantifies how well the parameters worked and depends on the goal of optimization. The cost value is the measure we will try to minimize. For example, for the transfer stage of our sequence, the cost function is set up to optimize for the number of atoms captured in the science chamber and ignores other properties of the final MOT like temperature. For the cooling stages a good cost function optimizes the temperature. This might be by looking at the waist of the atomic cloud after some time-of-flight while also making sure the number is also optimized.
4. **Online optimization**⁴⁶

The cost function, $f(\vec{X}_0)$, is then fed back into the MLOOP routine which then associates $f(\vec{X}_0)$ to \vec{X}_0 . Based on any earlier runs, the MLOOP machine learner provides a new set of parameters \vec{X}_1 to be run for the next loop. Here we briefly describe the basic features of the algorithms used.

⁴⁶Online optimization really means optimization on the fly where the fitting model used is updated after every iteration.

- MLOOP relies on **Gaussian Process (GP) regression** which invokes Bayesian inference on GP fits. More concretely, the cost function $f(\vec{X}_i)$, which maps the input parameters to corresponding cost values, is modeled as a GP. Gaussian processes really are Gaussian distributions of functions with a mean function $m(\vec{X}_i)$ of input parameters \vec{X}_i and a covariance matrix (referred to as the Kernel), $K(\vec{X}_i, \vec{X}_j)$. The Kernel defines the distance between two sets of parameters \vec{X}_i and \vec{X}_j i.e.

$$K(\vec{X}_i, \vec{X}_j) = \sigma_{\text{GP}}^2 \text{Exp} \left(-\frac{1}{2} \sum_{n=1}^N \frac{1}{\lambda_n} (\vec{X}_i(n) - \vec{X}_j(n))^2 \right) \quad (2.7)$$

is the length scale where σ_{GP} relates to the variance of the cost values over many iterations and λ_n is the characteristic length scale associated with the n th parameter. While it's typical to assume a Gaussian form for the Kernel different functional form might work better based on the nature of the data used. Based on the N input parameters, the GP learner can construct a model that best fits the underlying $f(\vec{X})$ and then use this model to predict $f(\vec{X}_{N+1})$. For MLOOP

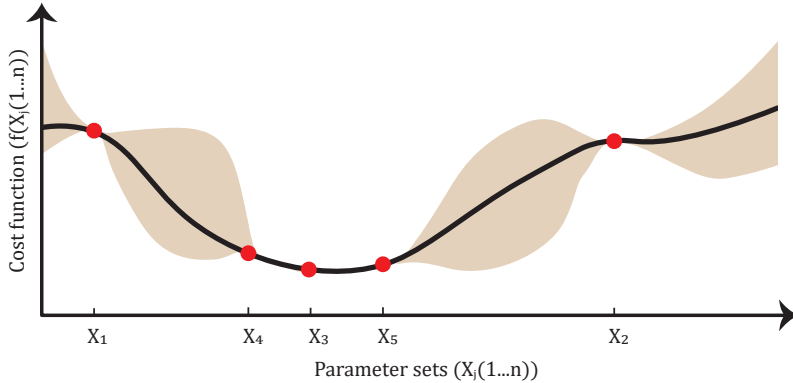


Figure 2.31: Cartoon showing online optimization using GP regression. After 5 iterations the routine has created a GP model with large uncertainties where no experimental data has been taken. Each point on the x axis is a unique set of experimental parameters tried at some specific iteration.

however the algorithm continues exploring the parameter space by suggesting further sets of parameters to try with an aim of (1) exploring uncertain regions of the parameter space in order to improve the efficacy of the model and (2) To further

investigate regions in the parameter space where the model has predicted lowest costs based on past data. A balance between (1) and (2) is important since it avoids a case where the GP learner gets caught up at a local minimum while also making sure that the learner can find other minima that might be more robust.

- So far I have not mentioned how the initial sets of parameters are generated. To generate an initial set of parameters, MLOOP uses a combination of randomly varying the parameters (creating training data on the fly) and parameters generated using **Differential Evolution (DE)**(inspired by evolution in biological systems [105]). Here DE begins with n random sets of parameters $\{X_0, \dots, X_n\}$ with cost functions $\{f(X_0), \dots, f(X_n)\}$ which constitute a *population* that has been built up over n runs. A new set of *offspring* parameters X_{n+1} is generated by combining features of the *parent* set of parameters and also randomly altering some of these features akin to *mutations* in biological evolution. The set X_{n+1} is evaluated by going through the loop to generate $f(X_{n+1})$. The DE algorithm then compares $f(X_{n+1})$ to the initial set of parent parameter settings and gets rid of the parameters that correspond to the worst cost function.
5. Steps 2-4 are repeated until the cost function begins converging to some value. Usually a number of runs is pre-defined at step 1 beyond which the routine stops and evaluates the predicted best cost and corresponding parameters.

Improved gray molasses cooling using MLOOP

Manual optimization discussed in the previous section was time consuming since it involved scanning the dependence between every pair-combination of parameters and iterating through until the final temperature achieved began converging to some value. Here we showcase results we get from optimizing the gray molasses cooling stage by applying GP regression using MLOOP. As compared to manual optimization where we achieved a best temperature of $\approx 7\mu\text{K}$ over days, machine learning using MLOOP allows us to achieve $\approx 3\mu\text{K}$ over a couple of hours! For us this is exciting since the lowest reported temperature achieved for ^{39}K using gray molasses cooling stand at $\approx 6\ \mu\text{K}$ [92].

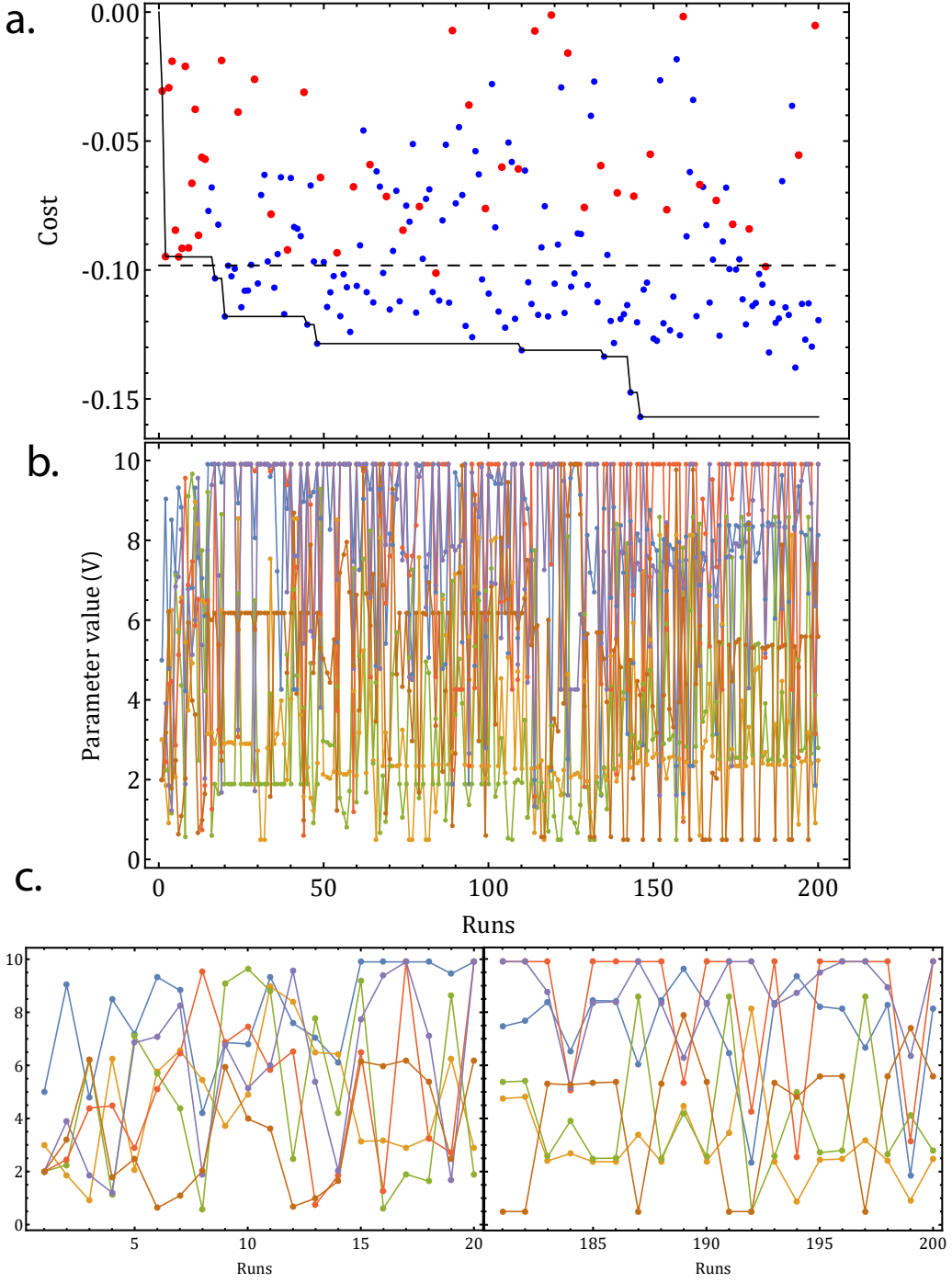


Figure 2.32: Optimization of gray molasses cooling stage using MLOOP. (a) Cost values as a function of runs. For the first 14 runs the machine learning acquires training data (red) which is used to build a Gaussian process model. These model is updated on subsequent runs based on new data (blue), where the machine learner explores different regions of the parameter space. (b,c) Cost function for different parameters used as a function of iterations. MLOOP tries out *seemingly random* parameter combinations but result in robust settings.

The parameters optimized in this specific run were (1) D1 total intensity at the beginning of a ramp and (2) at the end of a smooth ramp controlled through a double-pass AOM in the D1 set up as shown in Figure 2.26, (3) the ratio of the carrier to sideband components of the D1 cooling light as controlled through a free-space EOM (Qubig EO-K39M3-NIR), (4) The frequency detuning Δ of both the carrier and sideband above the $F = 2 \rightarrow F' = 2$ transition (one-photon detuning) at the beginning and (5) at the end of the ramp, and (6) the duration of the ramp. We then initialize the machine learning algorithm in a non-ideal (random) region in the six dimensional parameter space preferably at a large *Hamming distance* from already optimized parameters. This is to avoid 'trapping' the algorithm in the local minimum corresponding to already optimized parameter thus missing other minima that might be more robust and/or manifest lower cost values. Once the algorithm is initialized it first requests a few runs to build up a rough model of the cost function. This training data points are represented by red dots in Figure 2.32 (a). Based on this initial *population* the machine learner performs GP regression where it begins sampling the parameter space in order to improve the GP model and to optimize the lowest achieved cost function. The learning instances are represented by blue dots. The power of GP regression machinery manifests quite clearly where within just a few runs we already find a local minimum that is just as good as manually optimized parameters based on literature. The dashed line in Figure 2.32(a) shows the cost value that corresponds to manually optimized parameters. Despite a seemingly random and non-intuitive parameter search from run to run (shown in 2.32 (b,c)) the machine learner gets a better understanding of the 6D parameter space and finds better and better sets of parameters (indicated by the black line) in a much shorter time than a trained experimentalist would.

At the end of the 200 runs we compared the suggested best set of parameters \vec{X}_2 , based on a GP model $f(\vec{X}_2)$ generated by the routine to (1) the manually optimized parameters \vec{X}_1 from the previous section and to (2) parameters that exhibited the best cost values during the optimization $\vec{X}_{3 \rightarrow 13}$. Essentially here we assume that we did not in fact find the global minimum (assuming there is one). We therefore compare a couple of parameter settings that correspond to local minima in order to find the most robust set of parameters. In a final round of optimization we study the results we perform manual scans of each parameter.

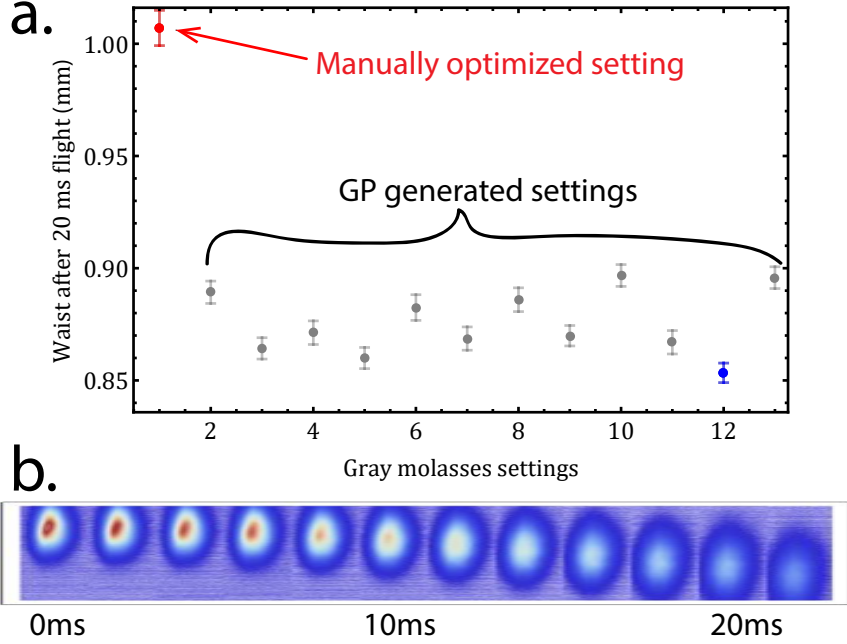


Figure 2.33: Comparison between GP generated settings with manually optimized settings. (a) Plotting the waist after 20ms time-of-flight (averaged over 10 images), we compare the 12 best settings ie. settings that gave the 12 lowest cost values during optimization to the best achieved settings by manual optimization. A smaller waist corresponds to lower temperatures achieved. (b) Time-of-flight images after gray molasses cooling using GP generated settings (blue in (a)). We achieve a final temperature of $\approx 3.7\mu\text{K}$.

This manual scan reveals for example that a longer duration of the cooling stage lowers the temperature of the atomic cloud while also increasing the the number of atoms that are cooled. This lesson is also already clear from the fact that the elements representing duration of cooling in $\vec{X}_{2 \rightarrow 13}$ were all at the maximum value of the searchable range specified at the beginning of the runs. Based on further optimization of \vec{X}_{12} , we achieve a final temperature of $T_{GM} 3.66(4) \mu\text{K}$ as measured from time-of-flight images (Figure 2.33(b)).

Final sequence

In summary the final sequence is shown on Figure 2.35. The sequence consists of five main stages

1. Loading of MOT1 in the octagon chamber using a continuous push beam that delivers atoms from a 2DMOT in the source chamber. This MOT1 is loaded for $\approx 3\text{s}$.

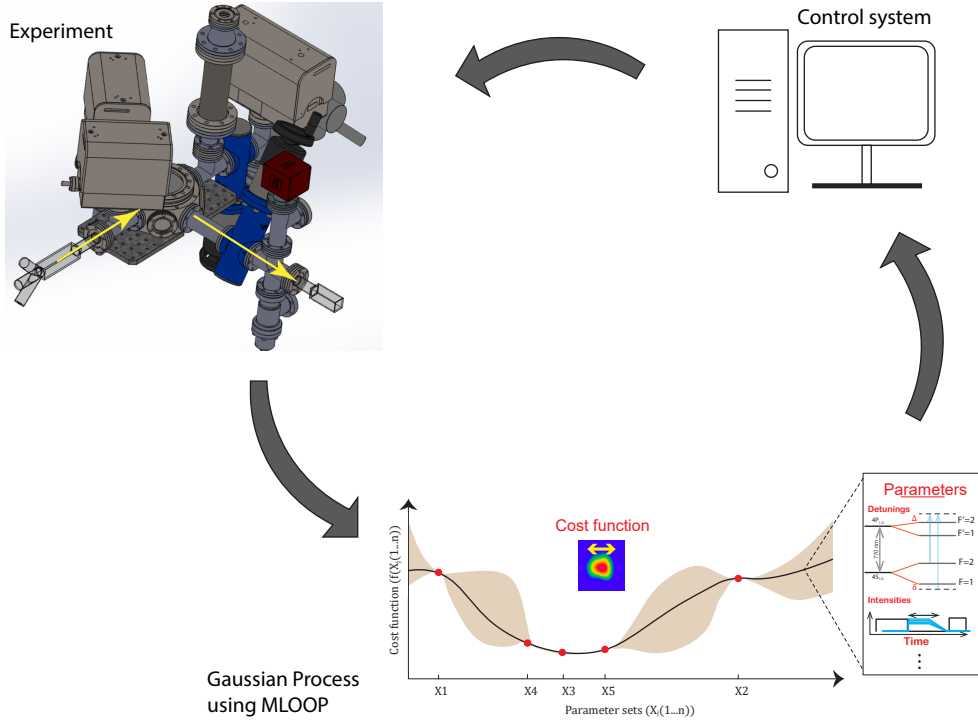


Figure 2.34: Summary of the machine learning sequence.

2. Rapid transport of atoms between the octagon chamber and the science chamber for ≈ 22 ms. The push beam is turned on for $\approx 240\mu\text{s}$ just after turning of MOT1 beams and magnetic field gradient thus accelerating the atoms towards the science chamber. During this stage the MOT beam intensity and detunings are ramped up to optimal values in preparation for re-capture in MOT2 at the science chamber. This arrangement is necessary since the beams used for both MOT1 and MOT2 are delivered using a 4 by 4 spliceless fiber array.

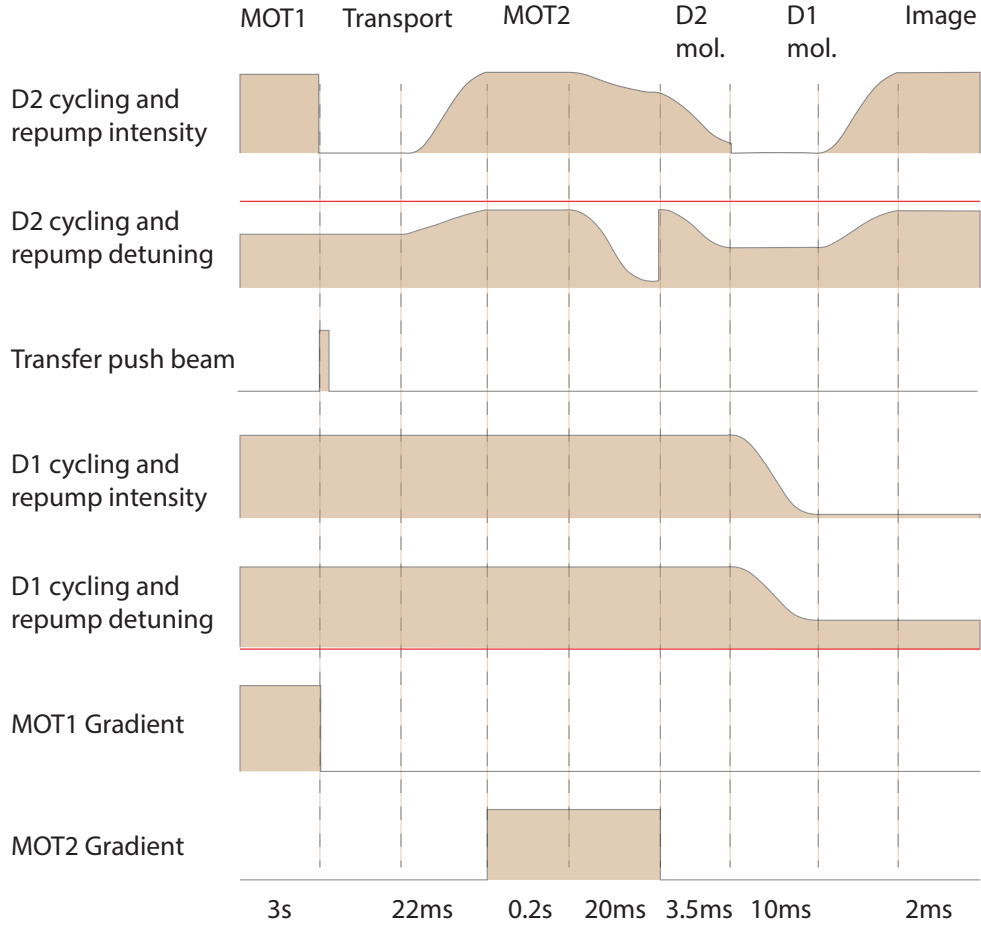


Figure 2.35: Experimental sequence. The sequence runs left to right with each timestep demarcated by dashed lines. While the time axis is not drawn to scale. The duration of each timestep is displayed at the bottom. From top to bottom we display different aspects of the experiment as labeled on the left. The red lines above/below D2/D1 cycling and repump detuning indicate that the detunings are below/above resonance. The exact values at each timestep are displayed on Table 2.3.

3. Catching atoms in MOT2 at the science chamber followed by ramping of MOT2 parameters to initially cool the atoms towards the Doppler limit. Here temperatures are lowered from $T_{\text{MOT}} > 1 \text{ mK}$ to $T_{\text{MOT}} \approx 250 \mu\text{K}$.
4. Sub-Doppler cooling using D2 molasses. Here the magnetic field gradient is turned off and the molasses beam intensities and detunings are ramped for 3.5 ms leading cooling the atoms down to $\approx 100 \mu\text{K}$. We think we are unable to get to lower temperatures due to heating because of the small energy separation in the excited state manifold.

Parameter	MOT1	Ramp to MOT2	Rampdown at MOT2	D2 molasses	D1 molasses	Imaging
Cycling intensity (mW/mm ²)	1.3	1.3 →1.18	1.18 → 1.07	1.27 0.41		0.41 → 1.3
Repump intensity (mW/mm ²)	0.25	0.25 →0.37	0.37 →0.2	0.2 0.03		0.01 → 0.37
Cycling detuning (Γ)	-1.2	-1.32 →-1.3	-1.3 →-8.1	-1.07 -0.01		-0.01 → -0.37
Repump detuning (Γ)	-1.23	-1.23 →-2.37	-2.37 →-4.81	-1.49 -3.03		-3.03 → -2.3
D1 detuning (Γ_{D1})					-3.47 → -4.63	
D1 intensity (mW/mm ²)					1.68 → 0.07	

Table 2.3: Optimized sequence for producing a cold sample of ^{39}K atoms.

5. Further cooling using Λ –enhanced gray molasses cooling. Parameters optimized by GP regression cool down the atoms to $\approx 3.7 \mu\text{K}$ ⁴⁷.

While specific beam intensities and detunings are shown on table 2.3, we have since modified these values based on the need to trap atoms in optical tweezers with in a 120 degree MOT beam configuration discussed in Chapter 3.

⁴⁷Further manual optimization was performed in the final configuration bringing this temperature down to around $3 \mu\text{K}$

Chapter 3

Single atom trapping in optical tweezers

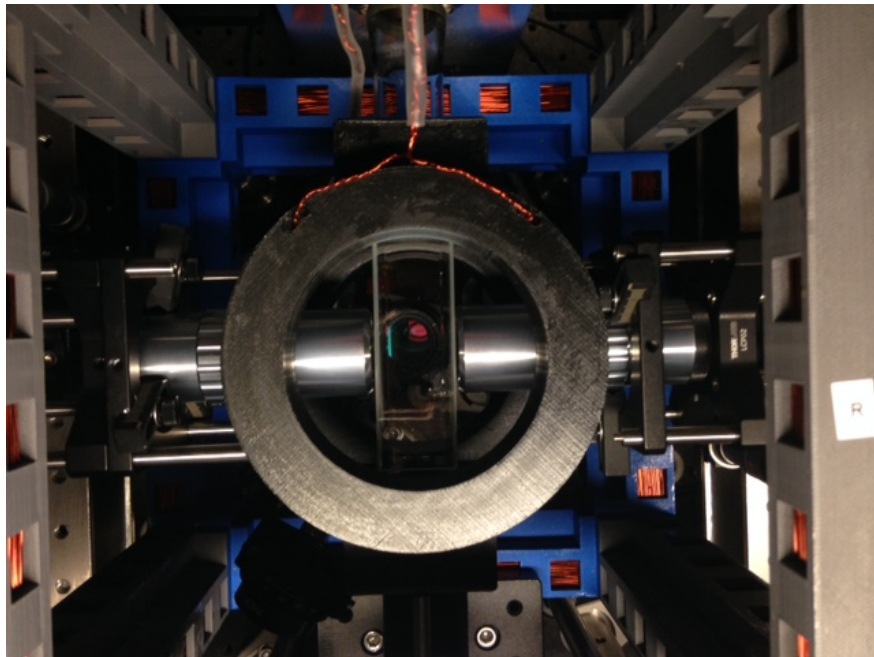


Figure 3.1: Image of objectives mounted next to cell for single atom trapping *ca.* 2021

3.1 Introduction

Optical tweezer arrays¹ (OTAs) have garnered interest recently as a powerful platform for the trapping, coherent manipulation, and imaging of single atoms due to their simple design yet versatile applications. Here, tightly focused beams form deep conservative traps (depths of $U/k_B \approx$ few mK) which then enable the steering of the position of the atom [9, 10] and creation of arbitrary defect-free geometries [11]. These kinds of ordered atomic arrays can be used as versatile platforms for quantum computing and analog simulation, i.e. of many-

¹Terminology: The term optical tweezers arrays is used interchangeably with optical micro-traps, optical tweezers and tweezer traps.

body spin systems [9, 12–17]. Deep traps also allow for non-destructive imaging, where the trapped atom is continuously cooled while emitted photons from fluorescing the atom are simultaneously collected for imaging without losing the atom from the trap [106, 107]. Since single atoms are directly loaded from a magneto-optical trap (MOT), the experimental run times for OTAs are typically of the order ≈ 1 s which provides good statistics. The loading of atoms into individual optical tweezers is probabilistic, with loading probabilities as high as roughly 90% achieved recently [106–108]. Still, such a probabilistic approach does not scale well to large arrays. Recently, a key advance in *deterministic* loading of large arrays has been achieved by the measurement of partially filled arrays and the subsequent distillation of vacancies by feedback on the atoms’ positions [10]. The fast cycle times, ability to create arbitrary trapping geometries, and the access to direct fluorescence imaging make OTAs appealing from an experimental perspective. The fact that this approach can still allow for strong interactions between the spatially separated particles (*e.g.*, for molecules or for neutral atoms excited to high-lying principle quantum number, Rydberg states) makes OTAs a powerful platform for quantum information science applications [20] and for the study of many-body phenomena [9].

In this chapter we describe a simple system developed for trapping and cooling potassium atoms in optical tweezer arrays. Specifically, by combining the use of a not-so-far-detuned optical dipole traps (780 nm) that induce moderate light shifts with robust cooling based Λ -enhanced gray molasses (GM) (on 770 nm D1 line) we demonstrate simple robust loading, cooling, and imaging in our system. Using GM cooling, we demonstrate enhanced ($\gtrsim 75\%$) loading efficiencies as well as robust in-trap cooling to low temperatures. The work presented in this chapter is prerequisite for our system of atoms that will be excited to Rydberg levels for the implementation of synthetic Rydberg lattices as was discussed in Chapter 1.

Concurrent work on trapping potassium atoms in optical tweezer arrays was already underway in the group of Christian Gross [64] (then at LMU München and now at Uni Tübingen), where the group has demonstrated cooling to very low temperatures using Raman-sideband cooling for trapped potassium atoms in a 1064 nm tweezer array followed by initial demonstrations of Rydberg excitation using a 286 nm laser. Discussion with Nikolas Lorenz and Christian Gross, both during my visit right before the global pandemic and

e-mail correspondence afterwards, was *very useful* at the later stages of our construction and is greatly appreciated. We also note that related work on ^{39}K has recently been done in the group of Shannon Whitlock at Université de Strasbourg, where they demonstrate preparation of ensembles of potassium atoms in arrays 780 nm optical tweezers [63] (≈ 30 atoms per trap) loaded from 1064 nm reservoir traps.

3.2 Optical set up

3.2.1 Science MOT setup

Our optical tweezer set up includes a pair of high numerical aperture (NA=0.5) objectives² where one objective delivers tightly-focused dipole traps at the center of the science chamber while the second objective collects fluorescence from trapped atoms which is imaged onto an electron-multiplying CCD (EMCCD) camera through a $\times 9.375$ magnification imaging system.

Our objectives, which are outside of the vacuum chamber, are set up very close ($\sim 1 \mu\text{m}$) to the glass science cell. This is because of the cross-sectional dimensions of our science cell (28 mm x 28 mm OD) and the relatively short working distance of the high-NA objectives (designed for a 15.08 mm working distance through a 3.5 mm thick glass cover slip). To make room for these objectives, we adjust the 3D MOT beam set up from the original configuration where horizontal MOT beams were set up at right angles with respect to each other to a new configuration where they are set up at 120 degrees. This helps to avoid clipping of the MOT beams on the objectives. While the number of atoms captured in the new MOT configuration is clearly lower than that of the standard "orthogonal beam" MOT, we are still able to maintain efficient cooling (achieving temperatures as low as $3 \mu\text{K}$ after the gray molasses stage).

²Mitutoyo G Plan Apo 50X

3.2.2 Optical tweezers

Optical tweezers are tightly-focused optical dipole traps where radial waist at the focus is typically on the order of the trap wavelength. The trapping mechanism relies on an AC Stark shift of the atomic ground state caused by electric dipole interaction with far-detuned light. In other words, the ground state is shifted to lower energies with increasing intensity so that atoms are *attracted* to regions of highest intensity. The trapping potential³ is given

³This equation is specific to alkali atoms with D line transitions and strictly refers to the ground state potential

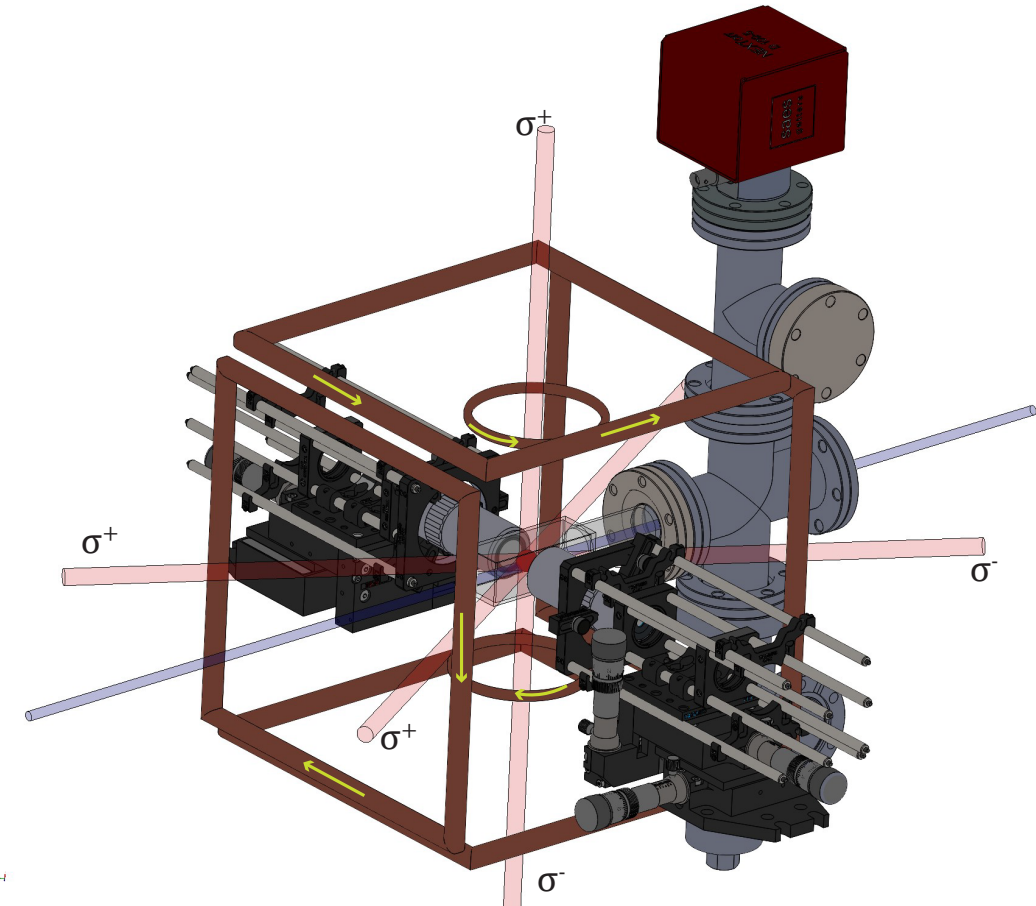


Figure 3.2: MOT beam layout at the science chamber. Three retro-reflected beam are overlapped at the center with the horizontal beams set at 120 degrees with respect to each other to allow the high-NA objectives to be set up within working distance. A NexTorr ion pump (in red) used to maintain low pressures has a small size to free up optical access for future Rydberg excitation beams. An imaging beam is set up perpendicular to the objectives (across the chamber through the differential pumping tube) to minimize scattering due to reflection on glass surfaces into the imaging system.

by [109]

$$U_{\text{dip}}(r, z) = \frac{-3\pi c^2}{2f_{\text{D}2}^3} \left(\frac{1}{3} \frac{\Gamma_{\text{D}1}}{\Delta_{\text{D}1}} + \frac{2}{3} \frac{\Gamma_{\text{D}2}}{\Delta_{\text{D}2}} \right) \times I(r, z) \quad (3.1)$$

where $I(r, z) = \frac{2P_0}{\pi\omega(z)^2} \exp\left[\frac{-2r^2}{\omega(z)^2}\right]$ is the intensity (at a given position r, z) of the tweezer with power P_0 . The beam profile in the axial direction is $\omega(z) = \omega_0 \sqrt{1 + \left(\frac{z}{z_R}\right)^2}$ where $z_R = \frac{\pi\omega_0^2}{\lambda}$ is the Rayleigh length. Linewidths that correspond to D1 and D2 transitions are given by $\Gamma_{\text{D}1} = 2\pi \times 5.956$ MHz and $\Gamma_{\text{D}2} = 2\pi \times 6.035$ MHz [110]. The detuning of the trap laser from D1 and D2 transitions is labeled as $\Delta_{\text{D}1}$ and $\Delta_{\text{D}2}$, respectively. We label the D1 and D2 transition frequencies as $f_{\text{D}1}$ and $f_{\text{D}2}$. A red-detuned optical tweezer therefore creates a 3D optical potential that can spatially confine atoms. In this chapter most of the work is performed using an optical tweezer focused down to $\approx 1 \mu\text{m}$ waist. For $P_0=1.14$ mW at the focus we expect $U_{\text{dip}}(0) \approx 1.5$ mK and radial and axial trap frequencies, $\{\Omega_{\text{radial}}, \Omega_{\text{axial}}\} = 2\pi \times \{174.3, 30\}$ kHz. Here, based on a harmonic approximation to the radial and axial trapping potentials, we have

$$\begin{aligned} \Omega_{\text{radial}} &= \sqrt{\frac{4U_{\text{dip}}(0)}{m\omega_0^2}}, \\ \Omega_{\text{axial}} &= \sqrt{\frac{2U_{\text{dip}}(0)}{mz_R^2}}. \end{aligned} \quad (3.2)$$

Trap depth estimates based on D1 loading spectroscopy (as described later in Section 3.5.2) suggest a trap depth of 1.13 ± 0.013 mK for a $1 \mu\text{m}$ waist trap for $P_0=1.14$ mW. This suggest a more severe loss of trap power in the objective and at the glass cell window than previously estimated.

3.2.3 Optical tweezer set up

Our tweezer light is supplied by a Toptica DL100 ECDL operated at 780 nm. The ≈ 70 mW of light is divided into two paths using a PBS. Each path is passed through a single pass AOM driven at 80 MHz and the first diffraction order is coupled into a PM fiber and sent

to the experiment. While one path is enough to generate optical tweezer arrays we set up a second *mini-trap* for alignment and diagnostics. At the experiment the tweezer beam out of the PM fiber is passed through a PBS for polarization clean up. Roughly 10% of the linearly polarized beam is picked off using a beam sampler (BSF10-B) and sent on to a photo-diode (PD) for power stabilization. Specifically, the “sampled” PD signal is sent to a commercial PID controller (SRS SIM960), where it is compared to a voltage setpoint provided by our experimental control system “Cicero” [37]. The PID loop feeds back on the diffraction efficiency into the PM fiber (through, *e.g.*, the voltage signal sent to a voltage-variable rf attenuator) to stabilize the optical power delivered to the atoms.

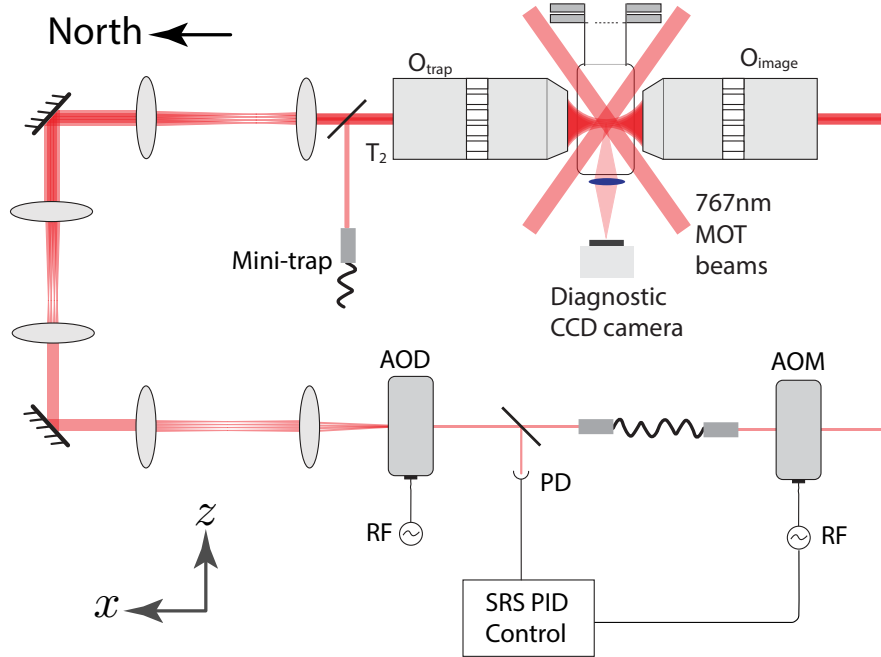
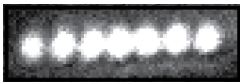


Figure 3.3: Optical set up for generating an array of optical tweezers

The tweezer beam is then aligned into an acousto-optic deflector (AOD) which is driven using multi-tone frequencies to create multiple slightly deflected beamlets whose power and position can be individually controlled directly by controlling the corresponding component of the multi-tone frequency drive. We pass these beamlets through an $f = 100$ mm 1:1 telescope so that they propagate parallel to each other. Coming out of the telescopes, each beam is now collimated ($\omega_0 \approx 1$ mm) and propagates parallel to the rest. A second 1:4 telescope is then used to magnify the beams. A final 3:2 telescope is set up with one of

Table 3.1: Generating tweezer arrays using multi-tone frequency drives

AOD drive	Traps
90, 102 MHz	
90, 96, 102 MHz	
93,96,102,105 MHz	
90MHz, 96-108MHz	
90-108 MHz (3 MHz steps)	

the lens in a μ meter mount (Thorlabs SM1Z) to simplify the final collimation of the beams before sending them into the objective. Once aligned through the objective, the trap beams are collected by a second objective meant for collecting fluorescence from trapped atoms and are blocked using ultra-narrow filters. Both the trapping and imaging optics are set up on optical breadboards (Thorlabs Nexus B1824T) mounted on dynamically damped posts (DP12A) for vibrational isolation. Diagnostic cameras and photodiodes for investigating the spatial and temporal profiles of the traps are not shown.

Objective mounts

The imaging system consists of a collection objective mounted on a RBL13D stage. A cage system beginning at the objective allows us to mount both $\varnothing 2''$ and $\varnothing 1''$ lenses roughly on a straight line. An initial $\varnothing 1'' f = 100$ mm lens is mounted to collimate collected light from a point source and results in a factor of 25 magnification for a collimated beam going into the objective- $f = 100$ mm-lens telescope. Appropriately set up is a 8:3 telescope (based on $\varnothing 2'' f = 200$ mm and $f = 75$ mm lenses). The final lens is set up on a Thorlabs LT1 one-axis mount for final focusing of the collected light into an EMCCD camera.

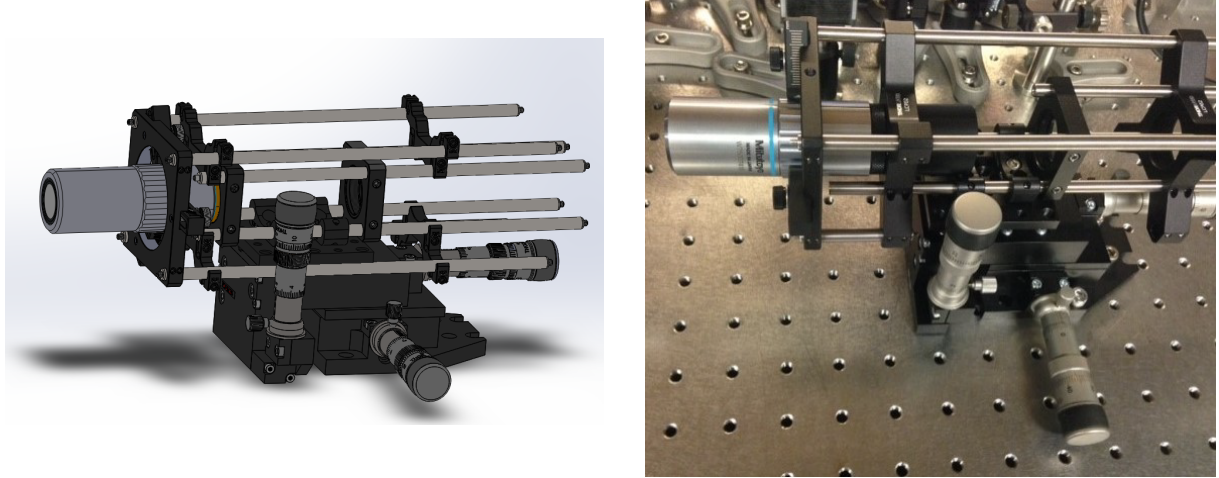


Figure 3.4: Mounting opto-mechanics for the Mitutoyo objective.

3.2.4 Tweezer alignment

The overlap between optical tweezers and the 3D MOT is one of the most critical ingredients for successful loading of atoms. Good (well-centered) overlap ensures a high local density of atoms around the tweezer which guarantees robust and repeatable loading of atoms despite shot to shot movement of the atomic cloud at the optical molasses stage.

The micrometer knobs on the 3-axis RBL13D objective stages facilitated fine control over the position of the optical tweezers (relative to the center of the MOT) in all three directions. Additionally, we further implemented an extra set of magnetic *shim* coils i.e. the square field coils in Figure 3.2. These coils are set up in a Helmholtz configuration in each of the three directions creating a small magnetic field that can shift the position of

Part	Part number
3-Axis RollerBlock Long-Travel Bearing Stage	RBL13D
Stage Adapter Plate	RB13P1
30 mm to 60 mm Cage Plate Adapter	LCP02
60 mm Cage-Compatible Adjustable Lens Mount	LH160C
Drop-In 30 mm to 60 mm Cage System Adapter	CDA1
SM1-Threaded 30 mm Cage Plate	CP33
30 mm Cage Mounting Bracket	CP02B
Cage Assembly Rod	ER8

Table 3.2: Opto-mechanical parts used to construct a mount for holding objective lenses.

zero magnetic field gradient thus changing the position of the 3D MOT. These extra set of coils⁴ are only turned on after the gray molasses stage in order to overlap the MOT during loading *after* atoms have already been cooled in the previous stage (which requires proper field cancellation).

Here we will outline an alignment procedure optimized for overlapping both the mini-trap and microtrap to the center position of the atomic cloud after the molasses stage. The directions x, y and z are used here to refer to the North-South, the Top-Bottom and the East-West cardinal directions in the lab.

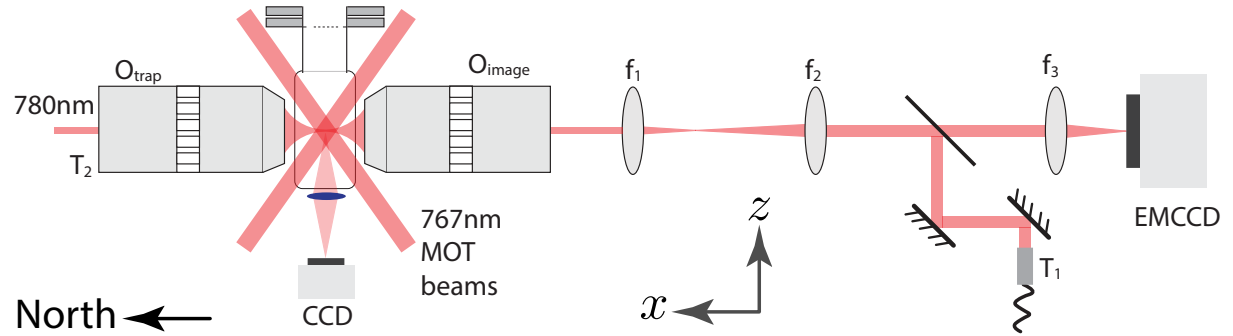


Figure 3.5: Alignment procedure for overlapping tweezer traps with MOT.

1. We confirm that beams T_1 (diagnostic beam) and T_2 (actual tweezer beam) are each collimated. For T_1 we confirm that the beam is collimated coming out of the fiber port while for beam T_2 we reflect the beam before objective O_{trap} and monitor it at some large distance. Micrometer mounts (Thorlabs SM1Z) at the fiber port output are useful for this step.
2. We then image the MOT atoms through O_{image} either by adding a mirror between f_1 and f_2 that reflects into a low magnification imaging system onto a spare CCD camera or directly on the EMCCD camera using the existing imaging system. This ensures that O_{image} is well centered in the y, z directions with respect to the MOT.

⁴These coils are an addition to magnetic field cancellation coils whose set currents that are already optimized to enable sub-Doppler cooling.

The objective position in the x direction is also adjusted to make sure the MOT is in focus at the EMCCD camera.

3. We align beam T_1 into the imaging system by reflecting at the dichroic DM1 (Semrock TBP01-790/12-25). Cage mountable irises (SM1D12) are useful to ensure that the beam is centered on the lenses.
4. We directly mount a mirror at the input port of the imaging objective O_{image} to retro-reflect beam T_1 . Specifically, the mirror is mounted in an SM1 threaded tube (SM30L10) that directly mounts onto a cage adapter (LCP02). To ensure that the beam is both centered and retro-reflecting a fiber adapter (SM1FC) is screwed against the mirror in the tube. Perfect retro-reflection can then be achieved by using mirrors M1 and M2 to align through an iris in front of lens f_1 , through the center of the fiber adapter and checking back close to the fiber port input.
5. With T_1 centered on O_{image} and retro-reflecting, we remove the retro-reflection mirror to let the beam through. We then adjust the position of O_{trap} so that T_1 goes through it and is collimated. Collimating T_1 ensures that O_{trap} is equidistant with O_{image} from the focal point of T_1 at the center of the science cell. To align the y and z positions of O_{trap} we ensure that the collimated beam coming out is centered on a cage system attached to the objective, i.e., using a cage-mountable iris.
6. For fine alignment of O_{trap} we first set up a mirror at the input port facing the science cell. This mirror now reflects T_1 back through both objectives. We then adjust the fine knobs to overlap the reflected beam at the fiber port output of T_1 .
7. Now that O_{trap} position is well referenced, we set up a mirror at its input facing *away* from the science cell. Using the final two mirrors before O_{trap} we reflect T_2 back on itself as was done in step 4.
8. Finally we set up a mirror right at the input of O_{image} and confirm that T_2 is centered and retro-reflected through both objectives.

9. With manual alignment done, we move on to test the alignment on MOT atoms. For the first step we replace T_2 with resonant or blue-detuned light T_{reso} at 767nm. At the beginning we use ≈ 1 mW of light.
10. We set up an experimental sequence where a MOT is loaded in the science chamber for 2 s followed by pulsing T_{reso} for 0.5 s to try and expel the atoms from the MOT. The CCD camera is operated on video mode to monitor the effect of T_{reso} on the MOT. We adjust the fine knobs on the 3-axis mount to maximize expulsion while reducing the power in T_{reso} (to increase sensitivity). At low powers, T_{reso} will be too weak to extinguish the MOT and will instead slightly displace the MOT in the x direction. Alignment at this point is optimized by maximizing displacement. We find that the z direction is usually quite well aligned before this step and slight adjustments in the x and y directions are necessary.
11. While we can tell whether T_{reso} is aligned to the MOT or not, at this stage we are still uncertain about alignment in the y direction (top-bottom). As a sanity check we increase the power in T_{reso} but then add an iris (or a pinhole) to decrease the size of the beam. When the alignment is right, this leads to a line of atoms pushed out of the MOT. We can now center the beam in the y direction by adjusting O_{trap} position so that this line is centered as imaged on the CCD camera.
12. Now that we are confident that light through O_{trap} is hitting the MOT at some point, we can now try to overlap its focal point with the center of the atomic cloud after the molasses stage. While the trap might be dead center with respect to the MOT, the atomic cloud might be slightly displaced at the end of the gray molasses cooling stage. You might be wondering why go through the trouble of aligning so well to the MOT in the first place? Well as it turns out aligning to the MOT center turns out to be a very good guess for atomic cloud center after molasses stage. In addition, aligning to the MOT is actually much easier, since it can be done with the monitoring CCD on live mode as opposed to alignment to molasses which requires triggered experimental runs.

13. Imaging the beam profile

Since the resonant beam is aligned to the expected dipole trap path, we plan to determine the focal point of this beam by directly imaging atoms using the resonant beam combined with some repump beam. Under the right conditions we expect atoms to fluoresce only along the resonant beam thus revealing the beam profile. By combining T_{reso} with $\varnothing 1 \text{ cm}$ MOT repump beams we are able to acquire enough signal to discern the position of the beam focus.

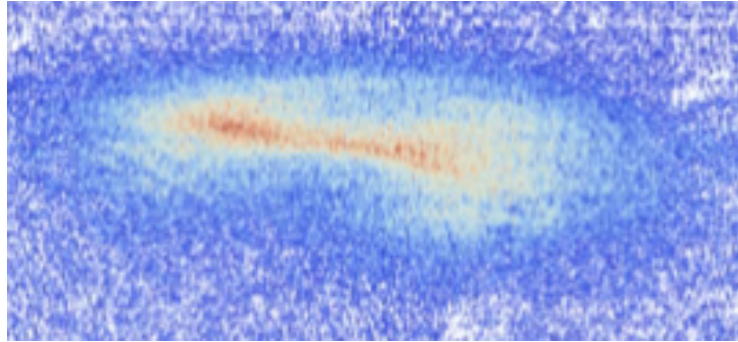


Figure 3.6: Reconstructed beam profile acquired by moving MOT around using small uniform magnetic fields and scattering photons using resonant beam.

At this stage we include an extra set of *overlap* coils wound in the same structure as the field cancellation coils. These coils allow us to move the center position of the atomic cloud by moving the zero-point of the magnetic field gradient in all three directions. By moving the atomic cloud around after the molasses stage we determine the focal point of our dipole trap path (as shown on Figure 3.6) and find corresponding coil current settings that optimize the dipole trap overlap with the center of the atomic cloud. Once the alignment is done we replace the resonant beam a 780 nm beam (both the micro-trap and the mini-trap case) in preparation for loading and imaging atoms.

Having learned how to properly overlap the dipole traps with atoms, we are now ready to load and image atoms in the dipole traps. Here we outline key steps that were followed towards successful loading and imaging of single atoms in optical tweezers:

- **Compensating for trap-induced light shifts:** By using a 780 nm trap trap-induced light shifts are moderate enough to be compensated using AOMs.

- **Background reduction** is necessary to allow us to detect the small amount of signal acquired from a single atom. In our set up this is achieved through careful spectral filtering as well as some spatial filtering (blocking stray light).
- **Loading multiple atoms** in deep and large traps. Initial loading is attempted on the mini-trap to acquire enough signal to allow us to optimize loading and imaging conditions.
- **Parity projection:** Once multiple atoms are loaded into the mini-trap we explore a few ways to induce pairwise loss of atoms from the trap due to light-assisted collisions.
- **In-trap Λ -enhanced gray molasses** is used to cool trapped single atoms, to demonstrate non-destructive imaging and finally to show enhanced loading using repulsive light-assisted collisions.

3.3 Imaging and cooling set up for 780 nm trap

Light shifts

While convenient for creating trapping potentials in the ground states, i.e., where the ground state energy is lowest at the trap focal point, optical tweezers can also shift the excited states in the opposite direction thus causing an anti-trapping potential. For a linearly polarized optical dipole trap the AC Stark shift is typically expressed in terms of a frequency-dependent polarizability [111, 112] $\alpha_{\text{total}}(\omega)$, i.e.,

$$\Delta E_{\text{AC}} = -\alpha_{\text{total}}(\omega)I_{\text{peak}}(0) = -\left[\alpha_0(\omega) + \alpha_2(\omega)\frac{3m_J^2 - J_\nu(J_\nu + 1)}{J_\nu(2J_\nu - 1)}\right]I_{\text{peak}}(0), \quad (3.3)$$

where J_ν is the total angular momentum for the state ν while m_J is the projection of the angular momentum along the polarization axis of the tweezer (assuming no stray B-fields are present) and $I_{\text{peak}}(0)$ is the tweezer peak intensity. The terms $\alpha_0(\omega)$ and $\alpha_2(\omega)$ refer to

the scalar and tensor polarizabilities which are expressed as

$$\begin{aligned}\alpha_0(\omega) &= \frac{2}{3(2J_\nu + 1)} \sum_{\mu} \frac{|\langle \mu || D || \nu \rangle|^2 (E_\mu - E_\nu)}{(E_\mu - E_\nu)^2 - (\hbar\omega)^2} \\ \alpha_2(\omega) &= 4A \sum_{\mu} (-1)^{J_\mu + J_\nu} \left\{ \begin{array}{ccc} 1 & 1 & 2 \\ J_\nu & J_\nu & J_\mu \end{array} \right\} \\ &\quad \times \frac{|\langle \mu || D || \nu \rangle|^2 (E_\mu - E_\nu)}{(E_\mu - E_\nu)^2 - (\hbar\omega)^2},\end{aligned}\tag{3.4}$$

where the pre-factor A is expressed as

$$A = \sqrt{\frac{5j_\nu(2J_\nu - 1)}{6(J_\nu + 1)(2J_\nu + 1)(2J_\nu + 3)}}.$$

The sum \sum_{μ} goes over all states $\{|\mu\rangle\}$ coupled to $|\nu\rangle$. The coupling is expressed in terms of a reduced matrix element $\langle \mu || D || \nu \rangle$ which can be calculated using the Wigner-Eckart theorem (for an avid reader). However, the reduced matrix elements can easily be read off on the newly updated NIST atomic properties website⁵.

Due to differential light shift between the ground and excited state, cooling and imaging conditions optimized for atoms in a MOT are no longer viable since free-space beams become significantly red-detuned (for deep traps we began with) with respect to the shifted transition for trapped atoms. For a hypothetical two-level atom, this differential light shift is just twice the energy shift experienced by the ground state. For real atoms of a given species [113, 114], this light shift varies with the applied wavelength and is dependent on the composition of available transitions to/from the ground state and the considered excited state. For strontium, for example, the differential Stark shift between the dominant $^1S_0 \rightarrow ^1P_1$ has a zero crossing at 813nm. This *magic wavelength*, allows in-trap cooling and imaging under conditions optimized for “free-space” atoms in a MOT [115, 116].

While a magic wavelength might not be available for different species at convenient trapping wavelengths, the bad effects of differential light shifts can be avoided by temporally strobing the trapping beam out of phase with the imaging and cooling beams [64, 117].

⁵<http://www1.udel.edu/atom/index.html>

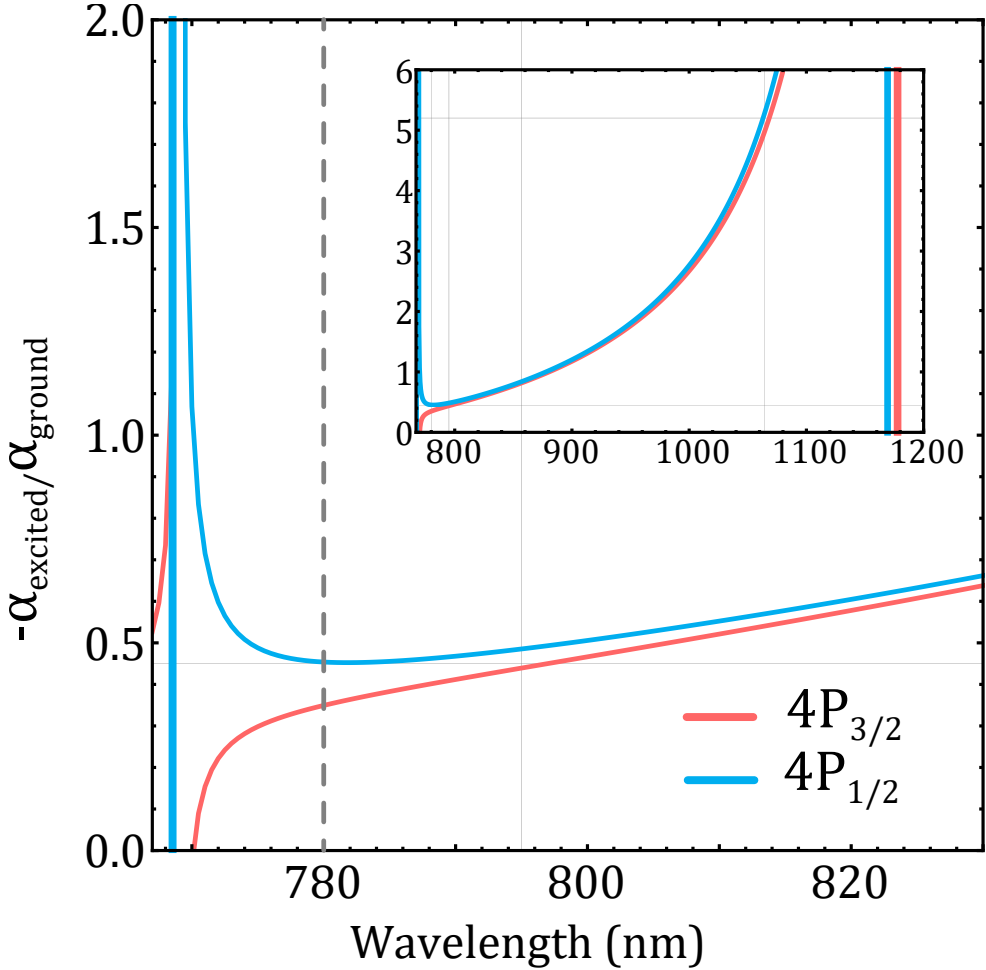


Figure 3.7: **Tweezer light shifts on the D1 and D2 transitions.** We plot the excited state polarizabilities for the D1 ($4P_{1/2}$, blue) and D2 ($4P_{3/2}$, red) transitions, normalized to the ground state ($4S_{1/2}$) polarizability. The main panel shows the excited-to-ground state polarizability ratio for tweezer wavelengths near-detuned from resonance, with the experimental value of 780 nm noted by the vertical black line. The inset shows the same quantities over a larger range of tweezer wavelengths.

This ensures that the trap and imaging and cooling beams are never on concurrently. The chopping frequency f_{chop} has to be fast (≈ 1 MHz) compared to twice the trap frequency (≈ 100 kHz) to avoid parametric heating of the atoms. Under this fast strobing, the atoms experience the time-averaged trapping potential. The chopping frequency f_{chop} also has to be smaller than the natural linewidth Γ to allow enough time for an atom in the excited state to decay back to the ground state before the trap is switched back on again. While this technique has recently been successfully implemented for trapping potassium atoms in 1064 nm optical tweezers [64], here we take a different approach to addressing trap induced

light shifts.

The differential light shift between the $4S_{1/2}$ and $4P_{3/2}$ for fixed ground state trap depth has a minimum around 785nm. By selecting 780 nm as the trap wavelength, the light shifts are on the order of 30 MHz for a ≈ 1 mK ground state potential. These shifts can be easily addressed using AOMs. Besides, since rubidium atoms (with a D2 transition at 780 nm) are a popular choice of species for laser cooling, lasers, filters and other optical elements that work for this wavelength are commercially available.

Vector light shifts

The discussion so far is limited to the case where the tweezer beam is linearly polarized and the paraxial approximation is assumed. For a tightly-focused dipole trap breakdown of paraxial approximation leads to Gouy phase shifts and trap-induced vector light shifts. Specifically as a linearly polarized trap beam is focused the polarization remains transverse to the propagation direction, but due to a sharp change in the beam profile, the linear polarization becomes elliptical at the diffraction limited volume close to the focal point. Elliptical polarization near the focus leads to a vector light shift of the ground state potential given by [118–121]

$$\Delta U_{\text{vector}} = U_{\text{scalar}} \mathbf{C}(\mathbf{r}) \cdot g_F \mathbf{F} \times \frac{\Delta_{D2} - \Delta_{D1}}{\Delta_{D2} + \Delta_{D1}} \quad (3.5)$$

where U_{scalar} is the scalar potential, Δ_{D1} and Δ_{D2} are detunings from the D1 and D2 transitions, \mathbf{F} is the total angular momentum operator and $g_F = \frac{F(F+1)-I(I+1)+J(J+1)}{F(F+1)}$. The polarization of the beam is expressed by $\mathbf{C}(r)$ where $\mathbf{C}(r) = 0$ and $\mathbf{C}(r) = \pm 1$ for linear and circular polarizations. Since these vector light shifts are akin to shifts induced by a local magnetic field they are typically referred to as fictitious magnetic fields. As such, vector light shift can lead to inefficient cooling and are typically cancelled (*shimmed away*) by applying external magnetic fields [118].

Perhaps one of the most important advantages of trapping potassium in optical tweezers is the fact that vector light shifts of linearly polarized tweezers is dependent on the fine structure splitting $\Delta_{\text{Fine}} = \Delta_{D2} - \Delta_{D1}$. A relatively small Δ_{Fine} compared to other species leads to less deleterious effects from vector light shifts induced near the trap focus.

3.3.1 Setting up in-trap imaging and cooling

Since the 780 nm trap wavelength used causes reasonably small light shifts to both the D1 and D2 transition (Fig. 3.7), our single atom set up is designed to explore in-trap imaging and cooling. To achieve this we only have to shift the imaging beam frequency detunings closer to resonance to scatter enough photons and shift the one-photon detuning related to D1 beams (blue-detuned from the $F = 2 \rightarrow F' = 2$ transition) to enable in-trap Λ -enhanced gray molasses cooling.

Our imaging beam consists of a cycling and repump beam path coupled into separate fibers in our laser preparation setup. We combine cycling and repump beams using a 50:50 NPBS and couple the combined beams into two separate fibers. Path P1 (as illustrated on Figure 3.8) is sent into a double-pass AOM system DP_{deep} set up to shift the frequency by $\approx 110 \text{ MHz} - 180 \text{ MHz}$. The output of this system is coupled into a fiber and sent to experiment. The second path P2 is sent to a double-pass AOM system DP_{shallow} which features an IntraAction AOM (AOM-40N) centered at 35 MHz to allow frequency tuning at $\approx 60 \text{ MHz} - 100 \text{ MHz}$. We set up two separates double-pass systems to make it easy for us to diagnose and optimize imaging for both deep and shallow traps separately. At the beginning while searching for a signal we found that it was useful to first try imaging and loading in a deep trap. Upon acquiring a signal it was then easier to move towards shallower traps and switch the imaging source to DP_{shallow} .

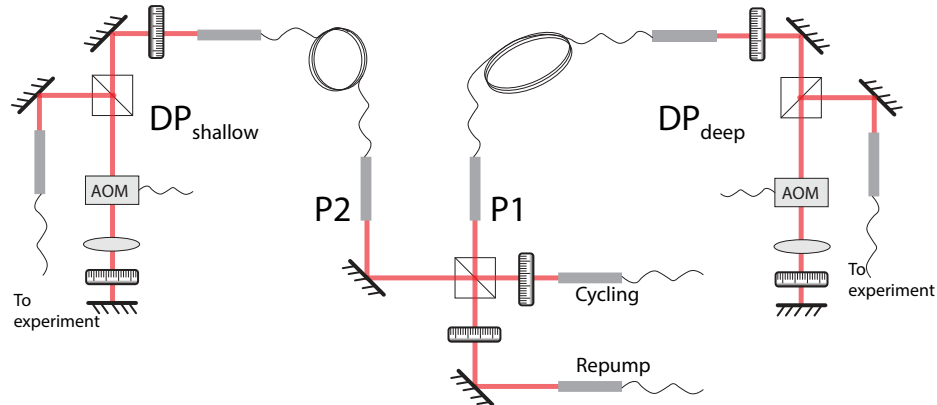


Figure 3.8: Double pass AOM systems for shifting imaging beam frequencies to compensate for trap induced light shifts. Our system consists of two double passes to address light shifts for both deep ($\gtrsim 3 \text{ mK}$) and shallow traps ($\lesssim 3 \text{ mK}$).

Since gray molasses cooling works for a broad range of one-photon detunings⁶ we expect to be able to load and cool using D1 light *without any significant changes to the set up*. The D1 laser preparation set up (described in Section 2.6.1) features a double-pass AOM with a total of $\approx 110\text{MHz} - 180\text{MHz}$ shift that already works quite well in free-space. While this shift is certainly enough to allow loading in shallow traps efficient loading and cooling in deeper traps typically requires further blue-detuning.

3.4 Loading a 780 nm trap: from zero to few atoms

Initial loading and imaging with unknown parameters is a Catch-22 situation where you cannot image atoms without loading but you can't tell whether you've successfully loaded atoms without imaging. Successful imaging of atoms in the tweezer therefore required us to increase the signal-to-noise ratio by both beating down the background and increasing the signal level. With no signal to look at we first embark on a journey to reduce the background as much as possible.

3.4.1 Background sources

Diagnosis of the background compared to imaging was done by using a very weak resonant beam combined with the optical tweezer to simulate the path that should be taken by fluorescence from trapped atoms. Some of the background sources include

1. **Leak-through 780 nm trap light.** Even though a filter (Semrock TBP01-790/12-25) was set up to reflect the 780 nm trap light, so that only light from trapped atoms makes it to the camera, we were still getting some leak-through light from the trap beam path. There were two reasons for this:
 - Since filtering is imperfect a small amount of leak-through light (through the filter) is focused onto $\approx 3 \times 3$ pixel area on the camera and is amplified enough (using EM Gain on the camera) to potentially be higher than the atomic signal.

⁶As long as the D1 ‘cycling’ and ‘repump’ are blue-detuned with respect to the $F' = 2$, and the Raman condition ($\delta = 0$) is fulfilled.

We include additional filters i.e. 2 short pass (FF01-766/13-25) and 1 bandpass (LL01-780-25) filter to mitigate this.

- Upon including more filters the focused “trap light” was reduced but still not eliminated. Further investigation revealed that this light was due to **Raman-scattering-generated beam frequencies in the trap light fiber** that were so close to imaging resonance that they could not be filtered out. By adding band-pass filters (Alluxa 780-1 OD6) at the fiber output of the trap light so that the tweezer light sent to the atoms only has components near 780 nm, we were able to eliminate this background source.
2. Both **stray room light and light from the octagon and source chamber set-ups** (which are constructed on the same optical breadboard). This could be reduced by turning off room light during operation and covering the imaging set up. Including an iris at the focal point of the intermediate trap focus on the imaging side further decreased the background light.
3. **Stray light from the imaging beam.** At the beginning our imaging beam configuration consisted of small ($\varnothing 1$ mm) beans co-propagating with and centered on the MOT beams (as was done in [10]) to minimize stray light due to reflection on the science cell glass surface. While the amount of background was significantly reduced it was still higher than the expected atomic signal.

Aligning the imaging beam along the vertical MOT beam path was not only easier, stray light from this path was also *low enough* (since this path is perpendicular to the imaging set up) to allow us to discern an atomic signal. Later on, we found that the best alignment configuration, i.e., one that led to least background, was along the pulsed push beam path. Here a tiny beam $\approx \varnothing 1$ mm is set up coming into the octagon chamber through a differential pumping tube and perpendicular to both the top-bottom science MOT beam and the imaging objectives, i.e., along the z direction. Both the small size of the beam and the fact that it reflects only on one surface (farther away from the objectives) considerably reduces stray light.

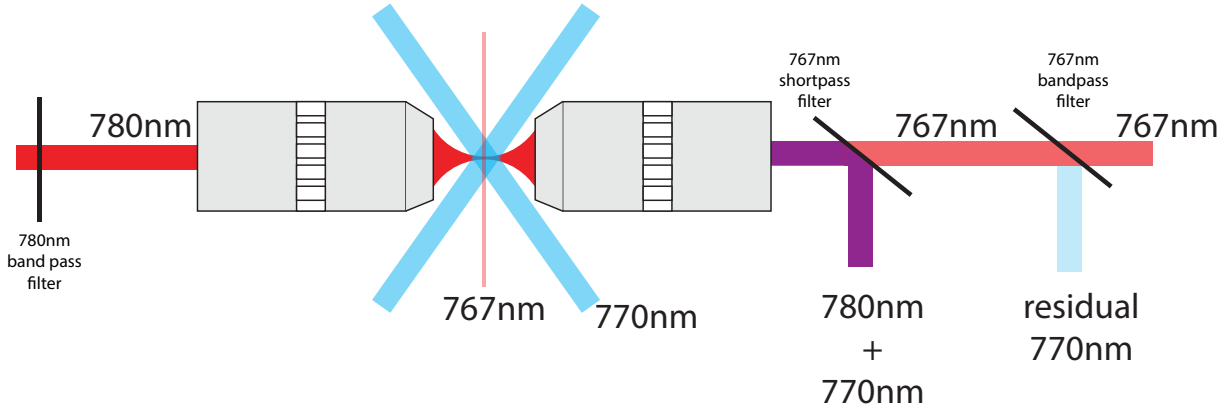


Figure 3.9: Background reduction using narrow-line filters.

4. Leak-through light from 770 nm cooling beams. Imaging atoms without simultaneous cooling leads to rapid loss of the atoms due to heating from the imaging beams. Since our gray molasses imaging beams are combined with the MOT beams on a 4×4 fiber array, the alignment and shaping of the cooling beams are identical to the MOT beams. Despite sufficient covering of the imaging set up, the large size of the cooling beams leads to high background levels due to refection on multiple surfaces at the science chamber. We reduced most of this background by tuning the short pass filters (FF01-766/13-25) so that the cut-off frequency is closer to 767 nm. Further addition of an ultranarrow 780 nm bandpass filter (LL01-780-25) at the imaging set up and a 770 nm normal incidence narrow filter (Alluxa 770-1 OD4) at the 4×4 fiber array fiber input significantly cuts down the background. The band pass filter at the fiber input cuts out unwanted frequencies due to a broad frequency pedestal coming out of a tapered amplifier that supplies D1 light.

An unfortunate consequence of using a 4×4 fiber array was that some of the background due to the cooling beam path is likely caused by Raman-scattering generated frequencies in the fiber array. We confirm this by adding 770nm band-pass filters at the science MOT beam outputs and observing a reduction in background while the amount of power in cooling beams is kept the same. However, since the MOT beams propagated along the same path as the cooling beams resolving this issue, which results in a low but non-negligible background accumulation rate, would likely involve doing

away with the 4x4 fiber array, and instead combining the D1 and D2 light paths using non-polarizing 50:50 beam splitters.

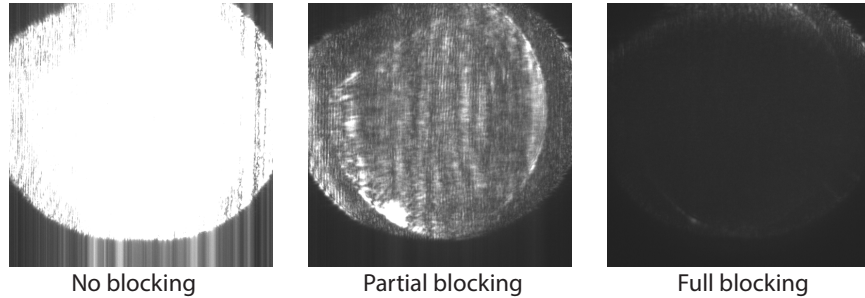


Figure 3.10: Blocking MOT beam stray light at focus points in the Fourier plane.

Further background reduction is explored by setting up to mask unwanted cooling beams. Specifically, we exploit the fact that the cooling beams are set up at a special angle (120°) with respect to the imaging objective. Consequently, light from these beams that makes it through the imaging system i.e. through the objective is focused at some Fourier plane before finally being blown up again at the imaging plane (camera sensor). We found that a large amount of this background can be blocked at its Fourier transform plane while still letting through light from the atoms that is focused at the imaging plane as demonstrated on Figure 3.10.

3.4.2 Loading multiple atoms in a mini-trap

To acquire the first signal we made significant adjustments to our optical set up. We first increase the size of optical mini-trap to increase the capture volume. The mini-trap was focused to $\approx 2.5 \mu\text{m}$ waist and aligned on directly onto the optical micro-trap path. Using a wider and deeper trap should lead to robust loading of multiple atoms and provide enough signal for us to optimize loading and imaging parameters. With a trap depth of $\approx 15 \text{ mK}^7$ we are able to load tens of atoms in our mini-trap. **Special thanks to Michael Highman and Garrett Williams** for lending us extra laser light at 780 nm from the ultra-cold molecule experiment (supplied by Thorlabs TPA780P20 TA) which was enough to acquire the first

⁷Here we blasted the atoms with as much light as we could get just to get that first signal. This was very useful.

signal!! The loading procedure involved performing free-space gray molasses followed by a 36 ms switch-off time where the MOT (D2) and cooling (D1) beams are turned off to allow molasses-cooled atoms to fall under gravity leaving only atoms that are confined in the dipole trap. Our strategy then entails varying the trap parameters to learn about best loading and

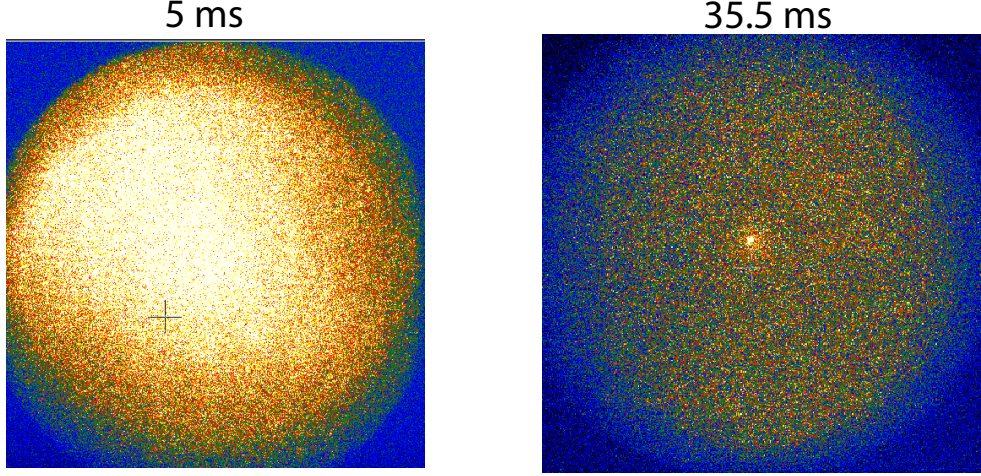


Figure 3.11: **First signal of trapped potassium atoms in a dipole trap.** Left 5 ms after free-space D1 cooling stage, the dipole trap signal is obscured by fluorescence from MOT atoms. Allowing these atoms to fall under gravity reveals remaining trapped atoms in the dipole trap.

imaging practices and then applying our lesson to the optical micro-traps already aligned to the optical mini-trap. By varying the trap depth, the D1 one-photon detuning, and D1 power, we quickly establish best imaging conditions in deep traps. It becomes apparent that loading is robust when the D1 beams are blue-detuned with respect to the $F' = 2$ excited state and as long as the beam intensity is above $\approx 0.75I_{\text{sat}}$.

To explore and optimize imaging in deep traps we by-pass the double-pass AOM system (since the ≈ 200 MHz shift is definitely not enough to compensate for light shifts) and pass the imaging light through a broadband fiber EOM driven at V_π using a DDS source (AD9915). This adjustment is particularly useful for deep traps because it allows us to scan the imaging frequency over a large range (0-1 GHz). Even though this worked well for deep traps we ran into serious issues when working with shallower traps since driving the EOM at a smaller frequency than the carrier leads to appearance of extra frequencies between the carrier and 0. This complicates the frequency spectrum of the imaging beam and further complicates our investigation. For shallow traps we set up the combined cycling and repump

beam to go through DP_{shallow} as explained in Section 3.3.1. Having optimized our imaging and loading parameters we shift our focus to loading single atoms in optical tweezers.

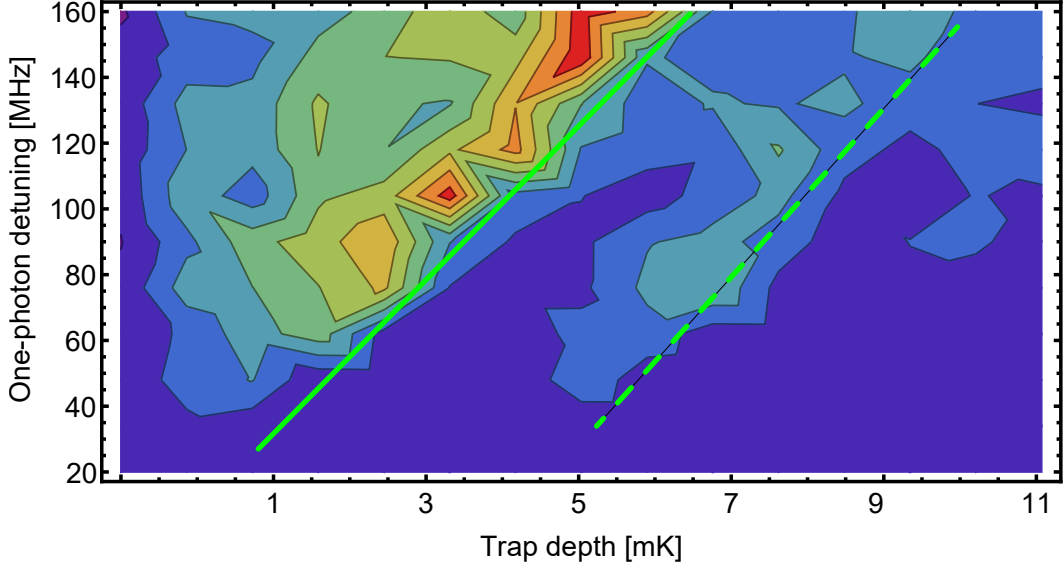


Figure 3.12: **Multi-atom loading in a mini-trap.** Loading is successful when the one-photon detuning compensates for light-shifts due to the trap as shown by solid green line. Here multiple atoms are loaded leading to 100% trap occupancy at ≈ 5 mK. This was useful for optimizing imaging, cooling and parity projection conditions. As indicated by the green dashed line some loading can be done when the one-photon detuning is blue compared to the $F' = 1$ transition.

3.5 Parity projection: killing two birds with one stone

The general recipe for preparing single atoms in optical tweezers involves overlapping the tweezers with atoms in a MOT followed by allowing MOT atoms to disperse. Light-assisted collisions due to the red-detuned MOT beams typically lead to pairwise loss of atoms trapped in the tweezer which distills the population in the trap to 0 or 1 depending on whether the trap was initially occupied by an even or an odd number of atoms [122].

Pairwise loss through light-assisted collisions can be described by considering inelastic collision between two atoms each in their $4S_{1/2}$ state. For such atoms the interaction potential (labeled $|4S_{1/2}, 4S_{1/2}\rangle$) is a van-der-Waals potential given by $U_{\text{vdW}} \propto \frac{C_6}{r^6}$ where C_6 is the interaction coefficient and r is the distance between the atoms. At some distance r_C (Condon point) a laser beam at frequency ω_L is resonant with a molecular (two-atom) potential $|4P_{3/2}, 4S_{1/2}\rangle + |4S_{1/2} + 4P_{3/2}\rangle$ also described as a long-range dipolar potential i.e. $U_{\text{dd}} \propto$

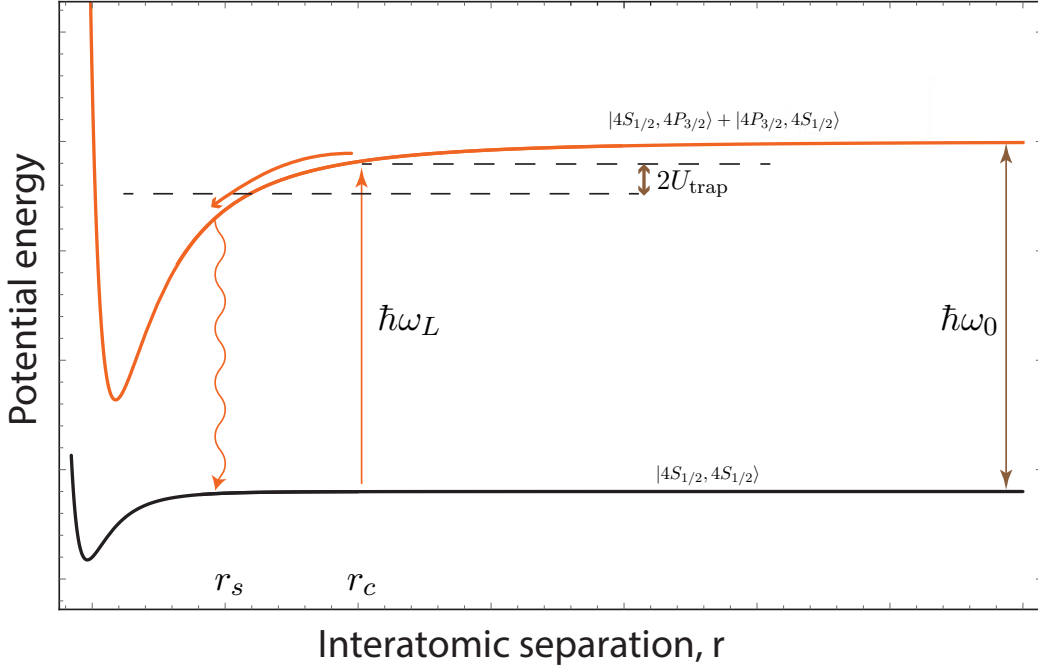


Figure 3.13: **Attractive red-detuned inelastic light-assisted collisions.**

$\frac{C_3}{r^3}$. When the distance between atoms in $|4S_{1/2}, 4S_{1/2}\rangle$ approaches the Condon point, r_c . The atoms absorb a photon and are excited to $|4P_{3/2}, 4S_{1/2}\rangle + |4S_{1/2} + 4P_{3/2}\rangle$. In the excited state the atoms accelerate towards each other down the molecular potential until they spontaneously decay back to $|4S_{1/2}, 4S_{1/2}\rangle$. If the kinetic energy gained during acceleration is larger than the trap depth, both atoms are lost from the trap. Light-assisted collisions are very efficient in tightly-focused traps (traps with small volume) due to a high collision and loss rate. This fast pairwise loss that ensures no more than one atom is left in a trap is referred to collisional blockade [108, 122].

While later we explore the more typical situation of a relatively shallow (~ 1 mK depth) trap with small ($\sim 1 \mu\text{m}$) waist, here we discuss our initial results on optimizing single-atom loading and imaging in deep (~ 5 mK depth) traps with a relatively large ($\sim 1.5 \mu\text{m}$) waist.

Our sequence involves first loading multiple atoms in a deep trap, i.e., performing D1 cooling in free space and then leaving the D1 beams on for 30 ms after the cooling stage. The micro-trap is left on throughout the sequence. After the loading stage the cooling/loading D1 beams are turned off to allow molasses-cooled atoms to fall under gravity leaving a few atoms in the micro-trap. A parity-projection (PP) beam (essentially a beam that is

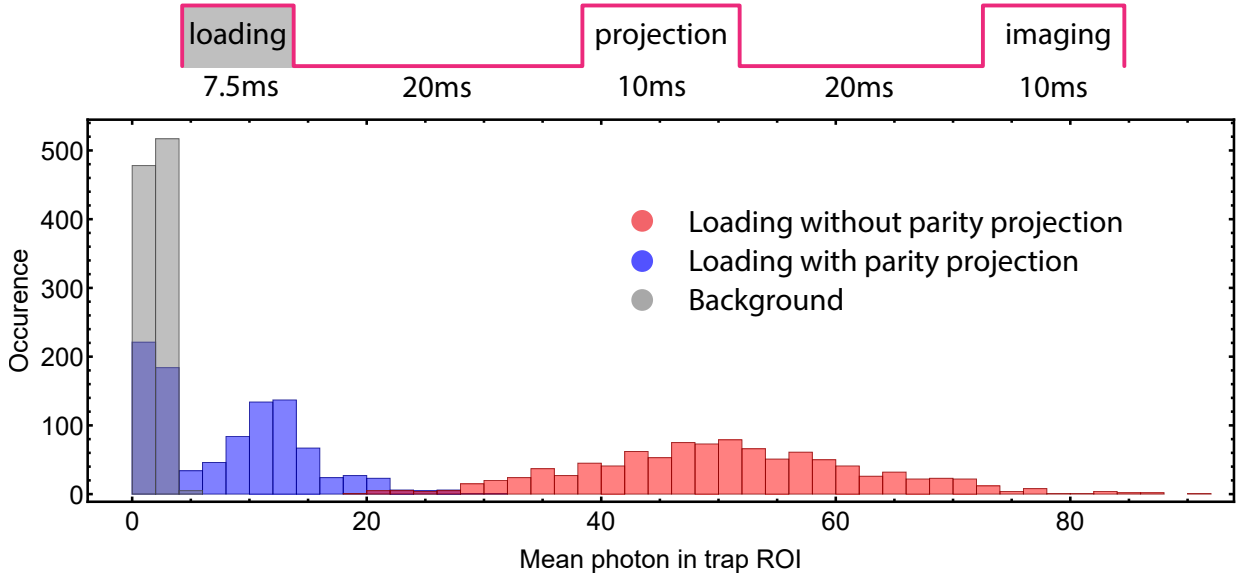


Figure 3.14: **Single atom preparation using parity projection.** A parity projection beam (i.e. just the imaging beam) is flushed on between the loading and imaging stages to induce pairwise loss through light-assisted collisions. As evident in the distribution of photons collected during imaging, including the projection beam kicks out pairs of atoms and modifies histogram from a Poisson distribution (red) corresponding to 4-7 atoms to a sub-Poissonian, bimodal distribution (blue). A histogram of pixels to the side of the trap ROI is also plotted to show the distinction between background and signal.

red-detuned with respect to the imaging D2 transition) is shone onto the atoms for 10 ms to induce pairwise loss from the trap thus projecting the population in the trap to 0 or 1 atom. A final imaging step after the PP stage confirms presence or absence of an atom in the trap. The evidence of single atom trapping reveals itself in a bimodal distribution acquired from hundreds of shots (the smoking gun signature of single atom trapping) as has been displayed on Figure 3.14. This bimodal distribution stands out from the Poisson distribution characteristic of multiple atoms taken under the same condition but without a parity projection stage.

3.5.1 Any beam can cause light-assisted collisions

At the beginning we use the imaging beam to induce parity projection since it is already close enough to resonance for atoms trapped in the tweezer. However, we learn that this beam does not only cause light-assisted collisions, it also heats up the remaining atom when close to resonance. A comfortable operating mode therefore entails detuning this beam farther

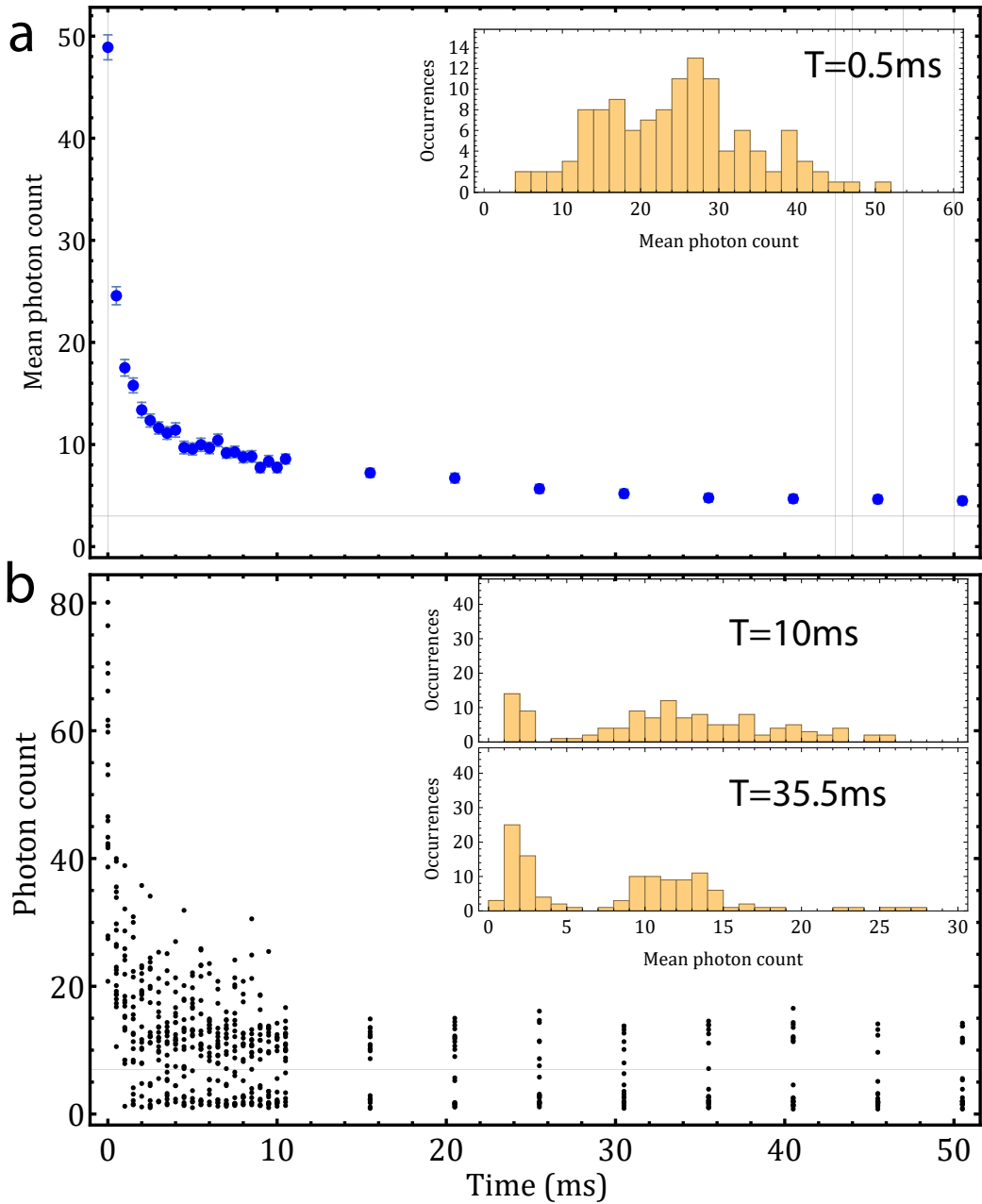


Figure 3.15: Pairwise loss induced by imaging beam.(a) Mean photon counts in the 3×3 trap ROI. As multiple atoms are expelled from the trap the signal decays and bottoms out once all the pairs have been removed leaving 0 or 1 atom in the trap. (b) A bimodal distribution emerges once the trap occupancy has been distilled to 0 or 1 atoms. The insets show histograms at different durations revealing a bimodal distribution at later times.

from resonance (here resonance as light-shifted by the trap depth) to reduce the scattering rate during the PP stage followed by some kind of in-trap cooling to keep the remaining atom in the trap. Although we have learned that any beam (of the relevant ones that we've

investigated) that interacts with the atom induces PP, an ideal scenario involves a beam that both induces PP and cools the remaining atom. We study PP induced using both the D2 and D1 molasses beams and learn that both beams can be used to prepare and cool single atoms. This is made possible, as Will Morong would say, “through either a remarkable accident or powerful display of the universality of physical law.”

Our goal is to set up an arrangement where the atom can be imaged while being cooled in the trap (non-destructive imaging) to allow us to perform multiple experiments on the atom without losing it. Since the D2 molasses beams are large in size ($\approx \phi 1$ cm) they scatter a lot of photons on the science cell glass into the imaging system which causes significant background increase. Imaging atoms while cooling using D2 molasses beams is therefore unfeasible.

In our experience gray molasses cooling using the D1 transition has worked much better compared to bright-molasses using the D2 transition (Section 2.6.1). Besides, we already learn that loading any dipole traps works very well when using the gray molasses⁸. We therefore implement an imaging scheme where the atoms are loaded and cooled using D1 beams at 770 nm (optimized for in-trap cooling) and imaged using a small beam that is light-shifted to be near-resonant with D2 transition (767 nm) and is set up perpendicular to the imaging system.

While the background level caused by D1 light reduces the signal-to-noise ratio for atoms imaged at low scattering rates, in-trap cooling works well enough so that higher scattering rates (using imaging beam closer to resonance or with higher intensities) can be tolerated. Here, the benefit of keeping D1 cooling beams outweighs the cost. Additionally, the background accumulation rate is lower than the scattering rate of the atom so that the signal-to-noise ratio markedly increases for longer imaging durations. This is indeed evidence for non-destructive cooling, i.e., as we continue to image the atom, the signal is further separated from the background without losing the atom. This is illustrated in Figure 3.16.

We successfully apply this loading scheme to a $1\text{ }\mu\text{m}$ trap and optimize imaging parameters. Moving on to shallow traps we find that fewer atoms can be loaded at the beginning before the parity projection stage. In general, for a $\approx 1\text{ mK}$ trap depth with $\approx 1\text{ }\mu\text{m}$ waist

⁸We were able to load deep traps purely using D2 molasses beams but with low probability

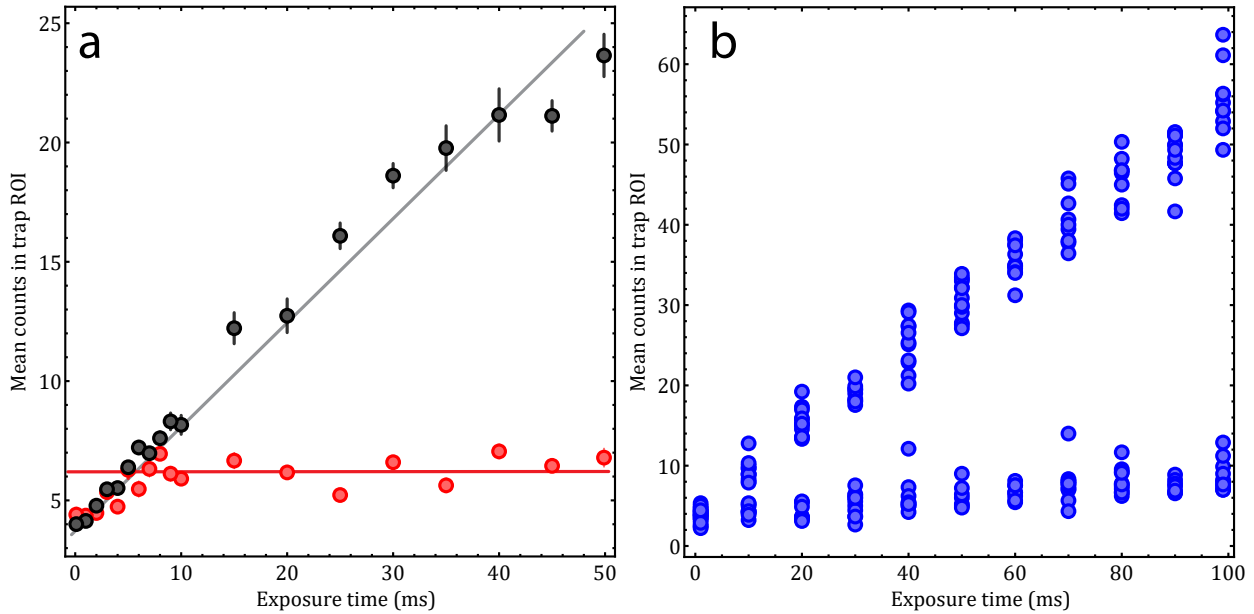


Figure 3.16: **Non-destructive imaging using Λ -enhanced gray molasses** (a) Accumulated signal as a function of camera exposure time. Red: Scattering photons using imaging beam addressing the D2 transition without cooling. The signal is accumulated over the first 10 ms followed by loss of the atom trapped as indicated by flattening of the signal after 10 ms. Black: Imaging using the D2 transition while cooling on the D1 transition. When cooling is added while imaging the atom is kept in the trap while photons are collected leading to a linear increase in the signal over time. (b) A demonstration of non-destructive imaging. As the camera exposure time is increased we collect more photons from the trapped single atom and the signal grows above background (data near the axis). A slight increase in the background signal with exposure time is an indication of the residual background contributions, particularly from filtering of the D1 cooling light. The difference in slope between the background and signal data is proportional to the scattering rate of the imaging beam.

collisional blockade distills the trap occupancy to at most one atom. The loading process is much cleaner when we increase the loading duration to not only load 1 atom but to also cool it down within the trap. While it is not necessary to have a designated loading and PP stage for shallower traps it is useful to have ‘clean up’ PP stages around experimental and imaging stages. In other words, pre-cooling the atom before each imaging and experiment block reduces loss and improves the overall quality of data taken.

3.5.2 Trap depth estimates

Loading, cooling and imaging of atoms in optical tweezers is typically challenging due to trap-induced light shifts. Inadequate knowledge of the trap depth and corresponding light shift can severely impede optimization of any signal achieved. To get an estimate of our trap

depth we take two different approaches:

- **Spectroscopy of the D1 transition based on loading**

As will be explained in Section 3.6, loading of shallow optical tweezers only happens when the shared detuning of D1 cooling and repump beams (one-photon detuning, Δ) is blue compared to the D1 transition. As a result, scanning the detuning of the D1 cooling beams (for a fixed trap depth) reveals a sharp step function where loading begins as soon as the trap-induced light shift is compensated. If the trap depth is varied a linear dependence of the step position on the trap depth emerges as indicated by a black line on Figure 3.20. Measuring the slope of the black line is used to calibrate the trap depth based on the calculated light shift of the D1 transition (shown in Figure 3.7).

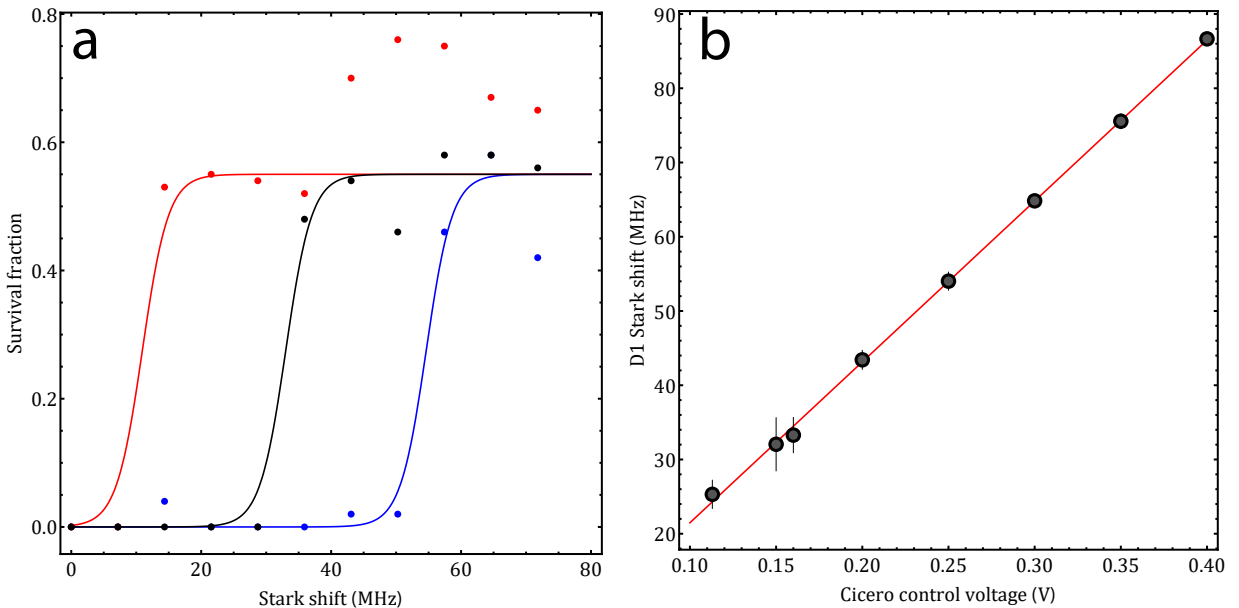


Figure 3.17: **Trap depth estimate based on D1 loading.** (a) D1 loading fraction as a function of one-photon detuning . (b) Fit to threshold one-photon detuning gives 216.664 ± 2.44 MHz/V. This predicts a trap depth of 1.13 ± 0.013 mK for the depth used in the Fig. 3.20.

The y axis on Figure 3.20(a) (originally taken in terms of sample-and-hold voltage) is converted into frequency units by independently shifting the frequency of the D1 light at the atoms using a single pass AOM. First, we fix the trap power at 1.14 mW and then scan the loading frequency (in units of sample-and-hold voltage) to reveal a jump in loading efficiency (from 0 to 50%) where loading just begins. We then *independently* shifted the one photon detuning using the single pass AOM in our setup and repeated

the measurement for various detunings. We observe a shift in the loading curve as a function of *known* AOM frequency shifts and use this to calibrate the frequency axis on Figure 3.20(a). Having calibrated the frequency axis we calculate the slope of the black line and use this to estimate corresponding trap depths based on light shift calculations depicted in Figure 3.7 (which predict a differential shift of 30 MHz/mK of the D1 transition). This calibration predicts a trap depth of 1.13 ± 0.013 mK for the standard trap power (1.14 mW) used (as indicated by the vertical orange dashed line in 3.20(a)) for experiments described for the rest of the chapter.

- **Directly scattering photons on the D2 transition**

As a supplement to estimated trap depths based on the D1 transition we now directly scattering photons on the D2 transition and use this to estimate the trap depth that corresponds to a given trap power. Here, we measure the differential Stark shift for a fixed depth by scattering photons at varying detunings while keeping the imaging intensity fixed at **3.6** I_{sat} (combined repump and cycling). We based the determined scattering rate from the number of photons collected in post-selected images (those determined to contain a single atom) and fit the data collected to a single atom scattering

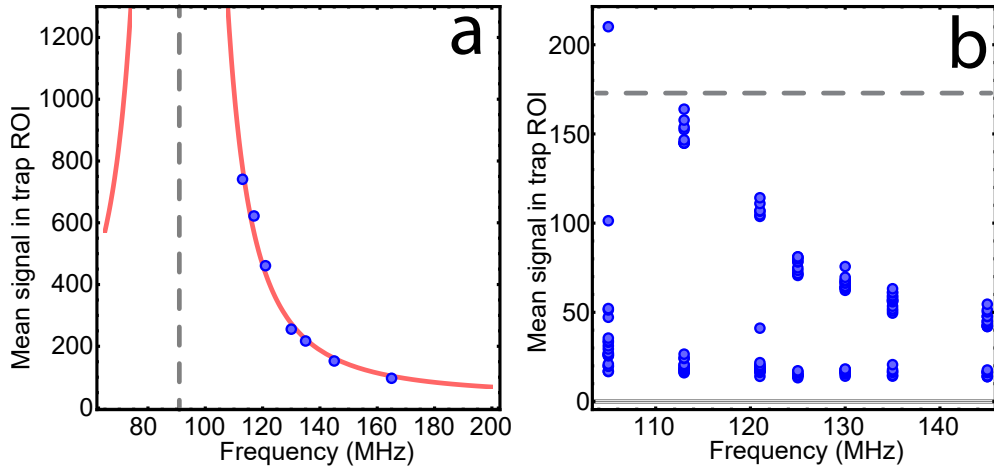


Figure 3.18: **Trap depth estimation.** (a) Scattering rate as a function of detuning is used to determine the light-shifted resonance frequency which is then used to estimate the trap depth based on Stark shift calculations (b) Unaveraged unsubtracted signal in the trap region-of-interest. The signal above background increases as the detuning approaches resonance and the atom begins to get lost below 115 MHz.

rate [59]

$$R_{\text{scattering}} = \frac{3\pi c^2}{2\hbar f_{\text{D}2}^3} \left(\frac{\Gamma_{\text{D}2}}{\Delta} \right)^2 \times I(0, 0) \quad (3.6)$$

where $\Delta = \omega - \omega_{\text{res}}$ is the detuning from resonance and ω_{res} is a fit parameter. Here, the ω_{res} extracted is a direct measurement of the trap-induced differential light shift.

Figure 3.18 shows single atom scattering rates as a function of imaging beam frequency measured for a trap power of 2.28 mW (which corresponds to twice the depth used in the D1 calibration above). Based in equation 3.6 we extract $\omega_{\text{res}} = 90.94 \pm 0.63$ MHz (Similar measurements at half the trap power yields $\omega_{\text{res}} = 43.29 \pm 1.79$ MHz). Here, 0 MHz corresponds to the resonant frequency in free space. The light used for in-trap imaging is separated from light optimized for free-space fluorescence imaging by the double-pass AOM. The frequency shift required to image an atom in the trap therefore gives an estimate of trap induced light shift.

Assuming a differential light shift of 28 MHz/mK as calculated in Figure 3.7, these measurements suggest a trap depth of 1.571 ± 0.032 mK for a trap power of 1.14 mW. We note that this represents a $\sim 50\%$ disagreement with the calibration based on D1 cooling. On its own, the D2 light shift calibration is more sensitive to errors based on the assumed position of the free-space pole (stemming from some uncertainty about the correspondence between the polarization spectroscopy lock-point and the $F = 2 \rightarrow F'' = 3$ transition), which is why we rely primarily on the D1-based calibration.

There are two other assumptions that underly both calibrations. One is that the measured light shifts reflect the atomic response at the highest intensity point in the trap, which is not strictly true at the temperatures explored. This issue could revise both calibrations slightly, potentially in different directions. Finally, both calibrations are strongly dependent on our calculated ground and excited state polarizabilities. Any refinement of those calculations would modify the calibrations.

3.6 Enhanced loading: the biased coin-flip

3.6.1 Background: Blue-detuned inelastic light-assisted collisions

As first demonstrated in Ref. [108] blue-detuned light can be used to enhance optical tweezer loading efficiency. Consider two atoms each in the ground state, $4S_{1/2}$, approaching each other. As shown in Figure 3.19 we represent the scenario in terms of a two-atom potential $|4S_{1/2}, 4S_{1/2}\rangle$. At some Condon point, r_c , a blue-detuned light ($\hbar\omega_L$) will be resonant with a repulsive molecular state $|4P_{1/2}, 4S_{1/2}\rangle - |4S_{1/2}, 4P_{1/2}\rangle$. In the presence of the blue-detuned light the atom pair will be photoassociated to the molecular state.

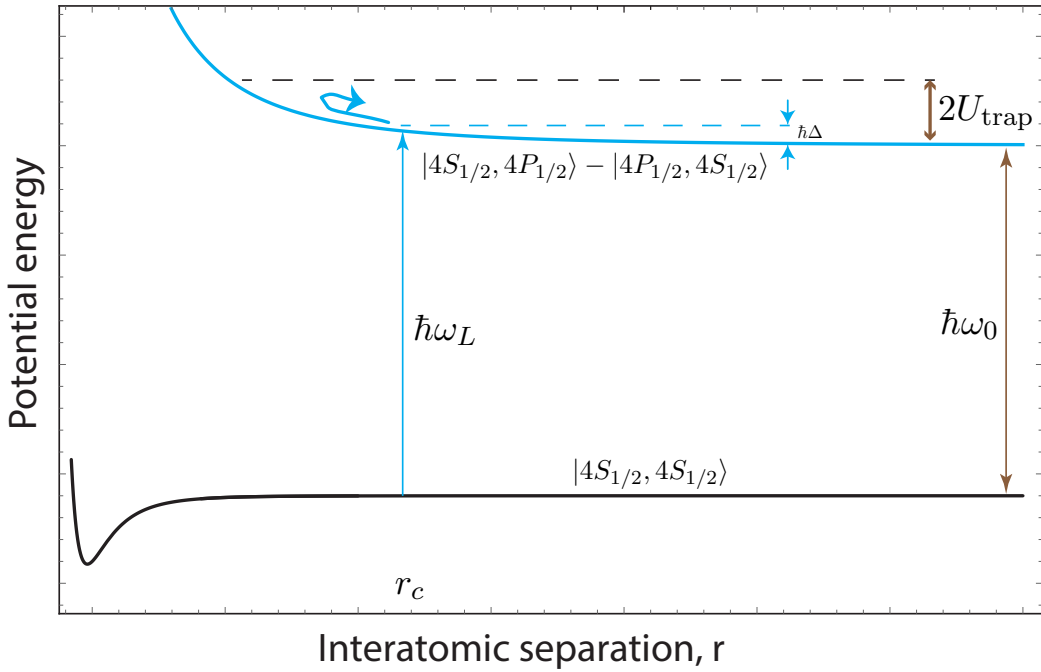


Figure 3.19: **Blue-detuned inelastic light-assisted collisions.**

In contrast to attractive light-assisted collision explained on Figure 3.13, the amount of energy gained by the atom pair, $\hbar\Delta = \hbar(\omega_L - \omega_0)$ depends on the detuning of the beam used and can therefore be controlled. The atoms once excited to the repulsive molecular potential move past the Condon point and slosh back again. If the energy absorbed by the pair is enough to expel both atoms from the trap, *i.e.* when $\hbar\Delta > 2U_{\text{trap}}$, the loading efficiency is limited to 50%. However, by tuning $\hbar\Delta$ so that the energy absorbed is just enough to expel one atom but not both from the trap we can increase the loading efficiency of the trap. For

this technique to work, a finite center-of-mass motion is necessary. Here, unequal kinetic energies between the two atoms ensures that the hotter atom is lost from the trap after the pair is excited to the molecular potential.

3.6.2 Enhanced loading in an optical tweezer

Even though we observed earlier that no more than 1 atom could be loaded into shallow and tight traps, the loading efficiency can still be increased above 50% using blue-detuned light-assisted collisions. In this section we study loading conditions of an optical tweezer using Λ -enhanced gray molasses cooling and confirm that the loading efficiency can indeed be increased by appropriately controlling the detuning of the D1 beams.

General experimental procedure

The experiments begin by transferring atoms from a continuously-loaded octagon chamber MOT into the science chamber MOT using a blue-detuned beam pulsed on for 200 μ s. After a 20 ms time-of-flight (over 54 cm distance between the MOTs) atoms are loaded in the science chamber MOT. The atoms are initially cooled down towards the Doppler limit using a detuned-MOT stage (where MOT beam parameters are varied to increase the phase-space density of the atomic cloud). While it is customary to implement a sub-Doppler cooling stage using red-detuned D2 molasses, this stage does not work very well for us. Instead we implement a Λ -enhanced gray molasses cooling/loading stage right after the detuned MOT stage. Here the magnetic field gradient is turned off and 770 nm (D1) beams are switched on for 100 ms to initiate loading into the optical tweezer. The D1 cooling beams consist of a pump ('cycling') and repump beams where the repump intensity is 1/3 of the cycling and is blue-detuned by 461.7 MHz to address the $F = 1 \rightarrow F' = 2$ transition.

During the loading stage, the D1 beams are also further blue-detuned from resonance than necessary in free-space to compensate trap-induced light shifts and enable in-trap cooling of single atoms. A 30 ms hold time is added after loading to allow 3D MOT atoms to fall under gravity. We then turn on the D1 molasses beams for 10 ms to 'clean up' the trap occupancy. Here the D1 beams are ramped to a detuning and intensity optimized for parity projection

and in-trap cooling. The remaining atoms are then imaged for 150 ms using a small (\varnothing 1 mm) beam while keeping the D1 molasses cooling beams on to overcome heating from the imaging beam. Even though the same signal-to-noise ratios can be achieved for shorter imaging durations by increasing the scattering rate of the atom (detuning the imaging beam closer to resonance or increasing intensity) high scattering rates lead to increased probability to lose the atom.

Loading studies

Our D1 laser preparation set up initially consisted of a double-pass AOM system for frequency tuning. While this set up is enough for both free-space cooling and loading single atoms into shallow traps, the relatively small frequency bandwidth of a double-pass system (\approx 30 – 50 MHz) makes it difficult to scan D1 detuning over a wide range.

To address this issue we use the sample-and-hold feature of the 770 nm DL Pro laser that supplies our D1 light. Here a TTL signal can be sent to the laser to *pause the lock* and allow the laser current to be scanned using an analog voltage input. Scanning the laser current corresponds to a change of the laser frequency with respect to the original lock-point and therefore allows us to effectively scan over a wide range of detunings only limited by the mode-hop free tuning range (\approx 10 GHz). Additionally, shifting the detuning using sample-and-hold does not lead to any change in laser power. This enables us to separately study the effect of the D1 laser detuning without changing the beam intensity at the atoms. We replace the original double-pass system with a single-pass AOM which is used to not only rapidly switch on the D1 light at the beginning of the loading stage. This AOM can also be used to separately study the dependence of loading on the intensity of the D1 beams.

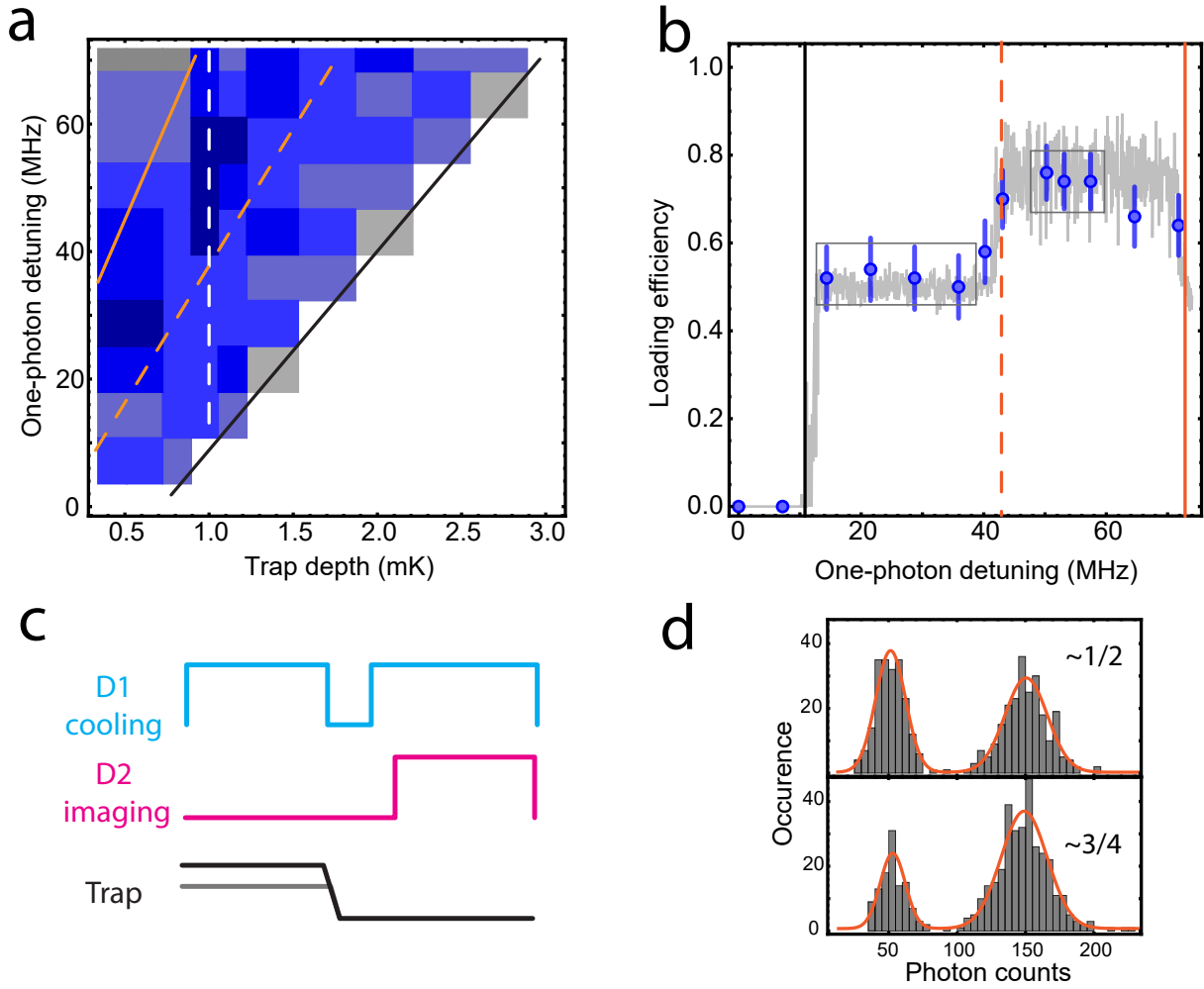


Figure 3.20: **Gray molasses loading of an optical tweezer.** (a) Loading efficiency at different trap depths as a function of Λ -enhanced GM one-photon detuning. Black line indicates linear a linear light shift of the $F = 2 \rightarrow F' = 2$ transition induced by increasing trap power. Above this line cooling beams are blue-detuned and gray-molasses works for atoms in the trap. The orange line indicates one-photon detuning (Δ) corresponding to twice the trap depth. Right below this line light-assisted collisions preferentially cause loss of one atom. (b) Loading efficiency taken at ≈ 1.13 mK (white dash in (a)) as a function of Λ -enhanced GM one-photon detuning. Below 12 MHz no loading takes place because cooling beams are red-detuned from light-shifted D1 transition. The loading efficiency jumps to $\approx 50\%$ once cooling beams are blue-detuned (black solid line). At one-trap depth (orange dashed line), the amount of energy absorbed by an atom pair during collision is only enough to eject one atom thus increasing the loading efficiency. Gray fit corresponds to a Monte-Carlo simulation of atom pair loss. (c) Experimental sequence for GM loading an optical tweezer. D1 cooling beams are turned on for 150 ms to load atoms at a specific trap depth and Δ . The beams are turned off for 40ms to let MOT atoms disperse and turned on briefly before imaging to ensure only one atom remains in the trap and cool it before imaging. Cooling beams are left on during imaging to prevent loss. (d) Histograms indicating enhanced loading efficiency (75%) when the one-photon detuning is set to $U_{\text{trap}} < 2\pi\hbar\Delta < 2U_{\text{trap}}$ above the light-shifted resonance. These histograms were plotted using data indicated by gray rectangles.

To study loading properties we set the trap depth to some value (between 0 and 4.5 mK) and vary the detuning of the D1 molasses beams during the loading stage. The D1 beams are switched off right after loading followed by ramping the trap depth back to ≈ 1 mK for imaging. Turning off the beams is necessary to prevent the D1 beams from heating the atom while the trap depth is changing. After letting MOT atoms to disperse we switch on D1 beams optimized for cooling and parity-projection for 10 ms before turning on the imaging beam to scatter photons for 150 ms.

As shown in Figure 3.20 (a,b) single atoms can only be loaded into the trap when the D1 beams are blue-detuned with respect to $F = 2 \rightarrow F' = 2$ transition. For each trap depth we observe a jump in the fraction of atoms loaded into the trap from 0 to 50% as we further detuning the D1 beams. Specifically, Δ in this region is less than the trap depth and the energy absorbed by the atom pair during photoassociation is not enough to expel any atom. Both atoms are removed from the trap during the pre-imaging parity projection stage. As we increase the trap depth (by varying the trap power) we find that further detuning is necessary to begin loading the atoms into the trap. The linear dependence (shown by the black line) between the one-photon detuning and the trap depth observed is a direct measurement of the linear light shift due to the 780 nm tweezer i.e. I/Δ_{trap} as we increase the trap power. As discussed previously, this measured line is in fact used to calibrate the depth of our optical tweezers.

Figure 3.20(b) shows loading efficiencies in a fixed trap depth (≈ 1.13 mK) as a function of Δ . Here we observe a clear increase in loading efficiency above 50% when $\Delta > U_{\text{trap}}$ above the light shifted resonance. Specifically, the amount of energy absorbed during photoassociation is enough to remove just one of the two atoms as long as the initial total energy of the pair is unevenly distributed between the atoms. We report a maximum loading efficiency of 76% at ≈ 1.13 mK evaluated over 110 experimental shots. Above the white line in Fig. 3.20(a) the loading efficiency drops back down to 50% since the energy absorbed is enough to eject both atoms from the trap.

3.7 Cooling and non-destructive imaging

In this section we demonstrate cooling of trapped single atoms based on Λ -enhanced GM. The temperature of atom is probed based on two techniques: (1) A release-and-recapture technique where the trap is briefly switched off for a couple of μs . The recaptured fraction when the trap is switched back is a measure of temperature. (2) A rampdown technique is also used to probe temperature. Here, the trap depth is ramped down to some low value to allow the atom to escape if its initial energy is higher than the lowest trap depth reached. Work in this section was done in direct collaboration with Chenxi Huang.

3.7.1 Release-recapture temperature measurement

The goal of our experimental apparatus is to prepare single atoms in optical tweezers and excited these atoms to Rydberg states for quantum simulation. Since excited atoms in Rydberg states are automatically removed from the trap (since Rydberg states are strongly anti-trapped) it is customary to switch off the trap during Rydberg excitation and subsequent experiment. The traps are then switched on at the end of the experiment once the atoms are transferred back to the ground state where a second image is taken. Given Rabi rates of $\mathcal{O}(\text{MHz})$ and Rydberg interaction strengths in the MHz range demonstrated in other groups, our entire Rydberg-based experiments are expected to take place within a couple of μs . We investigate the recapture probability of a single atom upon turning off the trap for a varied amount of time not only as a measure of temperature but to also increase the chances of recapturing the atom without performing any experiments during the release time. With higher survival fractions we expect to be able to run longer experiments before recapture in addition to acquiring more statistics for some fixed number of runs. The survival probability after release and recapture is therefore an important figure-of-merit.

To demonstrate cooling using Λ -enhanced GM cooling, we consider three cases.

- No cooling case: a first image is taken (50 ms exposure time) to confirm the presence of an atom before switching the trap off for a varied duration.
- Static cooling case: After taking the first image a static cooling block is included where

GM cooling beams are turned on for 100 ms at a fixed power optimized for cooling at the specific trap depth used.

- Dynamic cooling: Here we append an extra cooling block to the 100 ms imaging block where the GM cooling beam power is ramped down to some low value over 20 ms before the trap is switched off and on for a varied duration of time.

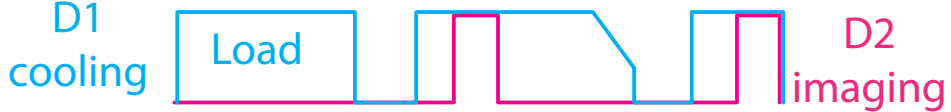


Figure 3.21: Dynamic, in-trap gray molasses cooling sequence.

A 50 ms cooling stage is included before each imaging stage to improve imaging fidelity. While the recapture probability falls quickly without any cooling (50% recapture at $\approx 6 \mu\text{s}$) we observe an immediate improvement for the static cooling case. Here the survival probability for $7 \mu\text{s}$ release time jumps up to $\approx 70\%$. Reminiscent of GM cooling in free space, we include a cooling stage where the power in the cooling beam is ramped down to reduce heating due to re-absorbed photons. By ramping down the power for 20 ms, the survival probability dramatically ($\approx 100\%$ at $\approx 6 \mu\text{s}$) increases in comparison to the first two cases considered. While this timescales would already allow for some reasonable time for Rydberg-based experiments, we note the one can also significantly increase the "recapture time" by adiabatically lowering the tweezer depth prior to release.

Temperature fits

To estimate the temperature of the atom for the three cases we implement a Monte-Carlo simulation. Here we consider a single atom in a $\approx 1.13 \text{ mK}$ trap with some initial position and velocity. The initial position is drawn from a Gaussian distribution with standard deviation given by $\sigma_z = \sqrt{\frac{k_B T}{m\omega_z^2}}$ and $\sigma_r = \sqrt{\frac{k_B T}{m\omega_r^2}}$ in the axial and radial directions respectively. Here ω_i is the trap frequency in the i^{th} direction, m is the mass of the atom and k_B is the Boltzmann constant. The initial velocity is also drawn from a Gaussian distribution with $\sigma_v = \sqrt{\frac{k_B T}{m}}$. The atom is evolved for some time t using kinematic equations of motion and the final total

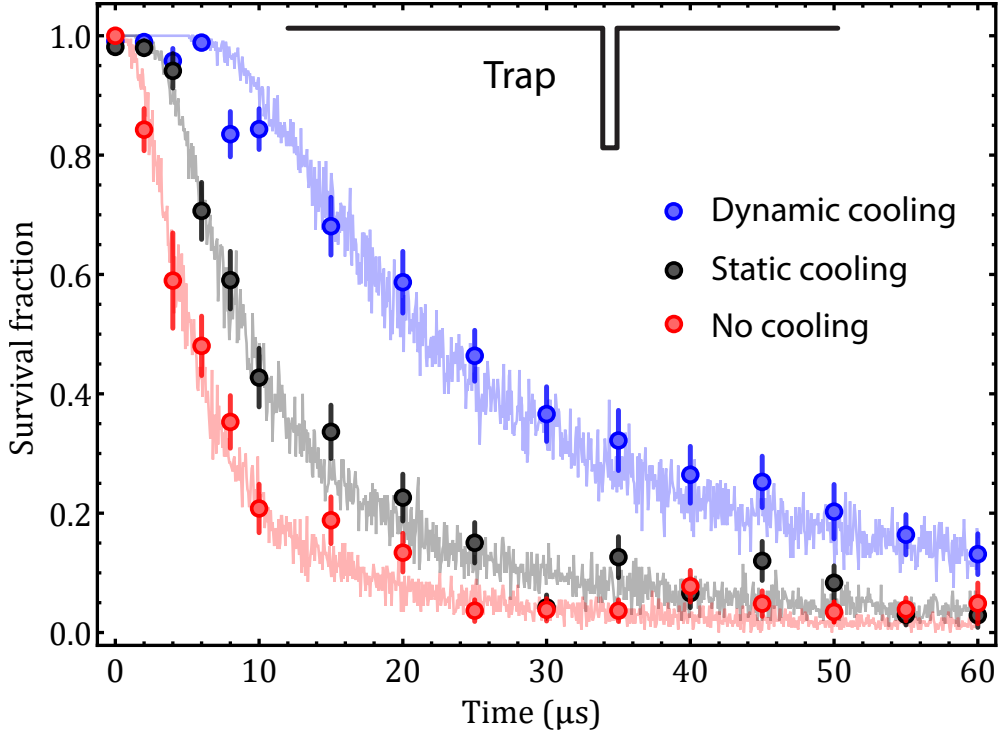


Figure 3.22: **Release-and-recapture technique.** Three scenarios are considered. Red, imaging the atom twice without any cooling. Black, adding a 100 ms static GM cooling block at fixed power and detuning. Blue, Adding a static cooling block and an additional time step where the cooling beam powers are ramped down to low values. All error bar corresponds to one standard error of the mean.

energy is calculated. Specifically the total energy is a sum of the kinetic energy of the atom and the potential energy due to trap potential (which includes modification due to gravity). If the total energy of the atom is larger/smaller compared to the trap depth ($\approx k_B \times 1.13$ mK) the atom is considered lost/re-captured and a trap occupation of 0/1 is assigned. We repeat the simulation 1000 times for each release time and average out the outcomes to obtain a survival probability.

The temperature is now estimated by running the simulation for a varying range of T to obtain survival probability curves as a function of time, followed by a least-square analysis to find the best fit. Based on these fits we extract temperatures of $16.2 \mu\text{K}$, $55.2 \mu\text{K}$, and $120.5 \mu\text{K}$ for the dynamic, static and no cooling cases. We note that lower temperatures can be (and recently have been [64]) achieved through careful Raman sideband cooling. However, some benefit lies in the simplicity of our implemented GM cooling. Specifically, we use the same optical set up used during free-space and only need to adjust the beam frequency to

compensate for trap induced light shifts. Beam frequency shifting is ridiculously easy due the sample-and-hold feature of the Toptica DL PRO laser that supplies cooling light.

3.7.2 Rampdown temperature measurement

Even though the release-and-recapture technique is necessary to benchmark the performance of in-trap gray molasses cooling as will be relevant during Rydberg excitation, it is less sensitive to temperature in the axial direction. As proposed in Ref. [123, 124] the temperature of an atom can be measured through a rampdown technique where the trap is adiabatically lowered to low variable trap depths for enough time for the atom to potentially escape before raising the depth again to image the atom. In essence, lowering to some minimum trap depth U_{esc} the atom would escape if its initial energy (or equivalently temperature) is higher than U_{esc} .

We implement this technique in experiment for the three different conditions already investigated in Section 3.7.1. Specifically, after the cooling stage the trap depth is lowered from ≈ 1.13 mK to some minimum depth U_{esc} for 2 ms, the trap is then kept at U_{esc} for 20 ms before being raised back to ≈ 1.13 mK for 2 ms. A second image is taken to determine whether the atom was lost. To minimize trap loss due to imperfect imaging fidelities a 50 ms cooling block is added before each imaging timestep. By varying U_{esc} and taking ≈ 180 shots per data point the survival fraction starts out at 1 and then begin to fall at lower trap depths.

While the data was initially recorded in terms of trap power we re-calibrate the x -axis following the procedure in Ref. [123, 124] in order to extract temperature fits as explained in more detail in Section 3.7.2.

Since the atom will escape only when its initial energy was higher than U_{esc} , we expect the survival fraction to remain high for lower trap depths when the atom temperature of the atom is low. In other words, higher survival fraction at low trap depths corresponds to lower initial temperatures of the atoms prior to the rampdown.

As we already established using release-and-recapture measurements, dynamic cooling outperforms the static and no cooling case. In particular, while the atom begins to escape

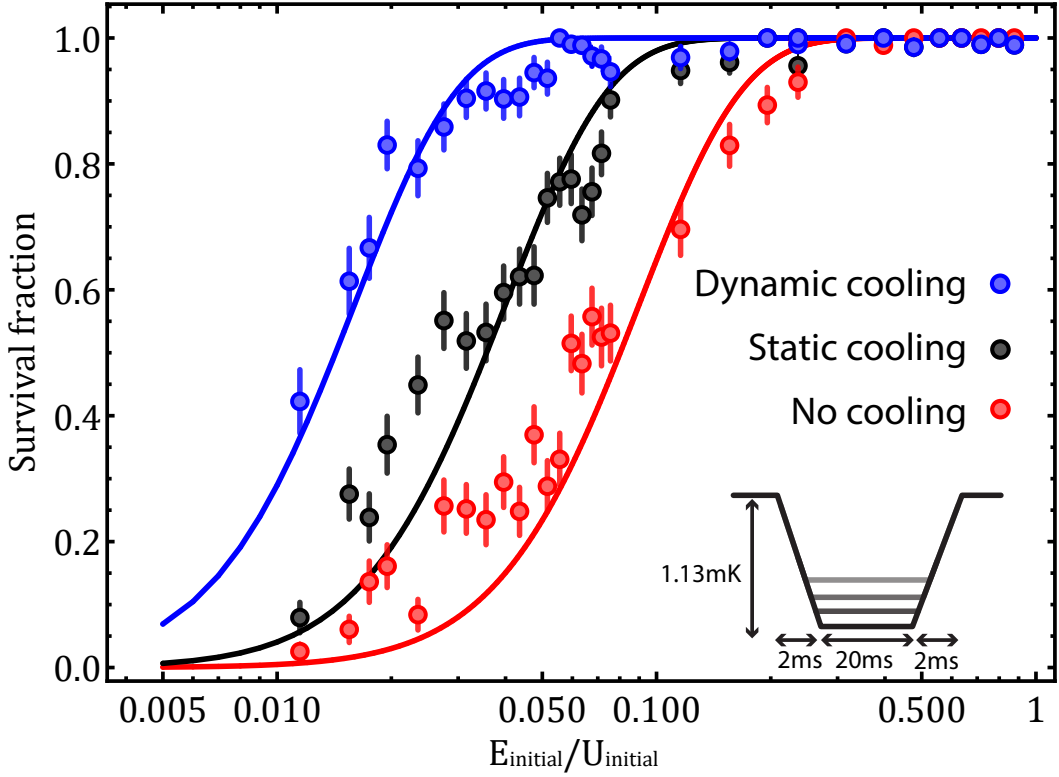


Figure 3.23: **Temperature measurement using rampdown technique.** Fits correspond to $T = 38.8 \mu\text{K}$, $98.9 \mu\text{K}$ and $160.9 \mu\text{K}$ for dynamic cooling (blue), static cooling (black) and no cooling (red).

at $\frac{2}{10}U_{\text{initial}}$ and $\frac{1}{10}U_{\text{initial}}$ for the no cooling and static cooling case, we observe a clear improvement using dynamic cooling. Here the loss begins to happen for $\frac{3}{100}U_{\text{initial}}$ which is an order of magnitude better than the first two cases!

This measurement is at least in qualitative agreement with the release-and-recapture technique where we learn that dynamic cooling seems to considerably lower the temperature of the atom as compared to not cooling at all while static cooling block is certainly better than not cooling at all.

Rampdown model for fitting the data

Temperature estimation using the rampdown techniques relies on the fact that the final trap depth at which the atom escapes U_{esc} will be a function of the initial total energy E_{initial} of the atom only if the trap depth is adiabatically lowered. Since the action $S = \oint pdx$ does

not change under adiabatic variation of the trap, the action at U_{esc} can be mapped back to the action before ramping down, i.e.,

$$S(E_{\text{initial}}, U_{\text{initial}}) = S(E_{\text{esc}}, U_{\text{esc}}) = S(U_{\text{esc}}, U_{\text{esc}}) \quad (3.7)$$

where

$$S(E, U) = \int_0^{x_{\max}} dx \sqrt{2m(E - V(x, U))} = \text{constant}. \quad (3.8)$$

and $E, V(x, U)$ and U are the total energy, the trap potential and max trap depth, respectively. x_{\max} is the position at which the trap potential is equal to the total energy of the atom i.e. $V(x_{\max}, U) = E$ as pictorially shown in Figure 3.24.

While calculating the action we account for the effect of gravity on the trap potential, which becomes significant for very low traps depths i.e. ($\approx 1 \mu\text{K}$). The data taken is expressed in terms of the final depth normalized to the initial depth. The standard approach for extracting temperature from rampdown measurements involves re-calibrating the x -axis in Figure 3.23 (using Eq. 3.7) so that the data is expressed in terms of the initial energy, E_{initial} .

We follow the mapping procedure outlined in [123, 124], i.e.,

- Calculate $S(U_{\text{esc}}^*, U_{\text{esc}}^*)$ and $S(E_{\text{initial}}, U_{\text{initial}})$ separately. Here U_{esc}^* corresponds to a specific final depth used during the experiment.
- From the curve $S(E_{\text{initial}}, U_{\text{initial}})$, find which E_{initial}^* that corresponds to a chosen U_{esc}^* and create a tuple $\{E_{\text{initial}}^*, U_{\text{esc}}^*\}$
- Repeat across all depths $0 \rightarrow U_{\max}$. Normalize both axes by U_{initial} ⁹ et voilá!

With the x -axis re-calibrated we can extract the temperature by fitting the measured survival probability to

$$P_{\text{survival}}(E, T) = \int_0^E f_{\text{M-B}}(E) dE \quad (3.9)$$

which is an integral over the Maxwell-Boltzmann distribution of the temperature of the

⁹we interchangeably use U_{initial} and U_0

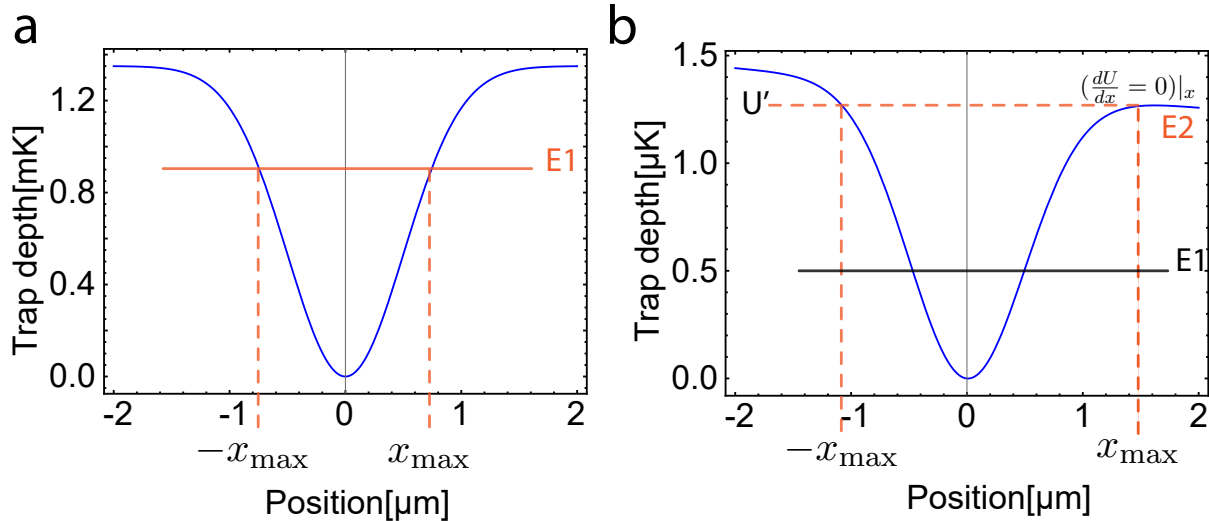


Figure 3.24: Calculating x_{\max} for a potential with/without gravity.

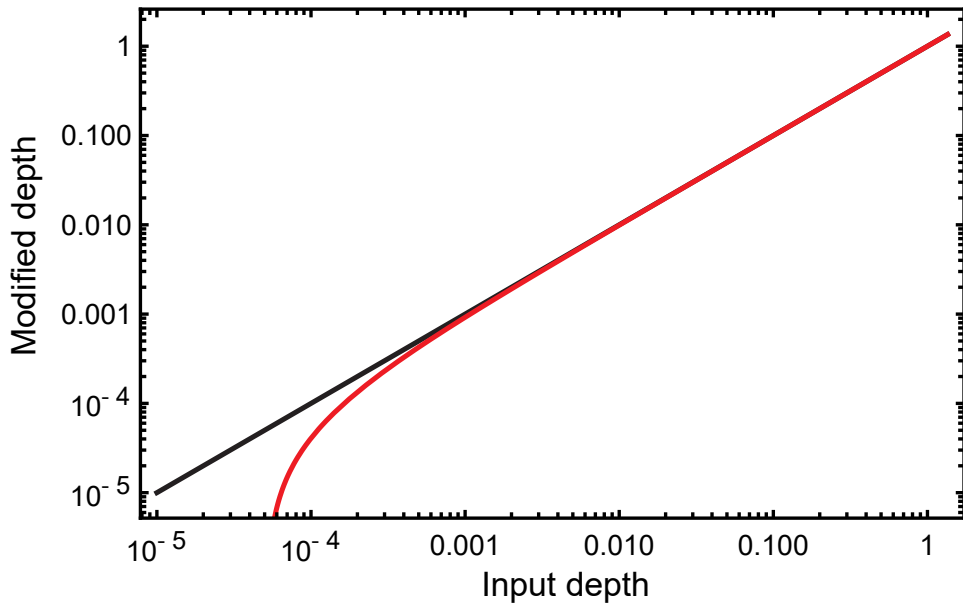


Figure 3.25: Deviation due to gravity.

atom,

$$f_{\text{M-B}}(E) = \frac{E^2}{2(k_B T)^3} \exp(-E/k_B T). \quad (3.10)$$

Based on these fits we extract temperatures of $T = 38.8 \mu\text{K}$, $98.9 \mu\text{K}$ and $160.9 \mu\text{K}$ for dynamic cooling (blue), static cooling (black) and no cooling (red) as shown in Figure 3.23. We note that these are preliminary estimates, that might change based on updated analysis.

We attribute the disagreement between these two methods to the fact that the release-recapture technique is not sensitive to temperature in the axial direction. A higher temperature in the axial direction therefore leads to higher overall temperatures estimated. In a typical experiment extra cooling is achieved by adiabatically lowering the trap right before switching it off for Rydberg excitation. In particular, the thermal distribution of the atom shrinks following roughly $T \propto \sqrt{U_{\text{initial}}}$ when the trap is lowered to some minimum trap U_{esc} leading to adiabatic cooling. As investigated in Ref. [64], the recapture probability for a ^{39}K atom is expected to increase with adiabatic cooling. We do not confirm this in our system but will certainly include it in future experiments.

3.7.3 Non-destructive interleaved imaging

To study the dynamics of the atom, typical experiments involve imaging multiple times. This allows for, e.g., post-selection or even sorting of atoms by on-the-fly feedback. Since most of our experiments involve measuring the survival probability of the atom during experiment, the likelihood to lose the atom during imaging will reduce the quality of data taken.

Typical loss of the atom happens due to heating from the imaging beam or due to one-body loss processes where background gas particles can knock the atom out of the trap. In this section we explore the prospects of interleaved imaging in our system where the imaging beam is chopped on and off while the cooling beam is left on throughout. Specifically, we implement 160 imaging repetitions where each imaging block consists of a 50 ms imaging duration (with both GM cooling beams and the imaging beam left on) followed by a 50 ms cool-off stage, where the imaging beam is switched off while the cooling beam is left on to mitigate heating effects from the first stage. The camera is exposed during the first imaging stage to record the presence of an atom. To benchmark the performance of this imaging scheme we repeat the same experiment without a cool-off stage. In particular, for each imaging repetition **both** the imaging beam and the cooling beam are left on and the camera is exposed for the first 50 ms. This measurement is a direct probe for lifetime under continuous imaging.

For continuous imaging (in red) the survival fraction begins to fall exponentially for the

first ≈ 3.5 s before a new loss mechanism kicks in and a second decay rate turns over the curve. We attribute the turn over point to the fact that the atom gets heat up during the first seconds of imaging and rises up the trapping potential. As the atom moves up the potential the effective detuning of the imaging beam decreases so that the imaging beam appears to move closer to resonance. This is accompanied by increased scattering and heating rates from the imaging beam which further heats up the atom leading to faster loss from the trap.

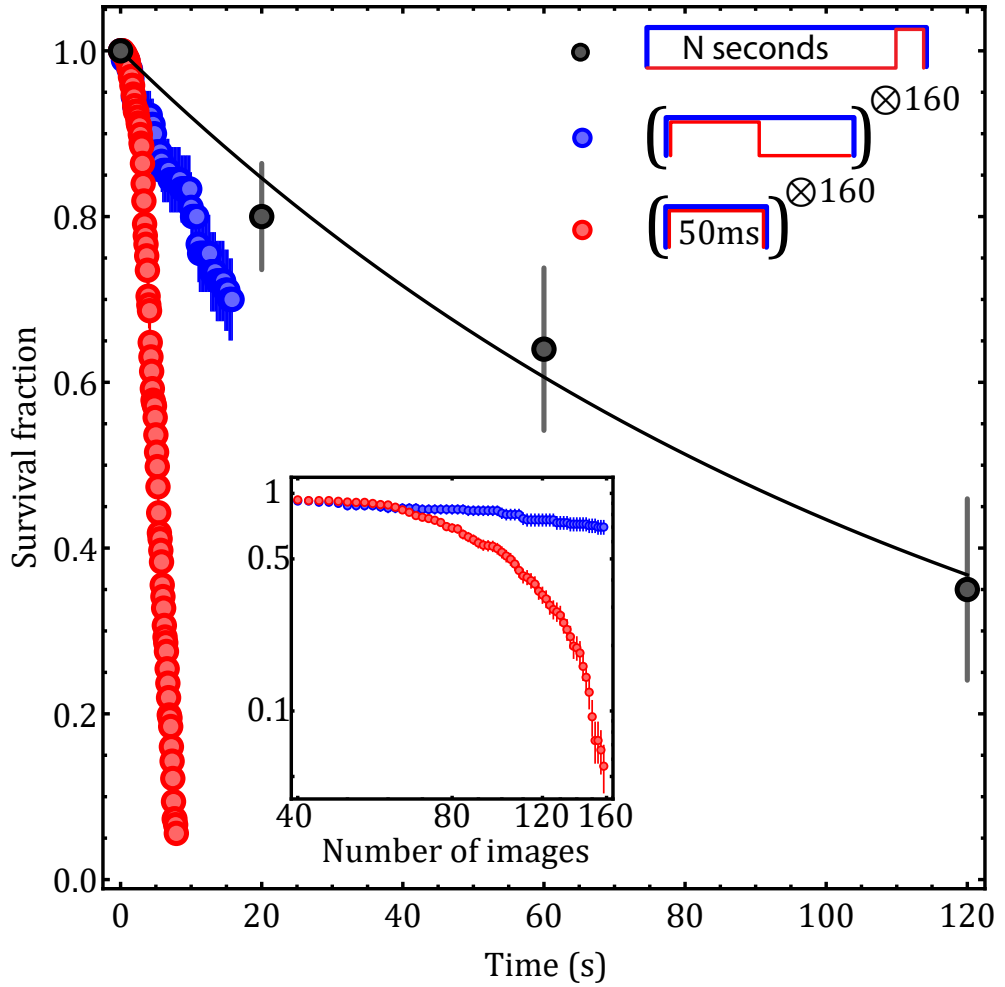


Figure 3.26: Low-loss imaging. Plot of the survival fraction of post-selected atoms in a ≈ 1.13 mK-deep trap under repeated imaging (red), repeated imaging with interleaved fixed GM cooling (blue), and holding in the trap with fixed D1 GM (black). In each case, non-destructive imaging is performed in 50 ms-long blocks. The ~ 2 minute decay of the black points serves as a lower limit on the vacuum lifetime, but is perhaps shorted due to thermal loss under the steady-state D1 GM conditions. Inset: log-log scale plot of survival fraction vs. number of imaging blocks. For continuous imaging, survival probability reaches $\sim 50\%$ after 100 imaging blocks (5 s of scattering). By introducing fixed interleaved cooling, we find that the survival probability remains above $\sim 70\%$ after 160 imaging blocks.

This behavior is mitigated in the interleaved cooling scheme because every time the atom gets heated up during scattering, it is cooled back down in the second half of the imaging block. The atom therefore remains low enough in the trap potential to roughly experience a uniform scattering rate in each imaging block and the sudden drop-off in survival fraction at 3.5 s does not happen. Even though the ability to image 130 times with a 50 ms imaging block before the survival fraction falls to 35% at our high scattering rate of 140 kHz is already a testament of in-trap GM cooling efficiency, interleaved cooling allows us to keep the atoms around for much longer. In the case of inter-leaved cooling, we are able to acquire 158 images before the survival fraction falls below 70%.

In an extra analysis, we compute an imaging fidelity, i.e, the likelihood to not lose an atom after each imaging block by solving ($x^N = P_{N,\text{survival}}$) where $P_{N,\text{survival}}$ is the survival probability after N -th image. While the fidelity drops with each subsequent imaging for the continuous imaging case (in red), we demonstrate a sustained imaging fidelity of $\approx 0.998\%$ over all the 160 images taken.

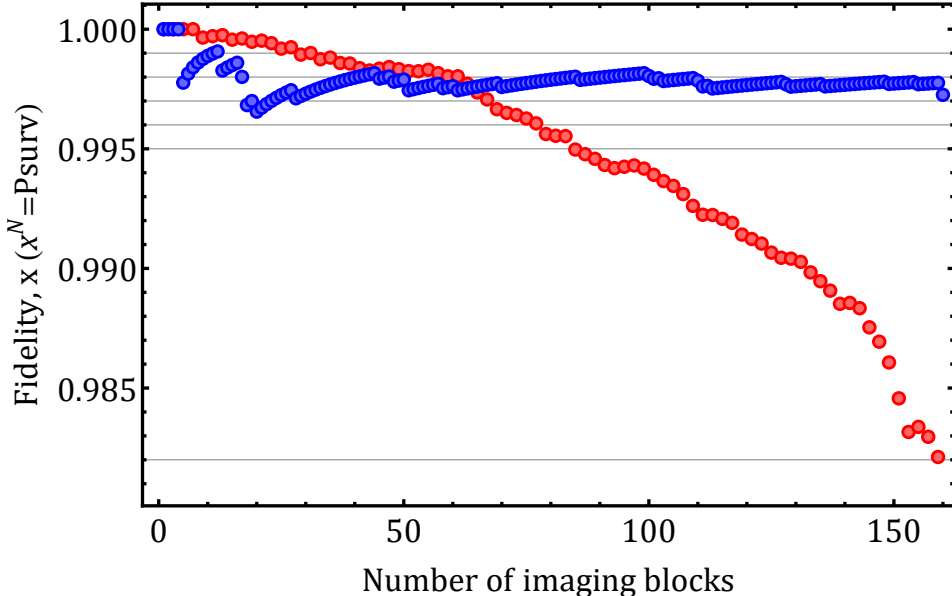


Figure 3.27: **Imaging fidelity with interleaved cooling.** For continuous imaging (in red) imaging fidelity continuously decreases throughout while for interleaved cooling (blue), we sustain an imaging fidelity of $\approx 0.998\%$ over all the 160 images taken.

3.8 Conclusion

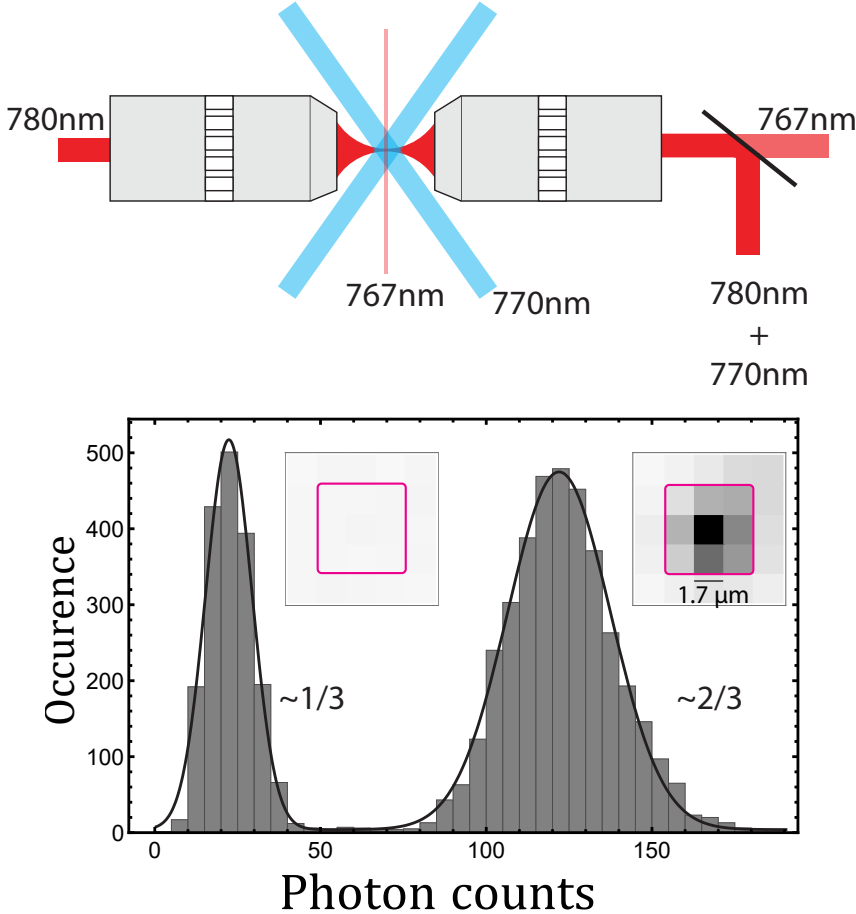


Figure 3.28: Histogram showing high detection fidelity of potassium atoms in optical tweezers. **Top.** Sketch of the experimental set up. One high-NA objective delivers optical tweezer light (780 nm, dark red). A small D2 scattering beam (767 nm, light red) aligned perpendicular to the imaging axis is used to scatter photons that are collected using a second objective. D1 gray molasses beams (770 nm, blue) are used to cool the atoms while performing D2 imaging. Scattered fluorescence at 767 nm is collected through a second objective lens and imaged onto a camera, while the trapping and cooling light at 780 nm and 770 nm are removed through the use of narrow spectral filters. **Bottom.** A histogram of photons collected from atoms loaded to an optical tweezer, collected over 5555 experimental shots under typical imaging conditions. The histogram demonstrates good detection efficiency (>99%) and ~66% loading efficiency. The insets show the averaged image of shots determined to have zero atoms (left panel) and a single atom (right panel), with the pink square showing the region used for photon counting. This histogram is based on atoms loaded into an optical tweezer with a trap depth of $U/k_B = 1.13$ mK, and the duration of exposure for these images is 50 ms.

In our experiment, we demonstrate preparation of single potassium atoms in optical tweezers for the second reported time in general. We show that simple and robust loading, cooling and imaging is achieved by combined addressing of the 767 nm D2 line for imaging

and cooling on the 770 nm D1 line. This configuration is made possible by moderate light shifts induced by our tweezer traps set at 780 nm, which can easily be compensated for using a double-pass AOM system. Since cooling based on Λ -enhanced GM is robust over a wide range ($\approx 5 \Gamma$) of one-photon detunings, as was established in Chapter 2, we observe that loading using Λ -enhanced GM was generally more robust. Additionally, we showed enhancement ($\gtrsim 75\%$) in loading efficiencies using Λ -enhanced GM. We further probe cooling based on the D1 line using both rampdown and release-and-recapture temperature measurement and estimate lowest temperatures of $\approx 15 \mu\text{K}$.

In a short study on the lifetime of trapped atoms in our system we demonstrate that interleaved imaging and cooling, where the imaging stage is divided into acquisition and cool-off blocks, clearly increases the lifetime under imaging compared to continuous imaging. Finally by continuously cooling the atom and only taking an image at the end, we measure a trap lifetime of at least 2 minutes.

Chapter 4

Outlook: Towards Rydberg synthetic lattices

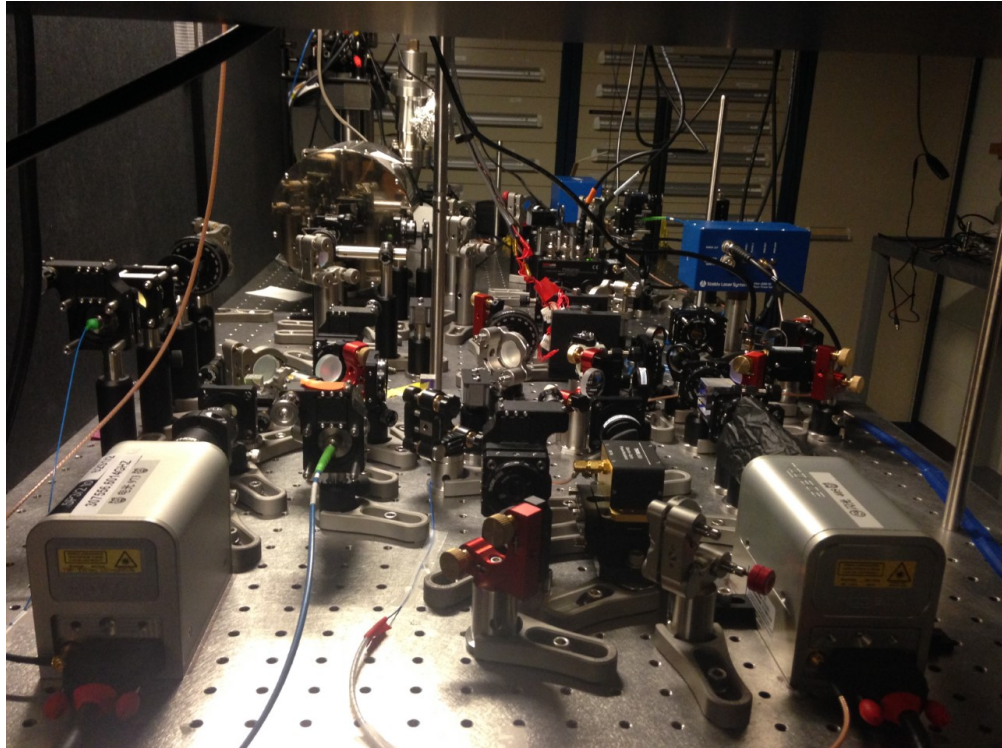


Figure 4.1: Picture of the Pound-Drever-Hall set up *ca.* 2021

4.1 Rydberg two-photon excitations

Our proposed Rydberg synthetic lattice involves population transfer to high-lying principle quantum number states (Rydberg states) followed by driving transitions between Rydberg states using microwave fields. Direct optical excitation of atoms to a Rydberg state requires optical fields in the ultra-violet (UV) range, *i.e.*, ≈ 286 nm¹ for $4S_{1/2} \rightarrow 69P_{3/2}$ in our case. Since laser sources in the UV range are difficult to acquire and work with at high powers,

¹Recent work [64] in Gross group in Tübingen has demonstrated one-photon Rydberg excitation using a 286 nm laser.

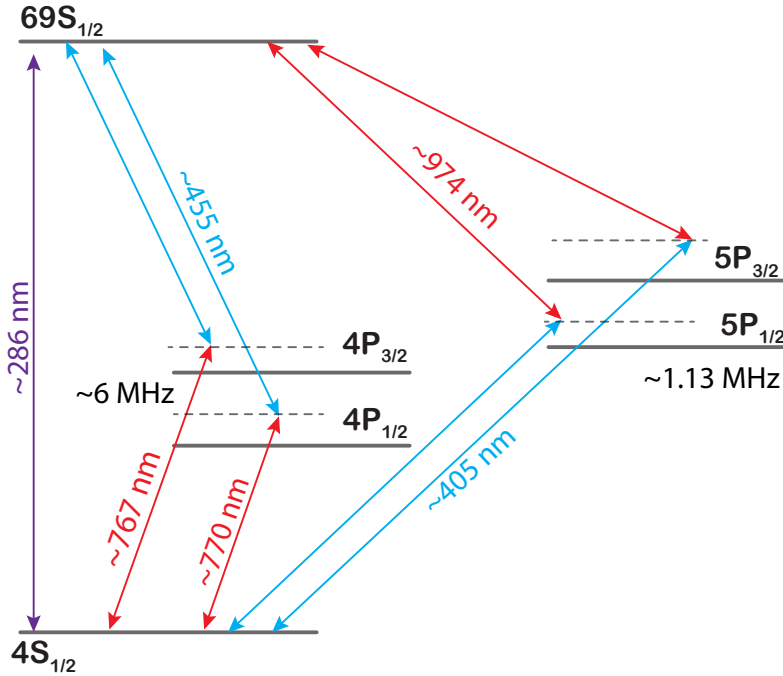


Figure 4.2: Rydberg excitation pathways.

an alternative approach involves implementing a two-photon excitation where the atom is excited to the Rydberg state via an intermediate state. Here two laser sources (both usually in the visible and near infra-red (IR) range) are used to address the two transition, *i.e.*, from ground to intermediate and from intermediate to Rydberg state. Due to a stronger coupling between the intermediate states and the ground state, any population in the intermediate state decays more rapidly to the ground state which leads to a decoherence of population transfer. To reduce population build up in the intermediate state the optical fields are detuned away from the transition by Δ . The effective Rabi oscillation of the excitation is given by $\Omega_{\text{eff}} = \frac{\Omega_1 \Omega_2}{2\Delta}$ where Ω_1 and Ω_2 are the Rabi rates associated with the first and second transition, respectively. For potassium there are two possible intermediate states as indicated on Figure 4.2: (1) Excitation using either the D1/D2 line at 767 nm/770 nm as the first transition followed by the $4P_J \rightarrow 69S_{1/2}$ at ≈ 455 nm. (2) Using $5P_J$ states as intermediate the first excitation $4S_{1/2} \rightarrow 5P_J$ using laser sources at ≈ 405 nm followed by $5P_J \rightarrow 69S_{1/2}$ at ≈ 974 nm. In our experiment we select the second option, *i.e.*, using the $5P_J$ levels as intermediate states for a two photon excitation for a few reasons. First, we consider the fact

Transition	RME (a_0e)	Transition	RME(a_0e)
$4S_{1/2} \rightarrow 5P_{1/2}$	0.275	$4S_{1/2} \rightarrow 4P_{1/2}$	4.098
$4S_{1/2} \rightarrow 5P_{3/2}$	0.406	$4S_{1/2} \rightarrow 4P_{3/2}$	5.8
$5P_{1/2} \rightarrow 69S_{1/2}$	0.013	$4P_{1/2} \rightarrow 69S_{1/2}$	0.006
$5P_{3/2} \rightarrow 69S_{1/2}$	0.018	$4P_{3/2} \rightarrow 69S_{1/2}$	0.009

Table 4.1: Reduced matrix elements calculated using ARC [125]

that the transition matrix element is a factor of 2 stronger for the $5P_J \rightarrow 69S_{1/2}$ compared to $4P_J \rightarrow 69S_{1/2}$. This stronger overlap between $5P_J$ levels with Rydberg states allow us to achieve more symmetric Rabi rates between the two transitions which is leads to increased Rabi rates (for a given intermediate state detuning, Δ).

Additionally, the relative reduced matrix elements between the two transitions in case (1) are severely uneven. For instance, the $4P_{3/2} \rightarrow 69S_{1/2}$ transition is $\frac{D_{767}^{\text{reduced}}}{D_{455}^{\text{reduced}}} = \frac{5.8a_0e}{0.009a_0e} \approx 640$ times weaker compared to $4S_{1/2} \rightarrow 4P_{3/2}$. For case (2) on the other hand, the relative transition strengths are less severe, *i.e.*, $\frac{D_{405}^{\text{reduced}}}{D_{974}^{\text{reduced}}} = \frac{0.406a_0e}{0.018a_0e} \approx 22.56$. Here D^{reduced} refers to reduced matrix element. The fact that the first transition at 405 nm is stronger is actually convenient since it is more difficult to generate high powers at short wavelengths. Even though it is difficult to acquire enough power at 405nm (due to loss at optics and cantankerous nature of 405 nm laser diodes used to supply light in a seed-follower systems), the strong matrix element for this transition allows us to work at lower powers and larger beam sizes at the atoms.

4.2 PDH locking

In this section I will describe the details of a PDH locking setup used to lock our 405 nm and 973 nm lasers in preparation for Rydberg excitation.

4.2.1 Background

Frequency stabilization for our Rydberg excitation lasers is achieved through a PDH locking technique. Here the laser frequency is stabilized using an ultra-low expansion (ULE) cavity as a reference. In particular, the laser frequency is compared to the cavity resonance frequency

whose stability can characterized by a cavity linewidth given by

$$\Delta\omega_{\text{cavity}} = \frac{\pi c}{n\mathcal{F}L_{\text{cav}}} \quad (4.1)$$

where n , c and L_{cav} is the refractive index, the speed of light and the length of the cavity, respectively. The cavity finesse, \mathcal{F} characterizes the overall quality of the cavity, and is expressed as

$$\mathcal{F} = \frac{\pi(R_1R_2)^{1/4}}{1 - \sqrt{R_1R_2}} \quad (4.2)$$

where $R_{1/2}$ refers to radius of curvature of the front and back mirror of the cavity.

When the incident beam frequency is an integer multiple of the cavity free spectral range, $\Delta\nu_{\text{fsr}} = c/L_{\text{cav}}$, the beam gets transmitted into the cavity.

The fact that the cavity transmission is symmetric (across resonance) presents a problem for frequency stabilization where laser drifts above and below the cavity resonance cannot be distinguished. By design, PDH locking avoids this issue by implementing a dispersive error signal which is asymmetric across resonance frequency. This allows for side-of-the signal locking so that frequency drifts below or above resonance are can be distinguished. More concretely, some of the light transmitted into the cavity (near resonance) leaks back out and interfere with reflected beam at the cavity input. At resonance, the leakage and reflected beams are 180° out of phase at resonance and therefore destructively interfere and suppress the total signal reflected. Close to resonance, the two beams are nearly out-of-phase and a small amount of light is reflected. The sign of the relative phase is exploited in PDH to generate a dispersive signal centered at the cavity resonance which can be used to stabilize the laser frequency.

More concretely, for an incident beam expressed as $E_{\text{incident}} = E_0 \exp\{i\omega_L t\}$, the initial reflected beam has undergoes a π phase shift while the leak-through beam consists of multiple phase components $\phi_{\text{leak}} = \frac{4\pi n L_{\text{cav}}}{\lambda}$. The reflected signal can be expressed in terms of a reflection coefficient given by

$$F(\omega_L) = \frac{E_{\text{reflect}}}{E_{\text{incident}}} = \frac{r(e^{i\omega_L/\Delta\nu_{\text{fsr}}} - 1)}{1 - r^2 e^{i\omega_L/\Delta\nu_{\text{fsr}}}} \quad (4.3)$$

where r is the reflectivity of the cavity mirrors.

An error signal can be generated from the reflected signal by phase-modulating the incident beam to create sideband frequency components, i.e.,

$$\begin{aligned} E_{\text{incident}} &= E_0 e^{i(\omega_L t + \beta \sin(\omega_{\text{mod}}))} \\ &= E_0 (J_0(\beta) e^{i(\omega_L t)} + J_1(\beta) e^{i((\omega_L + \omega_{\text{mod}})t)}) - J_{-1}(\beta) e^{i((\omega_L - \omega_{\text{mod}})t)} \end{aligned} \quad (4.4)$$

where J_m is the m -th order component of a Bessel order of the first kind and β is the modulation index. The total reflected signal upon reflection is expressed as [126]

$$\begin{aligned} |E_{\text{reflect}}|^2 &= P_c |F(\omega_L)|^2 + P_s (|F(\omega_L + \omega_{\text{mod}})|^2 + |F(\omega_L - \omega_{\text{mod}})|^2) \\ &\quad + 2\sqrt{P_c P_s} \Re\{F(\omega_L)F^*(\omega_L + \omega_{\text{mod}}) - F^*(\omega_L)F(\omega_L - \omega_{\text{mod}})\} \cos \omega_{\text{mod}} t \\ &\quad + 2\sqrt{P_c P_s} \Im\{F(\omega_L)F^*(\omega_L + \omega_{\text{mod}}) - F^*(\omega_L)F(\omega_L - \omega_{\text{mod}})\} \sin \omega_{\text{mod}} t \\ &\quad + \mathcal{O}(2\omega_{\text{mod}}) \end{aligned} \quad (4.5)$$

where $P_c = J_0^2(\beta)P_0$ and $P_s = J_1^2(\beta)P_0$ refer to the power in the carrier and sideband frequency components, respectively. This signal, which is acquired using a fast photodiode, is sent to a demodulation set up where a mixer and a low pass filter are used isolate terms proportional to $\sin \omega_{\text{mod}} t$ or $\cos \omega_{\text{mod}} t$. In particular a local oscillator signal at $\omega_{\text{LO}} = \omega_{\text{mod}}$ and a variable phase is mixed with the RF signal from the photodiode so that either of the two terms ($\sin \omega_{\text{mod}} t$ or $\cos \omega_{\text{mod}} t$) is eliminated. The remaining term, which contains a DC signal ($\omega_{\text{LO}} - \omega_{\text{mod}}$) and term corresponding to $\omega_{\text{LO}} + \omega_{\text{mod}}$, is passed through a low pass filter to remove the faster oscillating term and an error signal is generated [126], i.e.,

$$\epsilon_{\text{PDH}} = 2\sqrt{P_c P_s} \frac{d|F(\omega_L)|^2}{d\omega_L} \omega_{\text{mod}} \quad (4.6)$$

4.2.2 PDH setup

Our setup consists of an ultra-low expansion cavity (from Stable Laser Systems) of length 100 mm and measured finesse of $\mathcal{F} = 20000$. The cavity is housed in a vacuum chamber pumped down to 10^{-7} Torr to reduce cavity length fluctuations due to air currents and is

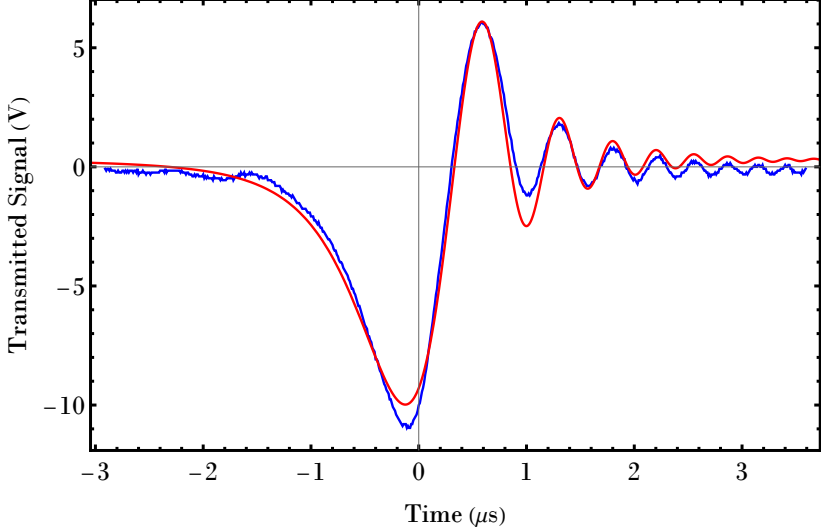


Figure 4.3: Cavity finesse estimation by fitting to ringdown signal on the reflected signal. $\mathcal{F} = 19542 \pm 213$.

also temperature stabilized making it insensitive to drifts in ambient temperature in the lab. The mirrors used are coated to allow high reflectivity at around 405 nm and 974 nm to allow locking of both of our Rydberg lasers to the same cavity. This scheme is useful for coherent transfer of atoms from the ground ($4S_{1/2}$) to the excited ($69P_{3/2}$) through a two photon transition.

405 nm setup

Rydberg excitation light at 405 nm is supplied by a MOGLabs Littrow ECDL (LDL) which features a monoblock chassis with no springs or fixtures, a feature that reduces vibrations [32]. A Faraday isolator is included at the output to prevent reflection of light back into the laser. The elliptical output beam profile from the LDL is passed through a 2:1 prism pair which shapes the profile into a Gaussian mode to improve coupling efficiency into PM fibers.

We pass the beam through a PBS and divide it into two paths. Path P1 is sent through a free-space EOM (EO-PM-NR-C4) modulated at 20 MHz to write sidebands that will be used to generate PDH error signal as described in Section 4.2.1. The output of the free-space EOM is sent to a double pass AOM system that allows us to shift the laser frequency around +160MHz above the intermediate $5P_{3/2}$ state used for a two-photon excitation to the final Rydberg state. The double pass output beam is then coupled into a PM fiber and sent

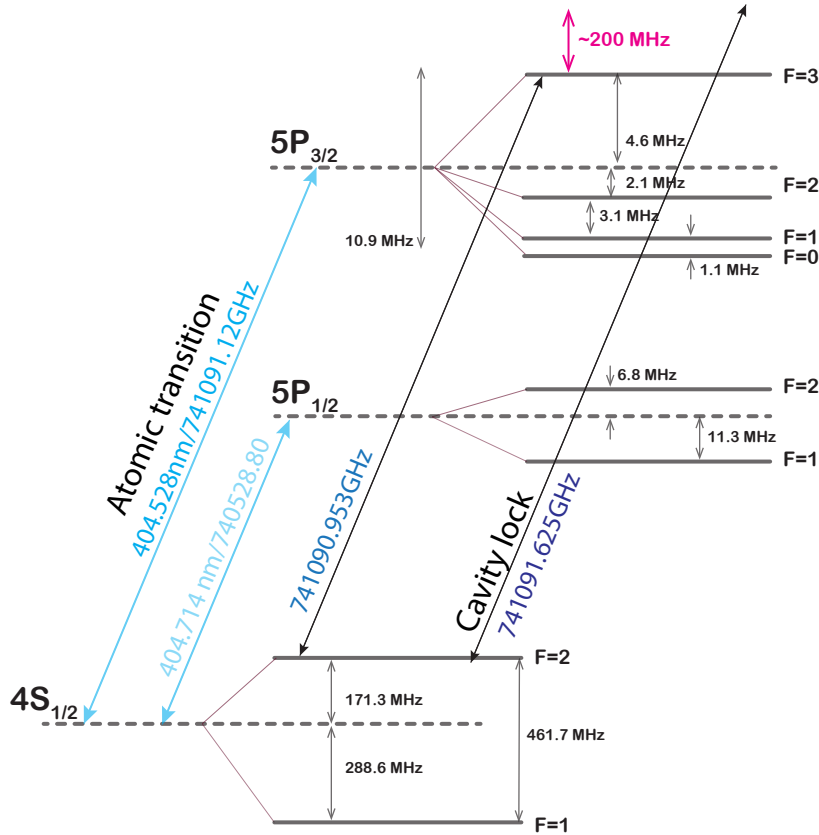


Figure 4.4: Potassium level diagram for the $4S \rightarrow 5P$ transition

into the PDH locking setup. We send the output of the PM fiber P1 through a PBS and a quarter-waveplate before reflecting it on a dichroic filter onto the cavity. A CCD camera and a photodiode are used at the cavity output to monitor the transmitted signal both during the alignment stage and as a visual confirmation of the lock signal during experiments.

The reflected signal from the front mirror is aligned to the incident beam and is reflected at the PBS into a SLS PDH locking unit (PDH-1000-5C). This integrated PDH unit consists of a photodiode input whose signal input can be directly sent to an oscilloscope for monitoring. The RF input created based on the reflected signal is sent to a built-in demodulation circuit that features a local oscillator whose phase can be directly controlled using a trimpot, a low pass filter, an RF output that is used to modulate the EOM used in the PDH setup and a fast transimpedance amplifier to increase the size of the generated output error signal. The whole unit is housed in a RF-shielded enclosure thus generating stable error signals that can be sent to a servo loop for laser frequency stabilization. Compared

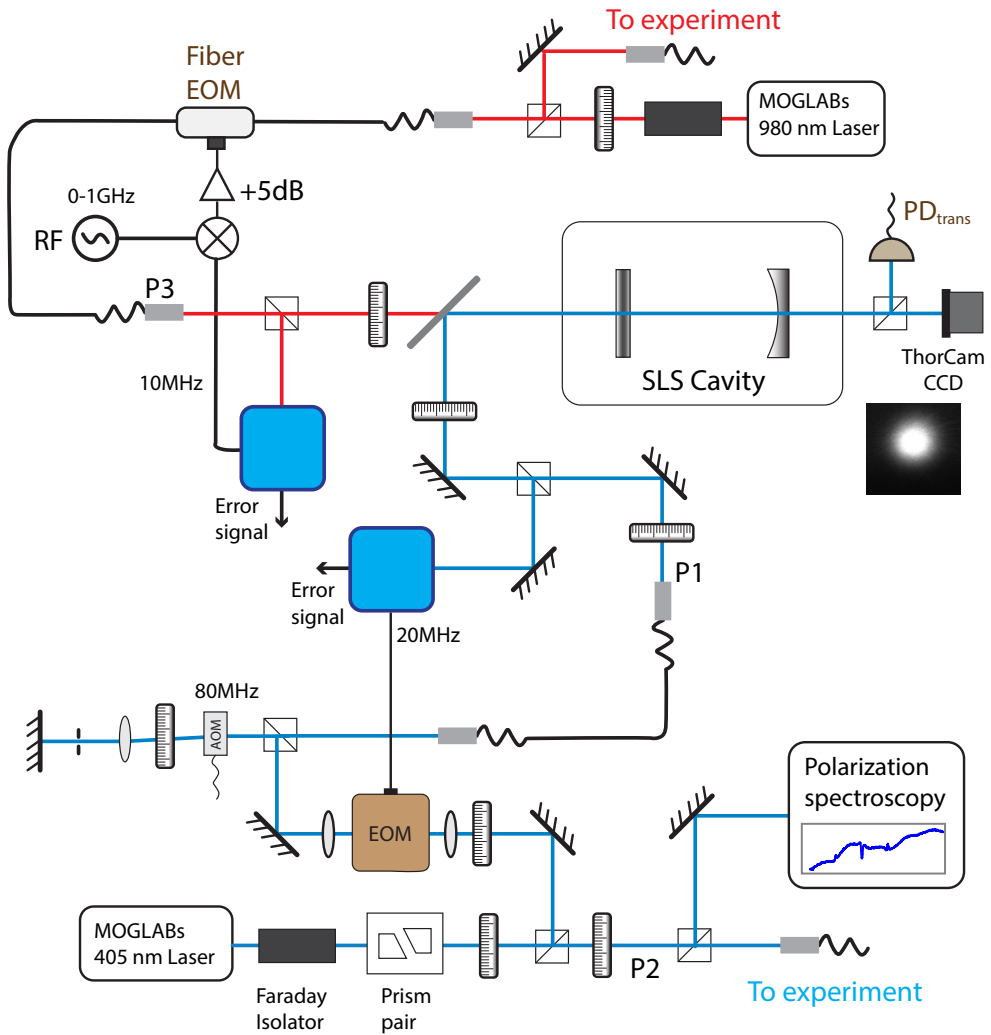


Figure 4.5: Setup for locking 973 nm and 405 nm lasers to an ultra-high finesse cavity

to a home-built demodulation circuit, the PDH signal unit was ideal for our application because of its "plug and play" nature, *i.e.*, one only needs to align a beam into the photodiode input and read out the PDH error signal output. Optimization of the error signal was also incredibly easy based on available trim pots that controlled local oscillator phase and amplitude. Additionally, the error signal obtained was more stable and less noisy compared to home-built demodulation circuit. Perhaps the most important advantage of using the integrated PDH unit was cost. In addition to reducing the length of connection between RF components and avoiding the use of long RF cables, the unit replaces a photo-diode, RF frequency sources and an amplifier.

Path P2 is passed through a PBS that divides it into two paths. One path is sent to a

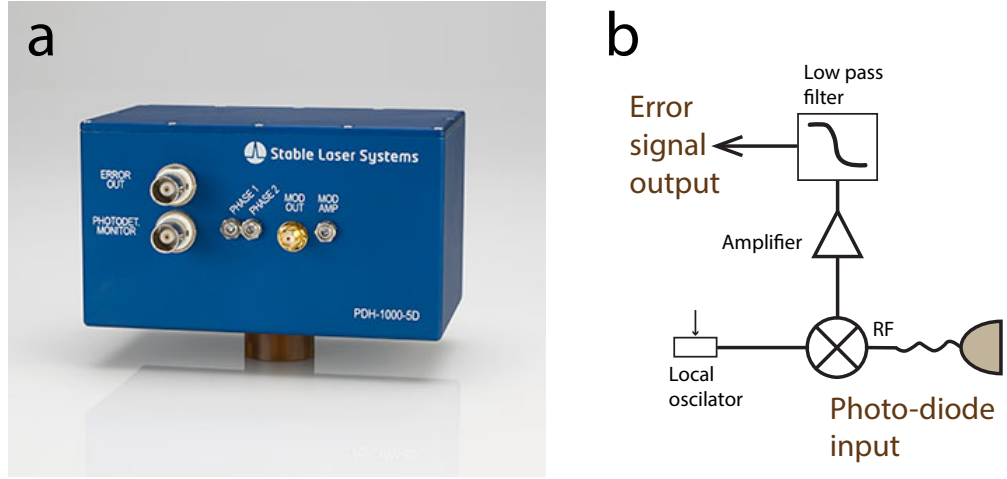


Figure 4.6: **Cost-saving Pound-Drever-Hall signal unit** (a) Stable laser systems PDH signal unit [127]. (b) A summary of the demodulation circuit

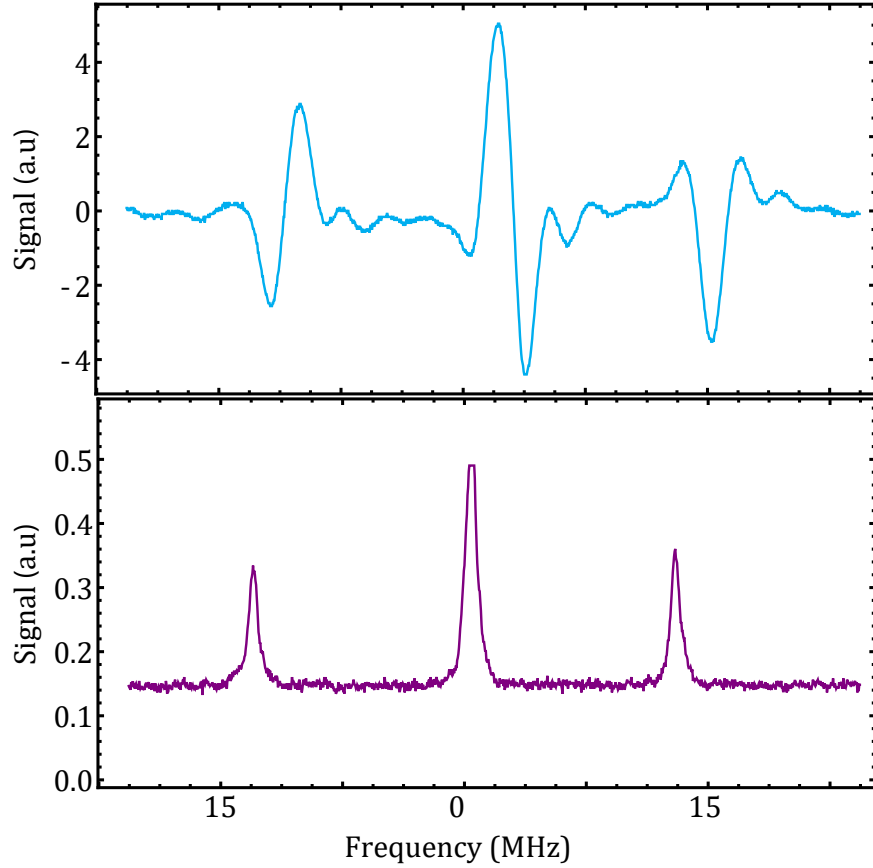


Figure 4.7: **Error signal generated using PDH-1000-5C.** Top: Dispersive error signal corresponding to ≈ 13 MHz EOM drive. Bottom: Transmitted photodiode signal.

poarization spectroscopy setup for frequency reference. We perform PS on the $4S_{1/2} \rightarrow 5P_{3/2}$ transition and compare the obtained signal to the error signal generated from the set up.

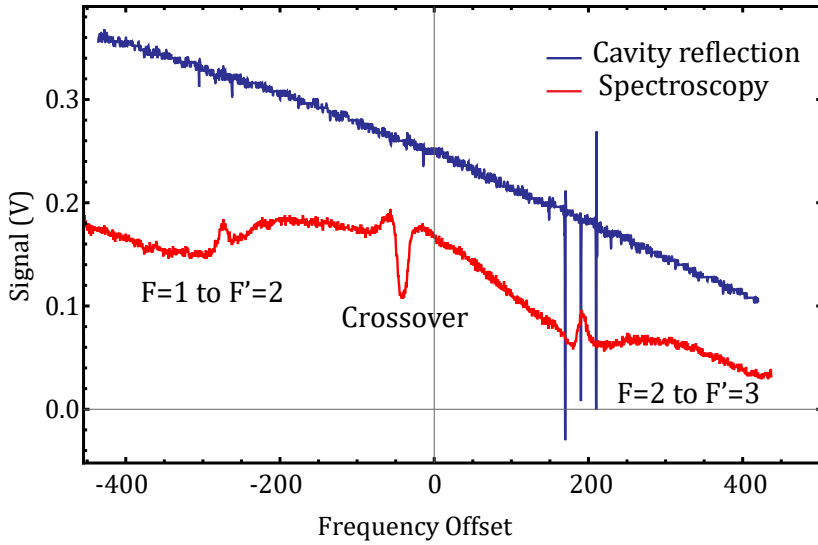


Figure 4.8: Comparison between PS signal and cavity reflection

Loss spectroscopy

As a first step towards Rydberg excitation we perform loss spectroscopy on the $4S_{1/2} \rightarrow 5P_{3/2}$ transition. The experiment begins by loading a single atom into a tweezer trap over 150ms followed by taking an image to confirm initial loading. A 405 nm beam aligned to the original 767 nm imaging beam is then turned on for 5 ms to scatter photons and induce loss of atoms. By tuning the frequency detuning of the 405 nm beam with respect to the cavity

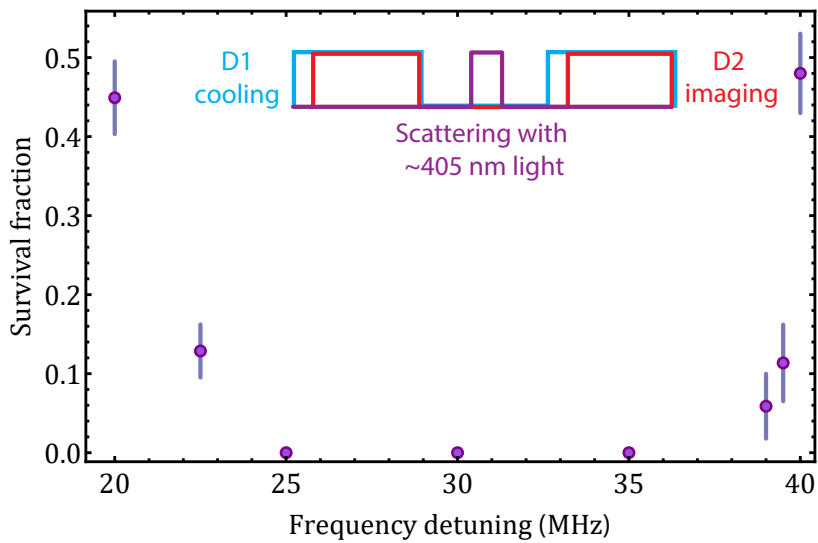


Figure 4.9: Loss spectroscopy of the $4S \rightarrow 5P$ transition

lock we expect loss of atoms to be severe near resonance. A second image is taken to confirm survival of atoms under exposure to the 405 nm beam. This measurements are repeated 200 times and a survival fraction is calculated.

Since the trap is kept on throughout the sequence, the resonance detuning measured is actually shifted. However, using 780 nm traps induce moderate light shifts thus enabling us to easily scan the 405 nm beam across resonance without too much effort. Furthermore, the fact that the cavity lock coincidentally happens to be close to the $4S_{1/2} \rightarrow 5P_{3/2}$ atomic transition improves our chances of success. As displayed on Figure 4.9, we see a drastic drop in survival fraction as the AOM is swept across resonance. In particular, loss of atoms in between the two images happens around 30 MHz detuning from the cavity lock (and most likely from free space atomic resonance ²) which suggests a differential light shift of the 405 nm transition of about 30 MHz.

With this information we proceed to detune the 405 nm beam by 200 MHz above (blue with respect to) resonance as a first leg of the two-photon excitation to Rydberg levels.

974 nm setup

Our 974 nm laser preparation setup consists of a MOGLabs tunable cateye laser (CEL) where diffraction gratings (common in ECDLs) are replaced with a combination of cateye reflector and an ultra-narrow filter [32]. The output of the laser is passed through a Faraday isolator to prevent reflections from going back into the laser which could make it unstable. The beam is then divided into two paths on a PBS. Path P3 is coupled into a PM fiber and sent into the PDH locking setup. Here the beam is combined with the 405 nm beam at the dichroic filter which enables locking of both lasers to the same cavity. Once incident on the front mirror the reflected light (counter-propagating with the incident light) is reflected into the integrated PDH unit at the PBS. In contrast to the optical setup for 405 nm laser preparation the PM fiber that supplies light into the PDH set up is passed through a broadband fiber EOM (from EOspace). The RF drive derived from the PDH unit for modulation ($\omega_{\text{mod}} = 10$ MHz) is mixed with a higher frequency ($\omega_{\text{DDS}} = 0-1$ GHz) to create three sets of frequencies at

²The relative detuning between the cavity resonance and atomic transitions shifted by around 20 MHz over 1 year.

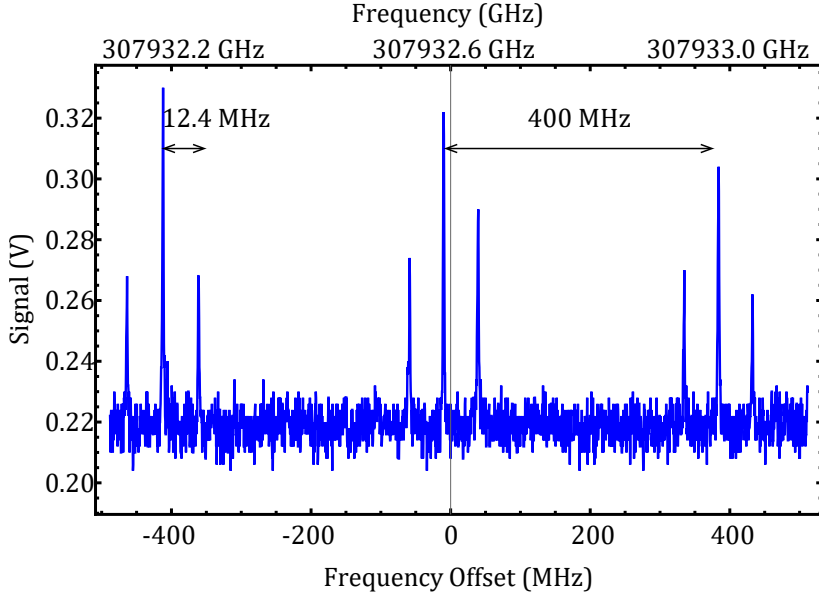


Figure 4.10: Transmission peaks corresponding to incident beam driven using two RF tones (12.4 MHz and 400 MHz)

$\omega_L \pm (\omega_{\text{DDS}} \pm \omega_{\text{mod}})$. The PDH unit creates error signals at the 9 corresponding frequencies thus allowing us to lock the laser to one of the sidebands. Locking to the sidebands gives us the freedom to change the relative frequency between the cavity lock (which can be moved by changing ω_{DDS}) and the light sent to experiment. This will be very useful for sweeping the laser frequency relative to the $5P_{3/2} \rightarrow nS_{1/2}$ transition when transferring atoms to Rydberg states.

Locking to the error signal

In our setup we incorporated a fast servo controller (FSC) for stabilization of the Rydberg excitation lasers. The error signal obtained from the integrated PDH unit is sent to the fast servo controller via an SMA cable. The FSC features a slow and fast PID loops used for feedback to the laser current and piezo.

With a visual monitoring of both the slow and fast error signal on an oscilloscope the lock stability was easily optimized through direct front panel access to PID loop parameters.

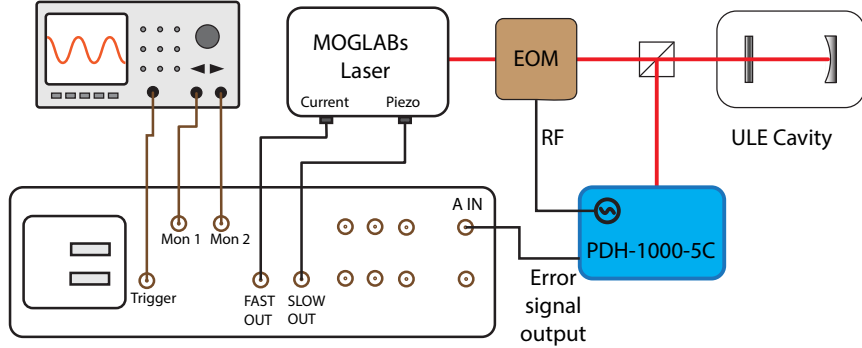


Figure 4.11: Frequency stabilization using MOGLabs Fast Servo Controller

4.2.3 Power amplification

In our setup we plan to implement Rydberg excitation with an effective Rabi rate of $\Omega_{\text{eff}} = \frac{\Omega_{973}\Omega_{405}}{2\Delta_{1-\text{photon}}} \approx 1$ to 2 MHz, where $\Delta_{1-\text{photon}}$ is the detuning above the intermediate $5P_{3/2}$ state. Since the $5P_{3/2} \rightarrow 69S_{1/2}$ transition (addressed by the 973 nm laser) is relatively weak compared to the $4S_{1/2} \rightarrow 5P_{3/2}$ (addressed by the 405 nm laser), *i.e.*, $\frac{D_{405}^{\text{reduced}}}{D_{973}^{\text{reduced}}} = \frac{0.406a_0e}{0.018a_0e} \approx 22.56$, more power is needed at 973 nm to drive the $5P_{3/2} \rightarrow 69S_{1/2}$ transition at similar Rabi rates achievable using reasonably low power at 405 nm. For example, for $\Delta_{1-\text{photon}} = 200$ MHz and similar Rabi frequencies can be achieved for 1 mW of 405 nm light focused to $80 \mu\text{m}$ (22.49 MHz) and 60 mW of 973 nm light focused to $30 \mu\text{m}$ (20.41 MHz). The effective Rabi frequency for this case is $\Omega_{\text{eff}} = \frac{\Omega_{973}\Omega_{405}}{2\Delta_{1-\text{photon}}} = 1.148$ MHz. In order to work at reasonable Rabi frequencies we plan to amplify the laser output to be sent to experiment for Rydberg excitation.

A typical approach taken to amplify the power needed is using tapered amplifiers. While we have demonstrated that TAs generally supply reasonably high power, TA output modes are usually of poor quality and require careful beam shaping to achieve any reasonable fiber

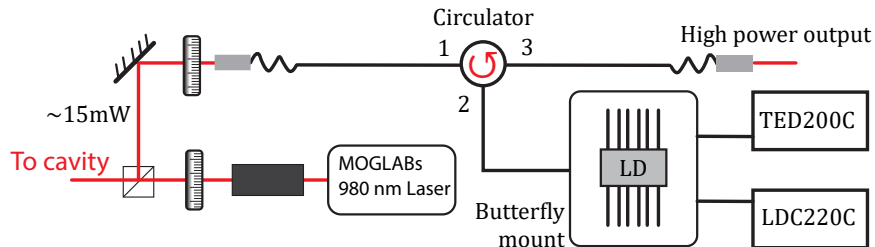


Figure 4.12: Fiber based injection-seeding of a 980 nm ECDL.

coupling efficiencies. Besides, free-space coupling of TAs turns out to be quite an arduous undertaking.

An alternative approach involves injection locking using fiber-circulators as already demonstrated by ref. [128]. Here the seed laser is coupled to a PM fiber that is directly connected to port 1 of a fiber circulator through a fiber-to-fiber adapter (ADAFCPM2). The output of the circulator at port 2 is injected into a fiber pigtailed high-power laser operated at 974 nm for injection locking. The high power output propagates back into the circulator through port 2 and comes out of port 3 through a PM fiber that can directly be sent to experiment.

In contrast to free space injection locking (demonstrated for 401 nm on appendix B) where the robustness of the lock is highly dependent on how well the seed and follower lasers are mode-matched, injection locking is fairly easy with this scheme since the PM fiber only accepts the correct mode necessary for fiber coupling. It is however necessary to ensure good polarization matching at the fiber adapters for stable operation.

4.3 Outlook

In preparation for microwave addressing of Rydberg levels, degenerate magnetic sublevels have to be separated in order to avoid off-resonant excitations from nearby unwanted states. Such effects, if not addressed, can complicate the spectrum of states used and forbid efficient population transfer between states. On Figure 4.13 we demonstrate that the degeneracy within each hyperfine manifold can be lifted (through Zeeman shifts) by applying moderate magnetic fields (≈ 30 G). Under such conditions, *i.e.* a minimum separation of 55 MHz from the nearest off-resonant state, other relevant parameters *e.g.* tunneling rate and interaction strength, are much slower (\approx few MHz). This allows for coherent transfer of population between Rydberg levels.

To this end, we plan to adapt our magnetic field gradient coils to provide a quantization field during the Rydberg experiment. In order to do this we will use an H-bridged based fast switching circuit designed, built and tested by Dr. Eric J. Meier. This circuit uses an H-bridge relay to switch the direction of current flowing through one of two coils to either create a field (in an Helmholtz configuration) or a gradient (in an anti-Helmholtz configuration).

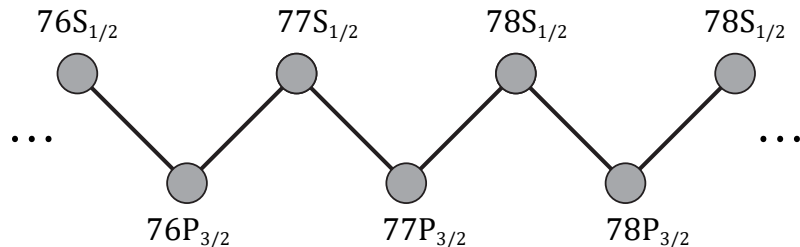
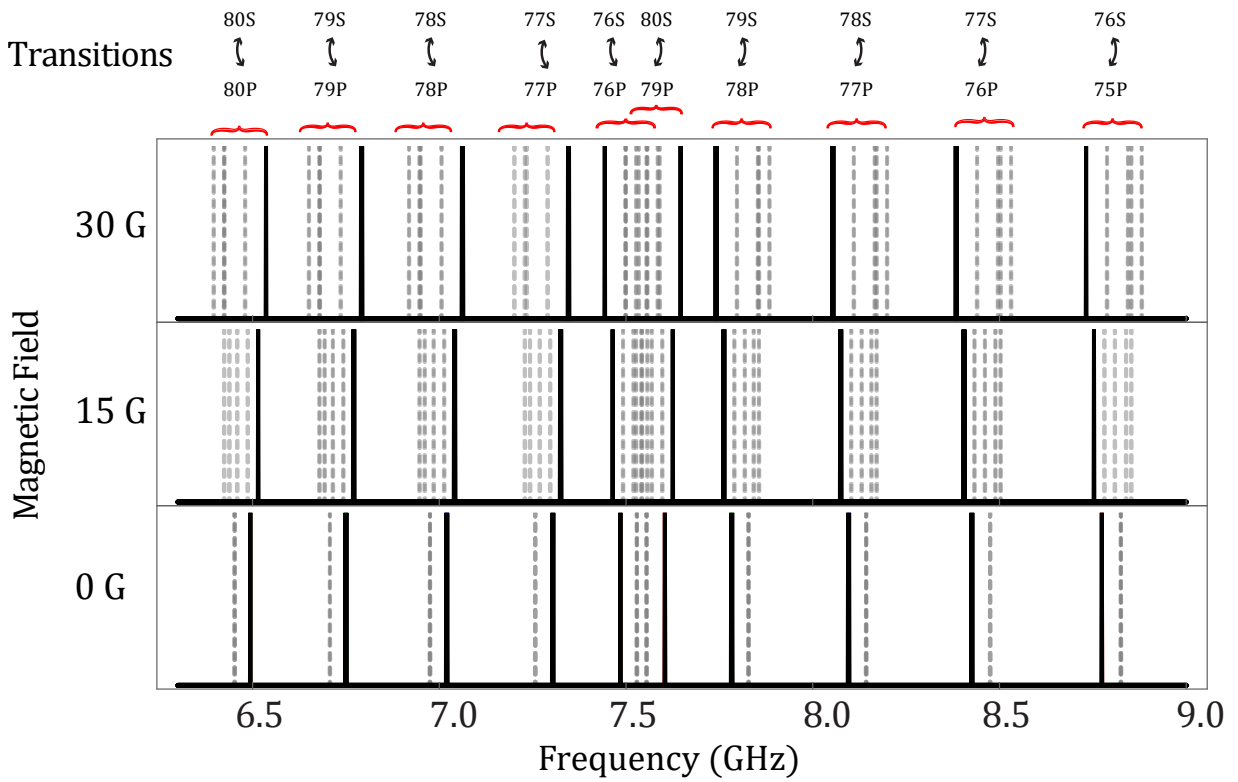


Figure 4.13: **Separating unwanted transitions from a Rydberg synthetic lattice by applying a quantization field.** Combination of all transitions within a few-GHz range, relevant to initialization in the state $|70, S\rangle$. Desired transitions $|n, S_{1/2,1/2}\rangle \rightarrow |n, P_{3/2,3/2}\rangle$ are shown in black solid lines while all other unwanted transitions appear in dashed and gray lines. The three panels show the distributions for fields of 30 G, 15 G, and 0 G, respectively. Bottom: Cartoon depiction of effective 1D tight-binding model when resonant transitions (solid black lines) are driven.

References

- [1] R. P. Feynman, *Int. J. Theor. Phys.* **21**, 467 (1982).
- [2] H. M. Price, T. Ozawa, and H. Schomerus, *Phys. Rev. Research* **2**, 032017 (2020).
- [3] B. K. Stuhl, H.-I. Lu, L. M. Aycock, D. Genkina, and I. B. Spielman, *Science* **349**, 1514 (2015), <https://science.sciencemag.org/content/349/6255/1514.full.pdf>.
- [4] M. Mancini, G. Pagano, G. Cappellini, L. Livi, M. Rider, J. Catani, C. Sias, P. Zoller, M. Inguscio, M. Dalmonte, and L. Fallani, *Science* **349**, 1510 (2015), <https://science.sciencemag.org/content/349/6255/1510.full.pdf>.
- [5] B. Gadway, *Phys. Rev. A* **92**, 043606 (2015).
- [6] E. J. Meier, F. A. An, and B. Gadway, *Phys. Rev. A* **93**, 051602 (2016).
- [7] L. F. Livi, G. Cappellini, M. Diem, L. Franchi, C. Clivati, M. Frittelli, F. Levi, D. Calonico, J. Catani, M. Inguscio, and L. Fallani, *Phys. Rev. Lett.* **117**, 220401 (2016).
- [8] S. Kolkowitz, S. L. Bromley, T. Bothwell, M. L. Wall, G. E. Marti, A. P. Koller, X. Zhang, A. M. Rey, and J. Ye, *Nature* **542**, 66 (2017).
- [9] H. Bernien, S. Schwartz, A. Keesling, H. Levine, A. Omran, H. Pichler, S. Choi, A. S. Zibrov, M. Endres, M. Greiner, V. Vuletić, and M. D. Lukin, *Nature* **551**, 579 (2017), arXiv:1707.04344 [quant-ph].
- [10] M. Endres, H. Bernien, A. Keesling, H. Levine, E. R. Anschuetz, A. Krajenbrink, C. Senko, V. Vuletic, M. Greiner, and M. D. Lukin, *Science* (2016), 10.1126/science.aah3752, <http://science.sciencemag.org/content/early/2016/11/02/science.aah3752.full.pdf>
- .
- [11] D. Barredo, V. Lienhard, S. de Léséleuc, T. Lahaye, and A. Browaeys, *Nature* **561**, 79 (2018), arXiv:1712.02727 [quant-ph].
- [12] D. Barredo, H. Labuhn, S. Ravets, T. Lahaye, A. Browaeys, and C. S. Adams, *Phys. Rev. Lett.* **114**, 113002 (2015).
- [13] S. de Léséleuc, D. Barredo, V. Lienhard, A. Browaeys, and T. Lahaye, *Phys. Rev. Lett.* **119**, 053202 (2017).

- [14] P. Scholl, M. Schuler, H. J. Williams, A. A. Eberharter, D. Barredo, K.-N. Schymik, V. Lienhard, L.-P. Henry, T. C. Lang, T. Lahaye, A. M. Läuchli, and A. Browaeys, “Programmable quantum simulation of 2d antiferromagnets with hundreds of rydberg atoms,” (2020), [arXiv:2012.12268 \[quant-ph\]](https://arxiv.org/abs/2012.12268) .
- [15] S. Ebadi, T. T. Wang, H. Levine, A. Keesling, G. Semeghini, A. Omran, D. Bluvstein, R. Samajdar, H. Pichler, W. W. Ho, S. Choi, S. Sachdev, M. Greiner, V. Vuletic, and M. D. Lukin, “Quantum phases of matter on a 256-atom programmable quantum simulator,” (2020), [arXiv:2012.12281 \[quant-ph\]](https://arxiv.org/abs/2012.12281) .
- [16] G. Semeghini, H. Levine, A. Keesling, S. Ebadi, T. T. Wang, D. Bluvstein, R. Verresen, H. Pichler, M. Kalinowski, R. Samajdar, A. Omran, S. Sachdev, A. Vishwanath, M. Greiner, V. Vuletic, and M. D. Lukin, “Probing topological spin liquids on a programmable quantum simulator,” (2021), [arXiv:2104.04119 \[quant-ph\]](https://arxiv.org/abs/2104.04119) .
- [17] D. Bluvstein, A. Omran, H. Levine, A. Keesling, G. Semeghini, S. Ebadi, T. T. Wang, A. A. Michailidis, N. Maskara, W. W. Ho, S. Choi, M. Serbyn, M. Greiner, V. Vuletić, and M. D. Lukin, *Science* **371**, 1355 (2021), <https://science.sciencemag.org/content/371/6536/1355.full.pdf> .
- [18] M. Saffman, T. G. Walker, and K. Mølmer, *Rev. Mod. Phys.* **82**, 2313 (2010).
- [19] S. K. Kanungo, J. D. Whalen, Y. Lu, M. Yuan, S. Dasgupta, F. B. Dunning, K. R. A. Hazzard, and T. C. Killian, “Realizing su-schrieffer-heeger topological edge states in rydberg-atom synthetic dimensions,” (2021), [arXiv:2101.02871 \[physics.atom-ph\]](https://arxiv.org/abs/2101.02871) .
- [20] M. Saffman, T. G. Walker, and K. Mølmer, *Rev. Mod. Phys.* **82**, 2313 (2010).
- [21] P. Schauss, “Hochauflösende detektion von ordnung in rydberg vielteilchensystemen,” (2015).
- [22] C. L. Vaillant, M. P. A. Jones, and R. M. Potvliege, *Journal of Physics B Atomic Molecular Physics* **45**, 135004 (2012), [arXiv:1203.3736 \[physics.atom-ph\]](https://arxiv.org/abs/1203.3736) .
- [23] N. Sibalic and C. S. Adams, in *Rydberg Physics*, 2399-2891 (IOP Publishing, 2018) pp. 1–1 to 1–27.
- [24] I. I. Beterov, D. B. Tretyakov, I. I. Ryabtsev, V. M. Entin, A. Ekers, and N. N. Bezuglov, *New Journal of Physics* **11**, 013052 (2009).
- [25] Gounand, F., *J. Phys. France* **40**, 457 (1979).
- [26] B. Sundar, B. Gadway, and K. R. A. Hazzard, arXiv e-prints , [arXiv:1708.02112 \[cond-mat.quant-gas\]](https://arxiv.org/abs/1708.02112) .
- [27] B. Sundar, M. Thibodeau, Z. Wang, B. Gadway, and K. Hazzard, arXiv e-prints , [arXiv:1812.02229 \[cond-mat.quant-gas\]](https://arxiv.org/abs/1812.02229) .

- [28] F. Cardano, A. D'Errico, A. Dauphin, M. Maffei, B. Piccirillo, C. de Lisio, G. De Filippis, V. Cataudella, E. Santamato, L. Marrucci, M. Lewenstein, and P. Massignan, *Nat. Commun.* **8**, 1 (2017).
- [29] S. Lapp, J. Ang'ong'a, F. A. An, and B. Gadway, *New Journal of Physics* **21**, 045006 (2019).
- [30] F. A. An, E. J. Meier, J. Ang'ong'a, and B. Gadway, *Phys. Rev. Lett.* **120**, 040407 (2018).
- [31] E. J. Meier, J. Ang'ong'a, F. A. An, and B. Gadway, *Phys. Rev. A* **100**, 013623 (2019).
- [32] MOG Laboratories, (2020), <https://www.moglabs.com/>, Last accessed on 2021-04-13.
- [33] F. A. An, “The cold atom toolbox in momentum space,” (2021), [Online; accessed 13. Jul. 2021].
- [34] E. A. Donley, T. P. Heavner, F. Levi, M. O. Tataw, and S. R. Jefferts, *Review of Scientific Instruments* **76**, 063112 (2005), <https://doi.org/10.1063/1.1930095>.
- [35] Gooch & Housego PLC, (2020), <https://gandh.com/>, Last accessed on 2021-04-13.
- [36] Intraaction Corp, (2020), <https://intraaction.com/>, Last accessed on 2021-04-13.
- [37] A. Keshet and W. Ketterle, *Review of Scientific Instruments* **84**, 015105 (2013), <https://doi.org/10.1063/1.4773536>.
- [38] E. J. Meier, “Momentum-space lattices for ultracold atoms,” (2021), [Online; accessed 13. Jul. 2021].
- [39] A. L. Schawlow and C. H. Townes, *Phys. Rev.* **112**, 1940 (1958).
- [40] S. Haroche and F. Hartmann, *Phys. Rev. A* **6**, 1280 (1972).
- [41] C. J. Bordé, J. L. Hall, C. V. Kunasz, and D. G. Hummer, *Phys. Rev. A* **14**, 236 (1976).
- [42] G. C. Bjorklund, *Opt. Lett.* **5**, 15 (1980).
- [43] J. H. Shirley, *Opt. Lett.* **7**, 537 (1982).
- [44] D. J. McCarron, S. A. King, and S. L. Cornish, *Measurement Science and Technology* **19**, 105601 (2008).
- [45] K. L. Corwin, Z.-T. Lu, C. F. Hand, R. J. Epstein, and C. E. Wieman, *Appl. Opt.* **37**, 3295 (1998).

- [46] S. Borri, S. Bartalini, I. Galli, P. Cancio, G. Giusfredi, D. Mazzotti, A. Castrillo, L. Gianfrani, and P. D. Natale, *Opt. Express* **16**, 11637 (2008).
- [47] A. Millett-Sikking, I. G. Hughes, P. Tierney, and S. L. Cornish, *Journal of Physics B: Atomic, Molecular and Optical Physics* **40**, 187 (2006).
- [48] P. Siddons, C. S. Adams, C. Ge, and I. G. Hughes, *Journal of Physics B: Atomic, Molecular and Optical Physics* **41**, 155004 (2008).
- [49] C. Wieman and T. W. Hänsch, *Phys. Rev. Lett.* **36**, 1170 (1976).
- [50] H. D. Do, G. Moon, and H. Noh, *Phys. Rev. A* **77**, 032513 (2008).
- [51] M. L. Harris, C. S. Adams, S. L. Cornish, I. C. McLeod, E. Tarleton, and I. G. Hughes, *Phys. Rev. A* **73**, 062509 (2006).
- [52] S. Zhu, T. Chen, X. Li, and Y. Wang, *J. Opt. Soc. Am. B* **31**, 2302 (2014).
- [53] J. Ang'ong'a and B. Gadway, *Journal of Physics B: Atomic, Molecular and Optical Physics* **51**, 045003 (2018).
- [54] C. P. Pearman, C. S. Adams, S. G. Cox, P. F. Griffin, D. A. Smith, and I. G. Hughes, *Journal of Physics B: Atomic, Molecular and Optical Physics* **35**, 5141 (2002).
- [55] L. Qiang, Z. Xianjin, Z. Junhai, and S. Weimin, in *2010 Academic Symposium on Optoelectronics and Microelectronics Technology and 10th Chinese-Russian Symposium on Laser Physics and Laser Technology Optoelectronics Technology (ASOT)* (2010) pp. 200–203.
- [56] R. de L. Kronig, *J. Opt. Soc. Am.* **12**, 547 (1926).
- [57] D. C. Hutchings, M. Sheik-Bahae, D. J. Hagan, and E. W. Van Stryland, *Optical and Quantum Electronics* **24**, 1 (1992).
- [58] A. B. Kuzmenko, *Review of Scientific Instruments* **76**, 083108 (2005), <https://doi.org/10.1063/1.1979470>.
- [59] C. Foot, *Atomic physics*, Oxford master series in physics (Oxford University Press, 2005).
- [60] H. Metcalf and P. van der Straten, *Laser Cooling and Trapping*, Graduate Texts in Contemporary Physics (Springer New York, 2001).
- [61] T. Grünzweig, A. Hilliard, M. McGovern, and M. F. Andersen, *Nature Physics* **6**, 951 (2010).
- [62] A. Gaëtan, Y. Miroshnychenko, T. Wilk, A. Chotia, M. Viteau, D. Comparat, P. Pillet, A. Browaeys, and P. Grangier, *Nature Physics* **5**, 115 (2009).

- [63] Y. Wang, S. Shevate, T. M. Wintermantel, M. Morgado, G. Lochead, and S. Whitlock, *npj Quantum Inf.* **6**, 1 (2020).
- [64] N. Lorenz, L. Festa, L.-M. Steinert, and C. Gross, “Raman sideband cooling in optical tweezer arrays for rydberg dressing,” (2020), [arXiv:2010.07838 \[physics.atom-ph\]](https://arxiv.org/abs/2010.07838) .
- [65] S. S. Kondov, W. R. McGehee, J. J. Zirbel, and B. DeMarco, *Science* **334**, 66 (2011), <https://science.sciencemag.org/content/334/6052/66.full.pdf> .
- [66] H. J. Lewandowski, D. M. Harber, D. L. Whitaker, and E. A. Cornell, *Journal of Low Temperature Physics* **132**, 309 (2003).
- [67] C. Klempert, T. Henninger, O. Topic, J. Will, S. Falke, W. Ertmer, and J. Arlt, *The European Physical Journal D* **48**, 121 (2008).
- [68] R. L. D. Campbell, R. P. Smith, N. Tammuz, S. Beattie, S. Moulder, and Z. Hadzibabic, *Phys. Rev. A* **82**, 063611 (2010).
- [69] M. Greiner, I. Bloch, T. W. Hänsch, and T. Esslinger, *Phys. Rev. A* **63**, 031401 (2001).
- [70] Optotune AG, (2020), <https://www.optotune.com/>, Last accessed on 2021-04-13.
- [71] J. Léonard, M. Lee, A. Morales, T. M. Karg, T. Esslinger, and T. Donner, *New Journal of Physics* **16**, 093028 (2014).
- [72] G. Ferioli, A. Glicenstein, L. Henriet, I. Ferrier-Barbut, and A. Browaeys, “Storage and release of subradiant excitations in a dense atomic cloud,” (2020), [arXiv:2012.10222 \[physics.atom-ph\]](https://arxiv.org/abs/2012.10222) .
- [73] T. B. Swanson, D. Asgeirsson, J. A. Behr, A. Gorelov, and D. Melconian, *J. Opt. Soc. Am. B* **15**, 2641 (1998).
- [74] N. Song, D. Hu, X. Xu, W. Li, X. Lu, and Y. Song, *Sensors* **18** (2018), 10.3390/s18030717.
- [75] Cacciapuoti, L., Castrillo, A., de Angelis, M., and Tino, G. M., *Eur. Phys. J. D* **15**, 245 (2001).
- [76] E. Dimova, O. Morizot, G. Stern, C. L. Garrido Alzar, A. Fioretti, V. Lorent, D. Comparat, H. Perrin, and P. Pillet, *The European Physical Journal D : Atomic, molecular, optical and plasma physics* **42**, 299 (2007), 10 pages, 8 figures.
- [77] C. J. Myatt, N. R. Newbury, R. W. Ghrist, S. Loutzenhiser, and C. E. Wieman, *Opt. Lett.* **21**, 290 (1996).
- [78] S. P. Ram, S. Tiwari, and S. R. Mishra, *Journal of the Korean Physical Society* **57**, 1303 (2010).
- [79] K. Dieckmann, R. J. C. Spreeuw, M. Weidemüller, and J. T. M. Walraven, *Phys. Rev. A* **58**, 3891 (1998).

- [80] W. Wohlleben, F. Chevy, K. Madison, and J. Dalibard, *The European Physical Journal D - Atomic, Molecular, Optical and Plasma Physics* **15**, 237 (2001).
- [81] S. J. Park, J. Noh, and J. Mun, *Optics Communications* **285**, 3950 (2012).
- [82] P. D. Lett, R. N. Watts, C. I. Westbrook, W. D. Phillips, P. L. Gould, and H. J. Metcalf, *Phys. Rev. Lett.* **61**, 169 (1988).
- [83] J. Dalibard and C. Cohen-Tannoudji, *J. Opt. Soc. Am. B* **6**, 2023 (1989).
- [84] M. Landini, S. Roy, L. Carcagní, D. Trypogeorgos, M. Fattori, M. Inguscio, and G. Modugno, *Phys. Rev. A* **84**, 043432 (2011).
- [85] V. Gokhroo, G. Rajalakshmi, R. K. Easwaran, and C. S. Unnikrishnan, *Journal of Physics B: Atomic, Molecular and Optical Physics* **44**, 115307 (2011).
- [86] C. J. Cooper, G. Hillenbrand, J. Rink, C. G. Townsend, K. Zetie, and C. J. Foot, *Europhysics Letters (EPL)* **28**, 397 (1994).
- [87] C. Triche, D. Boiron, S. Guibal, D. Meacher, P. Verkerk, and G. Grynberg, *Optics Communications* **126**, 49 (1996).
- [88] S. Rosi, A. Burchianti, S. Conclave, D. S. Naik, G. Roati, C. Fort, and F. Minardi, *Scientific Reports* **8**, 1301 (2018).
- [89] Y.-F. Hsiao, Y.-J. Lin, and Y.-C. Chen, *Phys. Rev. A* **98**, 033419 (2018).
- [90] Z. Shi, Z. Li, P. Wang, Z. Meng, L. Huang, and J. Zhang, *Chinese Physics Letters* **35**, 123701 (2018).
- [91] G. D. Bruce, E. Haller, B. Peaudecerf, D. A. Cotta, M. Andia, S. Wu, M. Y. H. Johnson, B. W. Lovett, and S. Kuhr, *Journal of Physics B: Atomic, Molecular and Optical Physics* **50**, 095002 (2017).
- [92] G. Salomon, L. Fouché, P. Wang, A. Aspect, P. Bouyer, and T. Bourdel, *EPL (Euro-physics Letters)* **104**, 63002 (2013).
- [93] D. Nath, R. K. Easwaran, G. Rajalakshmi, and C. S. Unnikrishnan, *Phys. Rev. A* **88**, 053407 (2013).
- [94] H.-Z. Chen, X.-C. Yao, Y.-P. Wu, X.-P. Liu, X.-Q. Wang, Y.-X. Wang, Y.-A. Chen, and J.-W. Pan, *Phys. Rev. A* **94**, 033408 (2016).
- [95] M. Bosch Aguilera, *An experimental setup for gray molasses sub-Doppler cooling of potassium gases*, Ph.D. thesis, UPC, Escola Tècnica Superior d'Enginyeria de Telecomunicació de Barcelona, Departament de Teoria del Senyal i Comunicacions (2014).
- [96] G. Colzi, G. Durastante, E. Fava, S. Serafini, G. Lamporesi, and G. Ferrari, *Phys. Rev. A* **93**, 023421 (2016).

- [97] A. T. Grier, I. Ferrier-Barbut, B. S. Rem, M. Delehaye, L. Khaykovich, F. Chevy, and C. Salomon, *Phys. Rev. A* **87**, 063411 (2013).
- [98] L. Gabardos, S. Lepoutre, O. Gorceix, L. Vernac, and B. Laburthe-Tolra, *Phys. Rev. A* **99**, 023607 (2019).
- [99] P. B. Wigley, P. J. Everitt, A. van den Hengel, J. W. Bastian, M. A. Sooriyabandara, G. D. McDonald, K. S. Hardman, C. D. Quinlivan, P. Manju, C. C. N. Kuhn, I. R. Petersen, A. N. Luiten, J. J. Hope, N. P. Robins, and M. R. Hush, *Scientific Reports* **6**, 25890 (2016).
- [100] A. D. Tranter, H. J. Slatyer, M. R. Hush, A. C. Leung, J. L. Everett, K. V. Paul, P. Vernaz-Gris, P. K. Lam, B. C. Buchler, and G. T. Campbell, *Nature Communications* **9**, 4360 (2018).
- [101] A. Seif, K. A. Landsman, N. M. Linke, C. Figgatt, C. Monroe, and M. Hafezi, *Journal of Physics B: Atomic, Molecular and Optical Physics* **51**, 174006 (2018).
- [102] A. J. Barker, H. Style, K. Luksch, S. Sunami, D. Garrick, F. Hill, C. J. Foot, and E. Bentine, *Machine Learning: Science and Technology* **1**, 015007 (2020).
- [103] E. T. Davletov, V. V. Tsyanok, V. A. Khlebnikov, D. A. Pershin, D. V. Shaykin, and A. V. Akimov, *Phys. Rev. A* **102**, 011302 (2020).
- [104] S. Xu, P. Kaeber, M. Stepanova, T. Poll, M. Siercke, and S. Ospelkaus, “Maximizing the capture velocity of molecular magneto-optical traps with bayesian optimization,” (2021), arXiv:2104.07984 [physics.atom-ph].
- [105] P. A. Vikhar, in *2016 International Conference on Global Trends in Signal Processing, Information Computing and Communication (ICGTSPICC)* (2016) pp. 261–265.
- [106] J. P. Covey, I. S. Madjarov, A. Cooper, and M. Endres, arXiv e-prints , arXiv:1811.06014 (2018), arXiv:1811.06014 [cond-mat.quant-gas].
- [107] M. O. Brown, T. Thiele, C. Kiehl, T. W. Hsu, and C. A. Regal, arXiv e-prints , arXiv:1811.01448 (2018), arXiv:1811.01448 [physics.atom-ph].
- [108] T. Grünzweig, A. Hilliard, M. McGovern, and M. F. Andersen, *Nature Physics* **6**, 951 (2010).
- [109] R. Grimm, M. Weidmüller, and Y. B. Ovchinnikov (Academic Press, 2000) pp. 95–170.
- [110] T. Tiecke, “Properties of potassium,” (2010).
- [111] D. Steck, “Quantum and Atom Optics,” (2018), [Online; accessed 25. Apr. 2021].
- [112] J. Mitroy, M. S. Safronova, and C. W. Clark, *Journal of Physics B: Atomic, Molecular and Optical Physics* **43**, 202001 (2010).

- [113] M. S. Safronova, U. I. Safronova, and C. W. Clark, *Phys. Rev. A* **87**, 052504 (2013).
- [114] M. S. Safronova, B. Arora, and C. W. Clark, *Phys. Rev. A* **73**, 022505 (2006).
- [115] A. Cooper, J. P. Covey, I. S. Madjarov, S. G. Porsev, M. S. Safronova, and M. Endres, arXiv e-prints , arXiv:1810.06537 (2018), [arXiv:1810.06537 \[cond-mat.quant-gas\]](https://arxiv.org/abs/1810.06537) .
- [116] M. A. Norcia, A. W. Young, and A. M. Kaufman, arXiv e-prints , arXiv:1810.06626 (2018), [arXiv:1810.06626 \[physics.atom-ph\]](https://arxiv.org/abs/1810.06626) .
- [117] N. R. Hutzler, L. R. Liu, Y. Yu, and K.-K. Ni, *New Journal of Physics* **19**, 023007 (2017).
- [118] J. D. Thompson, T. G. Tiecke, A. S. Zibrov, V. Vuletic, and M. D. Lukin, *Phys. Rev. Lett.* **110**, 133001 (2013).
- [119] S. Garcia, J. Reichel, and R. Long, *Phys. Rev. A* **97**, 023406 (2018).
- [120] K. L. Corwin, S. J. M. Kuppens, D. Cho, and C. E. Wieman, *Phys. Rev. Lett.* **83**, 1311 (1999).
- [121] I. H. Deutsch and P. S. Jessen, *Phys. Rev. A* **57**, 1972 (1998).
- [122] N. Schlosser, G. Reymond, I. Protsenko, and P. Grangier, *Nature* **411**, 1024 (2001).
- [123] C. Tuchendler, A. M. Lance, A. Browaeys, Y. R. P. Sortais, and P. Grangier, *Phys. Rev. A* **78**, 033425 (2008).
- [124] W. Alt, D. Schrader, S. Kuhr, M. Müller, V. Gomer, and D. Meschede, *Phys. Rev. A* **67**, 033403 (2003).
- [125] N. Sibalic, “Atom calculator,” (2021), [Online; accessed 16. Jul. 2021].
- [126] E. D. Black, *American Journal of Physics* **69**, 79 (2001), <https://doi.org/10.1119/1.1286663> .
- [127] “Pound-Drever-Hall Signal Unit - Stable Laser Systems,” (2017), [Online; accessed 16. Jul. 2021].
- [128] T. Shimasaki, E. R. Edwards, and D. DeMille, *Review of Scientific Instruments* **90**, 056102 (2019), <https://doi.org/10.1063/1.5079827> .
- [129] K. Metzger, *Arch. Elektrotech.* **59**, 229 (1977).
- [130] D. W., *Laser Spectroscopy Vol II* (Springer-Verlag Berlin Heidelberg, 2008).
- [131] Y. Yoshikawa, T. Umeki, T. Mukae, Y. Torii, and T. Kuga, *Appl. Opt.* **42**, 6645 (2003).
- [132] L. S. B. Wybourne, *Optical spectroscopy of lanthanides: Magnetic and hyperfine interactions*, edited by r (CRC Press, 2007).

Appendix A

3D MOT games

A.1 Test MOT

This appendix describes the trajectory followed at the beginning of trapping atoms. Even though I describe the 2D MOT as the first stage. It was useful at the beginning to first create a temporary 3D MOT at the beginning in the source cell in order to find out where our frequencies really lay with respect to the D2 atomic transitions. While it is expected that the MOT should *automatically* form with the detuning of the D2 cycling beam set at $\approx 3\Gamma$ with respect to the $F = 2 \rightarrow F' = 3$ transition, with the D2 repump beam detuning at resonance, with the D2 beam power set to a couple 10s of mW and with the cycling to repump ratio set at $\approx 3 : 1^1$; it is likely that the lockpoint of the polarization spectroscopy signal is shifted from the true $F = 2 \rightarrow F' = 3$ transition by some $\approx 10\text{MHz}$. This makes it relatively difficult to create a 2D MOT without any other way to determine the true location of the transition (this could include making a beat-note between your locked laser with a laser in an experiment that is already trapping and cooling ^{39}K atoms). In order to avoid searching too long in the dark, we set up a temporary 3D MOT at the source cell.

¹This is assuming that the alignment is good enough and that the direction of the field gradient matches the waveplate settings used. There are two sets of waveplate-Bfield orientation settings that work.

Beam Path	Initial Polarization	Final Polarization	Beam Power	Cycling detuning	Repump detuning
Top-Down	Horizontal	σ^+	35 mW	-14MHz	+436MHz
Left-Right 1	Vertical	σ^-	25 mW	-14MHz	+436MHz
Right-Left 2	Horizontal	σ^+	25 mW	-14MHz	+436MHz

Table A.1: Historical settings when we first trapped ^{39}K atoms. The cycling to repump power ratio was set to 3:2.

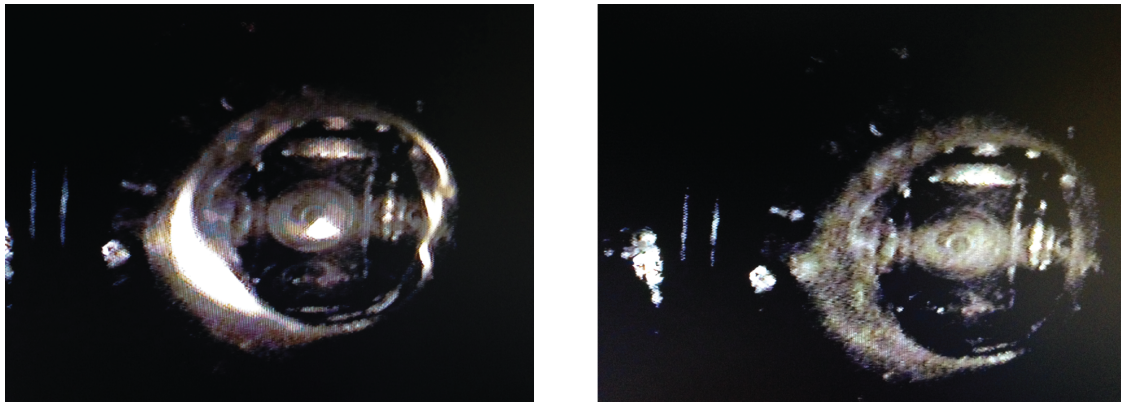


Figure A.1: Test MOT in the source cell. Left is 3D MOT when the B field is on and with correct polarization settings for the 3 pairs of MOT beams. Right shows that the MOT disappears when the B field is off.

A.2 Fun with MOTs



Figure A.2: Left, racetrack MOT in the octagon chamber. Right, dividing the MOT into two section while aligning the pulsed push beam used for transfer of atoms to the science chamber.

A.3 Nominal Octagon MOT parameters

Beam path	Frequency detuning (Γ)	Total intensity (I_{sat})
Spectroscopy	0	3.63
2D cycling	-4.17	9
2D repump	+0.17 (+73)	2.27
3D cycling	-1.33	8.38
3D repump	+0.17 (+73)	2.32
2D push	+2.5	12
3D pulsed push	+2.17	9.7

Table A.2: Beam frequencies in units of $\Gamma = 2\pi \times 6\text{MHz}$ and intensities in terms of $I_{\text{sat}}=1.75\text{mW/cm}^2$ for trapping and cooling atoms in our set up. Spectroscopy refers to the laser locking using polarization spectroscopy to the cycling $F=2 \rightarrow F'=3$ transition on the D2 line. The cycling and push beam detunings are defined with respect to the $F=2 \rightarrow F'=3$ cycling transition, while the repump beam detunings are defined with respect to $F=1 \rightarrow F'=2$ (which is $\approx 73\Gamma$ shifted from spectroscopy). Quoted intensity correspond to the total intensity at the atoms. For spectroscopy, total intensity going into the polarization spectroscopy is displayed.

Appendix B

Retired erbium project

B.1 Erbium 2D MOT preparation

This section summarizes some notable developments made in the initial phase of the experiment where we set out to trap and cool erbium atoms. Attempts made towards cooling erbium atoms discussed in this appendix were in collaboration with Sai Paladugu, Samantha Lapp, Muyan Du and Zhenyu Wei.

First we demonstrated the use of polarization spectroscopy for laser stabilization of a 401 nm laser that was supposed to be used for initial cooling of atoms on a broad $^3H_6 \rightarrow ^1P_1$ transition.

We designed and 3D printed and tested a structure for holding permanent magnets for the production of 50 G/cm field gradients for trapping erbium atoms in a 2D MOT.

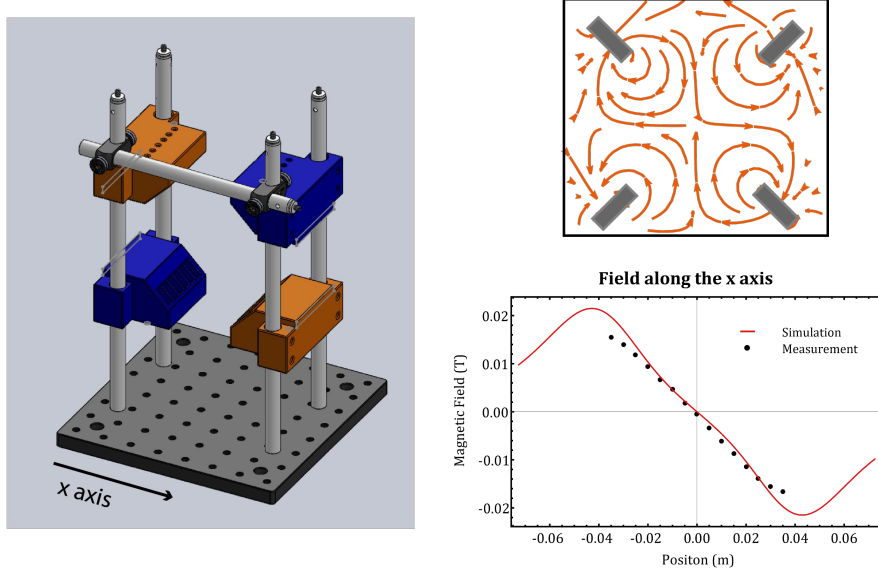


Figure B.1: (a) Magnetic support structure based on 3D printed permanent magnet holders.(b) Calculated quadrupole magnetic field lines generated using permanent magnets. (c) Measured field gradient ($50\text{G}/\text{cm}$) from assembled structure

B.1.1 Creating quadrupole magnetic fields using permanent magnets

In order to provide sufficient magnetic field gradients for trapping erbium atoms in a 2D MOT, a high magnetic field gradient of $\approx 50\text{G}/\text{cm}$ is required. A conventional approach to producing such high fields is using water-cooled magnetic field coils operated at relatively high currents. A simpler approach involves using permanent magnets organized along four corners to provide a quadrupole field the center.

The magnetic field from a rectangular permanent magnet is given by [129]

$$\begin{aligned}
B_x(x, y, z) &= \frac{\mu_0 m_x}{4\pi} \sum_{i,j,k=0}^1 (-1)^{i+j+k} \arctan \left[\frac{(y - y_j)(z - z_k)}{(x - x_i) \times r} \right] \\
&\quad - \frac{\mu_0 m_y}{4\pi} (-1)^{i+j+k} \operatorname{arsinh} \left[\frac{z - z_k}{\sqrt{r^2 - (z - z_k)^2}} \right] \\
&\quad - \frac{\mu_0 m_z}{4\pi} (-1)^{i+j+k} \operatorname{arsinh} \left[\frac{y - y_j}{\sqrt{r^2 - (y - y_j)^2}} \right] \\
B_y(x, y, z) &= \frac{\mu_0 m_y}{4\pi} \sum_{i,j,k=0}^1 (-1)^{i+j+k} \arctan \left[\frac{(x - x_i)(z - z_k)}{(y - y_j) \times r} \right] \\
&\quad - \frac{\mu_0 m_z}{4\pi} (-1)^{i+j+k} \operatorname{arsinh} \left[\frac{x - x_i}{\sqrt{r^2 - (x - x_i)^2}} \right] \\
&\quad - \frac{\mu_0 m_x}{4\pi} (-1)^{i+j+k} \operatorname{arsinh} \left[\frac{z - z_k}{\sqrt{r^2 - (z - z_k)^2}} \right] \\
B_z(x, y, z) &= \frac{\mu_0 m_z}{4\pi} \sum_{i,j,k=0}^1 (-1)^{i+j+k} \arctan \left[\frac{(x - x_i)(y - y_j)}{(z - z_k) \times r} \right] \\
&\quad - \frac{\mu_0 m_x}{4\pi} (-1)^{i+j+k} \operatorname{arsinh} \left[\frac{y - y_j}{\sqrt{r^2 - (y - y_j)^2}} \right] \\
&\quad - \frac{\mu_0 m_y}{4\pi} (-1)^{i+j+k} \operatorname{arsinh} \left[\frac{x - x_i}{\sqrt{r^2 - (x - x_i)^2}} \right]
\end{aligned} \tag{B.1}$$

We perform Monte-Carlo simulations as a confirmation of relevant MOT parameters. Our results show that a field gradient of ≈ 50 G/cm is sufficient for trapping atoms.

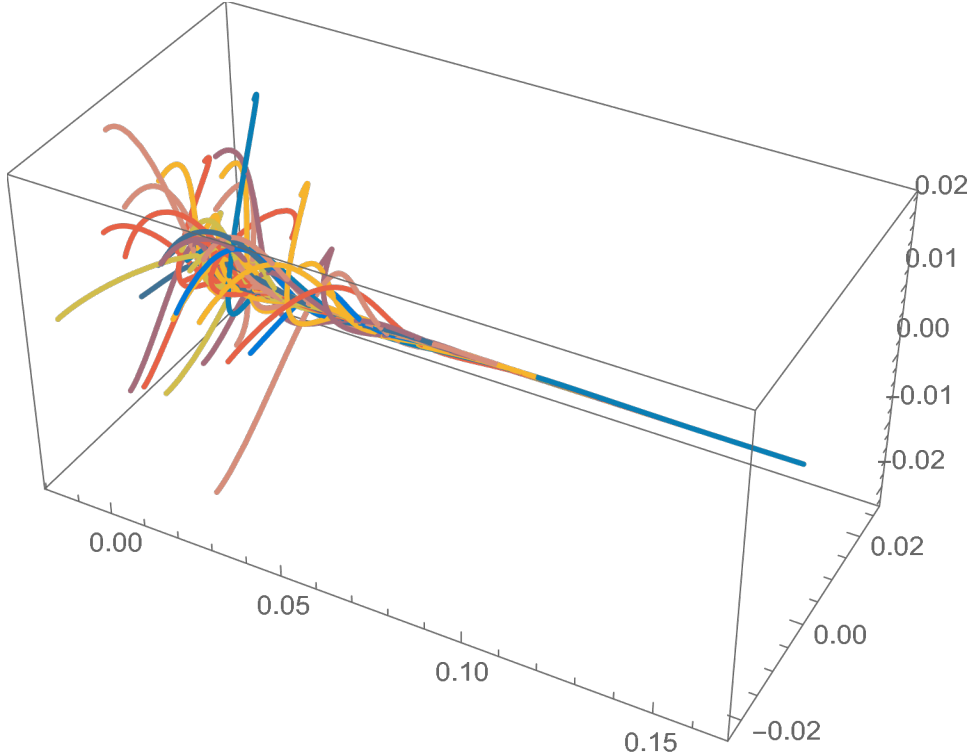


Figure B.2: Monte Carlo simulation of atom trajectories in a proposed erbium 2DMOT set up.

B.2 Injection locking of multi-mode diodes at 401nm

Using a seed-follower injection locking setup we demonstrate production of reasonable optical powers (≈ 300 mW) for trapping and cooling erbium atoms. Here we take advantage of commercially available UV diodes around 405 nm and show robust injection locking for relatively low seed powers (≈ 1 mW).

B.2.1 Optical set up

Here we tune the diode head temperature from 20° C and 32° C. For each value we take measurements for diode currents 360 mA, 390 mA and 420 mA and take the average. We obtain the center wavelength by fitting to a Gaussian.

We see that the diode center wavelength changes from 398.7 nm to 399.8 nm (here we have included the shift of +.4 nm from calibrating the optical spectrum analyzer properly)

Failure to successfully activate erbium dispenser (shown on Fig. B.5) crippled our

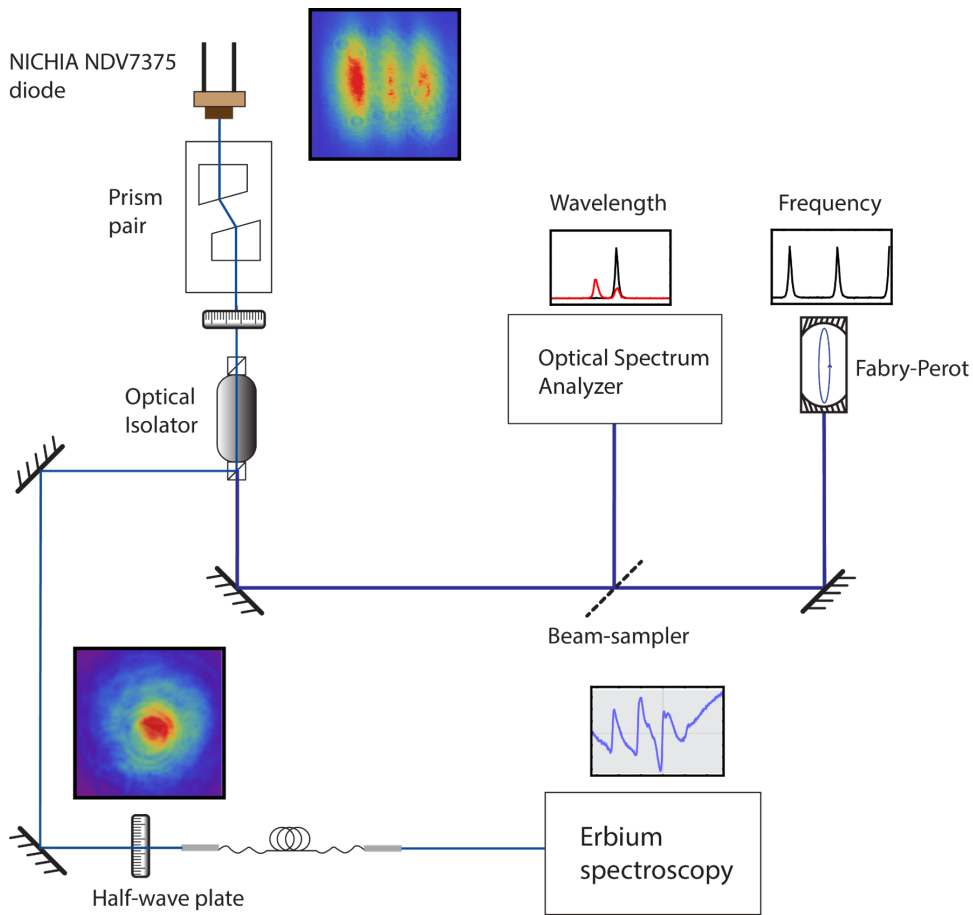


Figure B.3: Injection locking set up.

progress but ushered in a new phase of cooling and trapping potassium atoms (which was already ongoing) in an array of optical tweezers. Work done during this phase has led to published work that demonstrates polarization spectroscopy of erbium atoms in a hollow cathode lamp as a simple technique for laser stabilization in systems used for trapping and cooling lanthanide atoms [53].

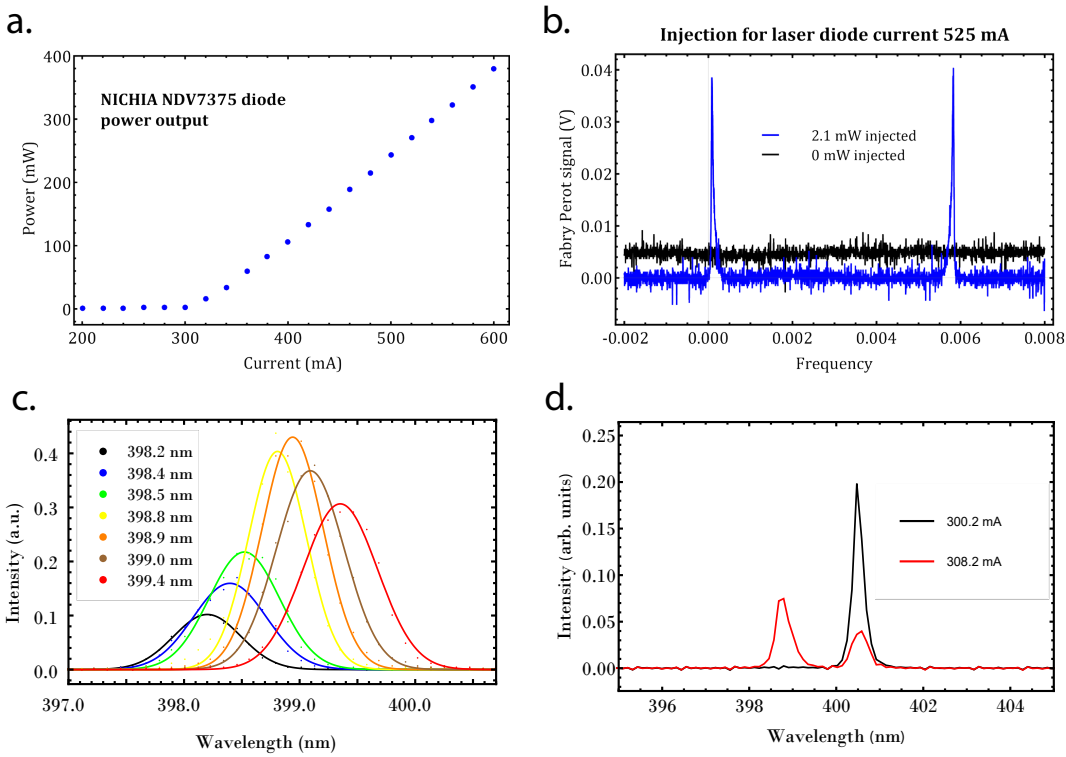


Figure B.4: Tuning the temperature of a diode in order to get it working around 401nm for laser cooling of erbium.

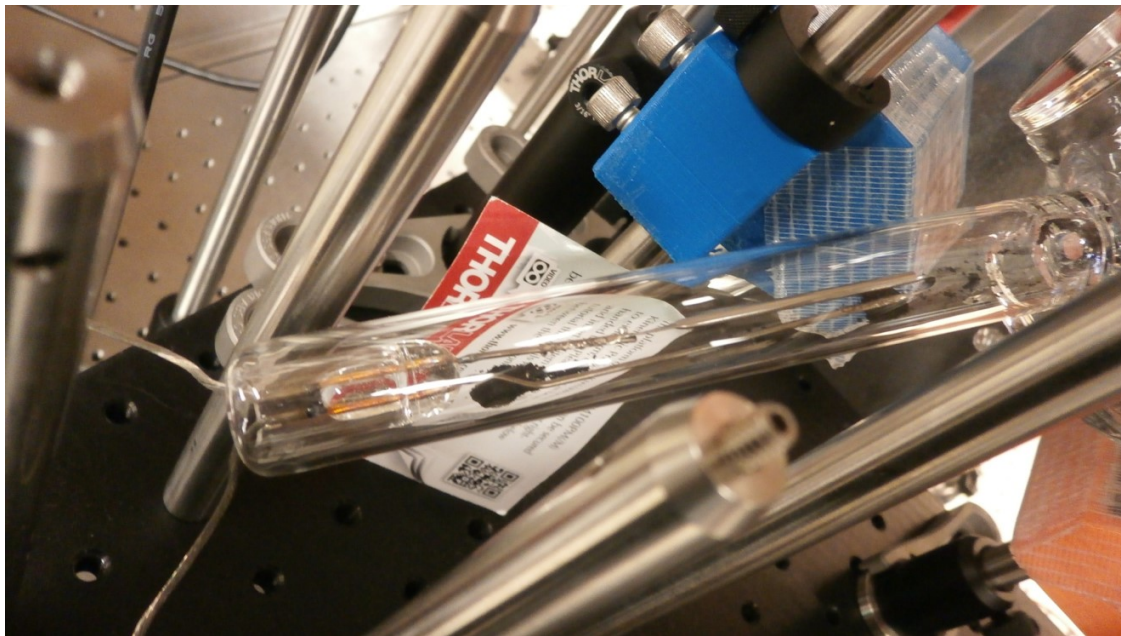


Figure B.5: Erbium dispenser after failed activation.

Appendix C

Thorlabs USB camera MATLAB control

This section contains Matlab code we use to control Thorlabs DCC3260M CCD camera as adapted from Thorlabs camera manuals. Parts of the code were inherited from the DeMarco lab courtesy of Laura Wadleigh and Will Morong.

```

%%  

close all  

%closes all open figure windows  

NET.addAssembly('C:\Program Files\Thorlabs\Scientific Imaging\DCx Camera Support\  

Develop\DotNet\uc480DotNet.dll'); %this imports the right file, you might have to change  

cam = uc480.Camera;  

% Creating folder according to the date  

ParentFold = 'C:\Users\gad\Desktop\data';  

[y,m,d] = ymd(datetime('today'));  

fold = sprintf('%s\\%d\\0%d\\%d',ParentFold,y,m,d);  

if ~exist(fold,'dir')  

    mkdir (fold)  

end  

% Optional line to create arbitrary file path  

% str = input('Enter the file path where you want to save the images: ', 's');  

% Input the file path where you wanna save the images  

% like 'C:\Users\gadwaylab\Desktop\HelloWorld\20181219', for example.  

% NumImage = input('Enter the number of the images you want to save: ');  

% Actual file path/folder and number of images is fixed  

% to previously created folder and to two images for this example  

str = fold;  

NumImage = 2;  

% Actual image naming--typically 'image'+index e.g. image1, image2,..., image1000  

% This image name is later concatenated with the folder that corresponds  

% to the specific day and saved  

% on the folder corresponding to that specific day.  

% Optional standard input/output to customize  

% DoName=input('Do you want to name your image files by yourself? 0 for No,  

%%           1 for Yes : ');\n  

% if DoName  

%     Name = input('Tell me the name : ','s');  

% else  

%     Name = 'Image';  

% end  

%% The name of the images will be displayed as Year-Month-Day-Name[##]  

Name = 'image';  

try  

    cam.Init(0);  

    cam.Display.Mode.Set(uc480.Defines.DisplayMode.DIB)  

    ;%Store image in memory, or something about that  

    cam.PixelFormat.Set(uc480.Defines.ColorMode.Mono12);

```

```
%12 bit data storage, I think, 8 and 16 are also options

%cam.Trigger.Set(uc480.Defines.TriggerMode.Hi_Lo) %Falling edge trigger
cam.Trigger.Set(uc480.Defines.TriggerMode.Lo_Hi); %Triggers on a rising edge

%cam.Trigger.Set(uc480.Defines.TriggerMode.Software);
%This option %works with out a trigger,
%taking an image as soon as "freeze" is %called

%% camera settings
gain=100; %Camera gain
cam.Timing.Exposure.Set(0.5); %set and check the exposure time in ms
[~,ExposureTime]=cam.Timing.Exposure.Get();

cam.Gain.Hardware.Scaled.SetMaster(gain);%1-100 is x24 gain

%%%%%%%%%%%%%
LH=addlistener(cam,'EventExtTrigger',@Read_Image);
%Read_Image is a separate routine
>Create a listener to make a new spot in memory and wait for a trigger everytime
%the camera is triggered

[~, MemId] = cam.Memory.Allocate(true);
%allocates memory for the image, the spot in memory is an integer MemId
[~, Width, Height, Bits, ~] = cam.Memory.Inquire(MemId);
%find the size of the image

cam.Acquisition.Freeze(uc480.Defines.DeviceParameter.DontWait);
%take an image, don't wait for the image to come in
%before moving on in the program. "Wait" is the other option

numMemIdList = NumImage + 1;
%how many memory spots are made
%(there's an extra one because it makes a spot in memory after the last image)

[~,memIdList] = cam.Memory.GetList();
%return a list of the labels of the memory spots


disp('starting the damn forloop')
while memIdList.Length < numMemIdList

%wait until there are the desired number of places in memory
pause(1);
[~,memIdList] = cam.Memory.GetList();
if j<NumImage
 [~, tmp] = cam.Memory.CopyToArray(MemId+j-1,uc480.Defines.ColorMode.Mono12);

%varvar=genvarname('Data',int2str(j))

Data1 = reshape(uint16(tmp), [Bits/12, Width, Height]);
```

```

Data1 = permute(Data1, [3,2,1]);
Data1 = double(Data1);

%%%%%Data1(Height/4:Height/2,Width/4:Width/2) trim data

%Trimmed image
minimH=floor(0.3*Height);
minimW=floor(0.3*Width);
maximH=floor(0.55*Height);
maximW=floor(0.55*Width);
Data1B=Data1(minimH:maximH,minimW:maximW);

%Save the image
fname = sprintf(strcat('%d-0\%d-%d-%s[%d]' ),y,m,d,Name,j+startidx);
imwrite(mat2gray(Data1B), strcat(fold,'\',Name,'_',int2str(j+startidx),'.bmp'), 'bmp'

%make a figure of each image
FIG = figure;
imagesc(Data1B'); %colorbar;
end
j=j+1;
end

catch ME
%this (allong with the try at the top) are here so the camera is
%closed even when the program throws an error.
%If you don't exit the camera you won't be able to open it again
%the next time you run the program
cam.Exit
rethrow(ME)
end

cam.Exit
OffFig = input('Do you wanna close all figures? 0 for No, 1 for Yes : ');
if OffFig == 1
    close all
end
%
startidx=startidx+NumImage;

```

```
%For loop for running a large number of shots

imagenum=100;
for a = 1:imagenum

ThorcamRunner
a
startidx
%cam.Timeout.Set(uc480.Defines.TimeoutMode,8640000); disp(imagenum-a)
end

%Read_Image routine called on the main code

function Read_Image(cam,~) tic
cam.Memory.Allocate(true); cam.Acquisition.Freeze(); toc
end
```

Appendix D

Simulating Polarization Spectroscopy Signals

This appendix continues the discussion from Section 2.3.1 in more detail. The first Section will show derivations of expected PS spectra while the second part will show a notebook example for simulating PS signals for the D1 transition of ^{39}K .

D.1 Theoretical modeling of polarization spectroscopy signal

We describe a general approach used to simulate polarization spectra by solving rate equations for all possible transitions that can be induced by the right-circularly-polarized pump beam resonant with the $4S_{1/2} \rightarrow 4P_{1/2}$ transition in potassium 39. The derivations in this sections are done for an arbitrary $F \rightarrow F'$ transition. As an example, however, we will model such transitions for the D1 line i.e. $F \rightarrow (1, 2)$ for the ground state and $F' \rightarrow (1, 2)$ for the excited state. Here, the hyperfine quantum number, F , ranges from $F = |I - J|$ to $F = |I + J|$, where $I = 3/2$ and $J = 1/2$. The projection of F onto the z -axis, m_F , is the hyperfine sub-level.

Additional cross-over peaks occur at a frequency half-way between two transitions. This happens where the velocity of some atoms in the vapor cell (at a frequency exactly half-way between two frequencies) leads to a Doppler shift of either the pump beam to a higher frequency or the probe beam to a lower frequency. We therefore end up with 9 transitions to consider for the D1 line as shown in Figure 2.9.

As shown in more detail in Ref. [54], the difference signal for a single transition is given by

$$S_{\text{diff}}(\omega) \propto e^{-\bar{\alpha}l} \left(\Delta\alpha l' \frac{x(\omega)}{1+x(\omega)^2} \right), \quad (\text{D.1})$$

where $x(\omega) = \frac{\omega-\omega_0}{\Gamma/2}$, Γ is the spontaneous decay rate of the atom ($\Gamma = 2\pi \times 5.956$ MHz for the D1 line [110]), l is the length of the active area of interrogation (effective length of cell), l' is the effective length of interrogation where the pump and probe beam overlap, $\bar{\alpha}$ is the average of the absorption coefficients corresponding to right- and left-circular polarizations pump beams, and $\Delta\alpha$ is the anisotropy, i.e. the difference between these two absorption coefficients.

The pump beam induced anisotropy corresponding with a transition $F \rightarrow F'$ is given by

$$\begin{aligned} \Delta\alpha(F, F', t) = & n\sigma_0 \sum_{m_F=-F}^F \mathcal{R}_{(F,m_F) \rightarrow (F',m_F+1)} (\rho_{F,m_F} - \rho'_{F',m_F+1}) - \mathcal{R}_{(F,m_F) \rightarrow (F',m_F-1)} (\rho_{F,m_F} - \rho'_{F',m_F-1}), \end{aligned} \quad (\text{D.2})$$

where n and σ_0 are the atomic density and resonant absorption cross-section, respectively [50, 51, 130]. The transition line strength, $\mathcal{R}_{(F,m_F) \rightarrow (F',m'_F)}$, is the square magnitude of the dipole matrix element for the transition between two levels [60, 131], i.e.

$$\begin{aligned} \mathcal{R}_{(F,m_F) \rightarrow (F',m'_F)} = & |e \langle n'L' || r || nL \rangle|^2 (2J' + 1)(2J + 1)(2F' + 1)(2F + 1) \\ & \times \left[\left\{ \begin{array}{ccc} L' & J' & S \\ J & L & 1 \end{array} \right\} \left\{ \begin{array}{ccc} J' & F' & I \\ F & J & 1 \end{array} \right\} \left(\begin{array}{ccc} F & 1 & F' \\ m_F & \Delta m & -m_{F'} \end{array} \right) \right]^2, \end{aligned} \quad (\text{D.3})$$

where the quantity $\langle \text{final} || r || \text{initial} \rangle$ is the reduced matrix element which can be simplified using the Wigner-Eckart theorem [132], L and S are the electronic orbital and spin angular momentum quantum numbers, respectively, while I is the nuclear spin angular momentum. The factors $\{ \dots \}$ and (\dots) are the 6J symbol and 3J symbol, respectively, and can be computed using symbolic software packages. The fractional population of the m_F sublevel

is labeled as ρ_{F,m_F} .

The population dynamics are therefore described by the rate equations generalized for multilevel atoms [51?], i.e.

$$\begin{aligned} \frac{d\rho_{F,m_F}}{dt} = & - \sum_{F'=F-1}^{F'=F+1} \mathcal{R}_{(F,m_F) \rightarrow (F',m_F+\Delta m)} \frac{\Gamma}{2} s \frac{(\rho_{F,m_F} - \rho'_{F',m_F+\Delta m})}{1 + 4(\tilde{\Delta}/\Gamma)^2} \\ & - \sum_{m_{F'}=m_{F+1}}^{m_{F'}=m_{F+1}} \sum_{F'=F-1}^{F'=F+1} \mathcal{R}_{(F,m_F) \rightarrow (F',m_{F'})} \Gamma \rho'_{F',m_{F'}}. \end{aligned} \quad (\text{D.4})$$

For the change in the hyperfine sub-level, $\Delta m = \pm 1$ represents σ^\pm transitions while $\Delta m = 0$ represents π transitions. The saturation parameter is given by $s = I/I_{\text{sat}}$ where I is the beam intensity and I_{sat} is the saturation intensity (1.75 mW/cm² for potassium 39). The detuning associated with the transition $F \rightarrow F'$ is given by $\tilde{\Delta} = \Delta + \Delta_{F,F'}$ where $\Delta_{F,F'}$ is the detuning from the $4S_{1/2} \rightarrow 4P_{1/2}$ line. The last term corresponds to spontaneous emission out of the excited state.

The difference signal measured in experiment is proportional to a time averaged anisotropy. Following the discussion in Ref. [51], we account for this in the model by introducing a weighting function that characterizes the atomic trajectories transverse to the direction of propagation of the beam. These trajectories correspond to a class of atoms with a vanishing velocity component along the beam. The weighting function, given by

$$W(t) = \int_0^{2a} f(z) g(z, t) dz, \quad (\text{D.5})$$

consists of a probability distribution $f(z)$ for different trajectory path lengths $z \in (0, 2a)$ where a is the radius of the beam. In our case we consider uniform probabilities for all path lengths, i.e. $f(z) = 1/2a$. The second component of the weighting function relates to the distribution, $g(z, t)$, of interrogation times for the trajectories of path length z transverse to the beam. The velocity profile of atoms in the vapor cell can be effectively captured by a

Maxwell-Boltzmann distribution. The expression becomes

$$W(t) = \int_0^{2a} \frac{1}{2a} \frac{mz^2}{k_B T t^2} \text{Exp}\left(-\frac{mz^2}{2k_B T t^2}\right) dz. \quad (\text{D.6})$$

The time averaged anisotropy is therefore given by citeharris

$$\mathcal{A}(F, F') = \int_0^{t_{\text{final}}} \frac{1}{t_{\text{final}}} \Delta\alpha(F, F', t) W(t) dt, \quad (\text{D.7})$$

where t_{final} is the total interrogation time. Considering the characteristic velocity ($\sim 3 \times 10^5$ mm/s) and the size of the pump beam (~ 1 mm), the dynamics have essentially ceased in a few microseconds. By choosing $t_{\text{final}} = 10 \mu\text{s}$ we take, effectively, the long time limit.

While $\mathcal{A}(F, F')$ only depends on the pump beam parameters, the attenuation of the probe signal, governed by the Beer-Lambert law, is captured in the pre-factor

$$e^{-\bar{\alpha}l} \sim T(\omega)/T_{\max}, \quad (\text{D.8})$$

where $T(\omega)/T_{\max}$ is the transmitted probe signal, normalized to the incident probe signal obtained from the A output of the photodetector. That is, we convolute the numerically simulated lineshape with $T(\omega)/T_{\max}$, the observed (normalized) absorption profile. Using Eq. (D.2) with $\Delta\alpha \rightarrow \mathcal{A}(F, F')$, we can now model the expected lineshapes. Crossover peaks between two features are calculated by taking the mean $\mathcal{A}(F, F')$ of the associated transitions [131]. The simulated polarization spectroscopy lineshape is therefore given by

$$S_{\text{diff}}(\omega) \propto \sum_{\{F, F'\}} \frac{T(\omega)}{T_{\max}} \left(\mathcal{A}(F, F') l' \frac{x(\omega)}{1 + x(\omega)^2} \right). \quad (\text{D.9})$$

The simulation assumes near-resonant pump beam frequency for each transition and adds up the dispersive signals relating to all the transitions to construct the final lineshape.

D.2 Solving rate equations with Mathematica

This section details a Mathematica example code for solving rate equations in order to simulate the polarization spectroscopy signal in the case of the D1 ($4S_{1/2} \rightarrow 4P_{1/2}$) transition in ^{39}K . The simulated signal is then compared to a recorded signal based on a vapor cell set up in the lab.

The code follows work done in [53] and [51] which is also described in chapter [apparatus] section [polarization spectroscopy] and was useful in our case for identifying which transitions to lock to in order to generate the correct laser frequencies for trapping and cooling of potassium atoms. While I choose the D1 transition for brevity as an example, the code can however be easily adapted to calculate expected signals for any other transitions and also for any other atomic species.

```
In[760]:= LineStrength[Lg_, Le_, Jg_, Je_, Fg_, Fe_, mFg_, mFe_, S_, II_] :=
  
$$\left( (-1)^{(*2Fg+*)} \cdot 1 + Jg + Je + S + Le + II - mFe \right) \cdot$$

  
$$\sqrt{(2Le+1) \cdot (2Je+1) \cdot (2Jg+1) \cdot (2Fe+1) \cdot (2Fg+1)}$$

  
$$\cdot SixJSymbol[\{Je, Fe, II\}, \{Fg, Jg, 1\}] \cdot SixJSymbol[\{Le, Je, S\}, \{Jg, Lg, 1\}] \cdot$$

  
$$ThreeJSymbol[\{Fg, mFg\}, \{1, mFe - mFg\}, \{Fe, -mFe\}] \right)^2$$

```

```
Rates[F_, Fprime_, mF_, mFprime_] := Module[{Lg, Le, Jg, Je, S, I},
  If[Abs[mFprime] > Abs[Fprime] || Abs[mF] > Abs[F], 0,
    S = 1/2;
    Jg = 1/2;
    Je = 1/2;
    I = 3/2;
    Lg = 0;
    Le = 1;
    (LineStrength[Lg, Le, Jg, Je, F, Fprime, mF, mFprime, S, I] /
     LineStrength[Lg, Le, Jg, 1/2, 1, 2, 1, 2, S, I])^1
  ]];

```

```
(*Initial Conditions and constraints for rate differential equations*)
FgList = {1, 2}; (*Ground state hyperfine levels*)
FeList = {1, 2}; (*Excited state hyperfine levels*)
varList = Join[Join[Flatten[Table[Table[p[i, j], {i, -j, j}], {j, Range[1, 2]}]], 1],
  Flatten[Table[Table[q[i, j], {i, -j, j}], {j, Range[1, 2]}]], 1]];
initCond = Join[Join[Flatten[Table[p[i, j][0] =  $\frac{1}{8}$ , {i, -j, j}],
  {j, Range[1, 2]}]], 1],
  Flatten[Table[Table[q[i, j][0] = 0, {i, -j, j}], {j, Range[1, 2]}]], 1]];
Constraints = {Total[Join[Flatten[
  Table[Table[p[i, j][t], {i, -j, j}], {j, Range[1, 2]}]], 1],
  Flatten[Table[Table[q[i, j][t], {i, -j, j}], {j, Range[1, 2]}]], 1]] == 1};

(*Function detailing the frequency offset from 391016GHz*)
Δprime[Fprime_, F_, Δ_] := Module[{Δ22, Δ21, ΔGS, ΔES},
  ΔGS = 288.6 * 2 π * 106;
  ΔES = (-173 * 2 π * 106);
  Δ21 = -34.7 * 2 π * 106;
  Δ22 = 20.8 * 2 π * 106;
  If[F == 2,
    Which[Fprime == 2, Δ + Δ22 + ΔES, Fprime == 1, Δ + Δ21 + ΔES],
    If[F == 1, Which[Fprime == 1, Δ + Δ21 + ΔGS, Fprime == 2, Δ + Δ22 + ΔGS], 0]]
  ]
]
```

```
In[768]:= (*Function calculating rate equations
for ground states pmF,F and excited states qmF,F)
func[t_, qpr_, FgList_, FeList_, A_, S0_] :=
Join[Join[
(*ReplacePart[*])Flatten[
Table[Table[ $p[mF, FF]'[t] = - \left( \sum_{\text{If}[(Fe > \text{Max}[FeList] \text{ || } Fe < \text{Min}[FeList])} \right.$ 
 $0, \text{Rates}[FF, Fe, mF, mF + qpr] * \frac{\Gamma}{2} \frac{S0}{1 + 4 \left( \frac{\Delta\text{prime}[Fe, FF, A]}{\Gamma} \right)^2}$ 
 $(p[mF, FF][t] - q[mF + qpr, Fe][t]), \{Fe, FF - 1, FF + 1\}] -$ 
 $\sum_{\text{Sum}[\text{If}[(Fe > \text{Max}[FeList] \text{ || } Fe < \text{Min}[FeList])}, 0, \text{Rates}[FF, Fe, mF,$ 
 $mFe] * \Gamma * q[mFe, Fe][t], \{Fe, FF - 1, FF + 1\}], \{mFe, mF - 1, mF + 1\}] \left. \right)$ ,
 $\{mF, -FF, FF, 1\}], \{FF, FgList\}], 1] (*,2→Constraints[[1]]*)],
Join[{}, Flatten[Table[Table[
 $q[mFe, Fe]'[t] =$ 
 $\sum_{\text{If}[(FF > \text{Max}[FgList] \text{ || } FF < \text{Min}[FgList])},$ 
 $0, \text{Rates}[FF, Fe, mFe - qpr, mFe] * \frac{\Gamma}{2} \frac{S0}{1 + 4 \left( \frac{\Delta\text{prime}[Fe, FF, A]}{\Gamma} \right)^2}$ 
 $(p[mFe - qpr, FF][t] - q[mFe, Fe][t]), \{FF, Fe - 1, Fe + 1\}] -$ 
 $\sum_{\text{Sum}[\text{If}[(FF > \text{Max}[FgList] \text{ || } FF < \text{Min}[FgList])}, 0, \text{Rates}[FF, Fe, mF,$ 
 $mFe] * \Gamma * q[mFe, Fe][t], \{FF, Fe - 1, Fe + 1\}], \{mF, mFe - 1, mFe + 1\}] \left. \right)$ ,
 $\{mFe, -Fe, Fe, 1\}], \{Fe, FeList\}], 1] ]], initCond]$$ 
```

```
S0 = 2.8; (*Saturation parameter*)
Γ = 2 π * √(1 + S0) * 5.9 * 106; (*Linewidth*)

Δ22 = (20.8) * 2 π * 106;
Δ21 = (-34.7) * 2 π * 106;
Δ11 = (288.6 - 34.7) * 2 π * 106;
Δ12 = (288.6 + 20.8) * 2 π * 106;
```

```

pol = 1; (*polarization of the pump beam*)
tfinal = 2 * 2500; (*Evolution time*)
(*Solving the rate equations for evolution
between all possible state at different detunings
corresponding to allowed transitions*)
aa21 = NDSolve[func[t, pol, FgList, FeList, Δ21, S0], varList, {t, 0, tfinal}];
bb21 = NDSolve[func[t, pol, FgList, FeList, Δ21, S0], varList, {t, 0, tfinal}];

aa22 = NDSolve[func[t, pol, FgList, FeList, Δ22, S0], varList, {t, 0, tfinal}];
bb22 = NDSolve[func[t, pol, FgList, FeList, Δ22, S0], varList, {t, 0, tfinal}];

aa11 = NDSolve[func[t, pol, FgList, FeList, Δ11, S0], varList, {t, 0, tfinal}];
bb11 = NDSolve[func[t, pol, FgList, FeList, Δ11, S0], varList, {t, 0, tfinal}];

aa12 = NDSolve[func[t, pol, FgList, FeList, Δ12, S0], varList, {t, 0, tfinal}];
bb12 = NDSolve[func[t, pol, FgList, FeList, Δ12, S0], varList, {t, 0, tfinal}];

```

In[822]:=

```

funcESRight[t_, mF_, FF_, bb_] := Evaluate[q[mF, FF][t]] /.
  (Which[bb == 0, aa21, bb == 1, aa22, bb == 2, aa11, bb == 3, aa12])
funcESLeft[t_, mF_, FF_, bb_] := Evaluate[q[mF, FF][t]] /.
  (Which[bb == 0, bb21, bb == 1, bb22, bb == 2, bb11, bb == 3, bb12])
funcGSRRight[t_, mF_, FF_, bb_] := Evaluate[p[mF, FF][t]] /.
  (Which[bb == 0, aa21, bb == 1, aa22, bb == 2, aa11, bb == 3, aa12])
funcGSLeft[t_, mF_, FF_, bb_] := Evaluate[p[mF, FF][t]] /.
  (Which[bb == 0, bb21, bb == 1, bb22, bb == 2, bb11, bb == 3, bb12])

```

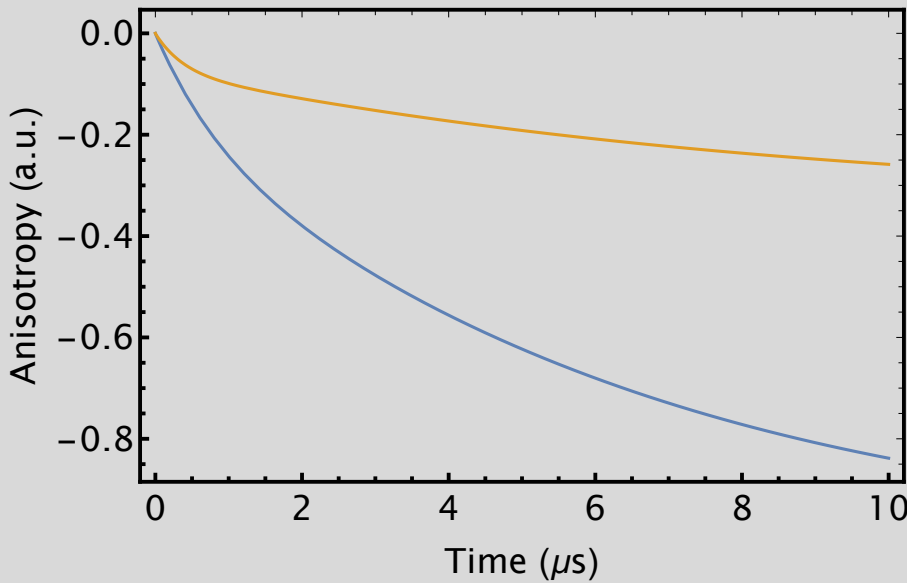
```

(*Time dependent anisotropy*)
An[t_, FF_, Fprime_] := Module[{bb},
  Which[FF == 2 && Fprime == 1, bb = 0, FF == 2 && Fprime == 2,
    bb = 1, FF == 1 && Fprime == 1, bb = 2, FF == 1 && Fprime == 2, bb = 3];
  Sum[Rates[FF, Fprime, mF, mF + 1] * (funcGSRRight[t, mF, FF, bb] - funcESRight[t,
    mF + 1, Fprime, bb]), {mF, -FF, FF}] - Sum[Rates[FF, Fprime, mF, mF - 1] *
  (funcGSLeft[t, mF, FF, bb] - funcESLeft[t, mF - 1, Fprime, bb]), {mF, -FF, FF}]]

```

```
In[897]:= Plot[Evaluate@Table[An[t * 10-6, 2, ii], {ii, 1, 2}], {t, 0, 10}, Frame -> True, ImageSize -> 500, FrameLabel -> {{{"Anisotropy (a.u.)"}, ""}, {"Time (μs)", ""}}, FrameStyle -> Directive[Thick, Black, FontSize -> 18, FontFamily -> "Myriad Pro"]]
```

Out[897]=



$a = 2.5 * 10^{-3}$; $KbT = 1.38 * 1000 * 10^{-23}$; $m = 6.47 * 10^{-26}$;
(*radius of beam area of overlap,
effective temperature of the vapor, mass of the atom*)

```
PathLength[l_, a_] :=  $\frac{l}{2 a \sqrt{4 a^2 - l^2}}$ ;
VelocityDist[t_, l_] :=  $\frac{m l^2}{KbT t^3} \text{Exp}\left[-\frac{m l^2}{2 KbT t^2}\right]$ 
HH[t_] := Integrate[ $\frac{1}{2 a \sqrt{4 a^2 - l^2}} * \frac{m l^2}{KbT t^3} \text{Exp}\left[-\frac{m l^2}{2 KbT t^2}\right]$ , {l, 0, 2 a}]
x[d_] :=  $\left(\frac{d}{r/2.}\right)$ 
```

```
In[898]:= (*Averaged anisotropy*)
AvgAn22 = NIntegrate[An[t, 2, 2] * HH[t], {t, 0, \[Infinity]},
  Method \[Rule] "AdaptiveQuasiMonteCarlo", MaxRecursion \[Rule] 40][[1]];
AvgAn21 = NIntegrate[An[t, 2, 1] * HH[t], {t, 0, \[Infinity]},
  Method \[Rule] "AdaptiveQuasiMonteCarlo", MaxRecursion \[Rule] 40][[1]];

AvgAn12 = NIntegrate[An[t, 1, 2] * HH[t], {t, 0, \[Infinity]},
  Method \[Rule] "AdaptiveQuasiMonteCarlo", MaxRecursion \[Rule] 40][[1]];
AvgAn11 = NIntegrate[An[t, 1, 1] * HH[t], {t, 0, \[Infinity]},
  Method \[Rule] "AdaptiveQuasiMonteCarlo", MaxRecursion \[Rule] 40][[1]];
```

```
(*Adding in the dispersive part of the signal*)
GenSig[avg_, \[Delta]_, \[Delta]prime_] := avg * 
$$\frac{x[-\Delta + \Delta prime]}{1 + (x[-\Delta + \Delta prime])^2};$$

CrossOver[avg1_, avg2_, \[Delta]_, \[Delta]prime1_, \[Delta]prime2_] :=

$$(avg1 + avg2) * 0.5 * \frac{x[-\Delta + (\Delta prime1 + \Delta prime2) * 0.5]}{1 + (x[-\Delta + (\Delta prime1 + \Delta prime2) * 0.5])^2};$$

```

```
(*Adjusting the x axis so that everything is detuned from F=2 \[Rightarrow] F'=1 transition*)
\Delta GS = 288.6 * 2 \[Pi] * 10^6;
\Delta 21 = (-173.1 - 34.7) * 2 \[Pi] * 10^6;
\Delta 22 = ((-173.1 + 20.8) * 2 \[Pi] * 10^6) + Abs[\Delta 21];
\Delta 11 = ((288.6 - 34.7) * 2 \[Pi] * 10^6) + Abs[\Delta 21];
\Delta 12 = ((288.6 + 20.8) * 2 \[Pi] * 10^6) + Abs[\Delta 21];
\Delta 21 = 0;
shiftby = (2 \[Pi]) * 10^6; (*Keep everything in MHz*)
```

```
In[892]:= (*Plot everything including a Gaussian dip corresponding to probe absorption dip*)
Plot[-250 * Evaluate[PDF[NormalDistribution[0, 250], Δ - 240]] +
  GenSig[AvgAn21, Δ * shiftby, Δ21] + GenSig[AvgAn11, Δ * shiftby, Δ11] +
  GenSig[AvgAn12, Δ * shiftby, Δ12] + GenSig[AvgAn22, Δ * shiftby, Δ22] +
  CrossOver[AvgAn11, AvgAn12, Δ * shiftby, Δ11, Δ12] +
  CrossOver[AvgAn11, AvgAn22, Δ * shiftby, Δ11, Δ22] +
  CrossOver[AvgAn11, AvgAn21, Δ * shiftby, Δ11, Δ21] +
  CrossOver[AvgAn12, AvgAn22, Δ * shiftby, Δ12, Δ22] +
  CrossOver[AvgAn12, AvgAn21, Δ * shiftby, Δ12, Δ21] +
  CrossOver[AvgAn22, AvgAn21, Δ * shiftby, Δ22, Δ21],
{Δ, -100, 600}, PlotRange → {All, All}, PlotStyle → Brown,
Frame → True, ImageSize → 500, FrameLabel →
{{"Signal (V)", ""}, {"Frequency Offset (MHz)", "Polarization Signal for K39 "}},
FrameStyle → Directive[Thick, Black, FontSize → 18, FontFamily → "Myriad Pro"]]
```

Out[892]=

